Università degli Studi di Torino
Doctoral School of the University of Torino
PhD Programme in Chemical and Materials Sciences XXXIV Cycle

Spectroscopic characterization of silica-supported ethylene polymerization catalysts

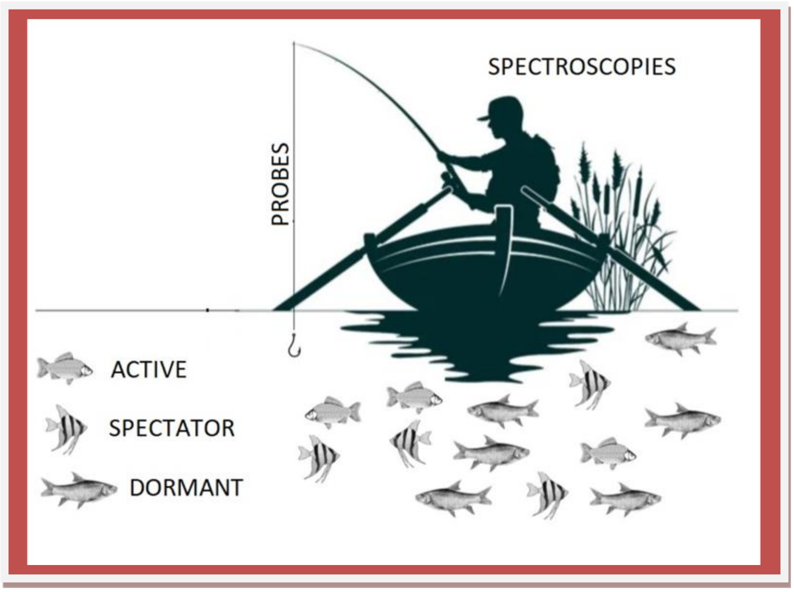

Jelena Zarupski

Supervisor:
Prof. Elena Groppo

Università degli Studi di Torino

Doctoral School of the University of Torino

PhD Programme in Chemical and Materials Sciences XXXIV cycle

Spectroscopic characterization of silica-supported ethylene polymerization catalysts

Candidate: **Jelena Zarupski**

Supervisor: Prof. **Elena Groppo**

Jury Members:
Dr. **Matteo Signorile**
Università di Torino
Dipartimento di Chimica

Prof. **Cristiano Zuccaccia**
Università di Perugia
Dipartimento di Chimica, Biologia e Biotecnologie

Dr. **Giuseppe Leone**
Italian National Council of Research (CNR) of Milano
Istituto di Scienze e Tecnologie Chimiche "Giulio Natta"

Head of the Doctoral School: Prof. Alberto Rizzuti
PhD Programme Coordinator: Prof. Bartolomeo Civalleri

Torino, 2023

To my grandmothers Milica and Mirjana, and to my mother Ljudmila

Мојој баби Милици, баки Мирјани и мајци Људмили

The research done within this PhD thesis was funded by a Dutch Polymer Institute (DPI, P.O. Box 902, 5600 AX Eindhoven, The Netherlands) and represents a part of the DPI Research Program project #813 MULTIPOL

Table of contents

Chapter 1

Chapter 2

Chapter 3

Chapter 4

Chapter 5

Chapter 6

CHAPTER 1

PREFACE

1. Polyolefins and their importance in everyday life

‘…polyolefins should be considered as a metastable state of the light fractions of refined oil. Rather than flaring them, as has happened in the past, these are temporarily solidified, used for all forms of smart applications at a nominal cost, and burned afterwards to produce energy (the most logical way of recycling/disposing). If this was understood by politicians, environmentalists, and opinion- makers, polyolefins would be recognized for what they are, namely the greenest and most environmentally friendly materials ever invented.’

Markus Gahleitner and John R. Severn[1]

Modern life is almost unimaginable without plastic: a material with very broad range of application that replaces traditional materials such are metals, glass, and wood and improves our everyday life.[2] In fact, plastics were introduced as average duplicate materials for traditional ones, but today after all engineering, they are advanced, hardly replaceable materials.[3] As data form EU commission says, plastic is mainly used for packaging (39.6%), but also in automotive and textile industry, in agriculture and medicine as well as in other fields of application, as can be seen from Figure 1. 1.[4]

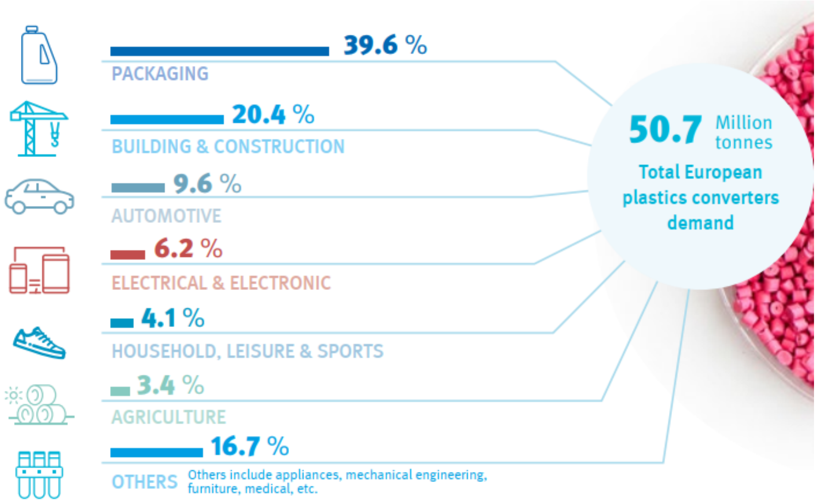

Figure 1. 1 Plastic demand by sector in 2019.[4]

Plastic has exceptionally good performances for low production price, making it even more attractive as a material. From global plastic production that reached astonishing 368 million tons in 2019 almost 50% are polyolefins (POs).[4] POs can be produced from both fossil fuel-based, bio-based and recycled feedstocks[5,6] so they indeed represent revolutionary materials that meet green polymer chemistry and sustainability requirements in an ideal way.[3,5,6] Produced in highly energy-efficient exothermic catalytic process generating heat, POs are hydrocarbon materials with high molar mass that have considerable amount of energy, in the range of oil. After end of use, POs can be thermally recycled to yield energy and light hydrocarbons that can be used as a feedstock in several industrial processes.[6] POs are composed just from two types of atoms – carbon and hydrogen – which makes them easily recyclable after end of use through thermo-mechanical or chemical routes.[7,8]

The fact that POs are composed from just two different atoms doesn't mean that they are simple and non-sophisticated materials, it is totally the opposite. By choosing the right catalytic system (controlling the polymerization process at molecular level) and polymerization conditions it is possible to tune POs properties to obtain desired product with wide range of properties and thus applications, which are the consequence of how monomer molecules are linked in polymer chain.[1,9,10] Hundreds of grades of POs with broad range of mechanical properties are present on the market, satisfying all customer's needs.[1]

POs, as all other plastic materials, exhibit the following properties:

- Exceptionally good cost/performance ratio
- High versatility in the terms of properties and application
- Low weight
- Resistance to corrosion
- Easy processing
- Versability regarding the feedstock (fossil-fuel based, bio-based, recycled)
- Highly resource-, eco-, cost- and energy-efficient production
- Energy content like oil and higher than wood
- Recyclability
- Low greenhouse gasses emission.[3,6]

Based on the monomer used as a feedstock POs can be divided in two main groups: polyethylene (PE) and polypropylene (PP) but can be further divided in several subgroups.[10] Since this thesis is devoted to the catalyst for PE synthesis focus will be just on it.

2. Polyethylene and catalysts for ethylene polymerization

2.1 Generalities

Polyethylene is the simplest polymer, represented with $(-CH_2-CH_2-)_n$ formula. It is a semicrystalline material (a mixture of crystalline and amorphous fractions in different proportions) and can have short and long branches.[9] Based on the average molecular weight (MW), PEs are divided in three main groups (Figure 1. 2):

1) Low density polyethylene (LDPE) with average MW 0.915–0.940 g cm^{-3},
2) Linear low-density polyethylene (LLDPE) with MW 0.915-0.94 g cm^{-3}, and
3) High-density polyethylene (HDPE) having MW from 0.945 to 0.97 g cm^{-3}.[10]

Low-density polyethylene (LDPE) is entirely produced through a radical process conducted at high temperature and high pressure.[10] All the other PE grades, instead, are produced in a catalytic way, requiring a polymerization catalyst. The generally assumed polymerization mechanism is the so-called Cossee mechanism, which requires the presence of a coordination vacancy around the active site, and an alkyl group (or a hydride). At first, the monomer coordinates to the active site, followed by the migratory insertion of the alkyl group into the coordinated monomer, and the consequent elongation of the chain.

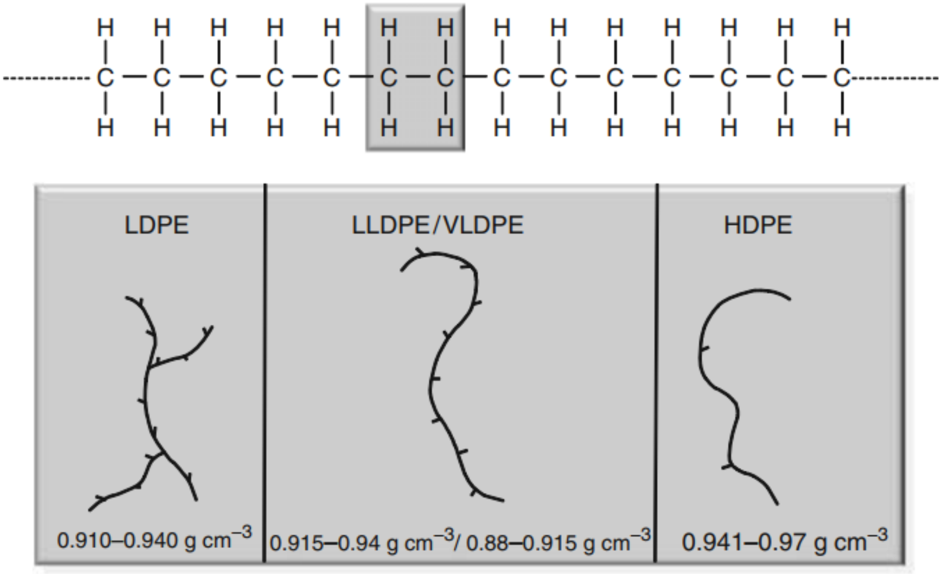

Figure 1. 2 Classification of PE based on branching, structure, and density.[10]

2.2 A short history and reasons for co-existence of several ethylene polymerization catalysts

Figure 1. 3 shows some of the main breakthroughs in the industrial PE production. For the first time PE was produced as a side product in thermal decomposition of diazomethane back in 19th century, but just later it was categorized as a polymer.[1] In 1933 LDPE was produced, by case, in high-pressure process, and some years later the first commercial PE production was established.[2] The biggest milestone in PE production occurred in 1950s when Phillips[11] and Ziegler-Natta [12,13] catalysts were discovered. Next milestone was in 1980s when Kaminsky and co-workers [14] discovered methylaluminoxane (MAO) as activator for metallocene-based catalysts. These big discoveries opened the door for industrial-scale POs production, reaching astonishing 181 million tons in 2019 and enabled tailoring PO properties to obtain advanced materials of integral importance for both human population and sustainability.[4,6] Although discovered decades ago, these catalysts are still evolving and improving, mainly by trial-and-error approach[1] due to lack of information on their active sites structure. The latter is the consequence of their high air and moisture sensitivity, complexity of the system, dilution of the metal sites, and the small concentration of the active sites.[15] What is very interesting when speaking about polymerization catalyst, is the fact that each new catalyst type/generation didn't push out of the market the older ones but generated a new type of the final product.[10] It is also important to mention that modern catalysts for olefin polymerization have so high activity that they are not removed neither recovered from the final product but remain in produced polymer.

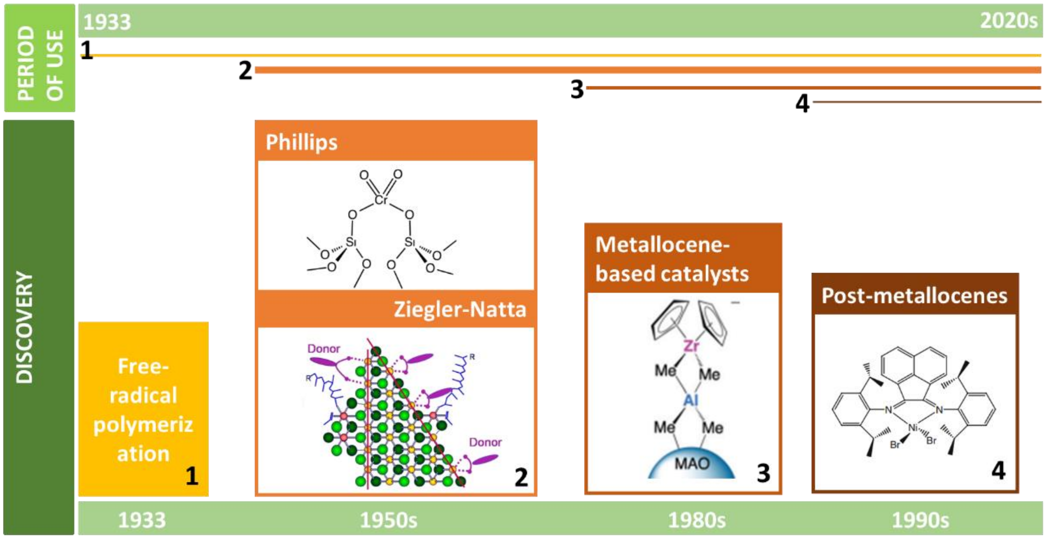

Figure 1. 3 Timetable of discoveries related to catalysts for olefin polymerization and period of their use. The weight of the lines indicate the catalyst/process scope of use

Industrial POs catalysts are considerably different in the structure and, consequently, in the type of polymer they produce.[16] Phillips catalysts are the leaders in HDPE production, yielding a product with broad polydispersity index (PDI, a measure of MW breadth). LLDPE and HDPE can be made also using Ziegler-Natta and metallocene-based catalysts (lowest PDI), as can be seen from Figure 1. 4.[10,16] Catalysts are responsible for such a broad range of properties of synthesized PE because their electronic and steric parameters have a direct impact on the polymer microstructure.[1,10,17]

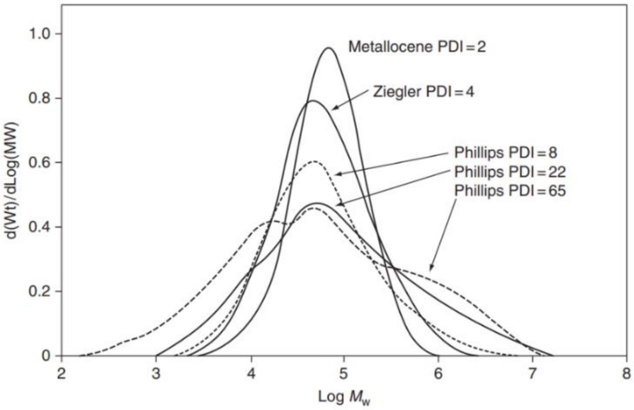

Figure 1. 4 Typical molecular weight (MW) and polydispersity index (PDI) for polyethylenes produced with the three main catalyst types for ethylene polymerization, as measured by size-exclusion chromatography.[16]

Thanks to the serendipitous discoveries occurred in the last century, nowadays it is possible not just to produce POs in huge amounts, but also to obtain materials with broad range of specific properties. This is directly related to the improvement in the design of polymerization catalysts and processes, and also due to understanding of kinetics and advances in computational chemistry, showing how far it is possible to arrive when the knowledge from different scientific fields is combined.

2.3 A main catalyst types for ethylene polymerization

Ethylene polymerization catalysts can be divided in four main groups, namely: i) Phillips, ii) Ziegler-Natta, iii) metallocene-based, and iv) late transition metal catalysts. They can be further divided into homogeneous and heterogeneous, depending on the presence or absence of supporting material. Each class of olefin polymerization catalysts is briefly described below, while the more detailed state-of-the-art for Ziegler-Natta and metallocene-based catalysts can be found in the chapters devoted to these catalytic systems.

Phillips catalysts. Heterogeneous Cr-based olefin polymerization catalysts are called Phillips catalysts, after the company where discovered, and can be divided in two main groups: i) those based on Cr-oxide, and ii) those based on organochromium compounds. Cr oxide must be supported on porous material, most usually amorphous silica. When catalyst comes in touch with ethylene at high temperatures in the polymerization reactor the Cr(VI) sites are reduced and alkylated.[1,16] Reduction and subsequent activation of Philips catalysts can be done also before the polymerization by using reduction agents such as CO or metal alkyl compounds.[18,19] Performance of Phillips catalysts is very dependent on the preparation procedure and silica properties, which enable the tailoring of the polymer properties.[1] Philips catalyst have multiple types of active sites, and are mainly used in manufacture of HDPE, with very broad PDI (Figure 1. 4).

Ziegler-Natta catalysts. When discovered, decades ago, heterogeneous Ziegler-Natta (ZN) catalysts together with Phillips catalysts revolutionized polymerization industry by enabling industrial production of POs (in particular PE and PP) in enormous quantities.[1] ZN catalysts are workhorses in polymerization industry mainly because they are extremely active (more than 100 kg of PO per g of the catalyst depending on desired product) and quite cheap to produce (tens € per kg of catalyst).[20] Moreover, they are constantly advancing and improving, causing better control and efficiency of process and product in terms of structure and properties.[1] ZN catalysts are hierarchical systems composed by: i) the support (usually $MgCl_2$, but also silica); ii) a metal sites (usually Ti in the form of titanium chloride); iii) an activator (usually an aluminum alkyl compound) and iv) molecules acting as electron donors (organic Lewis bases, which are necessary for achieving stereoselective propylene polymerization,[7] but not required for ethylene polymerization).

Traditional ZN catalysts are supported on $MgCl_2$,[21–23] but sometimes are also supported on silica, which is done in order to increase the surface area and to facilitate the control of polymer morphology.[24–27] ZN catalysts are multi-site catalysts yielding PE with broad MWD, though not so broad as in the case of Philips catalyst (Figure 1. 4).

Metallocene-based catalysts. A metallocene complex is defined as a sandwich structure because the metal cation is placed in between two aromatic ligands.[28] Metallocene-based catalysts were firstly introduced in 1950s,[29,30] but when activated with traditional ZN catalyst activators, aluminum alkyls, were not significantly active in olefin polymerization.[28] Just in 1980s, when MAO was discovered as activator for metallocene-based polymerization catalysts, the age of ‘single-site’ catalyst started.[1,14] Being single-site catalysts, they yield POs with very narrow MWD (Figure 1. 4). Good control of polymer properties/chain architecture (i.e. MWD, co-monomer incorporation, stereoselectivity, branching) is achieved by ‘rational’ design of steric and electronic properties of the catalysts. In order to make metallocene-based catalyst suitable for existing polymerization facilities it might be useful to support them, generally on amorphous silica, even though this has an unavoidable impact on their single-site nature.[1] However, as long as metallocene-based catalysts yield PE with defined quality and narrow MWD the divergence from single-site behaviour is allowed.[31]

Late Transition Metal (LTM) catalysts. Often called post-metallocenes, these catalysts were discovered in 1990s by Brookhart and co-workers and are defined as late transition metal complexes having sterically bulk ligands such are diamides and iminopyrrolides.[32–34] Chain walking is very interesting feature of some LTM catalysts and means that upon ethylene polymerization active centre move from the chain-end and walks through polymer chain causing formation of short branches (in the absence of co-monomer).[35] LTM catalysts are still scarcely used in industrial scale because their thermal instability makes them unsuitable for use in existing gas-phase polymerization plants.[36]

3. Aim of this PhD thesis

This PhD project is realized as a part of the MULTIPOL project, founded by the Dutch Polymer Institute (DPI). DPI is an industry-driven international collaboration platform for pre-competitive research in the field of polymers. The project was developed in collaboration with the group of Prof. Bert Weckhuysen at the Utrecht University, in strict synergy with the industrial partners in DPI. The main objective of the research was the investigation of industrially relevant silica-supported Ziegler-Natta and metallocene-based catalysts for ethylene polymerization in the early stages of the genesis of active sites and polymer formation by a multi-scale characterization approach under reaction conditions. Two PhD students jointly worked together on the same set of solid catalysts: 1) the Utrecht-based PhD student performed single catalyst particle characterization; 2) myself, based at UNITO, focused on the characterization at a molecular level of the whole catalyst ensemble.

The synergic use of spectroscopies and microscopies, employing light in a very large spectral range (from hard X-rays to microwaves), was a central approach for determining the properties of the catalysts both at the atomic scale (molecular structure, composition, and distribution of the active sites) and at the scale of the single polymerizing particle (volume, cracks, pressure build-up, temperature gradients). The key issues and experimental approaches addressed by the MULTIPOL project are schematically shown in Figure 1. 5, along with the respective contributions of the Utrecht and Torino research teams for integrated competencies and methodologies.

Regarding the UNITO research part, the main goals were to access the properties of the active sites at a molecular level, to understand the role of the activator in the formation of the active sites and to evaluate the role of silica in active site definition. This was mainly achieved by use of DR UV-Vis and IR spectroscopies also in the presence of probe molecules (typically CO and d-acetonitrile) and monomers (ethylene and 1-hexene). In addition, on selected samples X-ray adsorption spectroscopic measurements were performed to complement data obtained by DR UV-Vis and IR spectroscopies. Finally, the results were compared to those of reference samples, such as β-$TiCl_3$ in the case of Ziegler-Natta catalysts, and catalyst precursor in the case of metallocene-based catalysts, allowing more precise interpretation of the data. Homogeneous metallocene-based catalytic systems were also studied in order to better understand the more complex heterogenous systems. Working on the metallocene-based samples that were synthesised following exactly the same synthetic procedure and by using the same solvents and silica but varying in the type of ligand or metal site, allowed to asses the impact of the metal or ligands on the catalysts properties at molecular level.

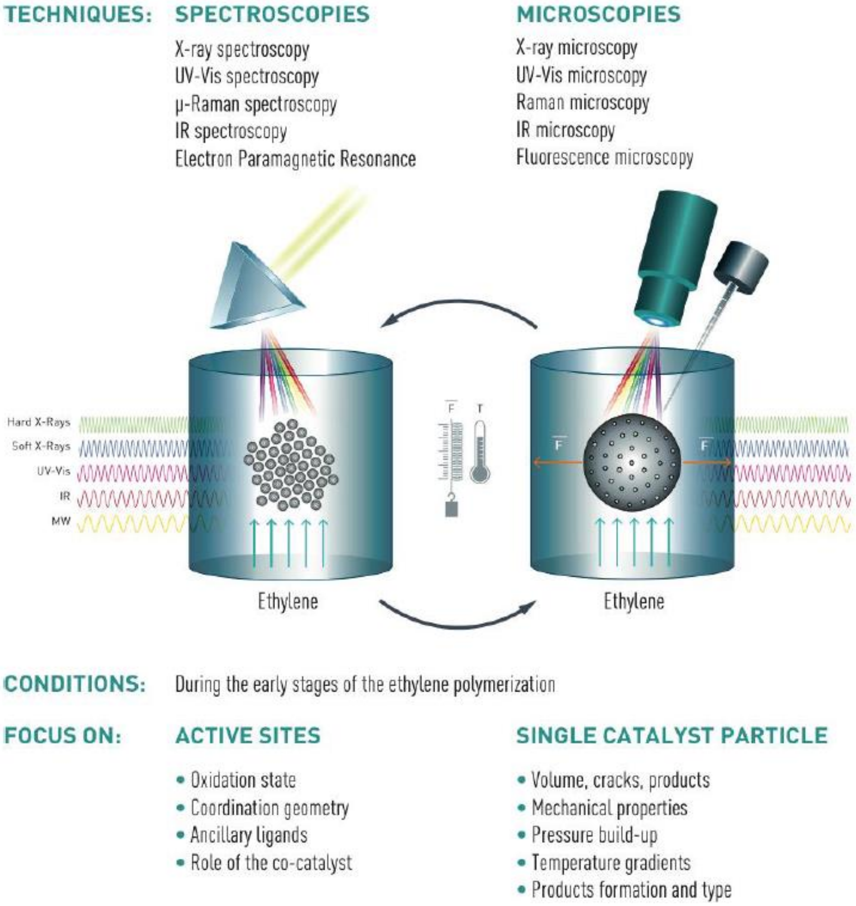

Figure 1. 5 Sinergy between spectroscopies and microscopies applied for characterizing silica-supported ZN catalysts and metallocene-based catalysts within MULTIPOL project, and fundamental information which can be obtained.

4. Outline of this PhD thesis

This thesis is constituted from two Parts that are divided in 6 chapters described as follows.

Chapter 1. Preface

Chapter 2. Materials and methods

Chapter 3. Silica-supported metallocene-based catalysts

1. State-of-the-art

References

1. Gagleitner, M. & Severn, J. R. Designing Polymer Properties. in *Tailor-made Polymers Via Immobilization of Alpha-Olefin Polymerization Catalysts* (eds. Severn, J. R. & Chadwick, J. C.) 1–39 (Wiley-VCH, 2007).

2. Feldman, D. Polymer history. *Des Monomers Polym* **11**, 1–15 (2008).

3. Mülhaupt, R. Green polymer chemistry and bio-based plastics: Dreams and reality. *Macromol Chem Phys* **214**, 159–174 (2013).

4. PlascticsEurope. *Plastics-the Facts 2020 An analysis of European plastics production, demand and waste data*.

5. Tabone, M. D., Cregg, J. J., Beckman, E. J. & Landis, A. E. Sustainability metrics: Life cycle assessment and green design in polymers. *Environ Sci Technol* **44**, 8264–8269 (2010).

6. Stürzel, M., Mihan, S. & Mülhaupt, R. From Multisite Polymerization Catalysis to Sustainable Materials and All-Polyolefin Composites. *Chem Rev* **116**, 1398–1433 (2016).

7. Kaminsky, W. *Polyolefins: 50 years after Ziegler and Natta II Polyolefins by Metallocenes and Other Single-Site Catalysts*. (Springer - Verlag Berlin Heidelberg, 2013).

8. Jubinville, D., Esmizadeh, E., Saikrishnan, S., Tzoganakis, C. & Mekonnen, T. A comprehensive review of global production and recycling methods of polyolefin (PO) based products and their post-recycling applications. *Sustainable Materials and Technologies* vol. 25 Preprint at https://doi.org/10.1016/j.susmat.2020.e00188 (2020).

9. Sauter, D. W., Taoufik, M. & Boisson, C. Polyolefins, a success story. *Polymers* vol. 9 Preprint at https://doi.org/10.3390/polym9060185 (2017).

10. Soares, J. B. P. & McKenna, T. F. L. *Polyolefin Reaction Engineering*. (WILEY-VCH Verlag GmbH & CO, 2012).

11. Hogan, J. P. & Banks, R. L. POLYMERS AND PRODUCTION THEREOF. vol. 825 (1956).

12. Ziegler, K., Breil, H. & Martin. H. High Molecular Polyethylenes. (1957).

13. Natta, G., Corradini, P. & Allegra, G. Struttura cristallina della forma y del tricloruro do titanio. *Rendiconti dell'Academia Nazionale dei Lincei. Classe di Scienze Fisiche, matematiche e naturali* **26**, (1959).

14. Kaminsky, W. The discovery of metallocene catalysts and their present state of the art. *Journal of Polymer Science, Part A: Polymer Chemistry* vol. 42 3911–3921 Preprint at https://doi.org/10.1002/pola.20292 (2004).

15. Groppo, E., Seenivasan, K. & Barzan, C. The potential of spectroscopic methods applied to heterogeneous catalysts for olefin polymerization. *Catal Sci Technol* **3**, 858–878 (2013).

16. McDaniel, M. P. A Review of the Phillips Supported Chromium Catalyst and Its Commercial Use for Ethylene Polymerization. in *Advances in Catalysis* vol. 53 123–606 (2010).

17. Chen, C. Designing catalysts for olefin polymerization and copolymerization: beyond electronic and steric tuning. *Nat Rev Chem* **2**, 6–14 (2018).

18. Groppo, E., Lamberti, C., Bordiga, S., Spoto, G. & Zecchina, A. The structure of active centers and the Ethylene Polymerization mechanism on the Cr/SiO2 catalyst: A frontier for the characterization methods. *Chem Rev* **105**, 115–183 (2005).

19. Mcdaniel, M. P. *Supported Chromium Catalysts for Ethylene Polymerization*. vol. 33 (1985).

20. Böhm, L. L. The Ethylene Polymerization with Ziegler Catalysts: Fifty Years after the Discovery. *Angewandte Chemie - International Edition* vol. 42 5010–5030 Preprint at https://doi.org/10.1002/anie.200300580 (2003).

21. Correa, A., Piemontesi, F., Morini, G. & Cavallo, L. Key elements in the structure and function relationship of the MgCl 2/TiCl4/Lewis base Ziegler-Natta catalytic system. *Macromolecules* **40**, 9181–9189 (2007).

22. Taniike, T. & Terano, M. Reductive formation of isospecific Ti dinuclear species on a MgCl 2 (110) surface in heterogeneous ziegler-natta catalysts. *Macromol Rapid Commun* **29**, 1472–1476 (2008).

23. Andoni, A., Chadwick, J. C., Niemantsverdriet, H. J. W. & Thüne, P. C. The role of electron donors on lateral surfaces of MgCl2-supported Ziegler-Natta catalysts: Observation by AFM and SEM. *J Catal* **257**, 81–86 (2008).

24. Garoff, T. *et al.* Procatalyst for ethylene polymer production, method for its preparation and use. (1995).

25. Spencer, L. & Springs, M. Supported Olefin Polymerization Catalysts. (1996).

26. Pullukat, T. J. & Hoff, R. E. Polymerization Catalyst and Method. (1983).

27. Pullukat, T. J. & Hoff, R. E. Silica-based Ziegler-Natta catalysts: A patent review. *Catal Rev Sci Eng* **41**, 389–428 (1999).

28. Kaminsky, W. *Highly active metallocene catalysts for olefin polymerization*. *J. Chem. Soc* (1998).

29. Fischer, E. O. & Jira, R. *Über den Di-cyclopentadienyl-Komplex des Kobalts*. *Z. Naturforschg* vol. 8 (1953).

30. Wilkinson, G. & Birmingham, J. M. Bis-cyclopentadienyl Compounds of Ti, Zr, V, Nb and Ta. *Journal of American Chemical Society* **75**, 901 (1954).

31. Severn, J. R. Methylaluminoxane (MAO), Silica and a Complex: The “ Holy Trinity ” of Supported Single - site Catalyst. in *Tailor-Made Polymers Via Immobilization of Alpha-Olefin Polymerization Catalysts* (eds. Severn, J. R. & Chadwick, J. C.) 95–135 (WILEY-VCH , 2008).

32. Johnson, L. K., Killian, C. M. & Brookhart, M. New Pd(II)-and Ni(II)-Based Catalysts for Polymerization of Ethylene and a-Olefins. *Journal of American Chemical Society* **117**, 123–134 (1995).

33. Gibson, V. C. & Spitzmesser, S. K. Advances in non-metallocene olefin polymerization catalysis. *Chem Rev* **103**, 283–315 (2003).

34. Britovsek, G. J. P., Gibson, V. C. & Wass, D. F. The Search for New-Generation Olefin Polymerization Catalysts Life beyond. *Angew. Chem. Int. Ed.* **38**, 428–447 (1999).

35. Guan, Z., Cotts, P. M., Mccord, E. F. & Mclain, S. J. Chain Walking: A New Strategy to Control Polymer Topology. *Science (1979)* **283**, 2059 (1999).

36. Ali, E. M., Abasaeed, A. E. & Al-Zahrani, S. M. Optimization and Control of Industrial Gas-Phase Ethylene Polymerization Reactors. *Ing. Eng. Chem. Res.* **37**, 3414–3423 (1998).

CHAPTER 2

Materials and Experimental Methods

This chapter is devoted to the description of the experimental procedures and equipment used for characterization of the samples. Although all the catalysts were provided by SABIC, their synthesis procedure will be shortly described since it has a significant impact on the properties of the catalysts. When appropriate, details on the procedure adopted to activate the SiO_2/ZN precatalyst will be also provided.

1. Catalysts synthesis and activation

1.1 Synthesis and activation of silica-supported Ziegler-Natta catalysts

The SiO_2/ZN precatalyst was synthetized according to the procedure described in patent US4374753.[1] Briefly, the synthesis consists in five subsequent steps:

1) SiO_2 (ES70X, specific surface area = 295 m^2/g, pore volume = 1.6 mL/g, average particle size 50 µm) was dried at 200 °C for 2 hours under inert flow;
2) Dried silica was then chemically dehydroxylated by hexamethyldisilazane (HMDS) at 25 °C, followed by removal of unreacted HMDS and NH_3 by-product;
3) The so-dehydroxylated silica was reacted with a heptane solution of dibutyl magnesium + TEA (added to promote $MgBu_2$ solubility in heptane) ($MgBu_2$•$xAlEt_3$, Mg:Al=6.1);
4) 1-butanol was added to the reaction mixture at 25 °C;
5) At the end, $TiCl_4$ was added, followed by drying under nitrogen flow at 90 °C to obtain free flowing powder. At the end the Mg:Ti ratio was 1.0 ± 0.1, and Ti % in the final precatalyst was 3.8 ± 0.2 wt%.

Activation of the SiO_2/ZN precatalyst was done as follows. First, a weighted amount of the SiO_2/ZN precatalyst powder is put in contact with anhydrous n-hexane in amount enough to wet all the powder. After that, a stochiometric amount of triethylaluminum (TEA) or tributylaluminum (TiBA) is added to achieve desired Al:Ti ratio. Then, the powder is gently mixed for about 1 min to promote contact between SiO_2/ZN precatalyst and activator. The next step depends on the type of experiment:

- For IR measurements, the mixture is left in the mortar until complete solvent evaporation (approx. 30 mins). Further, the powder is gently grinded and pressed in the form of self-supporting pellet, inserted into a gold-envelope and transferred inside a home-made IR cell equipped with KBr of CaF_2 windows. The small amount of solvent remained in the pores is removed by evacuation prior to the measurement.
- For UV-Vis measurements, the wet mixture is placed inside a quartz tube, which is removed from the glovebox and connected to the vacuum line for faster solvent removal. After solvent evaporates, the cell is left in vacuum for at least 15 minutes and then put again inside the glove box in order to transfer sample to the custom-made cell in optical quartz that is used for DR UV-Vis measurements.

- For kinetics tests, the procedure is the same as for UV-Vis measurements, just after solvent evaporation the measurements continues inside the quartz tube.

Activation of the precatalyst resulted in a colour change from light brown to dark brown, as illustrated in Figure 2. 1.

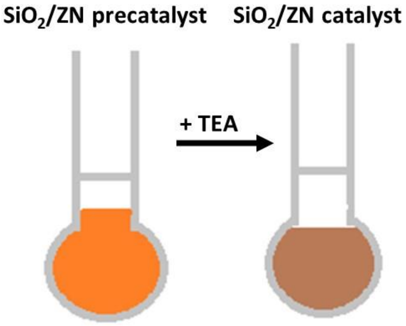

Figure 2. 1 Illustration of color change upon activation of SiO_2/ZN pre catalyst with TEA

1.2 Synthesis of silica-supported zirconocene- and hafnocene-based catalysts

Two SiO_2/MAO/Zr and one SiO_2/MAO/Hf catalysts were synthesized according to the following procedure.

1) Catalyst precursor (2,2′-biphenylene-bis-2-indenyl MCl_2 for SiO_2/MAO/Zr1 and SiO_2/MAO/Hf, and Me_2Si-bis(2-Me-1-indenyl) $ZrCl_2$ in the case of SiO_2/MAO/Zr2) was dissolved in toluene;
2) methyaluminoxane (30 wt% in toluene, MAO) was added in amount to obtain Al:M ratio 150 for all three catalysts.
3) The suspension was stirred until clear solution was obtained (15 minutes in the case of zirconocene-based catalysts, and 3h for hafnocene-based one).
4) After that, pretreated polymer-grade silica (ES757, specific surface area 283 m^2/g, pore volume 1.563 cm^3/g, average particle size 31.6 µm, precalcined at 600 °C for 4h) was added to form slurry;
5) The solvent was removed at room temperature by nitrogen stream for 20h until free-flowing powder was obtained.

Metal loading in final catalyst was 0.3 wt% for both zirconocene-based catalysts and 0.59 wt% for hafnocene-based catalyst. These catalysts were characterized as received, without additional activation or treatment. A picture of the SiO_2/MAO/Zr1 and SiO_2/MAO/Zr2 catalysts is reported in Figure 2. 2.

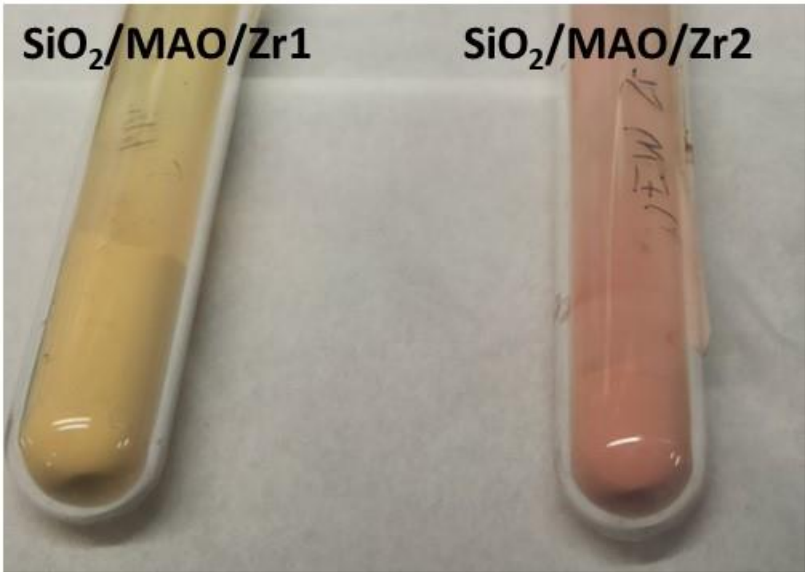

Figure 2. 2 A picture of SiO_2/MAO/Zr1 and SiO_2/MAO/Zr2 catalysts

1.3 Synthesis of silica-support treated with MAO

The synthesis of SiO_2/MAO is described as follows.

1) Silica (ES 757) was suspended in toluene;
2) MAO (30 wt% in toluene) was added to this slurry, and the slurry was stirred for a while.
3) The solvent was removed at room temperature by nitrogen stream until free-flowing powder was obtained.

1.4 Preparation of the homogeneous metallocene-based catalysts (for UV-Vis measurements)

Metallocene catalysts precursors were measured in solution, before and after activation by MAO, for comparison with the heterogeneous systems. The precursors were dissolved in toluene at the desired concentrations in round bottom flask until clear solution was obtained. An exact volume of solution was transferred to the measuring cell and MAO was added in amount to have targeted Al:M ratio.

2. Characterization techniques

2.1 Sample manipulation

Since olefin polymerization catalysts and their activators are extremely air and moisture sensitive, they were stored and manipulated inside a glovebox filled with Nitrogen, Figure 2. 3A. The spectroscopic measurements were done inside home-made cells ensuring that sample will not come in touch with air and moisture. Vacuum lines (Figure 2. 3B) were used to remove/add gasses from the measuring cells, again guaranteeing that no air will enter inside the cell.

Figure 2. 3 A) The glovebox and B) vacuum line with cell connected while interfaced with IR spectrophotometer

2.2 IR spectroscopy

IR measurements were performed in both Mid-IR and Far-IR region in transmission mode by using a Bruker Vertex70 spectrophotometer equipped with a MCT or a Far-IR DTGS detector, at resolution of 2 cm^{-1}.

In Mid-IR region the samples were measured in the form of thin, self-supporting pellet. Pellet was done inside the glovebox by using manual press, and then put inside a gold envelope which was inserted in a custom-made cell with two KBr or CaF_2 windows. Depending on the temperature at which measurement was done, two different types of cells were used: i) low temperature cell (Figure 2. 4A) that allows cooling down to approximately 100 K with liquid nitrogen; and ii) room temperature cell (Figure 2. 4B) allowing to perform measurements at room temperature. Both types of cells can be connected to the vacuum lines also while interfaced with the instrument, enabling removal/addition of gasses, and monitoring in situ spectral changes as a function of time and/or pressure.

For Far-IR measurements, the samples were deposited on a silicon wafer from a hexane suspension inside the glovebox. After drying, the wafer was inserted into a variant of the cell shown in Figure 2. 4B equipped with two PE windows.

ATR measurements were performed directly inside the glovebox, by means of a Bruker Alpha spectrophotometer equipped with an ATR accessory with a diamond crystal.

Figure 2. 4 A) Low temperature IR cell and B) room temperature IR cell adopted in this work for performing in situ IR experiments in the presence of probe molecules and/or reactants.

2.2.1 Low temperature IR measurements: CO adsorption at 100 K

A typical procedure for measuring CO adsorption at 100 K is as follows. After removal of nitrogen from the cell, the sample is left under dynamic vacuum (10^{-4} mbar) for the next 15 minutes or until no spectral changed are observed over time. A spectrum of the sample at room temperature is collected. Then, CO is dosed at room temperature, and a further IR spectrum is collected. After that the sample is cooled with liquid nitrogen. When the maximum CO coverage (Θ) is achieved, an IR spectrum is collected. At this point the P_{CO} pressure is decreased step-by-step, and IR spectra are acquired at each P_{CO} value, at constant temperature until all CO is completely removed from the cell and/or no further changes are observed in the spectra. The so-collected IR spectra are usually shown after subtraction of the spectrum collected before CO dosage (at room temperature).

2.2.2 Room temperature IR measurements: CO, d-ACN and 1-hexene adsorption at 300 K

A typical procedure adopted during IR experiments in the presence of inserting probes at room temperature is as follows. The sample is left under dynamic vacuum (10^{-4} mbar) for the next 15 minutes or until no spectral changed are observed over time. A spectrum of the sample at room temperature is collected. At this point, a well-defined equilibrium pressure of the probe molecule is admitted into the cell and IR spectra are collected continuously for certain time. At the end, the probe molecule is removed from the cell, while continuously collecting the IR spectra.

2.3 UV-Vis-NIR spectroscopy

2.3.1 DR UV-Vis-NIR spectroscopy, also in the presence of probe molecules

UV-Vis-NIR spectra in diffuse reflectance mode were collected using a Varian Cary5000 spectrophotometer equipped with a reflectance sphere. The samples were measured inside custom-made bulb cells in optical quartz (Figure 2. 5A), allowing to perform measurements in controlled atmosphere and/or in the presence of probe molecules.

For measurements in the presence of probe molecules, a typical procedure is as follows. The cell is filled with the sample in the glovebox, closed and removed from the glove box. After collecting the DR UV-Vis spectrum of the catalyst as such, the cell is connected to the vacuum line for removing the nitrogen atmosphere. When high vacuum is reached, the cell is left in degassing for another 15 minutes and then a certain pressure of the probe molecule is admitted in the cell, successively detached and ready for the measurement.

All the spectra were collected in reflectance mode and then transformed in Kubelka-Munk, F(R), function.

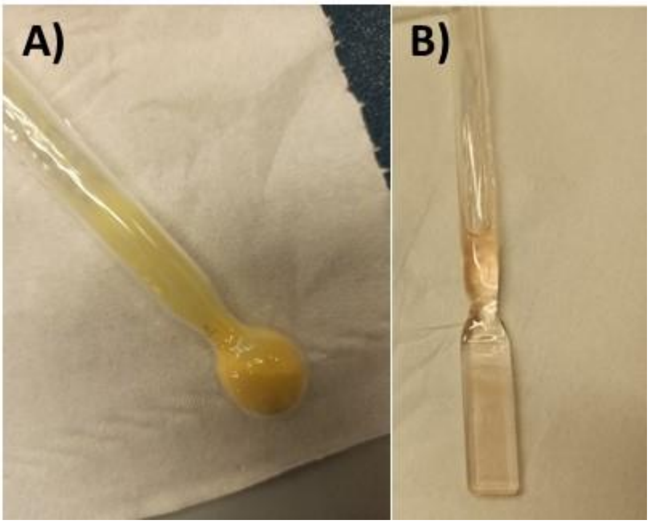

Figure 2. 5 A) Bulb cell in optical quartz suited for DR UV-Vis-NIR measurements and B) Cell with flat windows in optical quartz for UV-Vis spectroscopy in solution.

2.3.2 Transmission UV-Vis spectroscopy

UV-Vis spectra of samples in solution were collected using the same instrument as for DR UV-Vis-NIR spectra, but in transmission mode. Solutions were prepared in the glovebox and inserted inside custom-made cells equipped with a cuvette in optical quartz (Figure 2. 5B), allowing to perform measurements without exposing the sample to air.

2.4 Ti K-edge X-ray Absorption spectroscopy (XAS)

The Ti K-edge XAS measurements were performed at the XAFS beamline at the Elettra Sincrotrone facility in Trieste. The samples were measured in the form of pellet, diluted in dehydrated boron nitride to optimize the Ti concentration in such a way that the edge jump was around 0.4, which is the best compromise between edge-jump and total absorption for this composition. The pellets were done in the glovebox and sealed inside a LDPE envelope under vacuum. The envelope with the pellet was mounted on the XAFS sample-holder inside the glovebox. The sample holder was then removed from the glovebox, transferred to the measurement chamber at the beamline, and put under high vacuum. The whole procedure avoided exposure of the sample to air.

The white beam was monochromatized using a Si(111) double crystal. Harmonic rejection was performed by detuning the second crystal of the monochromator of 50%. The spectra were acquired in transmission mode using ionization chambers for the detection of the reference and transmitted X-rays. A third ionization chamber recorded a Ti foil reference for energy calibration.

The XANES spectra were aligned and normalized with the Athena software, by using standard procedures. EXAFS data analysis was performed using the Arthemis software. The $k^2\chi(k)$ functions were Fourier transformed (FT) in the Δk = 2.0 – 10.0 Å-1 interval. The fit was performed in R-space in the ΔR = 1.2 – 5.0 Å-1 range. Phase and amplitudes were calculated by FEFF6.0 code.

2.5 Ti $L_{2,3}$-edge NEXAFS spectroscopy

Ti $L_{2,3}$-edge NEXAFS spectra were collected at the APE-HE beamline of the Elettra Sincrotrone Trieste facility, in the total electron yield (TEY) mode. To ensure the electrical conductivity, the samples in powder form were pressed inside a thin indium plate and fixed inside an ambient-pressure NEXAFS cell, which allows to perform measurements in the presence of gases and is shown in Figure 2. 6.[2] This was done inside a N_2-filled glovebox to prevent contamination. The AP-NEXAFS cell was then inserted inside the high vacuum chamber of the APE-HE beamline and connected to a gas line, equipped with a liquid nitrogen trap to remove adventitious water contaminations. All the measurements were performed under a 5 mL min-1 He flow at 1 bar.

The spectra were collected with an energy step of 0.1 eV and an integration time per step of 0.18 s. The so-collected data were processed using THORONDOR software.[3]

Figure 2. 6 The ambient pressure NEXAFS cell with the sample pressed inside indium plate

References

1. Pullukat, T. J. & Hoff, R. E. Polymerization Catalyst and Method. (1983).

2. Castán-Guerrero, C. *et al.* A reaction cell for ambient pressure soft x-ray absorption spectroscopy. *Review of Scientific Instruments* **89**, (2018).

3. Simonne, D. H. *et al.* THORONDOR: A software for fast treatment and analysis of low-energy XAS data. *J Synchrotron Radiat* **27**, 1741–1752 (2020).

Chapter 3

Silica-supported metallocene-based catalysts

This Chapter is devoted to silica-supported metallocene-based catalysts for olefin polymerization, and it is divided into three main sections. The first section presents the state-of-the-art. Second and third sections are devoted to critically discuss the spectroscopic results achieved during this PhD work on industrially relevant SiO_2/MAO/metallocene systems.

1. State-of-the-art

1.1. Metallocenes and olefin polymerization

1.1.1 Setting the scene

Metallocene-based catalysts activated with MAO are highly active in olefin polymerization and thus very interesting subject for scientific research, especially because some of them found their industrial use.[1–3] Thanks to their 'single-site' nature they typically produce polymers having a very narrow MW distribution, with important implications in terms of processability.[2,4] Moreover, they formally allow to tune the polymer properties based on a 'structure-property' approach, i.e. by designing the steric and electronic properties of the catalyst it is possible to tailor the polymer properties.[4,5] It is important to note, however, that several studies[6] reported on non-single-site nature of metallocene-based catalysts for both ethylene[6] and propylene[6–8] polymerization in homogeneous conditions, which means that several types of active sites can be present also in homogeneous conditions, that differ in reactivity towards monomer and/or comonomer, chain transfer ability, regioselectivity and stereoselectivity. What makes them yielding polymers with narrow MW distribution is the fact that under certain process conditions they statistically behave in the same way from one polymer chain to the other.[4]

Generally speaking, metallocene-based catalysts for olefin polymerization are sandwich complexes composed by a metal cation (usually Ti, Zr of Hf) positioned between two aromatic ligands, typically cyclopentadienyl (Cp) or its derivatives (Figure 3. 1).[3,9,10] Alternatively, the ligands can be connected by intramolecular bridge and can also have some substituents. Mono-cyclopentadienyl catalysts with covalently attached alkyl, amide, imido, or other group also exists and are called half-sandwich complexes or constrained geometry catalysts.[11] The structure of metallocene-based catalysts, e.g. ligand symmetry and presence of the bridge, has a strong impact on the type of resin that they produce, as shown in Figure 3. 1. For example, unbridged metallocene-based catalysts produce mainly atactic PP, while bridged metallocenes produce atactic PP when in *meso*- form and isotactic PP when in *rac*- form.[12,13] Syndiotactic PP can be produced by metallocene catalysts having two different ligands, while half-sandwich complexes are used to produce olefin block copolymers and other more specific polymers.[12–14]

The ligand structure has a big impact on the electronic and steric properties of the catalyst, thus directly influencing the catalyst activity and the properties of the produced polymer.[15,16] To illustrate this concept, exchange of a Cp ligand in a sandwich complex $[Cp_2MR]^+$ with an alkyl group (R) to give the half-sandwich $[CpMR_2]^+$ complex causes significant changes in the electronic properties: the active site in the first case is a 14-electron species, while in the latter is a more electron-deficient 10-electron species.[17,18] Also, the half-sandwich complex is less sterically hindered.

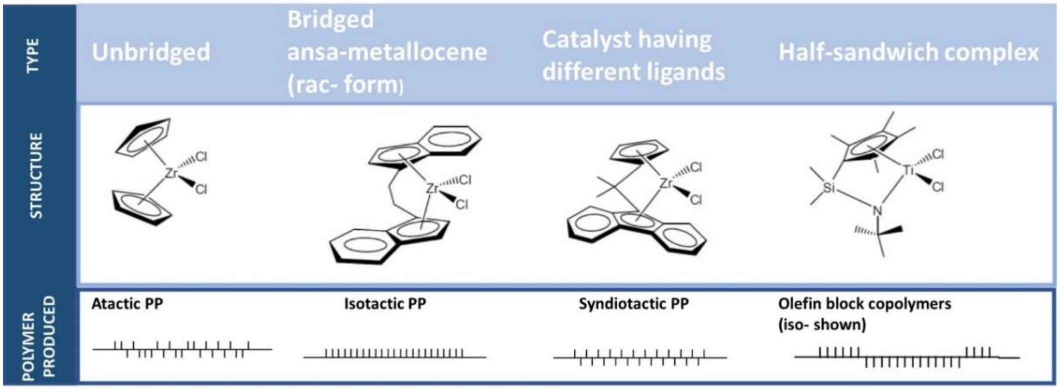

Figure 3. 1. Different metallocene-based catalyst structures and typical polymer they are producing.[12–14]

The catalyst's structure depends on the nature of the metal site, the steric and electronic properties of the ligand, and the symmetry around the metal center,[19,20] and can be quite easily modified by:[19,21–25]

1. changing the central metal atom,
2. changing the ligand (Cp, indenyl, fluorenyl) and ligands symmetry (rac- or meso-),
3. changing the ligand substituents (hydrogen or other functional groups such as alkyl, aryl, siloxy, etc.),
4. inserting an interannular bridge (e.g. dimethylsilandiol, ethanediyl).

1.1.2 Influence of the ligand structure on the catalytic performance

The ligand type affects both steric and electronic properties of the catalyst and determine its stability, activity, and selectivity.[26] It is important to note that just small changes in electronic properties drastically changes the activity and selectivity of the catalyst due to changes in the coordination sphere around the metal center.[25,27,28] One of the most notable work which illustrates the role of the ligand, ligand substitution and interannular bridge on catalysts behavior during olefin polymerization is that by Alt and co-workers, who prepared a few hundreds of homogeneous catalysts and examined them at the same polymerization conditions. The latter is of crucial significance if the intention is to compare different catalysts since small change in polymerization conditions can have big impact on the obtained results. The results are summarized in a review,[25] and here just a few of them will be mentioned.

Factors influencing the catalyst activity

The type of the ligand. The activity of unbridged Zr-based catalysts in ethylene polymerization depends on the type of the ligand: similar activities were observed for catalysts bearing cyclopentadienyl and indenyl ligands, while the less active catalyst was that with fluorenyl ligands. This observation was explained in terms of formation of less stable complexes in the latter case, due to a *ring-slippage phenomenon* (i.e. ligand coordination to the metal center via η^1, η^3 or η^5 bond).[25,29] As a matter of fact, the activity of Zr-based catalysts with fluorenyl ligands in ethylene polymerization can be boosted by methyl substitution on fluorenyl ligand, which prevents ring-slippage reactions.[29]

Two homogeneous Zr-based catalyst withs Cp and hydrido tripyrazolyl borate (HTB) ligands were compared. Although it was expected that they behave similarly, because both ligands can donate 6 electrons to the metal center, important differences in electronic and steric properties were observed. This is because the HTB ligand has a stronger *electron donation ability*. This causes an electron enrichment at the metal center, which lacks in Lewis acidity. Moreover, the higher bulkiness of the ligand leads to more protected metal center.[25,30,31]

Ligand substituents. Several studies showed that catalysts having ligands without and with alkyl substitutions have different activities in ethylene polymerization.[10,25,32–34] Zr-based catalysts with alkyl substituted Cp ligands have usually higher activity than the corresponding unsubstituted catalysts, because alkyls can increase electron donation ability of Cp ligands and stabilize cationic metal center. The drawback of alkyl substituted ligands is increased steric hindrance of the metal center which limits olefin coordination and insertion.

Similarly, Zr-based catalysts having alkyl substituents with aromatic end group on Cp ligand were investigated when activated with MAO[35] and fluorine-based activators[36]. It was demonstrated that the length of the alkyl substituent can significantly affect the polymerization due to a better separation of cation and anion and/or interaction between the aromatic end of substituent and the Lewis acid center of the catalyst. [35,36]

Interannular bridge. The presence of the bridge affects the steric properties of metallocene-based catalysts by making the geometry around the metal center more rigid and increasing the bite angle, i.e. the ligand-metal-ligand angle.[27,28] The type of the bridge affects the catalyst performance because it has an impact on the bite angle: bigger the bite angle, easier the monomer approach to the metal center.[25] However, electronic effects of the bridge cannot be neglected. Unbridged Zr-based catalysts are usually more active than the corresponding bridged ones despite the smaller bite angle, due to the steric effect that bridge bears to the system.[10]

Electronic factors. XPS measurements revealed correlation between electron deficiency on the metal center and catalyst activity for both homogeneous[10,32,33] and heterogeneous [37,38] unbridged catalytic systems: the more electron deficient is the metal center, the more active is the catalyst. However, it must be said that not just electronic properties have an impact on catalyst activity. In the case of bridged metallocene-based catalysts (also called ansa-metallocenes) the electronic factors are reported to have less influence on the activity, implicating that steric effects are more reliable in that merit.[10,37,39]

Factors influencing the catalyst selectivity

The stereoselectivity in propene polymerization can be controlled by the ligand structure. For example, indenyl ligands can undergo *rotation around the ligand-metal bond axis*, thus continuously changing the symmetry of the catalyst form rac- to meso- form and creating so-called oscillating catalysts, thus influencing propylene polymerization by controlling stereoselectivity.[7,8,40]

Similarly, the MW of produced PEs varies depending on the type of ligand, ligand substituents and bridge.[10] Higher molecular weight PE is mainly produced with catalysts having bulky substituents on the ligands, which shield the free coordination site that it necessary for β-hydrogen elimination. This also explains why LDPE is produced by unbridged Zr-based catalysts, because of big bite angle that favors the occurrence of chain transfer reactions. [25]

1.1.3 Influence of the metal on the catalytic performance

The employed metal center has a remarkable influence on both catalyst performances and polymer properties since it affects several processes occurring during olefin polymerization.[41] When comparing Ti, Zr and Hf, the general observation is that Zr-based catalysts have the highest activity, Hf-based ones yield the polymer with the highest molecular weight, while Ti-based catalysts are less used due to easier reduction processes leading to catalysts deactivation.[42–46]

Due to similar ionic radii (Zr=59 Å, Hf=58 Å), electronic configurations, and oxidation states, it is expected that catalysts based on Zr and Hf will show very similar properties yielding polymers of comparable MW, but that is not a case.[41,47,48] Differences in metallocene-based catalysts behavior were earlier attributed to the different strengths of M-C bond, in particular the Hf-C bond is the strongest one while Ti-C bond is the weakest one as demonstrated by titration calorimetric methods.[49–51] However, this must be considered with some reserve since the method can have a big experimental error. Recently, a multidisciplinary study conducted by Machat et al.[41] demonstrated that differences in the behavior of three structurally analogous metallocene-based catalysts for propylene polymerization are a consequence of the nature of the M-C bond. In particular, the Hf-C bond has an ionic character, while the Zr-C and Ti-C bonds have a covalent character. The activation barrier for monomer insertion in the case of Hf-C and Ti-C bonds is high, and mainly enthalpic; while the activation barrier for monomer insertion in the Zr-C bond is significantly lower and is mostly entropic.[41]

It was also shown that bite angles vary with the metal center: Zr-based catalysts have the biggest bite angle, followed by Hf-based catalysts, while the smallest angle is observed for Ti-based catalysts.[41]

1.2. MAO: an extraordinary activator

1.2.1 Discovery and structure of MAO

As briefly mentioned in Chapter 1, metallocene-based catalysts, firstly introduced in 1950s, when activated with alkyl aluminums were able to polymerize ethylene but not in significant amounts and were quite unstable.[52,53] The interest for metallocene-based catalysts increased after discovery of a new activator, methylalumoxane or MAO, because so-activated metallocene-based catalysts have a very high activity in olefin polymerization and much better stability.[3,54] Although the mostly used and the most efficient activator is MAO, it is not the only reactant that can be used to activate metallocene-based catalysts. Molecular activators such are borane- and fluorine-based Lewis acids in combination with aluminum alkyls (acting as alkylating agents and scavengers), or other alternative activators can be used.[55,56] However, since the only activator used within this thesis is MAO, we limit the discussion to it.

The biggest breakthrough in the field of metallocene-based catalysts for olefin polymerization was the discovery of MAO in 1980s in the group of Sinn and Kaminsky, which followed the serendipitously discovery that a small amount of water boosts the activity of the Cp_2TiCl_2/Al-alkyl system in ethylene polymerization.[25,28,29] Produced by partial hydrolysis of trimethylaluminum (TMA), MAO always contains some amount of TMA, in commercial MAO typically 10-30%.[57] TMA present in MAO can have impact on the activation process and in the mechanism of ion-pair formation, which will be discussed later.

Despite all the efforts done in order to disclose the exact structure of MAO, it is still ill-defined. The Al and O atoms are arranged alternately, saturated by methyl groups, with basic structure units having [$Al_4O_3Me_6$] formula.[58,59] Because Al atoms in the structure units are not saturated, they tend to form clusters and cages having high molecular weight from 1200 to 1600.[60] For this reason, MAO is constituted by a very complex mixture of linear, cyclic and cage oligomers of general formula [$Al-O-(Me)]_n$, as represented in Figure 3. 2.[60,61] To complicate the scenario, the structure of MAO strongly depends on the synthesis route and changes over time as a function of equilibria between oligomers and complexation of oligomers among each other and/or with unreacted TMA.[60–63] MAO is soluble in hydrocarbons, which is an important feature for use in homogeneous catalysis. In addition, it can be used also in heterogeneous conditions, since it can be heterogenized easily on silica or other supports.[60]

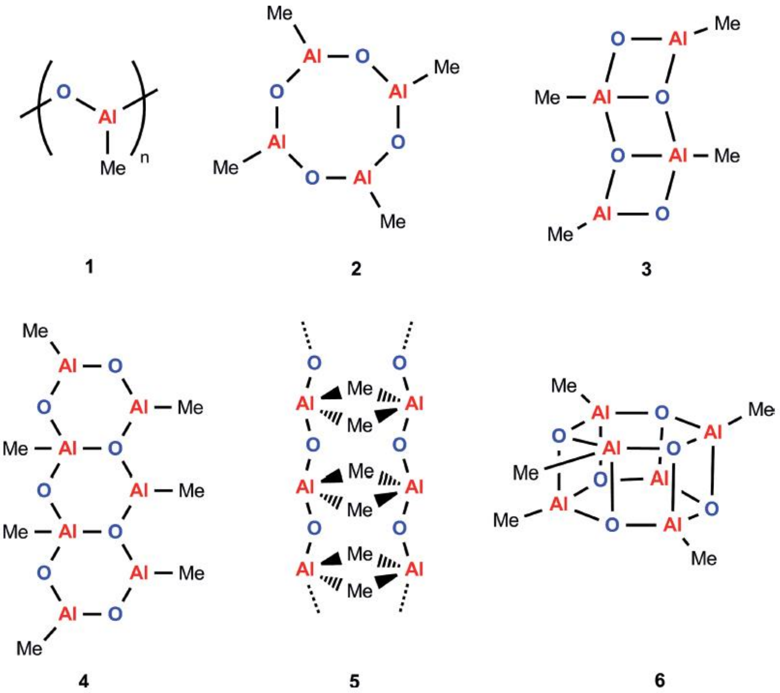

Figure 3. 2. A selection of proposed MAO structures showing different possible structural features.[62]

1.2.2 Mechanism of metallocene-based catalysts activation by MAO

Activation of metallocene-based catalysts with MAO depends on the structure of the catalyst precursor (e.g. ligand’s bulkiness, bite angle, etc.), the Al:Zr ratio and the amount of TMA present in MAO.[56,61,62] Activation is a complex process due to the number of species MAO is composed from, and is still not completely clear. In general, the activation of dichloride metallocene complexes is assumed to occur in two steps, as schematically depicted in Figure 3. 3:[62,64–67]

1. Alkylation of the dichloride complex via alkyl/halide exchange equilibrium, which takes place at lower Al:M ratios up to 50;
2. Cationization of the alkylated complex by subtraction of chlorine anion with the concomitant creation of a coordination vacancy, which occurs at Al:M ratios higher than 50.

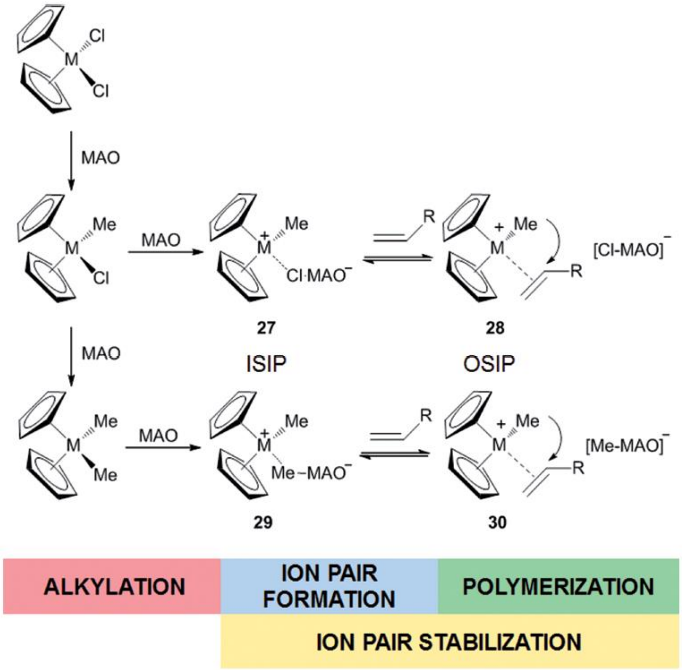

Figure 3. 3. The various roles of MAO in activation of a metallocene-based catalysts for olefin polymerization.[62]

Different species contained in MAO, as well as TMA, can act as alkylating agent, but several NMR studies[68–70] together with computational calculations[71] showed that main responsible are oligomeric MAO cages since they possess intrinsic alkylating potential. This was also confirmed by studies with MAO containing very low amount of TMA and MAO without TMA.[66,72–74] Initially, it was thought that cationization occurs due to latent Lewis acid sites that are sterically strained Al atoms in MAO cages.[75–78] However, today, it is recognized that this is due to strong Lewis acid sites, $[AlMe_2]^+$, formed when the neutral precursor reacts with MAO.[79–85]

The activation of the catalyst precursor by MAO results not just in alkylation and cationization, but also in ion-pair formation. In a very simplified way, ion-pairs are defined as ionic species composed by two oppositely charged moieties with a common solvation shell bonded together by electrostatic forces (i.e. Columbic forces).[55] An ion-pair, when considered as a classical charged species, can be classified as: contact, solvent separated, solvent shared or penetrated ion-pair.[86] In transition metal complexes, contact ion-pairs can be further divided into: i) inner sphere ion-pairs (ISIP) when the anion X^- is localized in the inner sphere of the metal cation and interacts with the metal through weak electrostatic interactions; and ii) outer sphere ion-pairs (OSIP), when the anion X^- remains in the second coordination sphere, as shown in Figure 3. 4. It is important to notice that both ISIP and OSIP are contact ion-pairs, meaning that nothing imposes between the anion and the cation.[55,86]

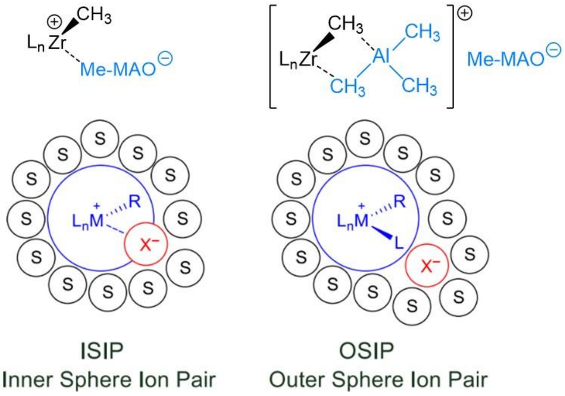

Figure 3. 4. Types of ion-pairs in ionic complexes of transition metals.[55]

Figure 3. 5 shows the complex equilibria between ISIP and OSIP species depending on the Al:M ratio, on the availability of free TMA and of the monomer. At low Al:M ratio, when not all of catalyst precursor is yet in the cationic form, the dominant species are ISIP of the type $[L_nZrMe^{\oplus}\cdots Me\text{-}MAO^{\ominus}]$ (2) formed between $[Me\text{-}MAO]^{\ominus}$ anions and mononuclear M-Me cations, and OSIP (3) formed between $[Me\text{-}MAO]^{\ominus}$ anions and homo-binuclear adducts of catalysts precursor.[87–89] At high Al:M ratio hetero-binuclear adducts of TMA in outer-sphere association (OSIP) with the $[Me\text{-}MAO]^{\ominus}$ anion, i.e. $[L_nZr(\mu\text{-}Me)_2]^{\oplus} \cdots [Me\text{-}MAO]^{\ominus}$ (4), are formed, and these species are considered to be the real active species in olefin polymerization since are able to coordinate the monomer (5).[87,88,90] There is also the possibility of formation of a hetero-binuclear adduct with TMA of type $[L_nZr(\mu\text{-}Me)_2AlMe_2]^{\oplus}[Me\text{-}MAO]^{\ominus}$ (6), considered as a dormant species.[88]

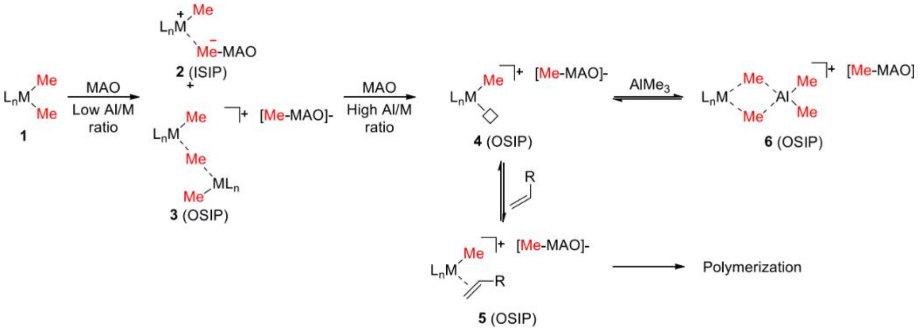

Figure 3. 5. Activation of metallocene-based dimethyl precatalyst with MAO. A similar activation route is proposed in the case of dichrloride precursors with two main differences: 1) 1-6 species can be found in different degrees of chlorination, depending on mixing between metallocene-based catalyst and MAO; 2) Species 3 are rather Cl- than Me-bridged.[55]

In this respect, hetero-binuclear adducts with TMA play an important role in the case of Hf-based catalysts activated by MAO, which are by far less active than structurally analogous Zr-based catalysts, but when activated with a proper activator (i.e. boron-based) have comparably high activities.[91] A study by Busico and co-workers[92] dealt with the role of TMA in activation of Hf-based catalysts and they reported that TMA binds stronger to Hf-based catalysts than to the Zr-based ones, thus inhibiting propylene polymerization. When the same catalysts were activated with MAO modified with sterically hindered phenol compound (TMA scavenger), the activity of Zr-based catalysts increased 4 times, while for Hf-based catalysts it was 35-fold higher, confirming the negative impact of TMA on Hf-based catalysts activation. DFT calculations demonstrated that Hf-based catalysts form more stable bridged hetero-bimetallic species with TMA, also in bigger amount, than analogous Zr-based catalysts.[92]

Finally, it is important to notice that beside activating metallocene-based catalysts, MAO also acts as impurity scavenger and the case of supported catalysts (depending on the order of reactant addition) as agent that prevents catalyst leaching from the support and scavenger for both silica hydroxyl groups and impurities.[55,85]

1.3 Polymerization mechanism over metallocene-based catalysts

Olefin polymerization over metallocene-based catalysts occurs according to the coordination-insertion mechanism described schematically represented on Figure 3. 6.

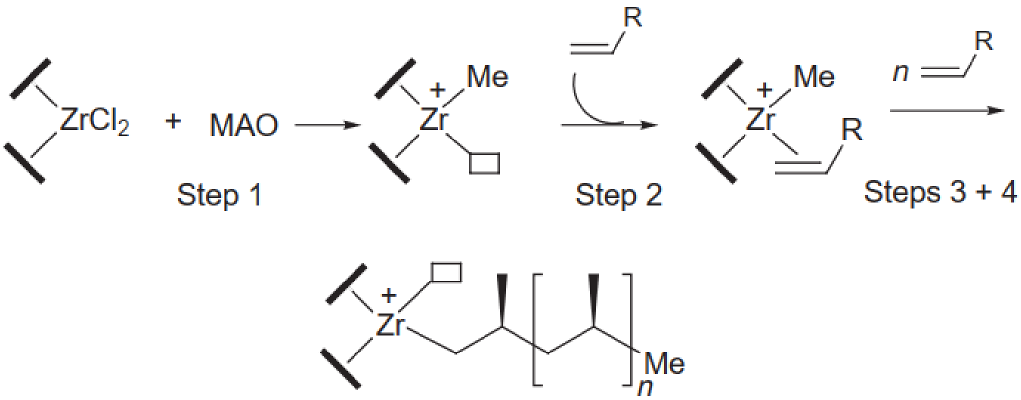

Figure 3. 6. Olefin polymerization mechanism over metallocene-based catalyst activated with MAO.[9] Step 1: activation of Zr-based catalyst with MAO. Step 2: Coordination of monomer to coordination vacancy. Steps 3 and 4: insertion of monomer into Zr-CH_3 bond and formation of new coordination vacancy where new monomer coordinate and subsequently insert to form polymer chain. [9]

The first step is monomer coordination to the metal cation, which acts as a Lewis acid. The next step is usually describing as the monomer insertion into the M-C bond to form the polymer chain, even though it is actually the alkyl group that migrates to the coordinated monomer, creating a new coordination vacancy where upcoming monomer can coordinate. The polymer chain grows by successive monomer coordination and insertion until chain transfer reaction takes place. The chain transfer can occur through β-hydride elimination or transfer to hydrogen, or other mechanisms. Transfer to hydrogen includes hydrogen bonding to active site to form metal-hydride site that act as an active site, while the other hydrogen atom goes to the end of polymer chain to form dead polymer chain. Dead polymer chain via β-hydride elimination mechanism is created when H atom from second C atom of the polymer chain is abstracted. In this case dead polymer chain has vinyl end-group, while metal-hydride is the same as in hydrogen transfer mechanism. The only difference between newly formed metal-hydride active site and the primary active site, is that the former bears H atom instead of alkyl (methyl) group resulting in the H at the end of new polymer chain.[9,12,25]

1.4 Metallocene-based catalysts investigated by UV-Vis and IR spectroscopies

1.4.1 Electronic properties of the precatalyst determined by UV-Vis spectroscopy

Although not so often, the electronic properties of metallocene complexes in solution have been investigated experimentally by means of UV-Vis spectroscopy. In metallocene complexes, two types of electronic transitions are observable by UV-Vis spectroscopy: i) π-π* transitions within the (aromatic) ligand and ii) ligand-to-metal charge-transfer (LMCT) transitions, the former occurring at higher energy than the latter. Since the metal is electron poor, no *d-d* transitions nor metal to ligand charge transfers can occur. The lowest energy absorption band in the UV-VIS spectrum of a d^0 metallocene arises from charge transfer between the highest occupied molecular orbital (HOMO) and the lowest unoccupied molecular orbital (LUMO). The HOMO of a d^0 metallocene is mainly Cp'-ligand based (Cp' = any η^5-Cp type ligand) while the LUMO is mostly of metal character. The energy of this particular absorption is of great importance, since it can be used to estimate the electron donating character of the Cp' ligand, as well as the electron deficiency of the metal center. Such variations in the electronic structures of metallocenes have a significant influence on olefin polymerization, as previously discussed.

The type of the metal. The metal center can influence the position of the LMCT band. It is reported that the position of LMCT band vary in three structurally analogous Ti-, Zr- and Hf-based catalyst depending on the metal site. Namely, (n-BuCp)$_2$HfCl$_2$ absorbs at 31750 cm^{-1} (315 nm), (n-BuCp)$_2$ZrCl$_2$ at 29500 cm^{-1} (339 nm), and (n-BuCp)$_2$TiCl$_2$ at 25500 cm^{-1} (392 nm). The LMCT for (n-BuCp)$_2$HfCl$_2$ occurs at higher energy due to more stable bonds between Hf and Cp' ligands. Moreover, LMCT absorption bands for Hf- and Zr-based catalysts appear at very similar positions due to similar size of metal center and thus similar bond angles, also indicating small effect of different bond angles on LMCT band energy.[41,47,48,93]

Ligand substituents. Ligand substitution is expected to have impact on the energy of LMCT band since it is well-known method for modifying the electronic (and steric) properties of the catalyst. It is demonstrated that each methyl substituent in Cp ligand in Cp$_2$ZrCl$_2$ catalyst cause a decrease in the energy of the LMCT band by 4 nm.[93] This is because methyl substituents destabilize the HOMO (i.e. brings it closer to the LUMO), so charge transfer between the two orbitals requires less energy.

Interannular bridge. Position of LMCT band in same metallocene-based complex can vary also depending on the type of the bridge: addition of 1,1' positioned bridges of type $(CH_2)_2$ or Me_2Si in bis(indenyl)zirconium dichloride catalysts cause a bathochromic shift of 41-59 nm.[93] When same bridges at same position were added to bis(cyclopentadienyl) zirconium dichloride complexes the LMCT band shifts bathochromicaly for 12-23 nm.[93] This indicate that the shift in LMCT band is not just due to electron donating ability of the bridge, but is also a consequence of the changes in ligands orientation (rac- or meso-form).[93]

1.4.2 Metallocenes activation mechanism explored by UV-Vis spectroscopy

Several research groups investigated the activation mechanism of different metallocene-based catalysts for olefin polymerization in solution by means of UV-Vis spectroscopy.[57,64–66,72,94–96] UV-Vis measurements, complemented by NMR, contributed to trace the activation mechanism discussed in Section 1.2.2: the activation of group 4 metallocene dichlorides by MAO/TMA proceeds first by methylation, to give the neutral monochloride metallocene species, and then by chloride or methyl abstraction to give cationic species.

Figure 3. 7 reports the evolution of the UV-Vis spectra for rac-$Et(Ind)_2ZrCl_2$ in the presence of increasing amounts of MAO (solvent, toluene, T=20°C). Addition of MAO for ratios $Al:Zr<20$ (Figure 3. 7A) leads to a shift of the main absorption band at higher energy (from 427, band I, to 390 nm, band II), through formation of an isosbestic point. This shift is explained on the basis of the molecular orbital theory, as due to an increase of the electronic density onto the zirconium atom, induced by the substitution of one chlorine atom (highly electronegative) of rac-$Et(Ind)_2ZrCl_2$ by a methyl group of MAO (less electronegative), so that the metal becomes more electron rich (i.e. it is more difficult to transfer electron density from the ligand to the metal). The same behavior is observed when using TMA instead of MAO and, more important, also when using TMA-free MAO, which indicates that MAO itself is a powerful alkylating agent, even in the quasi-absence of free TMA. Hence, *methylation brings about a shift of the LMCT band to higher energy*.

The addition of increasing amounts of MAO ($20<Al:Zr<150$) results in a reverse shift of the main absorption band from 390 (band II) to 440 nm (band III), again through formation of an isosbestic point (Figure 3. 7B). For higher Al:Zr ratios ($150<Al:Zr<4000$), the maximum band is again red-shifted to finally reach an upper limit at 470 nm (from band III to band IV, Figure 3. 7C). *The shift of the LMCT band to lower energy is a clear manifestation of zirconocene cationization*: when the metal is in its cationic form, electron density is more easily transferred (thus the transition requires less energy) from the electron rich ligands to the electron poor metal. As far as the assignment of the two bands at 440 and 470 nm (bands III and

IV), Coevoet works are not particularly clear. As a matter of fact, the authors found a relation between the shift of the LMCT band and the activity of the catalyst in 1-hexene polymerization, and they concluded that the two bands at 390 and 440 nm correspond to non-active species, while those only with an absorption band located at 470 nm are the active species. Nevertheless, this assignment is questioned on the basis of additional reports by the same authors. In fact, it has been reported that evolution from band III to band IV is not observed when TMA-free MAO is used instead of MAO: addition of TMA-free MAO at Al:Zr molar ratio much higher than 150 does not further modify the location of the main absorption band which remains centered at 440 nm. Only upon adding intentionally TMA to this system a further shift of the absorption band from 440 to 470 nm is observed. These experimental evidences suggest that band IV is associated with species containing TMA, as for example hetero-binuclear adducts of the type $[L_nZr(\mu\text{-}Me)_2AlMe_2]^{\oplus}[Me\text{-}MAO]^{\ominus}$.

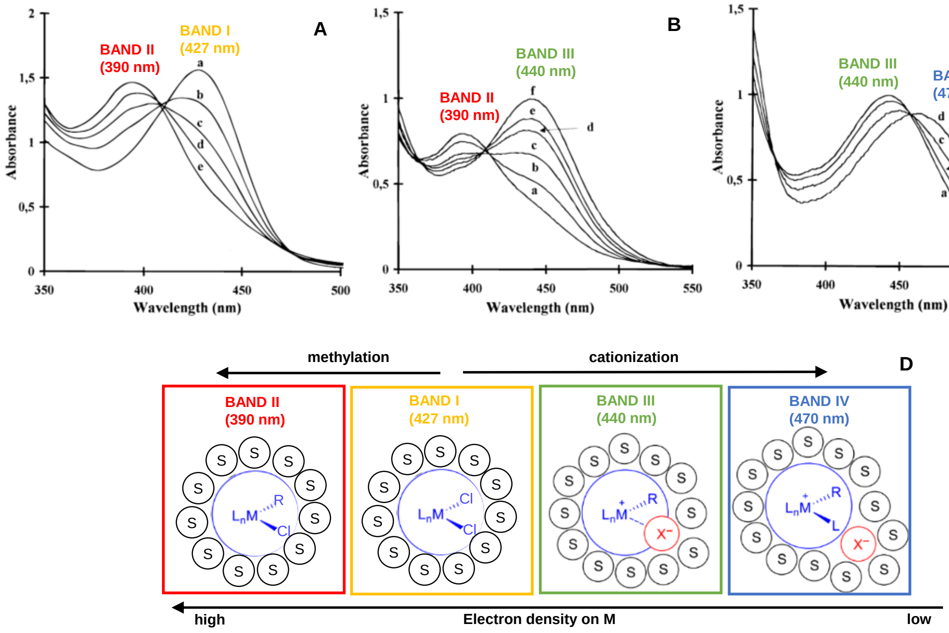

Figure 3. 7. UV-Vis spectra of rac-Et(Ind)$_2$ZrCl$_2$ in the presence of increasing amounts of MAO (solvent, toluene, T=20°C). Part A): from Al:Zr=0 (a) to Al:Zr=12 (e). Part B): from Al:Zr=24 to Al:Zr=80 (f); Part C): From Al:Zr=120 (a) to Al:Zr=2000. Part D) shows a general correlation between structure of the zirconocene species, electron density on the metal and position of the main LMCT band in the UV-Vis spectrum. In the example, X^- = MAO$^-$; L=TMA.

The type of ion-pair can change/rearrange over time, as demonstrated for Hf-based catalysts.[97] Particularly, when a Hf-based catalyst was activated with

MAO/TMA, the LMCT band shifted from 21300 cm^{-1} (470 nm) to 16400-16100 cm^{-1} (610-620 nm), indicating formation of ion-pairs. Interestingly, after 24 h, the band vanished, and a new band at 19000 cm^{-1} (525 nm) emerged. The new band was assigned to secondary Hf complexes, that however are quite stable, since after 1-hexene addition to this secondary complex no spectral changes were observed.[97]

1.4.3 UV-Vis spectroscopy to monitor olefin polymerization over activated metallocene catalysts

Coevoet et al. investigated also the influence of 1-hexene addition on the UV-Vis spectrum of Zr-based catalyst activated with MAO (Al:Zr=200). The results are reported in Figure 3. 8A. Immediately upon 1-hexene addition the LMCT band shifts at higher energy (from 450 nm to 432 nm), indicating 1-hexene coordination to Zr active species. As a matter of fact, after polymerization reaction was finished the band shifted back meaning that active species restored their initial form, confirming earlier observations regarding the stability of the active species and their ability to start polymerization after introducing the second batch of monomer.[65,98]

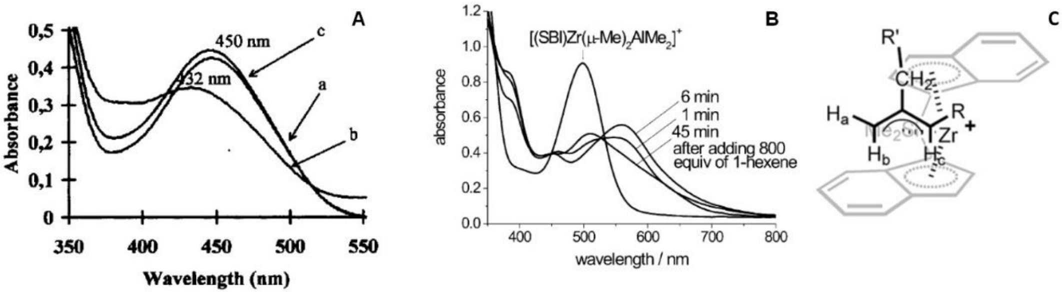

Figure 3. 8. Part A): UV-Vis absorption spectrum of rac-Et(Ind)$_2$ZrCl$_2$/MAO in the presence of 1-hexene in toluene at 20°C; [rac-Et(Ind)$_2$ZrCl$_2$] = 6x10^{-4} M, Al:Zr = 200; a) in absence of 1-hexene, b) during 1-hexene polymerization ([hex] = 0.8 M), c) after completion of 1-hexene polymerization. Part B): UV-Vis spectra of a 0.4 mm toluene solution of (Me$_2$Si(1-indenyl)$_2$Zr(μ-Me$_2$)AlMe$_2$ at 25°C, before and at various times after addition of 100 mL of 1-hexene. Part C): One of the possible structures of Zr-allyl species.

Brintzinger and co-workers, instead, for Me$_2$Si(1-indenyl)$_2$Zr(μ-Me$_2$)AlMe$_2$ observed an opposite behavior, as reported in Figure 3. 8B. Immediately after 1-hexene addition the LMCT band related to active species decreases in intensity, and new band starts to grow at lower energies with respect to LMCT band (it’s important to note that this is multi-stage process). These data were interpreted in terms of formation of Zr-allyl species (Figure 3. 8C). Earlier, this species were considered as deactivation products, but recent NMR and UV-Vis studies demonstrated that Zr-allyl species are present at early stages of polymerization reaction and make up to 90% of reaction pool.[99,100] Furthermore, Zr-polymeryl species can be formed from Zr-allyls trough several mechanisms, i.e., allyl vs. methyl exchange with Al-Me units of MAO/TMA or monomer insertion into Zr-allyl bond (thus forming polymer containing internal C=C bond).[99]

Another study dealing with Hf-based catalyst demonstrated that upon addition of 1-hexene into aged solution of Hf-based catalyst activated with both TiBA and borane-based activator, the LMCT band ascribed to active ion-pairs increases in intensity and at same time another band related to inactive secondary complexes decreases in intensity, clearly showing that 1-hexene can shift the equilibrium toward active species.[97] When 1-hexene were added together with mixture of activators (TiBA/borane-based) the intensity of the LMCT band associated with the active species was higher, confirming previous statement.[97]

1.5 Heterogeneous metallocene-based catalysts

1.5.1 Reasons for heterogenize metallocene-based catalysts

Although homogeneous metallocene-based catalysts have a very important feature – their thoroughly defined structure resulting in single-site nature – they must be supported to be used in available polymerization facilities (so-called drop-in technology because no modification of the process/facility is needed) designed for heterogeneous Ziegler-Natta and Philips catalysts.[4,60] To this aim, metallocene-based catalysts are heterogenized on supports like silica, alumina, magnesium chloride, zeolites, inorganic oxides, or other, and can be even self-immobilized.[5,9,101]

The heterogenization of metallocene-based catalysts is challenging because it is necessary to keep the features of homogeneous systems, for instance high activity, defined structure, stereoselectivity and co-monomer reactivity, and at the same time the catalyst should not leach from the support. There are a few ways to heterogenize metallocene-based catalysts: i) reacting the support with MAO, and then adding catalyst precursor; ii) grafting the catalyst precursor on support and subsequently activating it with MAO, and iii) reacting catalyst precursor and MAO in solution, and then supporting the mixture.[12,101] Sometimes, spacer groups can be used as connection between catalysts precursor and the support in order to minimize the influence of support on the catalyst properties. The order of reactants addition has significant impact on the formation of the active species.[12,101]

The main advantages of heterogenization of metallocene-based catalysts are: [12,102–106]

- Minimizing reactor fouling;

- Enabling continuous (& cheaper) gas- and slurry-phase polymerizations;
- Better polymer microstructure control and higher bulk density;
- Lowering MAO amount required to activate the catalyst: usually Al:Zr rates higher than 1000 are needed to achieve high activity in homogeneous conditions. In the case of supported catalysts Al:Zr ratios of few hundreds are enough for catalysts activation;
- Average MW of polymer is higher for heterogeneous catalysts than for corresponding homogeneous, and the MW distribution can broaden.

The requirements that must be satisfied when choosing catalyst support are surface properties, chemical composition, morphology (surface area, particle and pore size distribution, pore volume) and mechanical properties. Silica is the best choice as support because it satisfies all before mentioned criteria.[12,103,104,107] Additionally it is commercially available with a broad range of characteristics, and it is relatively cheap. Silica properties can be easily varied during the synthesis, while chemical properties (dictated by the surface silanol groups) can be modified by thermal and/or chemical treatments. [12,103] Although silica is declared to be inert, it is well known that it plays a role in the active site's definition, due to the interaction of catalyst precursor with silica surface groups, as well as in affecting the catalyst behavior during ethylene polymerization, for example the silica pore size influences the catalyst fragmentation behavior and mass transfer phenomena. [102–104]

1.5.2 DR UV-Vis spectroscopy applied to heterogenized metallocene catalysts

The literature about UV-Vis investigation of SiO_2-supported metallocene catalysts is rather scarce. Velthoen et al.[108] investigated a silica-supported Zr-based catalyst (bis(1-methyl-3-butylcyclopentadienyl, structure A in Figure 3. 9) activated with increasing amounts of MAO by means of DR UV-Vis spectroscopy complemented by TD-DFT calculation, to assess the influence of MAO amount on the formation of catalytic species.[85] The DR UV-Vis spectra of all catalysts show three main bands (I-III in Figure 3. 9), which however have a different relative intensity depending on the amount of MAO. Namely, band I in Figure 3. 9 does not change position upon MAO addition and was correlated with MAO (confirmed also by DR UV-Vis spectra of solid activator, SiO_2/MAO). Band II is attributed to methyl-bridged heterobinuclear adducts with TMA (species C in Figure 3. 9), while band III is assigned to cationic chloride-bridged heterobinuclear adducts with TMA (species B in Figure 3. 9). According to the authors, species C are dormant species of an active cationic structure 3 with open coordination vacancy, but it might become active after monomer insertion.[108]

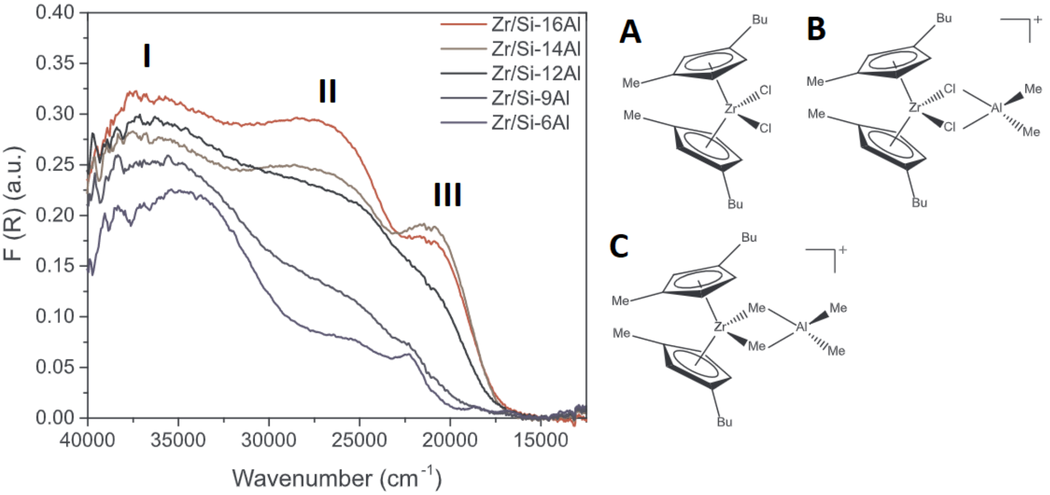

Figure 3. 9 DR UV-Vis spectra of SiO_2/MAO/Zr catalyst activated with increasing amount of MAO and structures of catalyst precursors (A), and proposed active (B) and dormant species (C).[108]

Similar conclusions were reached by other authors who reported on chlorinated and methylated SiO_2/MAO/Zr catalysts additionally activated with TiBA.[94] Particularly, for both catalytic systems upon TiBA addition the lowest-energy band shift to lower energies which was assigned to formation of methyl-bridged heterobinuclear adducts with TMA (species C in Figure 3. 9). Within the same study catalysts were also investigated by DRIFTS (CO and ethylene adsorption) which demonstrated that catalyst treated with TiBA have higher activity than those not treated with TiBA, leading to conclusion that methyl-bridged heterobinuclear adducts with TMA are the active species.[94]

1.5.3 IR spectroscopy of adsorbed probe molecules

Probe molecule IR spectroscopy is recognized as powerful technique for studying surface chemistry of materials[109] and was widely exploited to investigate heterogeneous catalysts, including heterogeneous catalysts for olefin polymerization.[85,110–116] To this aim, CO is the mostly used probe molecule because it can discriminate between different surface sites based on their acidity, but other probes such are pyridine[85] and d-acetonitrile[116] were used as well.

Carbon monoxide (CO)

CO is an almost ideal probe molecule since it has small molecule size and mild basic character, thanks to which CO can differentiate between surfaces sites based on their acidity.[109,117] When CO interacts with an electron acceptor, acting as Lewis acid site (LAS), electron density from C-end of CO is transferred to the metal cation causing σ-coordination. In an IR spectrum this is manifested by a shift of ν(CO) band to higher wavenumbers when compared to that of gaseous CO (2143 cm^{-1}):[109,117] higher the shift, stronger the acid sites. Moreover, a big advantage of using CO as a probe molecule for investigating metallocene catalysts for olefin polymerization is that, beside coordinating to the metal cation (acting as LAS), it can subsequently insert into the M-C bond to form metal-acyl species, thus imitating olefin polymerization process but without mass transfer limitations.[110]

It is important to notice that to evaluate CO coordination to LAS and insertion into M-C bonds two experiments at different temperature must be done. In fact, coordination of CO with weak LAS sites is negligible at room temperatures and requires working at 100 K. On the contrary, CO insertion into the M-C bond is an activated process and does not occur at 100 K.

A few studies are present in the literature reporting the IR spectra of CO adsorbed at low temperature on different SiO_2/MAO/metallocene catalysts. These studies demonstrate that CO is able to probe LAS of different strength, particularly moderate and weak LAS, belonging to MAO.[85,114,115] Absorption bands corresponding to CO coordinated to the metal cation were also observed but have rather low intensity, indicating that CO have difficulties to reach the metal cation.[85,114,115,118] When CO is adsorbed at room temperature on SiO_2/MAO/metallocene systems, bands in the 1735-1495 cm^{-1} region have been observed and assigned to Zr-acyl species formed upon CO insertion into the Zr-CH_3 bond.[114,115,118] The CO insertion into the Zr-CH_3 bond is irreversible, as associated bands remain present in the IR spectrum even after evacuation at room temperature.

Acetonitrile

Acetonitrile is another probe molecule highly suitable for characterization of surface species in heterogeneous catalysts, since it is a small molecule and displays mild basic character.[117] Acetonitrile is an electron-rich probe molecule, and it is expected to interact with any electron deficient species via σ-charge release from nitrogen lone-pairs.[119] In order to overcome bands splitting due to Fermi resonance, deuterated acetonitrile (d-acetonitrile) must be used instead of acetonitrile.[117] When interacting with LAS, the ν(CN) stretching frequency shifts to higher energies with respect to neat acetonitrile (2263 cm^{-1}), stronger the site larger the shift.[119] It is worth noticing that, differently from CO, acetonitrile is not able to distinguish between LAS of different strength owing to its stronger basic character when compared to CO.

As for CO, not only acetonitrile can coordinate to LAS, it can also insert into M-C bond to yield products called aza-alkenyldene,[120–123] again mimicking olefin polymerization process but without mass transfer limitations because no polymeric aza-alkenyldene species can be formed. Furthermore, ν(C=N) of aza-alkenyldene species falls in other well-defined region, 1720-1600 cm^{-1}, without overlapping with chemisorbed acetonitrile, easing discrimination between two contributions Nevertheless, it was scarcely exploited so far,[116] and never as IR insertion probe for olefin polymerization catalysts. Moreover, interactions with LAS are strong enough even at room temperature, meaning that coordination to LAS and insertion into M-C bond can be simultaneously examined.

2. Spectroscopic characterization of two zirconocene-based catalysts: SiO$_2$/MAO/Zr1 and SiO$_2$/MAO/Zr2

2.1 Motivation

The objects of this study are two SiO$_2$/MAO/zirconocene-based catalysts synthesized following the same procedure (described in Chapter 2, Section 2.1.2), activated with MAO at the same Al:Zr ratio (150) and having the same metal content (Zr wt%=0.3), but differing in the type of zirconocene precursor, as shown in Figure 3. 10. The first zirconocene precursor (Zr1) bears 2,2'-biphenylene-bis-2-indenyl ligand, while the second (Zr2) is an archetypal of zirconocene complexes and is based on the Me$_2$Si-bis(2-Me-1-indenyl) ligand. The corresponding catalysts will be referred to as SiO$_2$/MAO/Zr1 and SiO$_2$/MAO/Zr2, respectively.

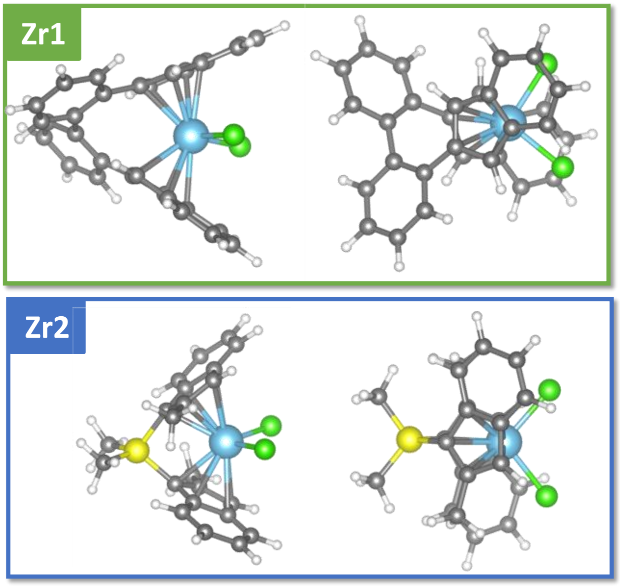

Figure 3. 10. Structure of the Zr1 and Zr2 zirconocene precursors from two different perspectives (blue=Zr, green=Cl, gray=C, yellow=Si, and white=H).

The two precursors have the same type of ligand (indenyl) but differ in the type of bridge. This affects all the main basic geometrical parameters reported in Figure 3. 11: the average Zr-Cp distance (*a*), the Cp-Cp' plane angle (α), the Cp-Zr-Cp' angle (β), and the ring slippage angle (Θ), which represents the displacement of the ring centroid from the normal to the ring plane. A further important parameter is the C(2)-centroid-centroid'-C(2') dihedral angle ϕ, or torsional angle, which expresses the degree of relative rotation of the two indenyl ligands.

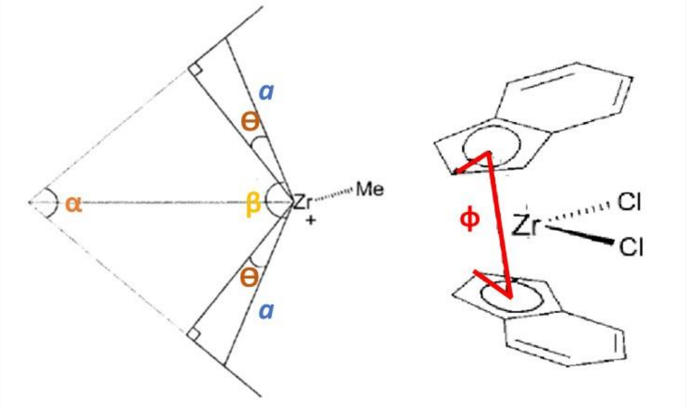

	a (Å)	α (°)	β (°)	ϴ (°)	ϕ (°)
Zr1	2.257	69.5	128.5	9	69.4
Zr2	2.175	81.5	118.6	10	150.8

Figure 3. 11. Main geometrical parameters of a zirconocene complexes and their values for Zr1 and Zr2 as calculated (courtesy of Edrisse Chermak, SABIC)

It has been demonstrated that all these parameters have a strong influence on the steric and electronic properties of the complexes. Some basic rules are summarized in the following.

- As far as steric parameters are concerned, the accessibility of the Zr cations increases upon increasing *a* and α, and to a lesser extent also β (i.e. concept of coordination gap aperture). This means that *Zr2 is expected to be sterically more accessible than Zr1*.
- As far as the electronic properties of the complex, these are also affected by *a,* as well as by the ring slippage angle ϴ. Longer is *a* (i.e. weaker is the bond between Zr and Cp) and greater is ϴ, the less easily an electron is detached and transferred from the ligand to the d orbitals of the Zr cation. This means that longer *a* distances and larger ϴ angles decrease the electron donating ability of the ligand to the metal, so that the cationic nature of the metal increases. The values reported in Figure 3. 11 indicate that *the Zr cation in Zr2 should be "more positive" than in Zr1*.
- Finally, the electronic properties of the complex are found to be strongly associated with the orientation of the indenyl ligands (i.e. by the ϕ angle).

Increasing ϕ reduces the overlap between filled indenyl π orbitals and empty Zr d orbitals. As a consequence, the HOMO level rises in energy, and the HOMO-LUMO gap decreases. From Figure 3. 11 we expect that *Zr2 should be characterized by a smaller HOMO-LUMO gap than Zr1*.

The difference in the steric and electronic properties of the two zirconocene precursors are expected to affect their reactivity towards MAO and the overall catalytic performances of the final catalyst. The two silica supported catalysts showed a similar activity in ethylene copolymerization with 1-hexene in HT-tests performed at SABIC. However, a non-uniform ethylene/1-hexene copolymer composition was reported for SiO_2/MAO/Zr2. This was attributed to the so called "filter effect", a term coined by Fink and coworkers[126] to indicate the formation, during the initial stages of polymerization, of a 1-hexene rich copolymer envelope around the catalyst particle, which works as a filter for the following monomer. The small ethylene molecules are able to diffuse through the copolymer filter and polymerize in the core of the catalyst particle. The larger 1-hexene molecules, instead, have problems to diffuse through the copolymer layer and consequently do not reach the active sites in the interior of the catalyst particles. This leads to polymer particles comprising an ethylene-rich center surrounded by an outer layer of the copolymer.

In order to gain insights on the properties of the two silica-supported catalysts at a molecular level, we performed a systematic investigation by means of spectroscopic methods. In particular, we explored three types of probe molecules to assess the accessibility of the Zr cations and their insertion ability, namely CO, d-acetonitrile and 1-hexene. IR spectroscopy of probe molecules is one of the most sensitive techniques to retrieve information on molecular properties of heterogeneous catalytic systems[109,127] and was widely exploited for characterization of heterogeneous polymerization catalysts such are Philips,[128,129] Ziegler-Natta catalysts,[112,113,130,131] and metallocene-based catalysts.[85,114,115] These measurements were complemented by data collected on the two catalyst precursors in toluene solution and on the homogeneous catalysts obtained upon activation of Zr1 and Zr2 with MAO at different concentrations.

2.2 Electronic properties of the two catalysts

2.2.1 Homogeneous catalysts

Before addressing the electronic properties of SiO_2/MAO/Zr1 and SiO_2/MAO/Zr2, we investigated the corresponding homogeneous systems. At first, we started to collect the UV-Vis spectra of the two catalyst precursors in toluene, which are reported in Figure 3. 12. The spectra are shown in the 35000 – 10000 cm^{-1} range: above 35000 cm^{-1} they saturate because of the solvent. In both cases, two bands are observed: at 32300 and 25400 cm^{-1} for Zr1, and at 30400 and 22300 cm^{-1} for Zr2. LMCT bands at positions very similar to those of Zr2 were reported for $Me_2Si(Ind)_2ZrMe_2$.[94] According to the literature, the band at lower-energy is due to the HOMO→LUMO transition, where the HOMO is prevalently centered on the indenyl ligand, while the LUMO is mainly centered on the Zr cation (hence, this is a LMCT transition).[93] The higher-energy band, instead, is assigned to a LMCT from molecular orbitals involving both Cl and indenyl ligands to molecular orbitals mainly centered on the Zr cation.

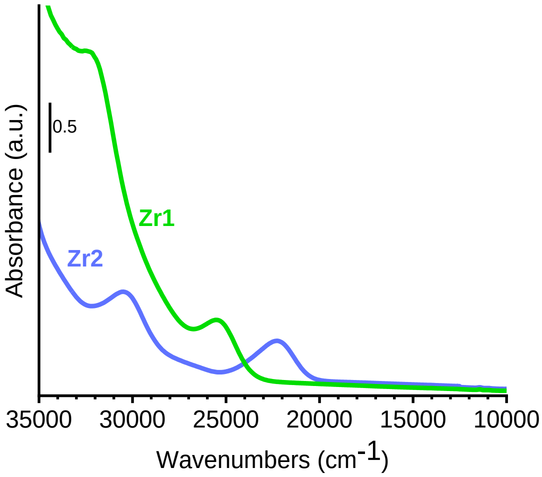

Figure 3. 12. UV-Vis spectra of Zr1 (green) (approx. C=5*10^{-4} M) and Zr2 (blue) (approx. C=5*10^{-3} M) catalyst precursors in toluene.

The position of these two bands is different for the two precursors, meaning that their electronic properties are different. This is something expected, since changing ligand and/or bridge are well-known and easy methods to change the electronic properties of the complex, as summarized in the previous sections.[26] The

HOMO→LUMO transition is found at higher energy for Zr1 than for Zr2, which means that transfer of electron density from the ligand to the Zr cation is more difficult. In other words, *the electron density on the Zr cation is higher in Zr1 than in Zr2, which also implies that cation formation in the presence of the activator should be less favored in the case of Zr1*.[93] This is in very well agreement with the predictions from the analysis of the geometrical parameters reported in Figure 3. 11.

In the next step, Zr1 and Zr2 catalyst precursors were activated with MAO in different Al:Zr ratios, and the activation process was monitored by UV-Vis spectroscopy. The results are shown in Figure 3. 13. Starting from Zr1 precursor (Figure 3. 13a), after the addition of MAO at all Al:Zr ratios (50, 150, 300) the band due to the HOMO→LUMO transition shifts to lower energies by about 1200 cm^{-1}, with small changes in the intensity, which however is affected by the fact that adding MAO the solution of the precursor becomes less concentrated. According to the literature on similar systems, at Al:Zr=50 monomethylation of the dichloride precursor (i.e. the exchange of the more electron withdrawing Cl with more electron donating CH_3 group) should occur, and this should bring to an increase in the energy required for electron transfer from the ligand to Zr, hence a shift of the HOMO→LUMO band at higher energy.[57,64–66,72] In contrast, we observe a shift towards lower energy, which is peculiar for monomethylated cationic zirconocene species. This indicates that in our experimental conditions an Al:Zr ratio of 50 eq. is enough to start the formation of cationic Zr1 species, while at higher Al:Zr ratio this is accomplished.[67]

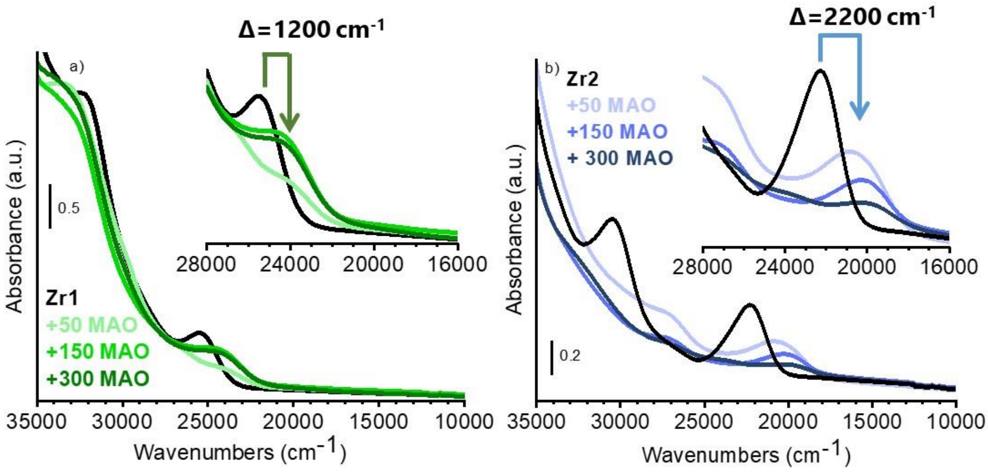

Figure 3. 13. UV-Vis spectra of a) Zr1 precursor in toluene (approx. C=5*10^{-4} M) activated with MAO in different amount (Al:Zr=50, 150 and 300) and b) Zr2 precursor in toluene (approx. C=5*10^{-3} M)

activated with MAO in different amount (Al:Zr=50, 150 and 300). The insets in both parts report a magnification of the low energy band, which is ascribed to the HOMO→LUMO transition.

The situation is very similar when Zr2 is activated with MAO in Al:Zr ratios of 50, 150, and 300 eq. (Figure 3. 13b). Upon addition of MAO the HOMO→LUMO transition downward shifts by about 2200 cm^{-1}. However, this shift is definitely more pronounced than in the case of Zr1 (1200 cm^{-1}), which indicates that hetero-binuclear*ion-pairs are formed with MAO in the case Zr2 catalyst than for Zr1*. *At this stage, we speculate that OSIP of the type* $[L_nZr(\mu\text{-}Me)_2AlMe_2]^{\oplus}[Me\text{-}MAO]^{\ominus}$ *are prevalently formed between Zr2 and MAO, while ISIP of the type* $[L_nZrMe^{\oplus}\cdots Me\text{-}MAO^{\ominus}]$ *are mainly formed between Zr1 and MAO.* Formation of $[L_nZr(\mu\text{-}Me)_2AlMe_2]^{\oplus}[Me\text{-}MAO]^{\ominus}$ OSIP is most probably a consequence of the larger bite angle and less steric hindrance in Zr2 when compared to Zr1. The combination of these two factors renders the Zr cation more available for TMA.

2.2.2 Silica-supported catalysts

Figure 3. 14 compares the DR UV-Vis spectra of the heterogeneous SiO_2/MAO/Zr1 and SiO_2/MAO/Zr2 catalysts with the absorbance UV-Vis spectra of the corresponding homogeneous catalysts at the same Al:Zr ratio (150 eq). Starting the discussion from SiO_2/MAO/Zr1 (Figure 3. 14a), its DR UV-Vis spectrum is much less resolved than the UV-Vis spectrum of the corresponding homogeneous system, which indicates a higher heterogeneity of species, i.e ion-pairs which are quite similar to each other but not exactly the same. We speculate that these are ISIP of the same type, $[L_nZrMe^{\oplus}\cdots Me\text{-}MAO^{\ominus}]$, where however the cations bound $MeMAO^{\ominus}$ counterion in different ways. In fact it was reported that ISIP with stronger and weaker bounded counterparts are present in homogeneous Zr-based catalysts ($Me_2Si(Ind)_2ZrCl_2$), and are formed after activation of catalyst precursor with MAO components of different Lewis acid strength.[67] These different types of ISIP species absorb at slightly different energy (just a few nm),[67] thus they are hardly discriminated between each other. Finally, the difference in the UV-Vis spectra of the homogeneous and heterogenous Zr1-based catalysts further implies that *silica is not just an inert dispersing agent but has some role in the definition of the active sites in* SiO_2*/MAO/Zr1 catalyst*.

Instead, the UV-Vis spectra of heterogeneous and homogeneous Zr2-based catalysts are very similar to each other. Namely, the DR UV-Vis spectrum of SiO_2/MAO/Zr2 reproduces almost perfectly that of Zr2 catalyst activated with the same amount of MAO, apart from a slight upward shift of the LMCT bands. This means that *__in the case of Zr2-based catalyst, silica has no big impact on the active site definition__*.

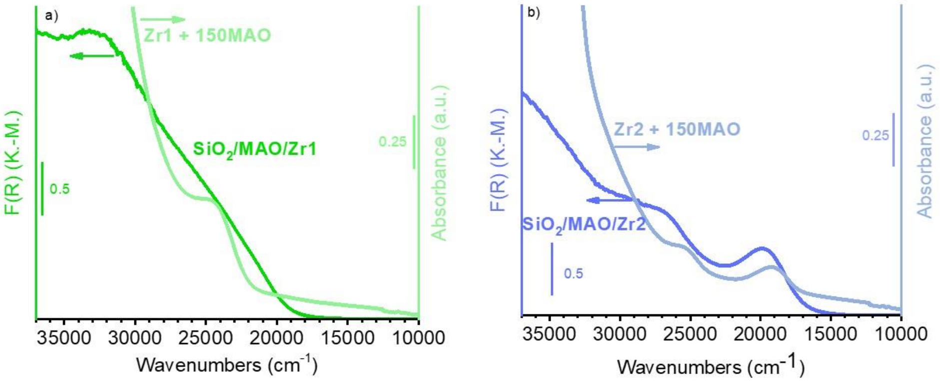

Figure 3. 14. Part a): DR UV-Vis spectra of SiO_2/MAO/Zr1 catalyst (dark green) compared to the absorbance UV-Vis spectrum of Zr1 in toluene (approx. C=5*10^{-4} M) activated with MAO (Al:Zr=150). Part b): the same as part a) for the Zr2-based catalysts.

Finally, Figure 3. 15 compares the DR UV-Vis spectra of the two heterogeneous catalysts and of SiO_2/MAO, in a larger energy range. It is interesting to observe that the spectrum of SiO_2/MAO shows a weak and resolved peak around 38000 cm^{-1}, which is due charge transfer transitions within MAO (specifically, from the oxygen lone pairs into the empty aluminum orbitals). UV-Vis experiments on MAO modified silica demonstrated that silica containing lower amount of MAO (5 wt% Al/Si) has absorption band at 36900 cm^{-1} (271 nm) with a shoulder at 34600 cm^{-1} (289 nm) and is assigned to nonbonding electrons of bridging oxygen atoms that are available for electronic transition. With increasing MAO loading on silica (up to 20 wt% Al/Si) the band shifted to lower energies, 33400 cm^{-1} (299 nm), indicating strong interaction of nonbonding oxygen with Al atoms in proximity. A reason for band shift to lower energy is increased amount of Al atoms that are available for oxygen to aluminum charge transfer.[8] This feature is completely hidden in the spectra of the silica-supported catalysts by the much more intense π-π* transitions within the aromatic ligand.[93]

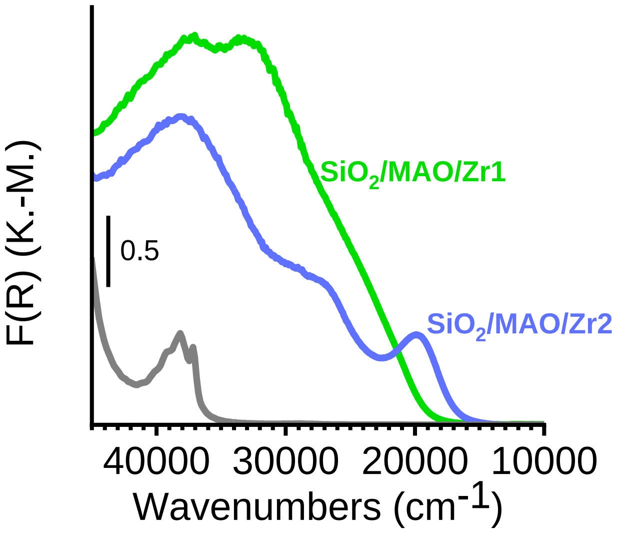

Figure 3. 15. DR UV-Vis spectra of SiO_2/MAO (gray), SiO_2/MAO/Zr1 (green) and SiO_2/MAO/Zr2 (blue)

2.3 Vibrational properties of the two catalysts

Figure 3. 16 compares the FT-IR spectra of SiO_2 (pre-activated at 600°C), SiO_2/MAO and SiO_2/MAO/Zr1 after normalization to the pellet thickness. The spectrum of bare SiO_2 (light gray) is dominated by an intense and out-of-scale absorption below 1300 cm^{-1}, which is due to the vibrational modes of the silica framework. The sharp band at 3757 cm^{-1} is ascribed to terminal OH groups present at the SiO_2 surface.[111,114,115,127] This band shows a pronounced tail at lower wavenumbers, indicating the presence of a certain fraction of OH groups in H-bonding interaction (likely in the silica pores).[127] After treatment of SiO_2 with MAO (gray), the band at 3757 cm^{-1} disappears, while a weak and broad band becomes visible at about 3680 cm^{-1}, indicating the presence of a few OH groups in H-bonding interaction. This agrees with the literature, according to which the terminal silanol groups react with the MAO solution upon impregnation. More specifically, it is actually the TMA present in the MAO solution, which reacts with the isolated silanol groups, whereas MAO itself is merely strongly adsorbed on silica but not chemically grafted.[101,115]

The bands at 3000-2700 cm^{-1} (very intense) and 1500-1350 cm^{-1} (weak), are assigned to the stretching and bending vibrational modes of CH_3 groups belonging either to MAO (i.e. Al−CH_3 species) or to Si−CH_3 and/or Si−O−Al−$(CH_3)_2$ species, which might originate from the reaction of MAO/TMA with the siloxane bridges at the silica surface.[132]

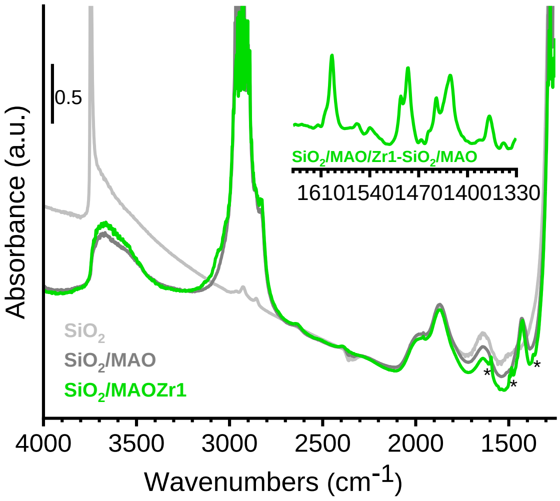

Figure 3. 16. IR spectra of SiO_2 (light gray), SiO_2/MAO (gray) and SiO_2/MAO/Zr1 (green). Spectra are normalized to the optical thickness of the pellet. The inset shows the spectrum of SiO_2/MAO/Zr1 after subtraction of that of SiO_2/MAO in 1650-1330 cm^{-1} region.

The spectrum of the SiO_2/MAO/Zr1 catalyst (green in Figure 3. 16) is pretty similar to that of SiO_2/MAO, except for very weak bands at 1595, 1485, 1444 and 1370 cm^{-1} (labeled with *), which are straightforwardly attributed to the vibrations of the zirconocene complex (more visible in the inset), more specifically to vibrations of indenyl ligands in activated SiO_2/MAO/Zr1 catalyst.[133] The spectrum of the SiO_2/MAO/Zr2 (not reported) is very similar, except that the bands associated with the vibration of the complex are different. Hence, hereafter the discussion will focus on the 1650-1340 cm^{-1} region, where vibrations from aromatic ligands contribute.

Figure 3. 17 shows the IR spectra of SiO_2/MAO/Zr1 and SiO_2/MAO/Zr2 catalysts after subtraction of spectrum of SiO_2/MAO, compared to ATR-IR spectra of the corresponding precursors, Zr1 and Zr2. The comparison allows us to evaluate if activation by MAO causes structural distortion in the ligand (which would lead to a shift in the IR bands associated to ligand vibrations). and the presence of Zr-CH_3 species in activated catalysts. While for SiO_2/MAO/Zr2 the spectrum is almost identical to that of the precursor Zr2, for SiO_2/MAO/Zr1 small differences are observed with respect to Zr1, suggesting that activation by MAO leads to some structural distortions in the ligand.

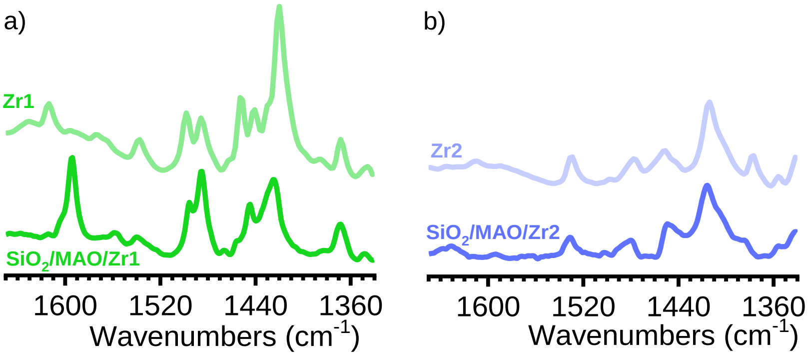

Figure 3. 17. IR and ATR-IR spectra of a) SiO_2/MAO/Zr1 catalyst and Zr1 precursor and b) SiO_2/MAO/Zr2 catalyst and Zr2 precursor. The spectra of SiO_2/MAO/Zr1 and SiO_2/MAO/Zr2 are shown after subtraction of spectra of SiO_2/MAO to highlight the vibration features of indenyl ligands in activated catalysts

2.4 Carbon monoxide as coordination and insertion probe

In order to assess the properties of the two catalysts at molecular level, attention was turned to IR spectroscopy of CO adsorption. As discussed in the previous sections, CO is a competent probe to test the coordination ability of activated metallocene cations, but also to investigate the insertion ability into the M-C bond. Moreover, when the experiment is performed at low temperature (100 K), CO is also able to probe the Lewis acid sites in the system.

2.4.1 IR spectroscopy of CO adsorbed at 100 K: detection of Lewis acid sites

Figure 3. 18 shows the IR spectra of CO adsorbed at 100 K on SiO_2, SiO_2/MAO, SiO_2/MAO/Zr1 and SiO_2/MAO/Zr2 in the ν(CO) region as function of CO coverage, after the subtraction of the spectrum taken before CO dosage. When CO is adsorbed on SiO_2 at the maximum CO coverage (Figure 3. 18a) two bands are observed at 2155 and 2137 cm^{-1}, which are ascribed to CO in interaction with surface OH groups[111,115,127] and to physisorbed CO[111,115,127], respectively. Both bands rapidly decrease in intensity upon lowering the CO coverage, indicating the weak nature of the interaction.

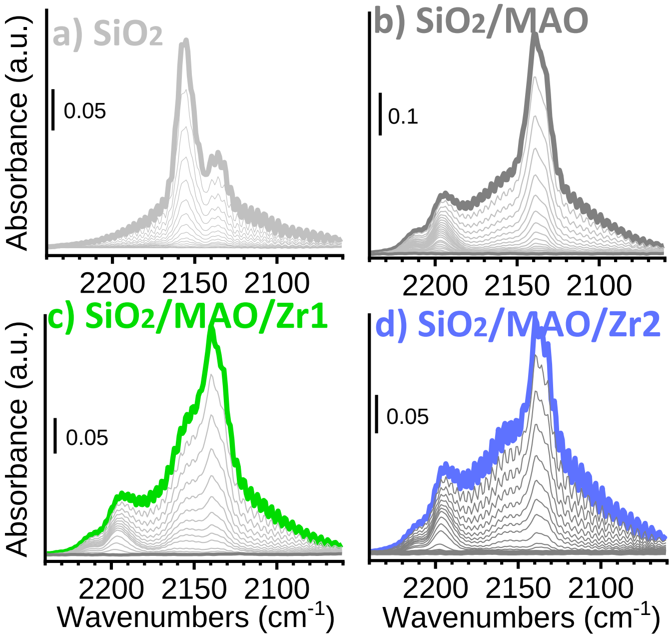

Figure 3. 18. IR spectra of CO adsorbed at 100 K on a) SiO_2, b) SiO_2/MAO, c) SiO_2/MAO/Zr1 and d) SiO_2/MAO/Zr2. Spectra are shown after subtraction of that collected prior CO dosage, in the ν(CO) region as a function of CO coverage.

When CO is adsorbed at 100 K on SiO_2/MAO (Figure 3. 18b) the band at 2155 cm^{-1} is no more observed as expected, since MAO (and the free TMA) reacts with most of the surface OH groups (as discussed above).[85,134] The band related to physisorbed CO, instead, dominates the spectrum at the maximum coverage. This band is not the same as that observed on pure SiO_2: its maximum is slightly shifted from 2137 cm^{-1} to 2134 cm^{-1}, suggesting that physisorbed CO is confined in some porosity generated by MAO and no more at the silica surface. In the same spectral region, a new band at about 2140 cm^{-1} is well evident, which was previously ascribed to CO interacting with O^{2-} ions on the MAO surface.[135] In addition, two bands are observed at 2213 and 2195 cm^{-1}, which are much more resistant to degassing, denoting a stronger interaction of CO with the adsorbing sites. These bands are ascribed to CO adsorbed at LAS with moderate and weak acidity, M-LAS and W-LAS, respectively. According to the literature, W-LAS are of type $AlOMe_2$ where tricoordinate Al atom is surrounded by two methyl groups and one oxygen. On the other hand, M-LAS are AlO_2Me where Al has attached one methyl group and two oxygen atoms that, having a greater electron-withdrawing nature, make Al atom to be a stronger LAS.[136] Observation of these species is important, because

LAS are considered, together with TMA and/or $AlMe^{2+}$ species, as activators for metallocene complexes.[114,115]

The spectra of CO adsorbed at 100 K on SiO_2/MAO/Zr1 and SiO_2/MAO/Zr2 are shown in Figure 3. 18c and Figure 3. 18d; they are very similar to each other and to those of CO adsorbed on SiO_2/MAO. The two most prominent bands are assigned to CO physisorbed in some porosity generated by MAO (at 2134 and 2140 cm^{-1}). The two bands at 2213 and 2195 cm^{-1}, which are more resistant to degassing, are assigned to CO in interaction with M-LAS and W-LAS, respectively. An additional band not observed when CO is dosed on SiO_2/MAO is detected at 2154 cm^{-1}. This band, which is easily removable upon degassing, falls in the position characteristic for CO in interaction with silica OH groups.[111,115,127] However, this assignment is discarded since in this case no OH groups are accessible at the surface. In contrast, the band is assigned to non-classical σ-carbonyl complexes of cationic zirconocene species.[85,109,114] Bands at similar positions were observed for CO adsorbed at 100 K on Na- and Ba-exchanged zeolites[137] and on SiO_2/MAO/Zr-based catalysts,[85] activated with higher MAO loadings. The easy reversibility of this band upon lowering the pressure indicates that CO competes with other ligands (i.e. the metallocene scaffold).

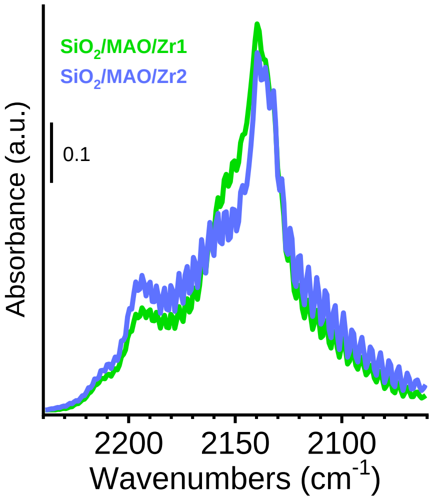

Figure 3. 19 Comparison between IR spectra of CO adsorbed at 100K on SiO_2/MAO/Zr1 and SiO_2/MAO/Zr2 and the maximum CO coverage. Spectra are shown after normalization to the optical thickness of the pellet in ν(C≡O) region.

Figure 3. 19 compares the spectra of CO adsorbed at 100 K on SiO_2/MAO/Zr1 and SiO_2/MAO/Zr2 catalysts at the maximum CO coverage and after normalization

to the optical thickness of the pellet. It is evident that the main features of the two spectra are exactly the same, even though the band at 2154 cm^{-1}, attributed to CO in interaction with cationic Zr species, is slightly higher for SiO_2/MAO/Zr1, indicating that *slightly more* $Zr^{\oplus}$ *are available for CO in* SiO_2*/MAO/Zr1 than in* SiO_2*/MAO/Zr2*. At same time, *the band assigned to CO in interaction with W-LAS, is more pronounced in the case of* SiO_2*/MAO/Zr2*.

2.4.2 IR spectroscopy of CO adsorbed at room temperature: formation of Zr-acyl species upon CO insertion into the Zr-C bond

In order to evaluate the potential CO insertion into the Zr-C bond in SiO_2/MAO/Zr1 and SiO_2/MAO/Zr2 catalysts, IR experiments of CO adsorption at 300 K were performed. At first, a blank experiment was performed on SiO_2/MAO, and no bands in the ν(C=O) region were observed (Figure 3. 20a).

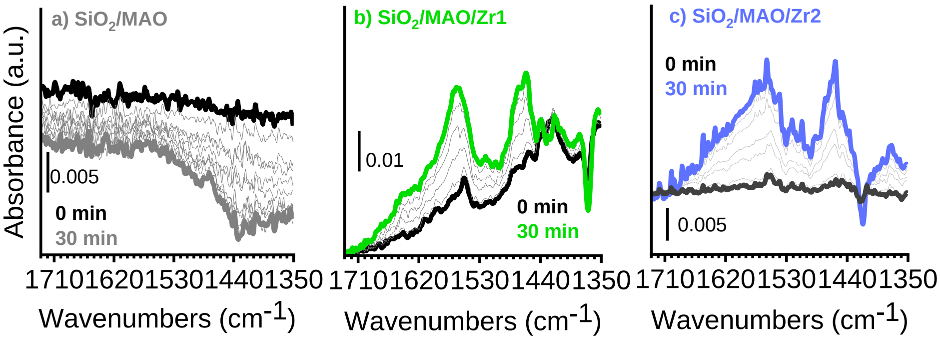

Figure 3. 20. IR spectra of CO adsorbed at 300 K on a) SiO_2/MAO, b) SiO_2/MAO/Zr1 and c) SiO_2/MAO/Zr2. The spectra are shown in ν(CO) region as a function of time (30 minutes) after subtraction of spectrum collected prior CO dosage.

When CO is adsorbed on SiO_2/MAO/Zr1 and SiO_2/MAO/Zr2 a few weak bands appear almost immediately at 1560 and 1460 cm^{-1}, and slowly grow in intensity as a function of time (Figure 3. 20b and Figure 3. 20c). Both bands are attributed to the ν(C=O) vibration of acyl complexes of Zr formed after CO inserted into diverse Zr-Me bonds.[114,118] Such a low ν(C=O) value for an acyl group was reported in the literature for different acyl complexes of Zr and it is explained by high oxidation number of Zr and an open shell configuration (16 electrons).[138] For now, it is not possible to discriminate between the two types of Zr-acyl species, that probably differ for the extent of the η^2-coordination to the cation. More than one type of Zr-acyl species were reported in the literature and only a few of them were declared to correspond to the acyl compounds of active Zr species.[114] The presence of more than one type of sites able to form Zr-acyl species is very well in agreement with work of Mehdiabadi *et al.*,[139] who demonstrated that 3 site model is needed to describe the MW distribution of PE produced by use of industrial SiO_2/MAO/Zr catalyst.

The IR spectra collected after 30 minutes of interaction of CO at 300 K on SiO_2/MAO/Zr1 and SiO_2/MAO/Zr2 are compared in Figure 3. 21 after normalization to the thickness of the pellet. The comparison allows to appreciate that the bands are almost identical, both in position and in intensity. This indicates that *the Zr-acyl species formed upon interaction with CO at room temperature are the same in SiO_2/MAO/Zr1 and SiO_2/MAO/Zr2*.

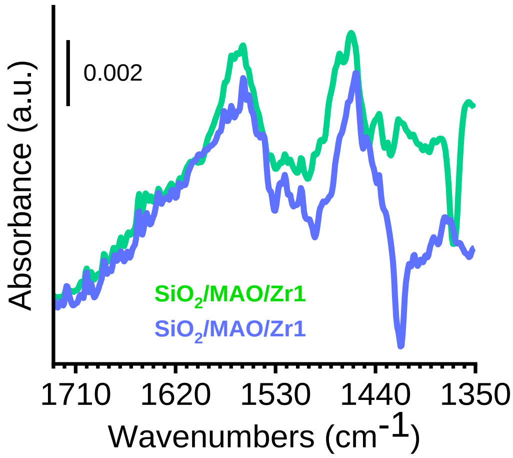

Figure 3. 21. Comparison between IR spectra of CO adsorbed at 300 K on SiO_2/MAO/Zr1 and SiO_2/MAO/Zr2 after 30 minutes of contact. Spectra are shown after normalization to the optical thickness of the pellet in v(C=O) region characteristic of Zr-acyl species.

In order to verify if formed Zr-acyl compounds involve the active sites, IR spectra of CO adsorbed at 300 K on SiO_2/MAO/Zr1 were collected before and after d-ethylene polymerization. The results are shown in Figure 3. 22. In order to avoid formation of PE layer on the catalyst surface, ethylene polymerization was performed at room temperature and low d-ethylene pressure (60 mbar) and d-ethylene was removed after a few minutes of reaction. Additionally, deuterated ethylene was used to discriminate the IR signatures of PE, which otherwise would be completely masked by the intense vibrational modes of MAO. The amount of Zr-acyl species formed upon CO adsorption on the SiO_2/MAO/Zr1 catalyst after the contact with ethylene (Figure 3. 22b) is significantly lower than those formed on the same catalyst prior ethylene dosage (Figure 3. 22a), suggesting that *the Zr sites*

<u>responsible for the formation of the Zr-acyl species in the presence of CO are also involved in ethylene polymerization</u>.

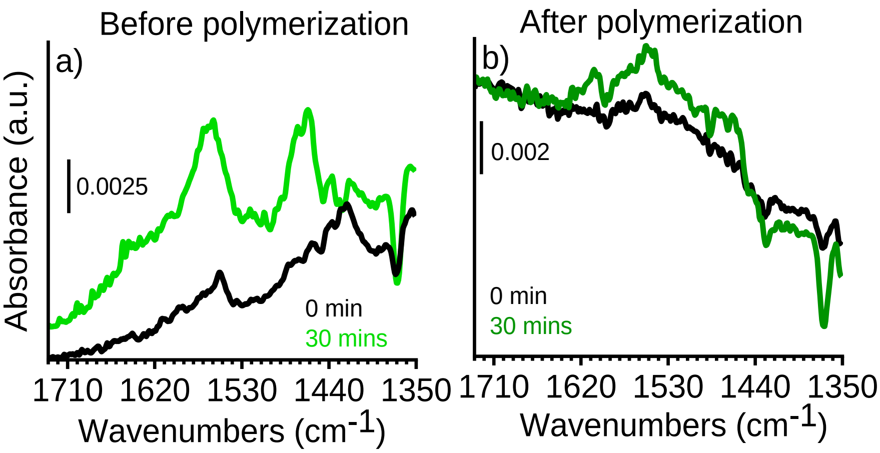

Figure 3. 22. IR spectra of CO adsorbed at 300 K on SiO_2/MAO/Zr1 before (part a) and after (part b) ethylene polymerization in mild condition (P_{C2H4}=60 mbar, room temperature, 5 min). Spectra are shown after normalization to the pellet thickness.

2.5 d-acetonitrile as coordination and insertion probe

Since CO was demonstrated to be a weak probe molecule for these catalytic systems, the attention was turned to d-acetonitrile, which has higher basicity than CO.[117,119,140–143] Moreover, d-acetonitrile can both coordinate to LAS and insert into M-C bond to yield a product called aza-alkenyldene.[119] As a first step, we investigated the interaction of the homogeneous catalysts with d-acetonitrile; then, we turned our attention to the silica-supported catalysts.

2.5.1 Homogeneous catalysts

Figure 3. 23 compares the UV-Vis spectra of Zr1 (part a) and Zr2 (part b) catalysts activated with MAO (Al:Zr=150) in toluene solution before and after d-acetonitrile addition (a few drops were added, d-acetonitrile is likely in excess with respect to Zr cations). In both cases, addition of d-acetonitrile causes a shift of the LMCT bands to higher energies. This indicates that *<u>the electron density on the Zr atom increases upon coordination of the electron-rich d-acetonitrile</u>*. Hence, more energy is required to transfer an electron from the aromatic ligand to the Zr cation. This is similar to what reported by Coevoet et al. when dibutyl ether is added to a zirconocene/MAO system (Al:Zr = 200): complexation of the zirconocenium species

by the ether molecule results in a similar shift of the LMCT band to higher energy (from 450 to 434 nm).

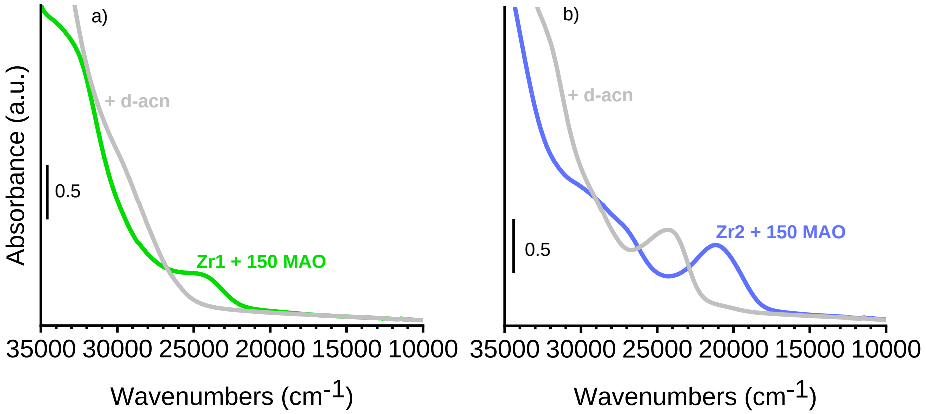

Figure 3. 23. UV-Vis spectra of MAO-activated (Al:Zr=150 eq) Zr1 (part a) and Zr2 (part b) catalysts in toluene solution, before and after interaction with a few drops of d-acetonitrile.

2.5.2 Silica-supported catalysts

Figure 3. 24 shows DR UV-Vis spectra of SiO_2/MAO/Zr1 and SiO_2/MAO/Zr2 catalysts before and after addition of d-acetonitrile. The changes in the DR UV-Vis spectra are very similar to what observed for the homogeneous counterparts.

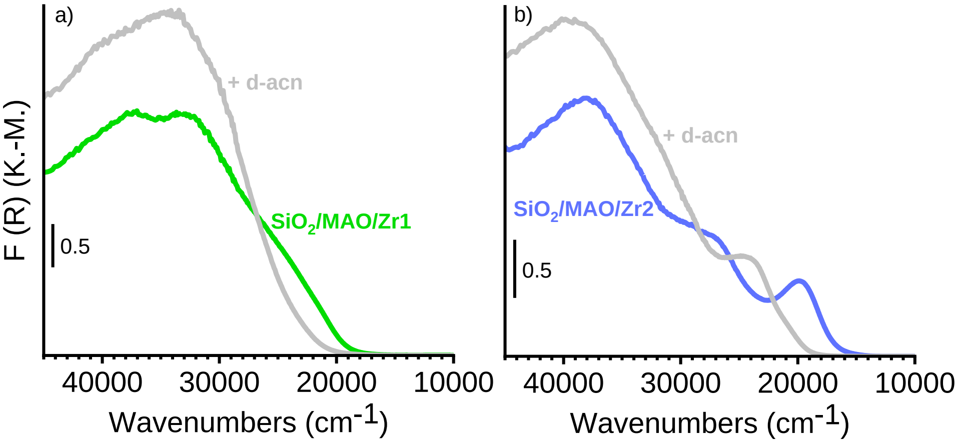

Figure 3. 24. DR UV-Vis spectra of d-acetonitrile adsorbed on a) SiO_2/MAO/Zr1 and b) SiO_2/MAO/Zr2

UV-Vis experiments clearly demonstrate that the Zr cations are accessible by d-acetonitrile at room temperature. In a second step, the coordination of d-acetonitrile to the Zr cations and its insertion rate into the Zr-C bond was followed by means of time-resolved IR spectroscopy. An additional blank experiment was performed for SiO_2/MAO, to ensure that no insertion is observed in that case. Figure 3. 25 shows the sequence of IR spectra collected for the three samples, SiO_2/MAO, SiO_2/MAO/Zr1 and SiO_2/MAO/Zr2, upon contact with d-acetonitrile over 3h, in the 2400 – 1300 cm^{-1} spectral region. The inset emphasizes the bands due to Zr-aza-alkenylidene species. As already discussed, IR spectra of three samples are very similar to each other and are dominated by vibrational modes of silica. However, in all cases new bands are observed immediately after d-acetonitrile was introduced. Starting the discussion with coordinated d-acetonitrile, three main absorption bands are observed in the 2400 – 2000 cm^{-1}, at different positions related to that of liquid-like d-acetonitrile (2265 cm^{-1}).[2]

The first one, at 2108 cm^{-1} (indicated as *T*, *total* in Figure 3. 25), is due to $\nu(CD_3)$ of all acetonitrile species present on the sample, it is not sensitive to the adsorption sites and thus not analytically relevant.[119] Therefore, this band will be used to quantify the total amount of d-acetonitrile on the sample, comprising d-acetonitrile coordinated to the LAS sites (belonging to both MAO/TMA and the metallocene cation) and physisorbed d-acetonitrile. It is worth noticing that the concentration of d-acetonitrile on the sample depends on both the equilibrium pressure and the sample mass, the latter being very difficult to evaluate during the experiment because of complexity of the experimental procedure.

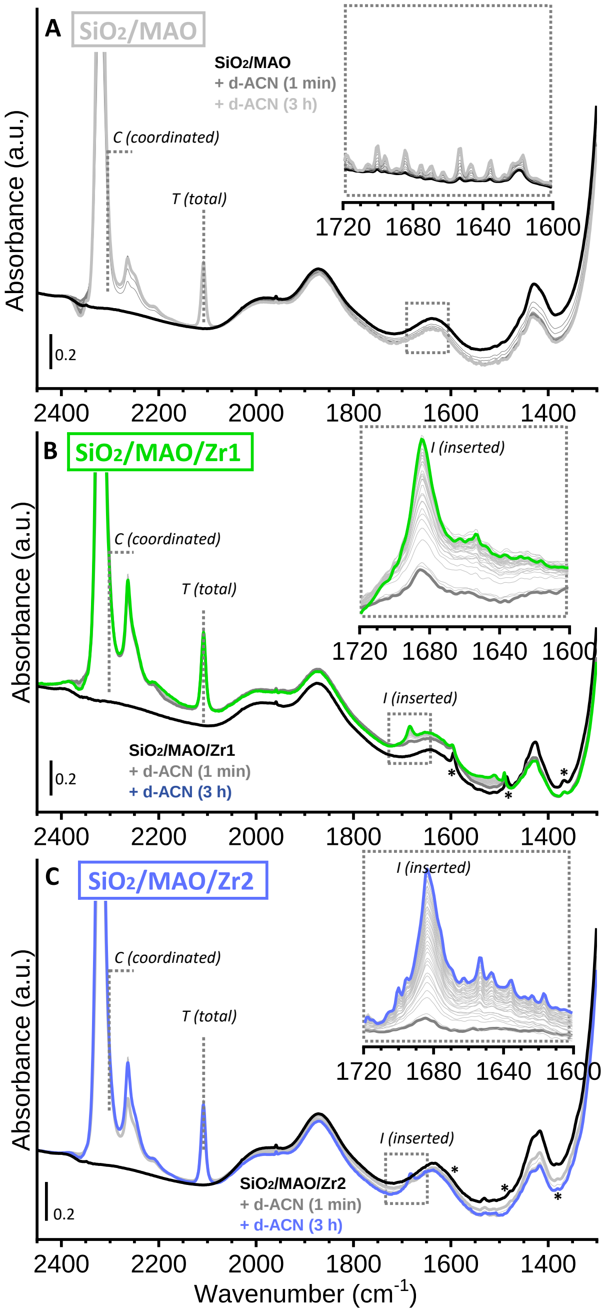

Figure 3. 25. Time-resolved IR spectra of d-acetonitrile adsorbed on a) SiO_2/MAO, b) SiO_2/MAO/Zr1 and c) SiO_2/MAO/Zr2. Spectra are shown as function of reaction time from 1 min (gray spectra) to 3h (spectra in corresponding color). In insets magnification of 1720-1600 cm^{-1} spectral region is shown after subtraction of spectra collected before d-acetonitrile dosage.

The second band, centered at 2320 cm^{-1}, actually dominates the ν(C≡N) region (2400-2200 cm^{-1}) in all cases. This band is upward shifted by 55 cm^{-1} with respect to that of liquid-like d-acetonitrile at 2265 cm^{-1}, which is due to the interaction of d-acetonitrile with LAS sites. The band accounts for both the LAS sites belonging to the MAO/TMA species (e.g. d-acetonitrile adsorbed on coordinatively unsaturated Al(III) sites on a triethylaluminum (TEA)-pretreated SiO_2 shows a band at 2317 cm^{-1})[116] and for the Zr cations. However, it is expected that the MAO/TMA species are mostly probed by d-acetonitrile since they are present in higher relative content (Al:M = 150). Because the associated band rapidly goes out of scale, the total amount of accessible LAS sites was derived from the spectral intensity at 2300 cm^{-1} for each experiment (indicated as *C*, *coordinated* in Figure 3. 25).

Finally, the third absorption band observed in this spectral region appears at 2265 cm^{-1} with a shoulder at around 2250 cm^{-1}. The former is ascribed to liquid-like d-acetonitrile and is the only absorption band that decreases in intensity upon degassing (not shown).[144] The assignment of the shoulder is quite complicated because the low frequency of the ν(C≡N) band suggests a bridging coordination mode, as was observed for other ligands and as suggested for nitriles interacting with two cations in zeolites.[145] The appearance of this absorption band indicates the presence of LAS sites that are close enough to each other to be simultaneously complexed by both the nitrogen lone pair and the π-type bonding electrons of the same acetonitrile molecule. A similar absorption band was also observed for d-acetonitrile adsorbed on a Cr(II)/SiO_2 Phillips catalyst activated with TEA and attributed to a Cr(II)···Al(III) bimetallic species.[116]

Moving the discussion to the insertion of d-acetonitrile into the Zr-CH_3 bond, additional weak bands appear and grow in intensity over time in the 1700-1300 cm^{-1} spectral region when d-acetonitrile is dosed on the two catalysts (Figure 3. 25b and c), but not for SiO_2/MAO (Figure 3. 25a). In particular, a well-defined absorption band appears at 1684 cm^{-1} (labeled as band *I*, *inserted* in Figure 3. 25). This band is assigned to the ν(C=N) of an aza-alkenylidene species that is formed when d-acetonitrile inserts into the Zr-CH_3 bond. At the same time, for SiO_2/MAO/Zr1 all the absorption bands ascribed to the activated metallocene complexes (labeled with asterisks in Figure 3. 25b) are perturbed. For instance, the absorption bands at 1593 and 1485 cm^{-1} are upward shifted by a few inverse centimeters, while the absorption band at 1370 cm^{-1} is decreased in intensity. Altogether, this suggests that, for SiO_2/MAO/Zr1, *the coordination modes of the indenyl ligand are changing concomitantly to the coordination of d-acetonitrile to the Zr cation and its subsequent insertion into the metal-alkyl bond*.

It is obvious that the absorption band ascribed to Zr-aza-alkenylidene species grow at a different rate for the two catalysts. Namely, the band assigned to Zr-aza-alkenylidene species grows faster for SiO_2/MAO/Zr1 than for SiO_2/MAO/Zr2. To further assess the differences between coordination ability and insertion rates in the two catalysts, the behavior of all the three bands (total-*T*, coordinated-*C,* and inserted-*I*) was monitored as a function of time, for two different d-acetonitrile concentrations (A and B). Noticeably, just one insertion of d-acetonitrile can occur per each site, meaning that no diffusion limitations due to product deposition on the particle surface (which is the case when monomer is used) can influence the obtained results. Thus, information about molecular level differences of two Zr-based catalysts bearing different ligands will be reached.

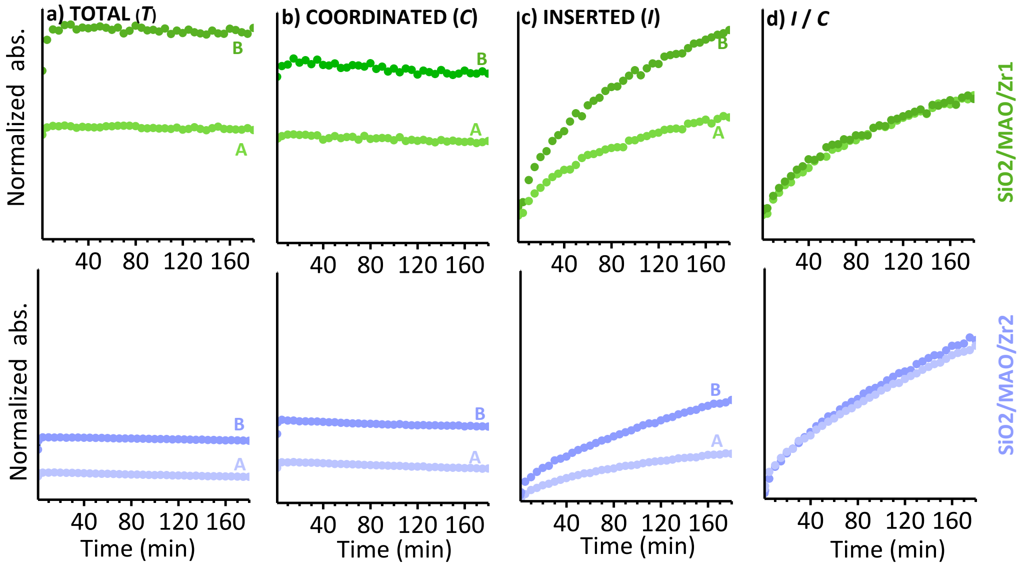

Figure 3. 26. Evolution of the intensities of the IR absorption bands *T* (total amount of d-acetonitrile), *C* (coordinated d-acetonitrile), and *I* (inserted d-acetonitrile) over time, as derived from a series of experiments in which SiO_2/MAO/Zr1 (top) and SiO_2/MAO/Zr2 (bottom) were treated with d-acetonitrile at two different concentrations (A and B). The data were normalized to the optical thickness of the pellets. Part d) shows the ratio between intensities of bands *I* and *C* over time.

The results of the above-mentioned strategy are shown in Figure 3. 26, which shows the evolution of the intensities for bands *T*, *C* and *I* (parts a, b and c, respectively) over time for SiO_2/MAO/Zr1 (top) and SiO_2/MAO/Zr2 (bottom) catalysts, after normalization of the IR spectra to the optical thickness of the pellet. The following observations can be done:

- In both cases, bands *T* and *C* reach their maximum intensity almost immediately, indicating that *there are no limitations for d-acetonitrile to diffuse inside the silica pores*.
- Band *C* slightly decreases in intensity for both catalysts (Figure 3. 26b) over time because coordinated d-acetonitrile further inserts into the Zr-CH_3 bond. Moreover, intensity of *C* band depends on the total amount of d-acetonitrile on the sample: *more d-acetonitrile on the sample more d-acetonitrile coordinated to LAS*.
- The intensity of band *C* (Figure 3. 26b) is systematically lower for SiO_2/MAO/Zr2 (bottom) than for SiO_2/MAO/Zr1 (top), irrespective of the total amount of d-acetonitrile, meaning that *there are less sites able to coordinate d-acetonitrile in SiO_2/MAO/Zr2 than in SiO_2/MAO/Zr1. This is in agreement with the presence of hetro-binuclearion-pairs in SiO_2/MAO/Zr2*, as predicated on the basis of the geometrical parameters and validated by (DR) UV-Vis spectroscopy.
- Finally, band *I*, which is proportional to the amount of inserted d-acetonitrile molecules, slowly grows over time for both catalysts (Figure 3. 26c). Roughly speaking, the insertion rate depends on the amount of coordinated d-acetonitrile and on the inherent insertion ability of each site. When normalized to the intensity of band *C* (i.e. to the amount of coordinated d-acetonitrile) however, all the curves overlap within the experimental error (Figure 3. 26d). This suggests that, *as far as acetonitrile is concerned, the inherent insertion ability is the same for both SiO_2/MAO/Zr1 and SiO_2/MAO/Zr2, and that the higher insertion rate observed for SiO_2/MAO/Zr1 is entirely ascribable to the larger fraction of accessible zirconocene cations*.

2.6 Homo-polymerization of 1-hexene monitored by spectroscopies

2.6.1 Homogeneous catalysts

In the next step, we explored the potential of UV-Vis spectroscopy in monitoring olefin polymerization on the two homogeneous catalysts. 1-hexene was selected as monomer because it is liquid at room temperature, and this allows us easier manipulation in the glovebox. Figure 3. 27 shows the evolution of the UV-Vis spectra of the two catalysts activated by MAO (Al:Zr=150 eq) after addition of 1-

hexene. The LMCT bands for both catalysts decrease in intensity, and at same time new bands at lower energies spring out. Following the literature, the new band is assigned to Zr-allyl species formed by σ-bond metathesis between cationic species and 1-hexene.[99,100] The presence of Zr-allyl species was confirmed also by NMR spectroscopy of rac-[$Me_2Si(1\text{-indenyl})_2ZrMe_2$] in toluene solution activated with borate-based activator. Moreover, it was demonstrated that Zr-allyl species dominate the reaction pool at the beginning of the polymerization reaction, contributing for 90% of all Zr species.[99] Active Zr species can be derived from Zr-allyl species by several mechanisms, such as olefin insertion into Zr-allyl bond or exchange of allyl group by methyl one.[99]

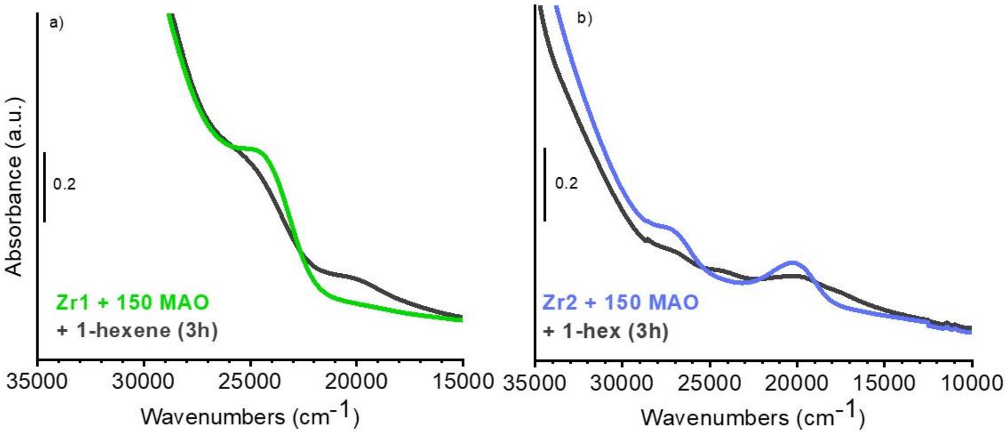

Figure 3. 27. UV-Vis spectra of a) Zr1 (approx. C=5*10^{-4} M) and b) Zr2 (approx. C=5*10^{-3} M) catalysts in toluene solution after activation by MAO (Al:Zr=150), before and after 1-hexene polymerization.

2.6.2 Silica-supported catalysts

Figure 3. 28 shows a similar experiment performed on the silica-supported zirconocene catalysts. 1-hexene was sent from the vapor phase on the catalysts in the powder form and UV-Vis spectra were collected in DR mode. Very minor spectral changes are observed even after 3 hours of reaction. Only a slight decrease in intensity of the LMCT band can be observed, more pronounced for SiO_2/MAO/Zr2 catalyst (Figure 3. 28b). The reason why DR UV-Vis spectroscopy seems insensitive to the interaction of the silica-supported catalysts with 1-hexene (while it is able to reveal their interaction with d-acetonitrile) might be searched in the experimental set-up. Indeed, 1-hexene is dosed from the vapor phase inside a cell with a vertical geometry, where the sample in the powder form is placed at the bottom, inside a bulb in optical quartz with a narrow entrance. The portion of the powder at the entrance of the bulb is the first one to come in contact with the monomer. If the

polymerization reaction is fast, a layer of polymer might form at the entrance of the bulb, preventing the diffusion of the monomer. As a consequence, the catalyst powder inside the bulb, which is that effectively measured by UV-Vis spectroscopy, is not accessed by 1-hexene.

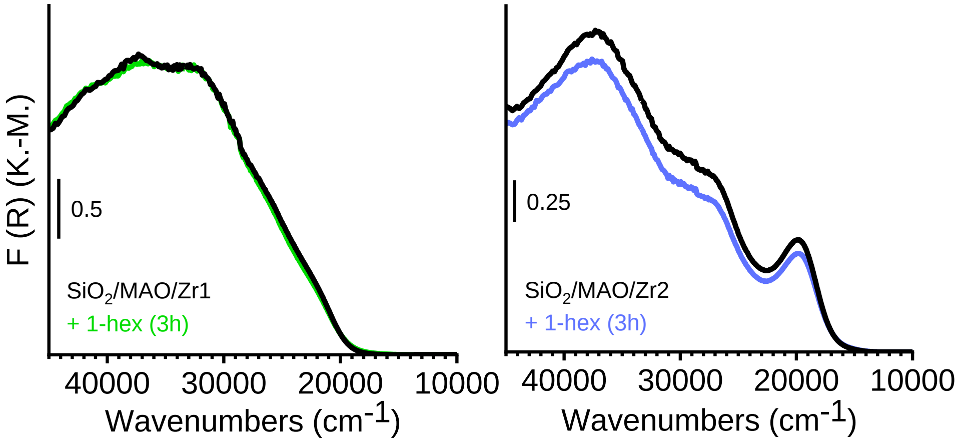

Figure 3. 28. DR UV-Vis spectra of SiO_2/MAO/Zr1 (part a) and SiO_2/MAO/Zr2 (part b) before and after interaction with 1-hexene (for 3 hours).

The same experiment was monitored by in situ IR spectroscopy as well. Figure 3. 29 shows the IR spectra collected during 1-hexene polymerization on SiO_2/MAO/Zr1 and SiO_2/MAO/Zr2 catalysts at room temperature as a function of time in the most informative spectral region. These experiments were conducted in order to extract information about coordination and insertion ability of each catalyst towards the monomer, as well as to validate our method of d-acetonitrile adsorption as a way to predict activity of the two SiO_2/MAO/Zr-based catalysts having different ligands. As can be seen from Figure 3. 29, several bands appear immediately in the 1680-1300 cm^{-1} region after 1-hexene addition, evolving with time in a different way.

- The band at 1640 cm^{-1} (indicated as *M* in Figure 3. 29), which appears immediately after 1-hexene dosage, is assigned to the ν(C=C) vibration of 1-hexene coordinated to Zr cationic species.[146]
- A series of absorption bands start to grow immediately after 1-hexene dosage in the 1470 – 1400 cm^{-1} region. These bands are due to the bending modes of CH_2 groups and denote the formation of poly(1-hexene) with different crystallinity as indicated by position of the bands related to bending modes of CH_2 group. Namely, the band at around 1470 cm^{-1} is

related to cristallyne phase, while the one at approx. 1460 cm^{-1} is related to amorphous one [ref Pracella].

- Finally, the band at 1378 cm^{-1} (indicated as *P* in Figure 3. 29) is attributed to the bending mode of the CH_3 group in poly(1-hexene).[146] This band, which is weaker than those associated to $\delta(CH_2)$ modes and hence remains in scale during the whole experiment, will be used to estimate the amount of polymer and hence to compare the polymerization ability of the two catalysts.

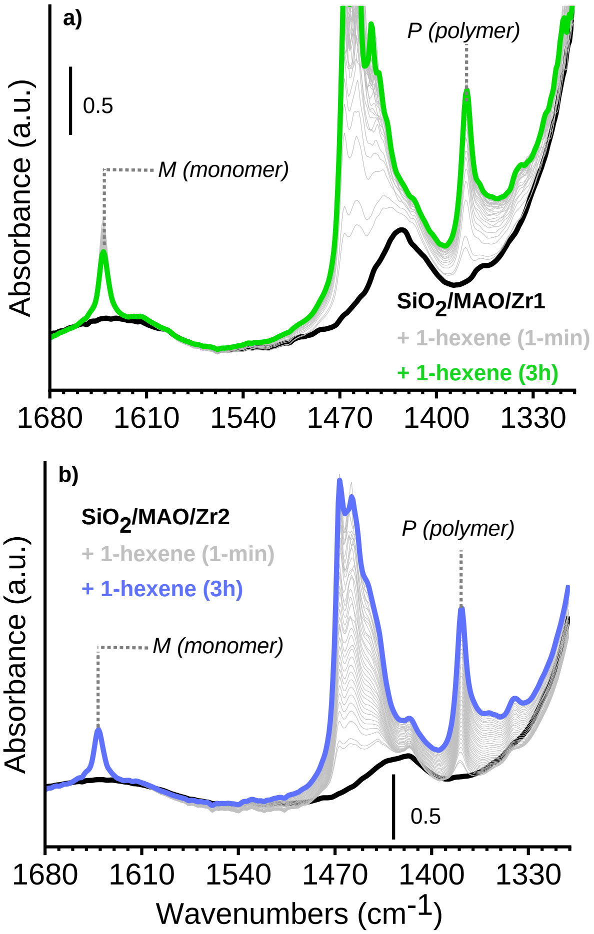

Figure 3. 29. Time-resolved IR spectra collected during polymerization of 1-hexene on SiO_2/MAO/Zr1 (part a) and SiO_2/MAO/Zr2 (part b) catalysts at 300 K. Spectra are shown as a function of time, starting from spectra collected before 1-hexene addition (black) to spectra collected after 3h (green or blue). The two bands used for quantifying the amount of coordinated monomer (*M*) and growing polymer (*P*) are also indicated.

The intensity of bands *M* and *P* over the first 30 minutes of reaction on both SiO_2/MAO/Zr1 and SiO_2/MAO/Zr2 is plotted in Figure 3. 30. Band *M* (Figure 3. 30a) has lower intensity for SiO_2/MAO/Zr2 relative to SiO_2/MAO/Zr1 suggesting that less 1-hexene coordinates to the Zr cations, as already observed for d-acetonitrile. This is likely due to the hetero-binuclearion-pairs present in SiO_2/MAO/Zr2. It can be also noted that band *M* decreases in intensity over time for SiO_2/MAO/Zr1, while it is not the case with SiO_2/MAO/Zr2 suggesting slower insertion of 1-hexene into Zr-CH_3 bond in SiO_2/MAO/Zr2. Consequently, this led to lower intensity of *P* band in SiO_2/MAO/Zr2 (Figure 3. 30b), which demonstrate a slower polymerization rates. Interestingly, when normalized to the intensity of band *M* (i.e. to the amount of coordinated monomer) the two curves do not overlap as previously observed by using d-acetonitrile as probe (Figure 3. 26d). The initial inherent insertion ability of SiO_2/MAO/Zr2 is greater than for SiO_2/MAO/Zr1. However, after the very initial stage of the reaction, the 1-hexene insertion rate for SiO_2/MAO/Zr2 drops.

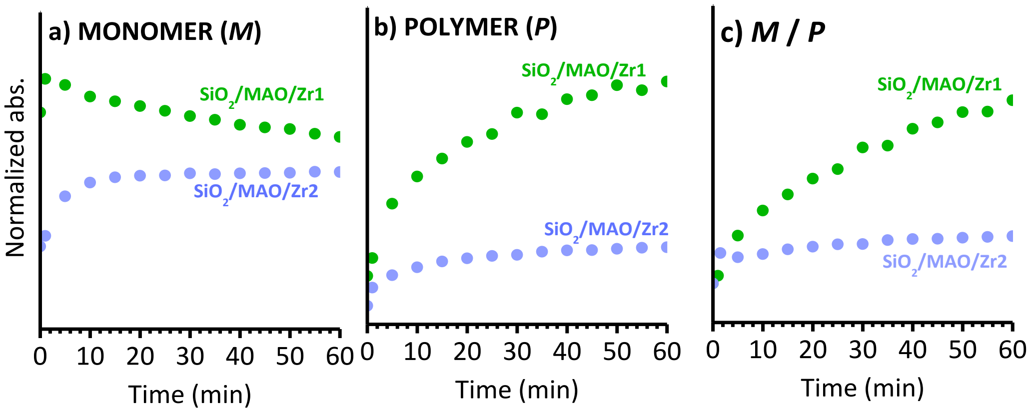

Figure 3. 30. Evolution of the intensities of the IR absorption bands *M* (monomer, part a) and *P* (polymer, part b), and over time, as for SiO_2/MAO/Zr1 and SiO_2/MAO/Zr2. The data were normalized to the optical thickness of the pellets. Part c) shows the ratio between intensities of bands *P* and *M* over time.

The behavior of SiO_2/MAO/Zr2 is in very well agreement with the “filter effect” discussed above. The lower 1-hexene insertion rate per site shown by SiO_2/MAO/Zr2 is only apparent. Indeed, *at the very early stages of the reaction SiO_2/MAO/Zr2 inserts 1-hexene much faster than SiO_2/MAO/Zr1. This likely leads to a layer of polymer at the exterior of the catalyst particles, which prevents the further diffusion of 1-hexene inside the particles*. These results confirm the “filter theory” proposed by Fink[126] on the basis of the non-uniform composition of the ethylene/1-hexene copolymer produced by SiO_2/MAO/Zr2.

2.7 Conclusions

The whole set of spectroscopic data discussed in this section indicate that hetero-binuclear ion-pairs are formed with MAO in the case Zr2 catalyst than for Zr1. We speculated that OSIP of the type $[L_nZr(\mu\text{-Me})_2AlMe_2]^{\oplus}[Me\text{-}MAO]^{\ominus}$ are prevalently formed between Zr2 and MAO, while ISIP of the type $[L_nZrMe^{\oplus}\cdots Me\text{-}MAO^{\ominus}]$ are mainly formed between Zr1 and MAO. The different propensity of Zr1 and Zr2 to form OSIP and ISIP is strictly related to their structure: in fact, Zr2 is expected to be sterically more accessible than Zr1. The same trend is observed on the silica-supported catalysts.

In agreement with the presence of hetero-binuclearion-pairs, SiO_2/MAO/Zr2 contains less $Zr^{\oplus}$ sites able to coordinate incoming monomers than SiO_2/MAO/Zr1. Both CO and acetonitrile are able to insert into the Zr-Me bond, forming very similar species in the two catalysts. As far as acetonitrile is concerned, the inherent insertion ability estimated by means of IR spectroscopy is the same for both SiO_2/MAO/Zr1 and SiO_2/MAO/Zr2, even though the former contains a larger fraction of accessible zirconocene cations. In contrast, at the very early stages of the reaction, SiO_2/MAO/Zr2 inserts 1-hexene much faster than SiO_2/MAO/Zr1. This likely leads to a layer of polymer at the exterior of the catalyst particles, which prevents the further diffusion of 1-hexene inside the particles, giving rise to the so called “filter effect” already reported in the literature.

These results indicate the d-acetonitrile is an excellent probe to determine the relative fraction of accessible cationic sites in zirconocene-based catalysts. It is also a good probe to predict the ethylene insertion rate, while it cannot be used to predict the 1-hexene insertion ability. This is probably due to the smaller size of d-acetonitrile compared to 1-hexene, for which steric factors become relevant.

3. Spectroscopic characterization of two structurally analogous SiO_2/MAO/Zr1 and SiO_2/MAO/Hf catalysts

3.1 Motivation

The objects of this chapter are two structurally analogous bis-indenyl Zr- and Hf-based catalysts (Figure 3. 31), synthesized according to the procedure described in Section 2.1.2. These catalysts represent two extremes in term of their activity, so they are perfect candidates for testing the potentials of our spectroscopic methods in correlating the properties of the catalysts at a molecular level to their catalytic performance.

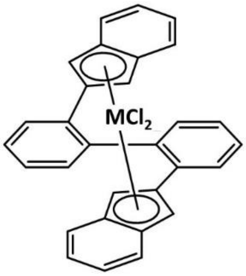

Figure 3. 31. Structure of the two metallocene precursors used for synthetizing SiO_2/MAO/Zr1 and SiO_2/MAO/Hf (M= Zr, Hf).

Despite their structural analogy, same synthesis and activation procedure (same M:Al ratio), the two catalysts showed significantly different productivities. Namely, when tested in gas-phase ethylene polymerization (15 bar ethylene, 87°C, average of two runs, experiments performed at SABIC) SiO_2/MAO/Hf catalyst gave more than 40 times lower PE yield than its structural analogue SiO_2/MAO/Zr1 catalyst. As discussed at the beginning of this chapter, the different catalytic performances of the two catalysts were expected due to the combination of a few factors:

- The stronger Hf-C bond, which causes lower chain propagation,[49–51]
- The more ionic character of the Hf-C bond, while the Zr-C bond has a covalent nature,[41]
- The tendency of Hf-based catalysts to form stable hetero-binuclear species with MAO.[92,147]

A lot of experimental evidences have been accumulated over the years, which demonstrate that metallocene catalysts based on these two metals are characterized by different productivities and polymer properties. However, information about their differences at molecular level are still lacking. To approach this problem, the two catalysts were characterized by means of DR UV-Vis and IR spectroscopies, both in the absence and in the presence of probe molecules.

3.2 Electronic and vibrational properties of the two catalysts

Figure 3. 32 shows the DR UV-Vis spectra of the two catalysts. The spectrum of SiO_2/MAO/Zr1 has been commented in the previous chapter. The most relevant absorption band is that at lower energy (around 23500 cm^{-1}), which was attributed to the HOMO→LUMO transition involving ISIP of the type $[L_nZrMe^{\oplus}\cdots Me\text{-}MAO^{\ominus}]$. As already discussed, the broadness of the band suggests a certain variability in the type of ion-pairs (likely weakly and strongly bounded to the MAO counter anion).[67] For SiO_2/MAO/Hf the main HOMO→LUMO transition occurs at about 25000 cm^{-1}. This band is attributed to ISIP of the type $[L_nHfMe^{\oplus}\cdots Me\text{-}MAO^{\ominus}]$. In addition, a weaker band is observed at about 18000 cm^{-1}, which is assigned to OSIP of the type $[L_nHf(\mu\text{-}Me)_2AlMe_2]^{\oplus}[Me\text{-}MAO]^{\ominus}$. *The presence of these OSIP species is expected on the basis of the documented tendency of hafnocene catalysts to form hetero-binuclear adducts with TMA.*[92]

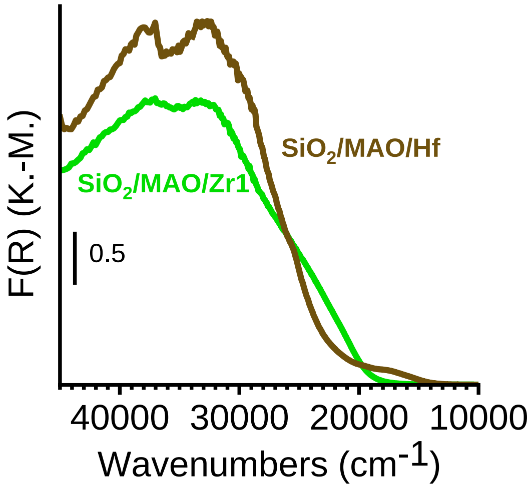

Figure 3. 32. DR UV-Vis spectra of SiO_2/MAO/Zr1 (green) and SiO_2/MAO/Hf (brown).

Figure 3. 33 compares the IR spectra of SiO_2/MAO/Zr1 and SiO_2/MAO/Hf catalysts. The two spectra are dominated by the same features already discussed in the previous section. However, minor differences can be seen in the 1650-1330 cm^{-1} region. The inset shows the same two spectra after subtraction of that of

SiO_2/MAO to emphasize the ligand contributions. It is evident that the bands due to vibrations of indenyl ligands in SiO_2/MAO/Hf are slightly shifted to higher energies with respect to those present in the spectrum of SiO_2/MAO/Zr1.

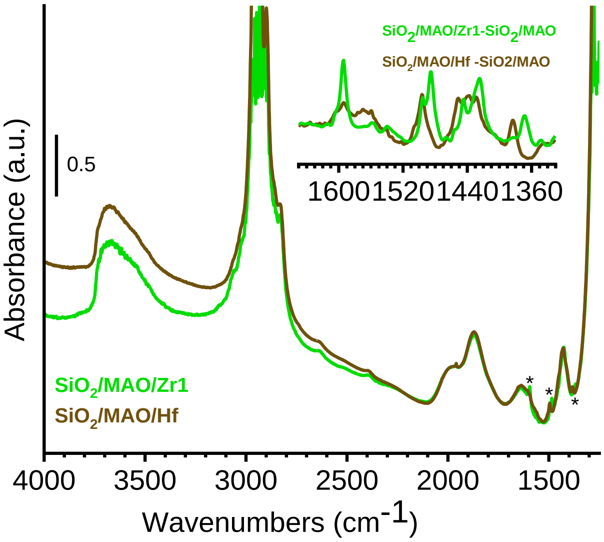

Figure 3. 33. IR spectra of SiO_2/MAO/Zr1 (green) and SiO_2/MAO/Hf (brown). The spectra are normalized to the optical thickness of pellet. The inset shows a magnification of the 1650-1330 cm^{-1} spectral region, after subtraction of the spectrum of SiO_2/MAO.

3.3 Carbon monoxide as coordination and insertion probe

3.3.1 IR spectroscopy of CO adsorbed at 100 K: accessibility of the cationic sites

The IR spectra of CO adsorbed at 100 K on SiO_2/MAO/Hf (Figure 3. 34b) are very similar to those collected for SiO_2/MAO/Zr1 (Figure 3. 34a) and already discussed in the previous section. The most intense bands at 2139 cm^{-1} and 2132 cm^{-1} are assigned to CO physisorbed in the porosities generated by MAO. The bands at 2212 cm^{-1} and 2194 cm^{-1}, less intense but more resistant to degassing, are assigned to CO in interaction with M-LAS and W-LAS, respectively. An additional band is observed at 2154 cm^{-1}, which is assigned to non-classical σ-carbonyl complexes of cationic hafnocene species. As already observed for CO adsorbed on SiO_2/MAO/Zr1, this band is easily removable upon decreasing the CO coverage, indicating that CO is competing with other ligands for coordination.

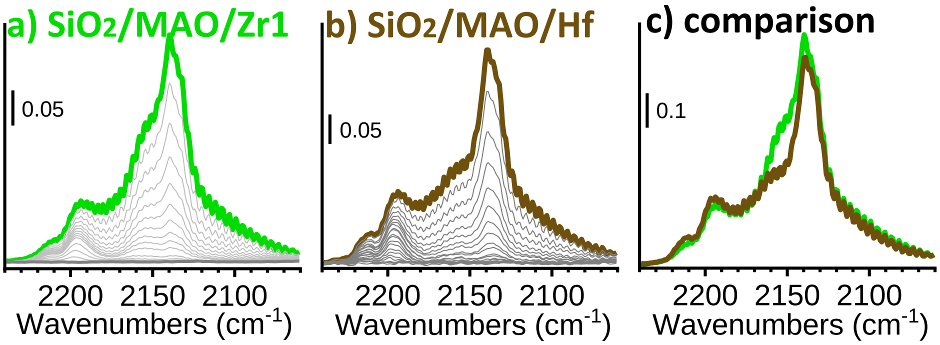

Figure 3. 34. IR spectra of CO adsorbed at 100 K on SiO_2/MAO/Zr1 (part a) and SiO_2/MAO/Hf (part b) as a function of CO coverage. Part c) Comparison between IR spectra of CO adsorbed on SiO_2/MAO/Zr1 and SiO_2/MAO/Hf at 100 K and maximum CO coverage. All the spectra are shown after subtraction of that collected prior CO dosage.

When the IR spectra of CO adsorbed at 100 K on SiO_2/MAO/Zr1 and SiO_2/MAO/Hf at the maximum CO coverage are normalized to the thickness of the pellet and compared each other (Figure 3. 34c), one important difference can be seen: the band at 2154 cm^{-1} is less intense for SiO_2/MAO/Hf. This indicates that *the fraction of cationic Hf⊕ species accessible to CO is smaller than the amount of cationic Zr⊕ species*. The reason behind this behavior is that a weak base, such as CO, has difficulties to interpose between strong OSIP present in SiO_2/MAO/Hf. These results agree very well the DR UV-Vis data discussed above as well as with literature.[92,147]

3.3.2 IR spectroscopy of CO adsorbed at room temperature: formation of M-acyl species upon CO insertion into the M-C bond

Figure 3. 35 shows the IR spectra of CO adsorbed at room temperature on the SiO_2/MAO/Zr1 and SiO_2/MAO/Hf catalysts, which are useful to evaluate the CO insertion ability into the M-C bond. The spectra of SiO_2/MAO/Zr1 (Figure 3. 35a) have been already commented in the previous section: the two bands at 1560 and 1460 cm^{-1} which grow in intensity as a function of time are both attributed to Zr-acyl complexes formed upon CO insertion into diverse Zr-C bonds.[114,118] When the same experiment is repeated for SiO_2/MAO/Hf (Figure 3. 35b), a single band centered at 1676 cm^{-1} grows in intensity over time. The band is assigned to Hf-acyl species, formed after CO inserted into Hf-C bond.

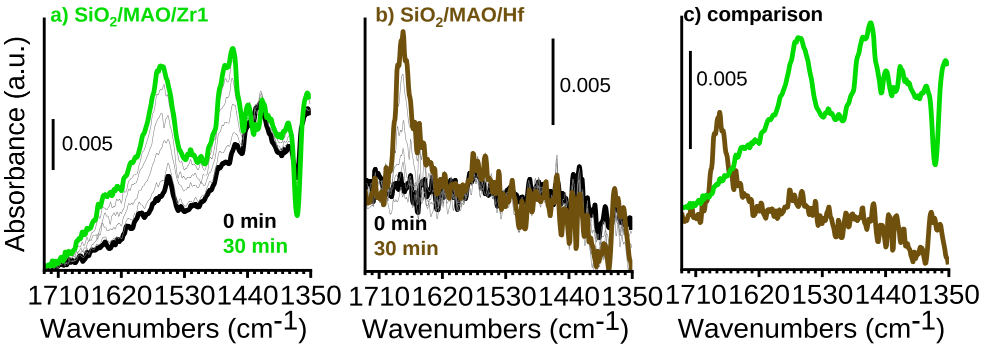

Figure 3. 35. IR spectra of CO adsorbed at 300 K on a) SiO_2/MAO/Zr1 and b) SiO_2/MAO/Hf. Spectra are shown in ν(C=O) region as a function of time after subtraction of that collected prior CO dosage. Part c) compares the spectra collected on the two catalysts after 30 minutes of contact with CO and after normalization to the thickness of the pellet.

Figure 3. 35c shows the IR spectra collected on the two catalysts after 30 minutes of contact with CO and after normalization to the thickness of the pellet. The following observations can be done:

- The integrated area of the bands associated to M-acyl species is larger for SiO_2/MAO/Zr1 than for SiO_2/MAO/Hf. This indicates that more acyl species are formed in the case of SiO_2/MAO/Zr1 than in SiO_2/MAO/Zr1.
- Two bands are observed in the spectrum of SiO_2/MAO/Zr1 while only one band appears in that of SiO_2/MAO/Hf. The band at lower frequency observed for SiO_2/MAO/Zr1 is likely due to a Zr-acyl species η^2-coordinated to the cation, which requires the presence of an additional coordination vacancy.

Both observations are perfectly compatible with the previously discussed spectroscopic data, which demonstrate that in SiO_2/MAO/Hf there are hetero-binuclear OSIP, absent in SiO_2/MAO/Zr1. As a consequence, *a smaller amount of accessible cations is present in SiO_2/MAO/Hf, and the formed Hf-acyl species have not the possibility to assume a η^2-coordination to the cation*.

3.4 d-acetonitrile as coordination and insertion probe

Figure 3. 37 shows the DR UV-Vis-NIR spectra of the two catalysts before and after interaction with d-acetonitrile. In both cases, a color change was observed almost immediately, indicating that d-acetonitrile effectively coordinates at least to a fraction of the metal sites, and that this is a very fast process. As a consequence,

the spectrum of SiO_2/MAO/Zr1 drastically changes. In particular, the HOMO→LUMO LMCT band shifts to higher energies, indicating that acetonitrile can enter Zr coordination sphere, at the same time increasing the electron density on the Zr cation, hence more energy is required to transfer an electron from ligand to Zr. Oppositely, changes in the spectrum of SiO_2/MAO/Hf catalyst after addition of d-acetonitrile are not so drastic: the band at 18000 cm^{-1}, ascribed to hetero-binuclear OSIP, is almost unchanged (i.e. acetonitrile have difficulties to impose between hetero-binuclear OSIP), while that at 25500 cm^{-1}, attributed to ISIP, slightly shifts to higher energies, indicating increase of electron density on Hf atom.

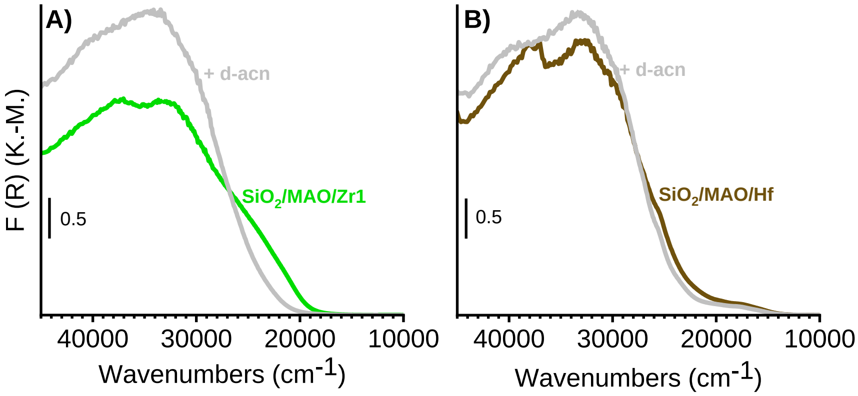

Figure 3. 36 DR UV-Vis spectra of d-acetonitrile adsorbed on SiO_2/MAO/Zr1 (Part A) and SiO_2/MAO/Hf (Part B).

The same experiment was monitored by means of time-resolved IR spectroscopy. Figure 3. 38 shows the sequence of spectra collected within the first 3 minutes after dosing d-acetonitrile on the two catalysts in the whole 2400 to 1300 cm^{-1} region and magnified in the 1720-1600 cm^{-1} region, which contains the spectroscopic signature of the Zr- and Hf- aza-alkenylidene species formed upon insertion of d-acetonitrile into M-C bond. As discussed in the previous section, the evolution over time of three main bands was followed, in two experiments with two different d-acetonitrile concentration:

1) the band at 2108 cm^{-1} (*T*, total) was used to quantify the total amount of d-acetonitrile on the sample, comprising d-acetonitrile coordinated to the LAS sites and physisorbed d-acetonitrile.
2) the band at 2300 cm^{-1} (*C*, coordinated) was used to estimate the d-acetonitrile coordinated to LAS sites, accounting for both the LAS sites of the MAO/TMA species and the Zr or Hf cations.

3) The two well-defined absorption bands at 1684 cm^{-1} for SiO_2/MAO/Zr and 1690 cm^{-1} for SiO_2/MAO/Hf (band *I*, inserted) were used to monitor the insertion rate of acetonitrile into the M-C bond.

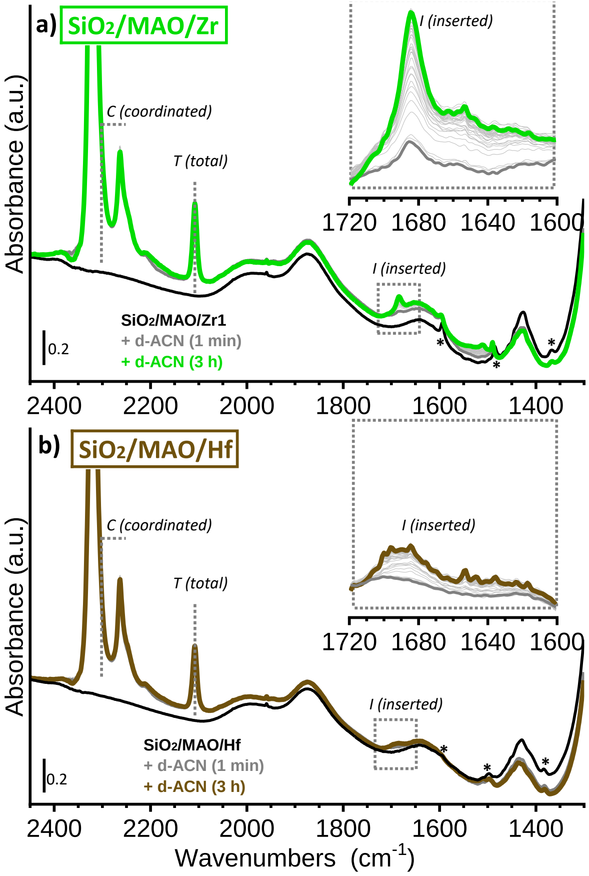

Figure 3. 37 IR spectra of d-acetonitrile adsorbed on a) SiO_2/MAO/Zr1 and b) SiO_2/MAO/Hf. Spectra are shown as function of time from 1 min (black spectra) to 3h (spectra in corresponding color). In insets magnification of 1720-1600 cm^{-1} spectral region is shown after subtraction of spectra collected before d-acetonitrile dosage

Figure 3. 38 shows the evolution of the intensities of bands *T*, *C*, and *I* over time. For both catalysts, *T* and *C* bands reach maximum intensity almost immediately, indicating that there are no diffusion limitations. A slightly decrease of band *C* over time can be seen, which is related to the slow insertion of d-acetonitrile to M-CH_3 bond. The rate of d-acetonitrile insertion into M-CH_3 bond is constant after 30 minutes, and *I* band does not reach saturation level neither after 3 h indicating that insertion of d-acetonitrile into M-CH_3 bond is slow, as reported in the literature for other Zr- and Ti-based complexes.[120,121,123,148]

For SiO_2/MAO/Zr1 the amount of coordinated d-acetonitrile depends on the total amount of d-acetonitrile on the sample: more d-acetonitrile on the sample higher the fraction able to coordinate it. Moreover, its insertion rate scales perfectly with the fraction of sites able to coordinate it, as demonstrated by the perfect overlap of *I*/*C* curves related to experiments A and B. In contrast, for SiO_2/MAO/Hf bands *T* and *C* reach saturation level very rapidly. In addition, *for same d-acetonitrile concentrations the amount of coordinated d-acetonitrile (band C) is much lower for SiO_2/MAO/Hf than for SiO_2/MAO/Zr1*. These differences are even more pronounced at higher d-acetonitrile concentrations and stands with the literature reports about detrimental effect of MAO/TMA on Hf-based complexes related to comparable Zr-based ones.[92,147] Nevertheless, *the lower amount of coordinated d-acetonitrile contributes only in part to lower the insertion rate in the case of SiO_2/MAO/Hf when compared to SiO_2/MAO/Zr1.* In fact, when comparing the behavior of the I/C bands in the two cases, it is evident that *insertion of electron-rich d-acetonitrile into the M-CH_3 bond is inherently slower in the case of SiO_2/MAO/Hf*.

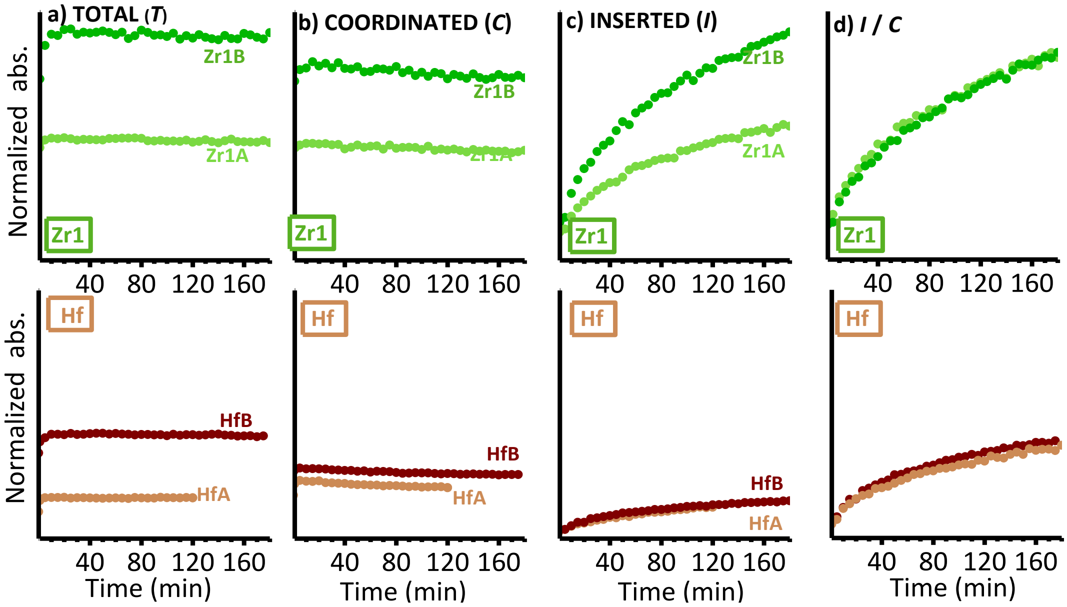

Figure 3. 38 Evolution of the intensities of the IR absorption bands T (total amount of d-acetonitrile), C (coordinated d-acetonitrile), and I (inserted d-acetonitrile) over time, as derived from a series of experiments in which SiO_2/MAO/Zr1 (top) and SiO_2/MAO/Hf (bottom) were treated with d-acetonitrile at two different concentrations (A and B). The data were normalized to the optical thickness of the pellets. Part d) shows the ratio between intensities of bands I and C over time.

3.5 Homo-polymerization of 1-hexene monitored by IR spectroscopy

Polymerization with 1-hexene over SiO_2/MAO/Zr1 and SiO_2/MAO/Hf catalysts at same conditions (room temperature, low pressure) was followed by means of time-resolved IR spectroscopy. The results are shown in Figure 3. 39 in the most interesting spectral region. As discussed in previous section, the band at 1640 cm^{-1} (*M*-monomer) was used to evaluate the monomer concentration on the sample, while band P-polymer, was taken as an indication of the amount of growing polymer.

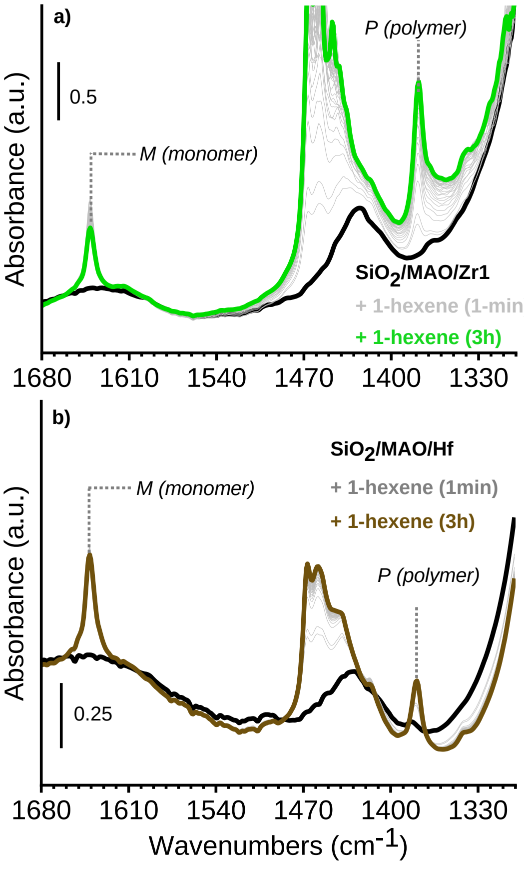

Figure 3. 39 IR spectra of 1-hexene adsorbed on SiO_2/MAO/Zr1 (a) and SiO_2/MAO/Hf (b) catalysts at 300 K. Spectra are shown as a function of time, starting from spectra collected before 1-hexene addition (black) to spectra collected after 3h (corresponding color).

The behavior of *M* and *P* bands in Figure 3. 39, was followed as a function of time in Figure 3. 40. The intensity of band *M* is much higher for SiO_2/MAO/Zr1 than for SiO_2/MAO/Hf (Figure 3. 40a) indicating that 1-hexene has more difficulties to detachion-pairs in SiO_2/MAO/Hf catalysts and agrees with what was expected based on previous data (UV-Vis and IR of CO and d-acetonitrile adsorption) and literature.[92,147] In the case of SiO_2/MAO/Zr1 catalyst the decrease in intensity of band *M* over time is more pronounced then for SiO_2/MAO/Hf, and consequently band *P* grows faster (Figure 3. 40b), indicating a faster polymerization rate. Figure 3. 40c reports the ration between bands P and M, and indicates that *the inherent insertion rate of the two catalysts is different, being SiO_2/MAO/Zr1 inherently faster than SiO_2/MAO/Hf*, in well agreement with literature.

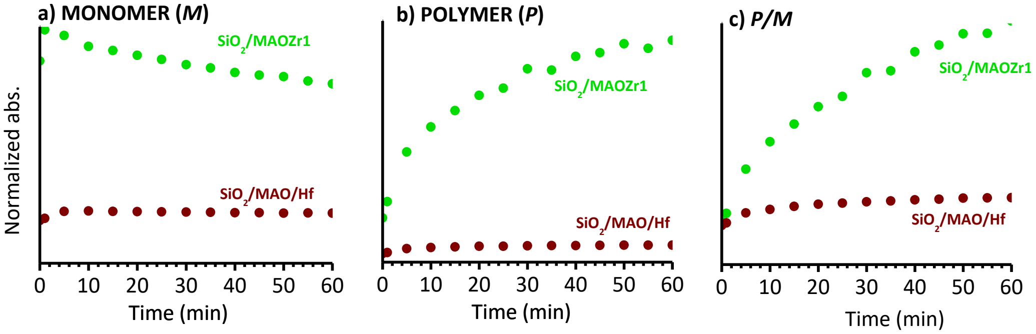

Figure 3. 40 Evolution of M and P bands in SiO_2/MAO/Zr1 (green lines) and SiO_2/MAO/Hf (brown lines) over 30 minutes. The data are shown after normalization to the optical thickness of the pellet.

3.6 Conclusions

The spectroscopic data discussed in this section demonstrate that the fraction of cationic species accessible to molecular probes is smaller in SiO_2/MAO/Hf than in SiO_2/MAO/Zr1, as expected on the basis of the documented tendency of hafnocene catalysts to form hetero-binuclear adducts with TMA. Beside the monomer (1-hexene), also CO and acetonitrile are able to insert into the $M\text{-}CH_3$ bond. Interestingly, different types of Zr-acyl species are formed in SiO_2/MAO/Zr1 in the presence of CO, a fraction of them characterized by an extensive η^2-coordination to the metal. In contrast, only a single type of Hf-acyl species is observed in SiO_2/MAO/Hf, with no η^2-coordination. This suggests that not only the $Hf^{\oplus}$ are less accessible, but also that the accessible $Hf^{\oplus}$ are more shielded than the accessible $Zr^{\oplus}$.

The lower amount of coordinated probe/monomer contributes only in part to the lower the insertion rate in the case of SiO_2/MAO/Hf when compared to SiO_2/MAO/Zr1. Spectroscopic data demonstrate in a direct way that insertion of both d-acetonitrile and 1-hexene into the $M\text{-}CH_3$ bond is inherently slower in the case of SiO_2/MAO/Hf, in good agreement with the literature.

References

1. Sauter, D. W., Taoufik, M. & Boisson, C. Polyolefins, a success story. *Polymers (Basel)* **9**, (2017).

2. Stürzel, M., Mihan, S. & Mülhaupt, R. From Multisite Polymerization Catalysis to Sustainable Materials and All-Polyolefin Composites. *Chem Rev* **116**, 1398–1433 (2016).

3. Kaminsky, W. The discovery of metallocene catalysts and their present state of the art. *Journal of Polymer Science, Part A: Polymer Chemistry* vol. 42 3911–3921 Preprint at https://doi.org/10.1002/pola.20292 (2004).

4. Gagleitner, M. & Severn, J. R. Designing Polymer Properties. in *Tailor-made Polymers Via Immobilization of Alpha-Olefin Polymerization Catalysts* (eds. Severn, J. R. & Chadwick, J. C.) 1–39 (Wiley-VCH, 2007).

5. Alt, H. G. & Görl, C. Self - immobilizing Catalysts for Olefin Polymerization. in *Tailor-Made Polymers Via Immobilization of Alpha-Olefin Polymerization Catalysts* (eds. Severn, J. R. & Chadwick, J. C.) 305–322 (Wiley-VCH, 2008).

6. Möller, A. C. *et al.* On the nonsingle-site character of bis(2-dimethylsilyl-indenyl) zirconium(IV) dichloride/MAO and bis(2-trimethylsilyl-indenyl)zirconium(IV) dichloride/MAO: Polymerization characteristics and mechanistic implications. *Journal of Physical Chemistry A* **112**, 4074–4089 (2008).

7. Coates, G. W. & Waymouth, R. M. OscillatingStereocontrol:AStrategyfortheSynthesisofThermoplasticElastomericPolypropylene. *Science (1979)* **267**, 217 (1995).

8. Kravchenko, R., Masood, A. & Waymouth, R. M. Propylene Polymerization with Chiral and Achiral Unbridged 2-Arylindene Metallocenes. *Organometallics* **16**, 3635–3639 (1997).

9. Kaminsky, W. Highly active metallocene catalysts for olefin polymerization. *Journal of the Chemical Society, Dalton Transactions* 1413 (1998).

10. Silveira, F., de Sá, D. S., da Rocha, Z. N., do Carmo Martins Alves, M. & dos Santos, J. H. Z. Structural and electronic effects in metallocene catalysts studied by x-ray techniques. *X-Ray Spectrometry* **37**, 615–624 (2008).

11. Stevens, J. C. Constrained Geometry and Other Single Site Metallocene Polyolefin Catalysts: A Revolution In Olefin Polymerization. *Stud Surf Sci Catal* **101**, (1996).

12. Soares, J. B. P. & McKenna, T. F. L. *Polyolefin Reaction Engineering*. (WILEY-VCH Verlag GmbH & CO, 2012).

13. Nakayama, Y. & Shiono, T. Developments of Chiral Metallocenes as Polymerization Catalysts. *Molecules* **10**, 620–633 (2005).

14. Damavandi, S., Ahmadjo, S., Sandaroos, R. & Zohuri, G. H. FI Catalyst for Polymerization of Olefin. in *Polymerization* (ed. de Souza Gomes, A.) (InTech, 2012). doi:10.5772/46187.

15. *Metallocene-based polyolefins — preparation, properties and techniques,Scheirs and W. Kaminsk*. (Wiley, 1999).

16. *Polymers and copolymers of higher α-olefins*. (Carl Hanser Verlag, 1977).

17. Crowther, D. J., Jordan, R. F., Baenziger, N. C. & Verma, A. Synthesis and Structural Characterization of (C5Me5)Zr(R)2(L)n+ Complexes. *Organometallics* **9**, 2574–2580 (1990).

18. Bochmann, M., Karger, G. & Jaggar, A. J. Electron-deficient Group IV Metal Alkyl Cations, and the Synthesis of Zr(CH2Ph)3(n6-C6H5)BPh3: a Fluxional Arene pi-Complex of a d0 Metal. *J. CHEM. SOC., CHEM. COMMUN* (1990).

19. Mulhaupt, R., Duschek, T. & Rieger, B. Functional Polypropylene Blend Compatibilizers. *Macrom. Chem., Macrom. Symp.* **48/49**, 317–332 (1991).

20. Suhm, J., Schneider, M. J. & Mulhaupt, R. Influence of metallocene structures on ethene copolymerization with 1-butene and 1-octene. *J Mol Catal A Chem* **128**, 215–227 (1998).

21. Spaleck, W. *et al.* The Influence of Aromatic Substituents on the Polymerization Behavior of Bridged Zirconocene Catalysts. *Organometallics* **13**, 954–963 (1994).

22. Carvill, A., Tritto, I., Locatelli, P. & Sacchi, M. C. Polymer Microstructure as a Probe into Hydrogen Activation Effect in ansa-Zirconocene/Methylaluminoxane Catalyzed Propene Polymerizations. *Macromolecules* **30**, 7056–7062 (1997).

23. Busico, V., Cipullo, R., Chadwick, J. C., Modder, J. F. & Sudmeijer, O. Effects of Regiochemical and Stereochemical Errors on the Course of Isotactic Propene Polyinsertion Promoted by Homogeneous Ziegler-Natta Catalysts. *Macromolecules* **27**, 7538–7543 (1994).

24. Kaminsky, W. *Polyolefins: 50 years after Ziegler and Natta II Polyolefins by Metallocenes and Other Single-Site Catalysts*. (Springer - Verlag Berlin Heidelberg, 2013).

25. Alt, H. G. & Köppl, A. Effect of the nature of metallocene complexes of group IV metals on their performance in catalytic ethylene and propylene polymerization. *Chem Rev* **100**, 1205–1221 (2000).

26. Silveira, F. *et al.* Effect of the silica texture on the structure of supported metallocene catalysts. *J Mol Catal A Chem* **298**, 40–50 (2009).

27. Wang, B. Ansa-metallocene polymerization catalysts: Effects of the bridges on the catalytic activities. *Coord Chem Rev* **250**, 242–258 (2006).

28. Möhring, P. C. & Coville, N. J. Group 4 metallocene polymerisation catalysts: Quantification of ring substituent steric effects. *Coord Chem Rev* **250**, 18–35 (2006).

29. Alt, H. G. & Samuel, E. Fluorenyl complexes of zirconium and hafnium as catalysts for olefin polymerization. *Chem Soc Rev* **27**, 323 (1998).

30. Curtis, D. M., Shiu, K.-B., Butker, W. M. & Huffman, J. C. Syntheses, Structures, and Molecular Orbital Analysis of Hydridotris(pyrazolyl)borate (Tp) Molybdenium Carbonyls: Paramagnetic TpMo(CO)3 and Triply Bonded Tp2Mo2(CO)4 (Mo=Mo). *Journal of American Chemical Society* **108**, 3335–3343 (1986).

31. Schmid, M. A., Alt, H. G. & Milius, W. Unbridged cyclopentadienyl-fluorenyl complexes of zirconium as catalysts for homogeneous olefin polymerization. *J Organomet Chem* **501**, 101–106 (1995).

32. Chien, J. C. W. Metallocene-Methylaluminoxane Catalysts for Olefin Polymerization. V. Comparison of Cp2ZrCl2 and CpZrCl3. *J Polym Sci A Polym Chem* **28**, 15–38 (1990).

33. Ewen, J. A. Ligand effects on metallocene catalyzed ziegler-natta polymerizations. *Stud Surf Sci Catal* **25**, 271–292 (1986).

34. Tian, J. & Huang, B. Ethylene polymerization with catalyst systems based on metallocenes with varying steric hindrance and methylaluminoxane. *Macromol. Rapid Commun* **15**, 923–928 (1994).

35. Licht, E. H., Alt, H. G. & Karim, M. M. Synthesis and characterization of bis(cyclopentadienyl)zirconium dichloride complexes with-fluorenylalkyl or silyl substituents and their application in catalytic ethylene polymerization. *J Mol Catal A Chem* **164**, (2000).

36. Doerrer, L. H., Green, M. L. H., Häußinger, D. & Saßmannshausen, J. Evidence for cationic Group 4 zirconocene complexes with intramolecular phenyl co-ordination. *J. Chem. Soc., Dalton Trans.* 2111–2118 (1999).

37. dos Santos, J. H. Z. *et al.* Supported metallocenes using inorganic-organic hybrid xerogels. *J Mol Catal A Chem* **158**, 541–557 (2000).

38. Haag, M. C. *et al.* Effects of Al/Zr ratio on ethylene-propylene copolymerization with supported-zirconocene catalysts. *J Mol Catal A Chem* **169**, 275–287 (2001).

39. Gassman, P. G., Deck1, P. A., Winter, C. H., Dobbs, D. A. & Cao, D. H. Understanding Electronic Effects in Organometallic Complexes. Electron Donation by the Trimethylsilyl Group. *Organometallics* **11**, 959–960 (1992).

40. Wagener, K. B. Oscillating catalysts: A new twist for plastics. *Science (1979)* **267**, 191 (1995).

41. Machat, M. R. *et al.* Behind the Scenes of Group 4 Metallocene Catalysis: Examination of the Metal-Carbon Bond. *Organometallics* **37**, 2690–2705 (2018).

42. Kaminsky, W., Engehausen, R., Zoumis, K., Spaleck, W. & Rohrmann, J. Standardized polymerizations of ethylene and propene with bridged and unbridged metallocene derivatives: a comparison. *Makromolecular Chemistry* **193**, 1643–1651 (1992).

43. Ewen, J. A., Haspeslagh, L., Atwood, J. L. & Zhang, H. Crystal Structures and Stereospecific Propylene Polymerizations with Chiral Hf Metallocene Catalysts. *Journal of American Chemical Society* **109**, 6544–6545 (1987).

44. Machat, M. R., Jandl, C. & Rieger, B. Titanocenes in olefin polymerization: Sustainable catalyst system or an extinct species? *Organometallics* **36**, 1408–1418 (2017).

45. Resconi, L., Cavallo, L., Fait, A. & Piemontesi, F. Selectivity in propene polymerization with metallocene catalysts. *Chem Rev* **100**, 1253–1345 (2000).

46. Bryliakov, K. P. *et al.* Ansa-titanocene catalysts for α-Olefin polymerization. Syntheses, structures, and reactions with methylaluminoxane and boron-based activators. *Organometallics* **24**, 894–904 (2005).

47. Shannon, R. D. & Prewitt, C. T. Effective Ionic Radii in Oxides and Fluorides. *Acta Cryst* **25**, 925 (1969).

48. Shannon, R. D. Revised Effective Ionic Radii and Systematic Studies of Interatomie Distances in Halides and Chaleogenides. *Acta Cryst* **32**, 751 (1976).

49. Martinho Simoes, J. A. & Beauchamp, J. L. Transition Metal-Hydrogen and Metal-Carbon Bond Strengths: The Keys to Catalysis from the. *Chemistry Reviews* **90**, 629–688 (1990).

50. Schock, L. E. & Marks, T. J. Organometallic Thermochemistry. Metal Hydrocarbyl, Hydride, Halide, Amide, and Alkoxide Bond Enthalpy Relationships and Their

Implications in Pentamethylcyclopentadienyl and Cyclopentadienyl Complexes of Zirconium and Hafnium. *J. Am. Chem. Soc* **0**, 703 (1988).

51. Dias, R., Salema, M. S., Martinho Simoes, A., Pattiasina, J. W. & Teuben, J. H. Stepwise Ti-Cl, Ti-CH, and Ti-C,H, bond dissociation enthalpies in bis(pentamethylcyclopentadienyl) titanium complexes. *J Organomet Chem* **346**, 4–6 (1988).

52. Fischer, E. O. & Jira, R. *Über den Di-cyclopentadienyl-Komplex des Kobalts*. *Z. Naturforschg* vol. 8 (1953).

53. Wilkinson, G. & Birmingham, J. M. Bis-cyclopentadienyl Compounds of Ti, Zr, V, Nb and Ta. *Journal of American Chemical Society* **75**, 901 (1954).

54. Sinn, H., Kaminsky, W., Vollmer, H.-J. & Woldt, R. 'Living Polymers' on Ploymerization with Extremely Productive Ziegler Catalysts. *Angew. Chem. Int. Ed. Engl.* **19**, (1980).

55. Zaccaria, F., Sian, L., Zuccaccia, C. & Macchioni, A. Ion pairing in transition metal catalyzed olefin polymerization. *Advances in Organometallic Chemistry* **73**, 1–78 (2020).

56. Collins, R. A., Russell, A. F. & Mountford, P. Group 4 metal complexes for homogeneous olefin polymerisation: a short tutorial review. *Appl Petrochem Res* **5**, 153–171 (2015).

57. Pedeutour, J.-N., Radhakrishnan, K., Cramail, H. & Deffieux, A. Reactivity of Metallocene Catalysts for Olefin Polymerization: Influence of Activator Nature and Structure. *Macromol Rapid Commun* **22**, (2001).

58. Sinn, H. PROPOSALS FOR STRUCTURE AND EFFECT OF METHYLALUMOXANE BASED ON MASS BALANCES AND PHASE SEPARATION EXPERIMENTS. *Macromol Symp* **97**, 27–52 (1995).

59. Koide, Y., Bott, S. G. & Barron, A. R. Alumoxanes as Cocatalysts in the Palladium-Catalyzed Copolymerization of Carbon Monoxide and Ethylene: Genesis of a Structure-Activity Relationship. *Organometallics* **15**, 2213–2226 (1996).

60. Kaminsky, W. Discovery of methylaluminoxane as cocatalyst for olefin polymerization. *Macromolecules* **45**, 3289–3297 (2012).

61. Bochmann, M. The chemistry of catalyst activation: The case of group 4 polymerization catalysts. *Organometallics* **29**, 4711–4740 (2010).

62. Zijlstra, H. S. & Harder, S. Methylalumoxane - History, production, properties, and applications. *European Journal of Inorganic Chemistry* vol. 2015 19–43 Preprint at https://doi.org/10.1002/ejic.201402978 (2015).

63. Bochman, M. The Use of Spectroscopy in Metallocene-based Polymerisation Catalysis. in *Mechanisms in Homogeneous Catalysis: A Spectroscopic Approach* (ed. Heaton, B.) 840 (Wiley-VCH, 2003).

64. Coevoet, D., Cramail, H. & Defsieux, A. U.V./visible spectroscopic study of the rac-Et(Ind)~ZrCl2/AMO olefin polymerization catalytic system, 2a Investigation in CH2C12. *Macromol Chem Phys* **199**, 1459–1464 (1998).

65. Coevoet, D., Cramail, H. & Defsieux, A. U.V./visible spectroscopic study of the rac-Et(Ind)2ZrCl2/MAO olefin polymerization catalytic system, 1 Investigation in toluene. *Macromol Chem Phys* **199**, 1451 (1998).

66. Pédeutour, J. N., Radhakrishnan, K., Cramail, H. & Deffieux, A. Elementary mechanisms of metallocene activation by methylaluminoxane cocatalysts for olefin polymerization. *Polym Int* **51**, 973–977 (2002).

67. Wieser, U., Schaper, F. & Brintzinger, H.-H. Methylalumoxane (MAO)-Derived MeMAO- Anions in Zirconocene-Based Polymerization Catalyst Systems-A UV-Vis Spectroscopic Study. *Macromolecular Symposa* **236**, 63–68 (2006).

68. Tritto, L., Sacchi, M. C., Locatelli, P. & Li, S. X. Metallocenes/Methylaluminoxanes: A 13C NMR Study of the Reaction Equilibria and Polymerization. *Macromol Symp* **97**, 101–108 (1995).

69. Tritto, I., Sacchi, M. C., Locatelli, P. & Li, S. X. Metallocene Ion Pairs: A Direct Insight into the Reaction Equilibria and Polymerization by 13C NMR Spectroscopy. *Macromol Symp* **89**, 289–298 (1995).

70. Tritto, I., Sacchi, M. C. & Li, S. NMR study of the reactions in Cp2TiMeCl/AIMe3 and Cp2TiMeCl/methylalumoxane systems, catalysts for olefin polymerization. *Macromol Rapid Commun* **15**, 217–223 (1994).

71. Laine, A., Linnolahti, M. & Pakkanen, T. A. Alkylation and activation of metallocene polymerization catalysts by reactions with trimethylaluminum: A computational study. *J Organomet Chem* **716**, 79–85 (2012).

72. Pédeutour, J.-N., Radhakrishnan, K., Cramail, H. & Deffieux, A. *Use of 'TMA-depleted' MAO for the activation of zirconocenes in olefin polymerization*. *Journal of Molecular Catalysis A: Chemical* vol. 185 (2002).

73. Zaccaria, F. *et al.* BHT-Modified MAO: Cage Size Estimation, Chemical Counting of Strongly Acidic Al Sites, and Activation of a Ti-Phosphinimide Precatalyst. *ACS Catal* **9**, 2996–3010 (2019).

74. Rocchigiani, L., Busico, V., Pastore, A. & MacChioni, A. Probing the interactions between all components of the catalytic pool for homogeneous olefin polymerisation by diffusion NMR spectroscopy. *Dalton Transactions* **42**, 9104–9111 (2013).

75. Zurek, E. & Ziegler, T. Theoretical studies of the structure and function of MAO (methylaluminoxane). *Prog Polym Sci* **29**, 107–148 (2004).

76. Zurek, E. & Ziegler, T. A theoretical study of the insertion barrier of MAO (Methylaluminoxane)-activated, Cp2ZrMe2-catalyzed ethylene polymerization: Further evidence for the structural assignment of active and dormant species. *Faraday Discuss* **124**, 93–109 (2003).

77. Zurek, E. & Ziegler, T. Toward the identification of dormant and active species in MAO (methylaluminoxane)-activated, dimethylzirconocene-catalyzed olefin polymerization. *Organometallics* **21**, 83–92 (2002).

78. Zurek, E. & Ziegler, T. A combined quantum mechanical and statistical mechanical study of the equilibrium of trimethylaluminum (TMA) and oligomers of (AlOCH3)n found in methylaluminoxane (MAO) solution. *Inorg Chem* **40**, 3279–3292 (2001).

79. Kuklin, M. S., Hirvi, J. T., Bochmann, M. & Linnolahti, M. Toward Controlling the Metallocene/Methylaluminoxane-Catalyzed Olefin Polymerization Process by a Computational Approach. *Organometallics* **34**, 3586–3597 (2015).

80. Zijlstra, H. S., Joshi, A., Linnolahti, M., Collins, S. & McIndoe, J. S. Modifying methylalumoxane via alkyl exchange. *Dalton Transactions* **47**, 17291–17298 (2018).

81. Hirvi, J. T., Bochmann, M., Severn, J. R. & Linnolahti, M. Formation of octameric methylaluminoxanes by hydrolysis of trimethylaluminum and the mechanisms of catalyst activation in single-site a-olefin polymerization catalysis. *ChemPhysChem* **15**, 2732–2742 (2014).

82. Linnolahti, M., Severn, J. R. & Pakkanen, T. A. Formation of Nanotubular Methylaluminoxanes and the Nature of the Active Species in Single-Site α-Olefin Polymerization Catalysis. *Angewandte Chemie* **120**, 9419–9423 (2008).

83. Linnolahti, M., Luhtanen, T. N. P. & Pakkanen, T. A. Theoretical studies of aluminoxane chains, rings, cages, and nanostructures. *Chemistry - A European Journal* **10**, 5977–5987 (2004).

84. Linnolahti, M., Severn, J. R. & Pakkanen, T. A. Are aluminoxanes nanotubular? Structural evidence from a quantum chemical study. *Angewandte Chemie - International Edition* **45**, 3331–3334 (2006).

85. Velthoen, M. E. Z. *et al.* The Multifaceted Role of Methylaluminoxane in Metallocene-Based Olefin Polymerization Catalysis. *Macromolecules* **51**, 343–355 (2018).

86. Macchioni, A. Ion pairing in transition-metal organometallic chemistry. *Chem Rev* **105**, 2039–2073 (2005).

87. Babushkin, D. E. & Brintzinger, H. H. Activation of dimethyl zirconocene by methylaluminoxane (MAO)-size estimate for Me-MAO- anions by pulsed field-gradient NMR. *J Am Chem Soc* **124**, 12869–12873 (2002).

88. Babushkin, D. E., Semikolenova, N. v, Zakharov, V. A. & Talsi, E. P. Mechanism of dimethylzirconocene activation with methylaluminoxane: NMR monitoring of intermediates at high Al/Zr ratios. *Macromol Chem Phys* **201**, 558–567 (2000).

89. Beck, S. *et al.* Binuclear zirconocene cations with p-CH ,-bridges in homogeneous Ziegler-Natta catalyst systems. *J Mol Catal A Chem* **111**, 67–79 (1996).

90. Theurkauff, G. *et al.* Discrete Ionic Complexes of Highly Isoselective Zirconocenes. Solution Dynamics, Trimethylaluminum Adducts, and Implications in Propylene Polymerization. *Organometallics* **35**, 258–276 (2016).

91. Rieger, B., Troll, C. & Preuschen, J. Ultrahigh molecular weight polypropene elastomers by high activity 'dual-side' hafnocene catalysts. *Macromolecules* **35**, 5742–5743 (2002).

92. Busico, V., Cipullo, R., Pellecchia, R., Talarico, G. & Razavi, A. Hafnocenes and MAO: Beware of trimethylaluminum! *Macromolecules* vol. 42 1789–1791 Preprint at https://doi.org/10.1021/ma900066n (2009).

93. Mäkelä-Vaarne, Nora. Characterisation of group 4 metallocenes and metallocene catalysts : UV/VIS spectroscopic study. (Borealis Polymers Oy, R&D, Finland and Laboratory of Inorganic Chemistry, Faculty of Science, University of Helsinki, Finland, 2003).

94. Panchenko, V. N., Zakharov, V. A. & Paukshtis, E. A. Study of the supported zirconocene catalysts by means of UV/vis and DRIFT spectroscopy. *J Mol Catal A Chem* **240**, 33–39 (2005).

95. Mäkelä, N. I., Knuuttila, H. R., Linnolahti, M., Pakkanen, T. A. & Leskelä, M. A. Activation of racemic ethylene-bridged bis(indenyl)-type siloxy-substituted

zirconocenes with methylaluminoxane. A combined UV/vis spectroscopic and ab initio Hartree-Fock study. *Macromolecules* **35**, 3395–3401 (2002).

96. Carlos, A. M., Carrion, P., Fernando, C. H., Antonio Anti ňolo & Otero, A. UV-visible spectroscopy for zirconocene activation by MAO in olefin polymerization: Activity versus wavenumber. *Appl Organomet Chem* **23**, 241–244 (2009).

97. Santamäki, S. *et al.* Activation of hafnocene catalyzed polymerization of 1-hexene with MAO and borate. *Eur Polym J* **45**, 863–869 (2009).

98. Coevoet, D., Cramail, H. & Deffieux, A. Activation of rac-ethylenebis(indenyl)zirconium dichloride with a low amount of methylaluminoxane (MAO) for olefin polymerizations. *Macromol Chem Phys* **197**, 855–867 (1996).

99. Babushkin, D. E., Panchenko, V. N. & Brintzinger, H. H. Zirconium allyl complexes as participants in zirconocene-catalyzed α-olefin polymerizations. *Angewandte Chemie - International Edition* **53**, 9645–9649 (2014).

100. Panchenko, V. N., Babushkin, D. E., Bercaw, J. E. & Brintzinger, H. H. Catalyst speciation during ansa-Zirconocene-catalyzed polymerization of 1-Hexene Studied by UV-vis spectroscopy-formation and partial re-activation of Zr-Allyl intermediates. *Polymers (Basel)* **11**, (2019).

101. Severn, J. R., Chadwick, J. C., Duchateau, R. & Friederichs, N. 'Bound but not gagged' - Immobilizing single-site α-olefin polymerization catalysts. *Chemical Reviews* vol. 105 4073–4147 Preprint at https://doi.org/10.1021/cr040670d (2005).

102. Tisse, V. F., Prades, F., Briquel, R., Boisson, C. & McKenna, T. F. L. Role of silica properties in the polymerisation of ethylene using supported metallocene catalysts. *Macromol Chem Phys* **211**, 91–102 (2010).

103. Severn, J. R. Methylaluminoxane (MAO), Silica and a Complex: The " Holy Trinity " of Supported Single - site Catalyst. in *Tailor-Made Polymers Via Immobilization of Alpha-Olefin Polymerization Catalysts* (eds. Severn, J. R. & Chadwick, J. C.) 95–135 (WILEY-VCH , 2008).

104. Tran, D., Zhang, C. & Choi, K. Y. Effects of Silica Support Properties on the Performance of Immobilized Metallocene Catalysts for Ethylene Polymerization. *Macromol React Eng* (2022) doi:10.1002/mren.202200020.

105. Ribeiro, M. R., Deffieux, A. & Portela, M. F. Supported Metallocene Complexes for Ethylene and Propylene Polymerizations: Preparation and Activity. *Industrial & Engineering Chemistry Research* **36**, 1224–1237 (1997).

106. Guimarães, R., Stedile, F. C. & dos Santos, J. H. Z. Ethylene polymerization with catalyst systems based on supported metallocenes with varying steric hindrance. *J Mol Catal A Chem* **206**, 353–362 (2003).

107. Shinde, P. S. *et al.* A brief overview of recent progress in porous silica as catalyst supports. *Journal of Composites Science* **5**, (2021).

108. Velthoen, M. E. Z., Boereboom, J. M., Bulo, R. E. & Weckhuysen, B. M. Insights into the activation of silica-supported metallocene olefin polymerization catalysts by methylaluminoxane. *Catal Today* **334**, 223–230 (2019).

109. Lamberti, C., Zecchina, A., Groppo, E. & Bordiga, S. Probing the surfaces of heterogeneous catalysts by in situ IR spectroscopy. *Chem Soc Rev* **39**, 4951–5001 (2010).

110. Piovano, A., Zarupski, J. & Groppo, E. Disclosing the Interaction between Carbon Monoxide and Alkylated Ti3+Species: A Direct Insight into Ziegler-Natta Catalysis. *Journal of Physical Chemistry Letters* **11**, 5632–5637 (2020).

111. Piovano, A., Martino, G. A. & Barzan, C. A spectroscopic investigation of silica-supported TiClx species: a case study towards Ziegler–Natta catalysis. *Rend Lincei Sci Fis Nat* **28**, 43–49 (2017).

112. D'Amore, M. *et al.* Surface Investigation and Morphological Analysis of Structurally Disordered MgCl2 and MgCl2/TiCl4 Ziegler-Natta Catalysts. *ACS Catal* **6**, 5786–5796 (2016).

113. Pletcher, P., Welle, A., Vantomme, A. & Weckhuysen, B. M. Quality control for Ziegler-Natta catalysis via spectroscopic fingerprinting. *J Catal* **363**, 128–135 (2018).

114. Panchenko, V. N., Danilova, I. G., Zakharov, V. A. & Paukshtis, E. A. An IR-Spectroscopic Study of the State of Zirconiumin Supported Zirconocene Catalysts. *Kinetics and Catalysis* **45**, 547–553 (2004).

115. Panchenko, V. N., Semikolenova, N. v, Danilova, I. G., Paukshtis, E. A. & Zakharov, V. A. IRS study of ethylene polymerization catalyst SiO2/ methylaluminoxane/zirconocene. *J Mol Catal A Chem* **142**, 27–37 (1999).

116. Martino, G. A. *et al.* Rationalizing the Effect of Triethylaluminum on the Cr/SiO2 Phillips Catalysts. *ACS Catal* **10**, 2694–2706 (2020).

117. Knozinger, H. INFRARED SPECTROSCOPY AS A PROBE OF SURFACE ACIDITY. in *Elementary Reaction Steps in Heterogeneous Catalysis* (eds. Joyner, R. W. & van Santen, R. A.) 267–285 (1993).

118. Marsella, J. A., Curtis, C. J., Bercaw, J. E. & Caulton, K. G. *Low-Temperature Infrared Study of d° Carbonyl Complexes*. *J. Am. Chem. Soc* vol. 102 https://pubs.acs.org/sharingguidelines (1980).

119. Morterra, C., Peñarroya Mentruit, M. & Cerrato, G. Acetonitrile adsorption as an IR spectroscopic probe for surface acidity/basicity of pure and modified zirconias. *Physical Chemistry Chemical Physics* **4**, 676–687 (2002).

120. Bochmann, M. & Wilson, L. M. Synthesis and Insertion Reactions of Cationic Alkylbis(cyclopentadienyl)titanium Complexes. *J Chem Soc Chem Commun* 1610–1611 (1986).

121. Jordan, R. F., Bajgur, C. S., Dasher, W. E. & Rheingold, A. L. Hydrogenation of Cationic Dicyclopentadienyl Zirconium(IV) Alkyl Complexes. Characterization of Cationic Zirconium(IV) Hydrides. *Organometallics* **6**, 1041–1051 (1987).

122. Bochmann, M., Wilson, L. M., Hursthouse, M. B. & Short, R. L. Cationic Alkylbis(cyclopentadienyl)titanium Complexes. Synthesis, Reactions with CO and t-BuNC, and the Structure of [Cp2Ti{7j2-C(Me)N-f-Bu)(CN-f-Bu)]BPh4e*MeCN. *Organometallics* **6**, 2556–2563 (1987).

123. Alelyunas, Y. W., Jordan, R. F., Echols, S. F., Borkowsky, S. L. & Bradley, P. K. *Insertion Reactions of (C5H4R)2Zr(R)(L)+ Complexes*. *Organometallics* vol. 10 https://pubs.acs.org/sharingguidelines (1991).

124. Linnolahti, M. & Pakkanen, T. A. Theoretical study on the factors controlling the accessibility of cationic metal centers in zirconocene polymerization catalysts. *Macromolecules* **33**, 9205–9214 (2000).

125. Wieser, U. *et al.* Effects of an interannular bridge on spectral and electronic properties of bis(cyclopentadienyl)- and bis(indenyl)zirconium (IV) complexes. *Organometallics* **21**, 541–545 (2002).

126. Przybyla, C., Tesche, B. & Fink, G. Ethylene/hexene copolymerization with the heterogeneous catalyst system SiO2 /MAO/rac-Me2Si[2-Me-4-Ph-Ind]2ZrCl2 : The filter effect. *Macromol Rapid Commun* **20**, 328–332 (1999).

127. Zecchina, A. & Otero Arean, C. Diatomic Molecular Probes for Mid-IR Studies of Zeolites. *Chem Soc Rev* **25**, 187–197 (1996).

128. Groppo, E., Martino, G. A., Piovano, A. & Barzan, C. The Active Sites in the Phillips Catalysts: Origins of a Lively Debate and a Vision for the Future. *ACS Catal* **8**, 10846–10863 (2018).

129. Groppo, E., Lamberti, C., Bordiga, S., Spoto, G. & Zecchina, A. The structure of active centers and the Ethylene Polymerization mechanism on the Cr/SiO2

catalyst: A frontier for the characterization methods. *Chem Rev* **105**, 115–183 (2005).

130. Zakharov, V. A. *et al.* SURFACE ACIDIC SITES OF HIGHLY DISPERSE MAGNESIUM CHLORIDE IR AND ESR SPECTROSCOPY STUDIES. *Macromol. Symp* **89**, 55–61 (1995).

131. Thushara, K. S., D'Amore, M., Piovano, A., Bordiga, S. & Groppo, E. The Influence of Alcohols in Driving the Morphology of Magnesium Chloride Nanocrystals. *ChemCatChem* **9**, 1782–1787 (2017).

132. Ystenes, M. *et al. Experimental and Theoretical Investigations of the Structure of Methylaluminoxane (MAO) Cocatalysts for Olefin Polymerization*. *J Polym Sci A: Polym Chem* vol. 38 (2000).

133. Jezequel, M. *et al.* Supported metallocene catalysts by surface organometallic chemistry. Synthesis, characterization, and reactivity in ethylene polymerization of oxide-supported mono- and biscyclopentadienyl zirconium alkyl complexes: Establishment of structure/reactivity relationships. *J Am Chem Soc* **123**, 3520–3540 (2001).

134. Bianchini, D., Bichinho, M. K. & dos Santos, J. H. Z. Polyethylenes produced with zirconocene immobilized on MAO-modifed silicas. *Polymer (Guildf)* **43**, 2937–2943 (2002).

135. Hadjiivanov, K., Penkova, A. & Centeno, M. A. FTIR indication of CO interaction with O2- ions: A new adsorption form in the gap between chemi- and physisorbed CO. *Catal Commun* **8**, 1715–1718 (2007).

136. Talsi, E. P. *et al.* The metallocenermethylaluminoxane catalysts formation: EPR spin probe study of Lewis acidic sites of methylaluminoxane. *J Mol Catal A Chem* **139**, 131–137 (1999).

137. Martra, G., Ocule, R., Marchese, L., Centi, G. & Coluccia, S. *Alkali and alkaline-earth exchanged faujasites: strength of Lewis base and acid centres and cation site occupancy in Na-and BaY and Na-and BaX zeolites*. *Catalysis Today* vol. 73 (2002).

138. Fachinetti, G., Fochi, G. & Floriani, C. Carbon Monoxide Insertion into Zirconium- and Hafnium-Carbon σ Bonds: Synthesis, and Structural and Thermodynamic Data for Alkyl- and Aryl-η-acylbis(η-cyclopentadienyl)derivatives of Zirconium (IV) and Hafnium(IV). *Journal of Chemical Society, Dalton* 1946–1951 (1977).

139. Mehdiabadi, S., Lhost, O., Vantomme, A. & Soares, J. B. P. Ethylene Polymerization Kinetics and Microstructure of Polyethylenes Made with Supported Metallocene Catalysts. *Ind Eng Chem Res* **60**, 9739–9754 (2021).

140. Knoezinger, H. & Krietenbrink, H. *Infrared Spectroscopic Study of the Adsorption of Nitriles on Aluminium Oxide Fermi Resonance in Coordinated Acetonitrile*. (1975).

141. Morterra, C., Cerrato, G., Novarino, E. & Peñarroya Mentruit, M. On the adsorption of acetonitrile on pure and sulfated tetragonal zirconia (t-ZrO2). *Langmuir* **19**, 5708–5721 (2003).

142. Cerruti, M., Bolis, V., Magnacca, G. & Morterra, C. Surface chemical functionalities in bioactive glasses. The gas/solid adsorption of acetonitrile. *Physical Chemistry Chemical Physics* **6**, 2468–2479 (2004).

143. Escalona Platero, E., Peñarroya Mentruit, M. & Morterra, C. Fourier transform infrared spectroscopy study of CD3CN adsorbed on pure and doped γ-alumina. *Langmuir* **15**, 5079–5087 (1999).

144. Zecchina, A., Guglielminotti, E., Coluccia, S. & Borello, E. *Infrared Spectra of Nitriles on a Chromia-Silica Catalyst*. *J. Chem. SOC. (A)* (1969).

145. Montanari, T., Bevilacqua, M. & Busca, G. Use of nitriles as probe molecules for the accessibility of the active sites and the detection of complex interactions in zeolites through IR spectroscopy. *Appl Catal A Gen* **307**, 21–29 (2006).

146. Ahmadjo, S. Preparation of ultra high molecular weight amorphous poly(1-hexene) by a Ziegler–Natta catalyst. *Polym Adv Technol* **27**, 1523–1529 (2016).

147. Ehm, C., Cipullo, R., Budzelaar, P. H. M. & Busico, V. Role(s) of TMA in polymerization. *Dalton Transactions* **45**, 6847–6855 (2016).

148. Bochmann, M., Wilson, L. M., Hursthouse, M. B. & Motevalll, M. Insertion Reactions of Nitriles in Cationic Alkylbls(cyclopentfrdlenyl)tltanlum Complexes:The Facile Synthesis of Azaalkenylidene Titanium Complexes and the Crystal and Molecular Structure of [(Indenyl)2Ti(NCMePh)(NCPh)]BPh4. *Organometallics* **7**, 1148–1154 (1988).

CHAPTER 4

Silica-supported Ziegler-Natta catalysts

This chapter is devoted to silica-supported Ziegler-Natta catalysts. Discussion will start with the state-of-the-art in the field and will continue with the discussion of the results obtained for both Ziegler-Natta precatalyst and corresponding catalysts. Ziegler-Natta precatalyst and catalysts were investigated by a set of complementary spectroscopic techniques, which allowed us to puzzle the properties at molecular level. Moreover, in order to better understand these complex systems, the results were compared to those obtained on reference samples.

1. State-of-the-art

1.1 Ziegler-Natta catalysts: a brief introduction

The history of Ziegler-Natta (ZN) catalysts traces back in 1950s when Karl Ziegler understood that Ti chlorides combined with alkyl aluminum can polymerize ethylene.[1] The second breakthrough occurred the year later when Giulio Natta discovered that Ziegler catalyst can produce isotactic PP at relatively mild conditions.[2] Since that time, these catalysts are constantly changing, improving, and intriguing scientific world.

Generally speaking, modern Ziegler-Natta catalysts are based on:

- A transition metal chloride: predominately Ti, but also V can be used,
- A support: $MgCl_2$ or SiO_2,
- An activator: alkyl aluminum compounds, such as triethylaluminum (TEA) or triisobutylaluminum (TiBA).[3]
- Electron donors: Lewis bases, which are fundamental in the case of propylene polymerization to boost the stereoregularity of the catalyst.[3,4]

Supported transition metal chlorides are called pre-catalysts since they are not active in polymerization until activated with alkyl aluminum compound, which is, in turn, called activator or co-catalyst.

Since their discovery, ZN catalysts evolved passing through several generations (this applies especially for PP production).[5,6] At the beginning, ZN catalysts were composed just from $TiCl_3$ in different structure (α-, β or γ-$TiCl_3$) activated with alkyl aluminum (or diethyl aluminum chloride).[7,8] These catalysts had several drawbacks, such as low activity (because the majority of Ti sites were inside the catalyst crystal and thus not accessible to monomer) and selectivity (very low isotactic index). Also, removing of the catalyst and atactic PP (in the case of propylene polymerization) from the final product were required in order to gain desired product quality.[3,9] The next steps in ZN catalyst evolution were the addition of monoester-based internal electron donor[10,11] and the use of activated $MgCl_2$ as catalyst support.[9,12,13] By these two modifications, catalysts stereoselectivity and productivity, as well as the morphology of the polymer product, were much improved and product purification step was eliminated, saving time and money, two components of crucial importance in the industry.

However, ZN catalysts continued their journey by evolving and improving so the next upgrade was the use of both internal (phthalate esters) and external (alkoxysilane of type $RR'Si(OMe)_2$ or $RSi(OMe)_3$) electron donors.[14] The role of an external donor is to compensate the loose of internal electron donor due to catalysts activation with alkyl aluminum and, hence, to ensure good stereoselectivity of the catalyst.[9] Also, new routes of chemical activation of $MgCl_2$, alternative to mechanical ones, were discovered, leading to better particle size and porosity control reached by chemical treatment of $MgCl_2$.[3] To further ameliorate the catalyst performances, significant efforts were made in finding the best electron donors. This applies in particular for internal donors, who previously were found to be removed by alkylation and complexation reactions with alkyl aluminum. So, new internal donors with O-O distances that ensure effective donor coordination to $MgCl_2$ and are not removed from the $MgCl_2$ after catalyst activation with alkyl aluminums started to be used. This means that no external donor is needed to reach satisfying stereoselectivity.[3]

When $MgCl_2$ started to be used as a support for ZN catalysts it was thought that it has no role in catalysis. Now, it is well known that $MgCl_2$ is more than just dispersing agent for catalyst particles. It is known that $MgCl_2$ takes place in defining of morphology of produced polymers and in distribution of the active sites.[7,15,16] However, despite all efforts the real role of $MgCl_2$ in catalysis is still not completely clear.[17]

1.2 Silica-supported Ziegler-Natta catalysts

At the beginning of 1980s silica was implemented as a carrier for $MgCl_2$/ZN catalytic systems in order to further improve the performance of $MgCl_2$-supported ZN catalysts in ethylene polymerization and today, SiO_2/$MgCl_2$/ZN catalysts are big players in the field of PE production.[18–21] This applies in particular to catalysts used in gas-phase processes, where the control of particle size and distribution is mandatory.[3] Supporting of $MgCl_2$/ZN catalysts on silica was also a way to make amorphous and disordered $MgCl_2$, providing an alternative to ball milling.

Initially silica was considered just as dispersing agent offering large pore volume and surface area, but several studies demonstrated that silica takes part in the active sites architecture. [22–25] More specifically, chemical properties of silica such as the relative amount of silanols and siloxane bridges, can define the structure of the active sites at a molecular level. On the other hand the physical properties (e.g. porosity and specific surface area) rule phenomena like the diffusion of the monomer into the pores, the steric accessibility, and the particle fragmentation.[26] The combination of the two factors explain why silica-supported ZN catalysts are so widely used in the slurry and gas-phase ethylene polymerization processes, in which the particle size of the final PE granule is fundamental for maintaining good reactor continuity. This is supported by the fact that varying surface properties of silica a whole new set of catalysts can be obtained altering the properties of produced polymers. Hence, modifying silica properties can be seen as a way to fine tune the polymer properties. Indeed, $SiO_2/MgCl_2$/ZN catalysts are reported to yield polymers with improved chemical composition distribution in ethylene co-polymerization.[3] Although also not pre-treated silica can be used for supporting the $MgCl_2$/ZN catalytic systems, chemical dehydroxylated silicas were demonstrated to work better than no pre-treated ones.[27]

There are a lot of procedures to synthesize $SiO_2/MgCl_2$/ZN catalysts, and it is well documented that the order of reactant addition has a strong impact on the properties of the final catalyst.[28,29] In an extremely simplified way, the procedure of precatalyst preparation involves:

- Reacting dehydroxylated silica with organomagnesium compound, and
- Grafting of $TiCl_4$ on SiO_2/Mg support.[30–33]

To be highly active in ethylene polymerization, the so-prepared precatalysts must be activated with an alkyl aluminum compound. The roles of alkyl aluminums are to alkylate the Ti sites forming a Ti-R bond and to abstract a Cl ligand creating a coordination vacancy. In this sense, in theory there are no big differences between the performance of different alkyl aluminums, except that ones with bulkier ligands can cause steric hindrance of Ti sites.

1.3 The active sites in ZN catalysts

The reason why ZN catalysts are so intriguing is that, even after decades of intensive research, the nature of the active site is still not completely elucidated. This is due to: i) small concentration of the metal sites, and even smaller of the active sites, ii) high air and moisture sensitivity, and iii) complexity of the system.[22] The fact that even small changes in synthesis route (including support pre-treatment, reactant addition, etc.) have significant impact on the properties of the final catalyst does not help in filling this knowledge gap. Altogether, the combination of all these factors disabled rational design of ZN catalysts leading to trial-and-error designing approach, that is not always yielding the best results. Although, modern science uses advances technologies such as high-throughput screening of all the possible parameters as a tool for designing ZN catalysts and also theoretical calculations to elucidate catalyst structure, lack of knowledge on active sites properties at molecular level is still a major obstacle to progress in the field.[34]

The nature of active sites is an enigma, and different structures have been proposed and some of them are illustrated in Figure 4. 1. Fist, an alkylated Ti(III) site (structure B) has been proposed as a possible form of the active sites since it is known that alkyl aluminum compounds reduce Ti(IV) to Ti(III).[35] This is supported by studies that demonstrated that the polymerization activity depends on the amount of Ti(III) in the catalyst[36,37] and it is in agreement with the Cossee mechanism of olefin polymerization according to which the active site should have both an alkyl group in its coordination sphere and a coordination vacancy.[38] Theory is further confirmed by spectroscopic studies demonstrating that neutral Ti(III)-alkyls and silica-supported Ti(III)-hydrides are active in ethylene polymerization.[39–42] Structure C is inspired by the fact that bimetallic complexes of the type $Ti(C_2H_5)Cl_2$-(μ-Cl)-$Al(C_2H_5)_2$ can be active in ethylene polymerization even without activation with alkyl aluminum compound due to weak π character of Ti-alkyl bond, which favors ethylene insertion into Ti-C bond.[39,41] Finally, structure A is based on analogy with metallocene-based catalysts, and suggests that active sites in ZN catalysts are cationic Ti(IV) sites.[43] However, this is less probable explanation since it is know that, most usually, ZN catalysts are not active unless they are activated with alkyl aluminum based activator which is responsible for reduction of Ti sites.

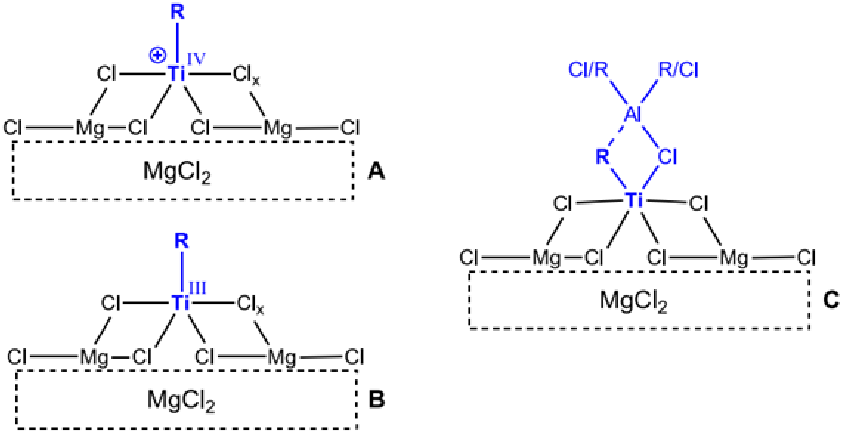

Figure 4. 1 Possible structures of Ti sites active in ethylene polymerization as proposed in Ref.[41]

Differently from metallocene-based catalysts that are considered to be single-site catalysts, ZN catalysts are multi-site catalysts having four to five different types of active centers.[44] These active sites have different activities and stabilities, produce polymers with different MW distribution and differently respond to the reaction conditions.[45] However, each specific type of active sites produce polymer with sharp MW distribution, uniform composition and stereoregularity. Some general differences between active sites are: i) MW of produced polymer significantly differ from site to site, ii) rate of active site formation is different for each type of sites and concentration of active sites decay differently from type to type, iii) each type of sites differently react to catalyst poisons, and iv) ability for copolymerize ethylene with other α-olefins is different for each active site type.[8,43–47]

1.4 The mechanisms of ethylene polymerization over ZN catalysts

There are several mechanisms of olefin polymerization over ZN catalysts, and here just the two most popular ones will be mentioned.[38,48]

According to the Cossee mechanism of olefin polymerization[38] (Figure 4. 2) a typical active site in a ZN catalyst is a transition metal in pseudo-octahedral geometry, with one ligand position free (coordination vacancy), one position occupied by an alkyl group, and the others by halogens. The first step of the reaction is monomer coordination to the metal via π bonding. The next step is the insertion of the alkyl group into the coordinated monomer, and this rearrangement step is considered as rate determining. After the first monomer insertion, the active site is still bonded to an alkyl group (elongated of one monomer unit) and still possess a coordination vacancy, but position of these two will be inverse. The polymerization will continue by subsequent monomer coordination and insertion until termination occurs.

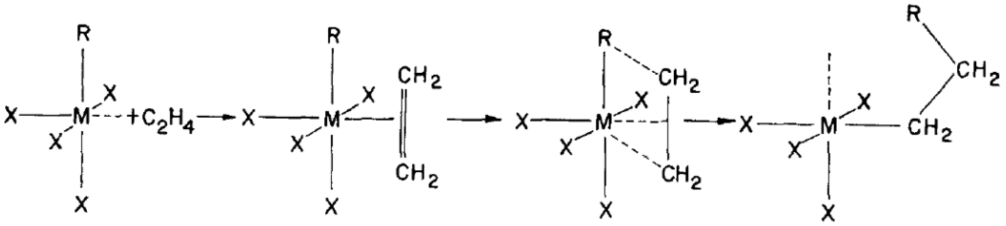

Figure 4. 2 Mechanism of ethylene polymerization catalyzed by transition metal-based catalysts proposed by Cossee.[38]

A modification of the Cossee mechanism is the so-called trigger mechanism proposed by Ystenes and represented in Figure 4. 3.[48] According to this mechanism the monomer coordinates to free coordination vacancy in a pseudo-seven coordinated complex. In this pseudo-seven complex two monomers are present and interact with each other and with central atom as well. The next monomer will coordinate as soon the firstly coordinated monomer inserts into transition metal-alkyl bond. Coordinated monomer will not insert if there is no monomer available for subsequent coordination, and this is how the mechanism got its name: new monomer triggers the insertion of firstly coordinated monomer. These means that a monomer is always occupying the coordination vacancy enabling flipping of the polymer chain and of the other ligands. Furthermore, based on dynamic equilibria the active site formation includes monomer thus meaning that reaction order is between 1 and 2 relative to the monomer concentration.[48]

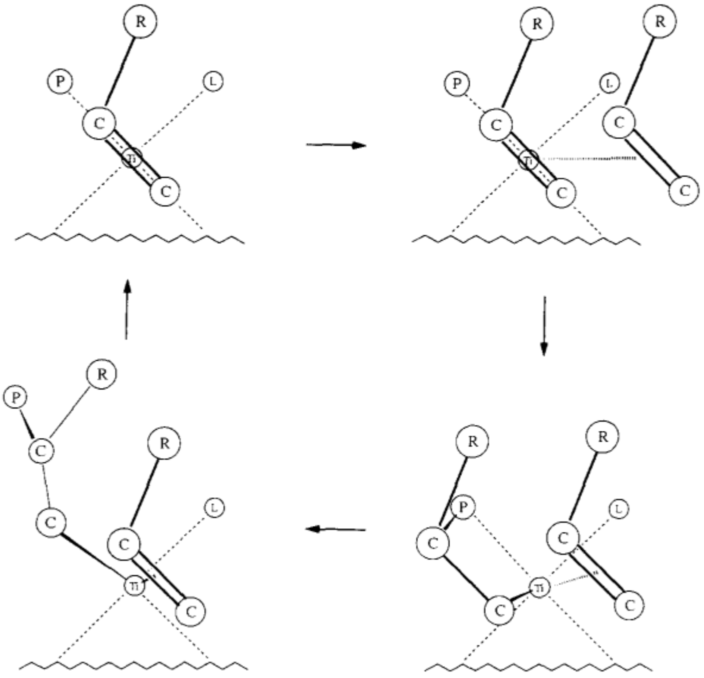

Figure 4. 3 Schematic representation of the four-stage trigger mechanism. L-inert ligand (here: chlorine, ester or an alkoxy group), P-polymer, R alkyl group of the alkene.[48]

It is important to say that some generalities observed in α-olefin polymerization[3] cannot apply to ethylene polymerization that demonstrates some peculiarities. Those peculiarities are: i) rate of ethylene homopolymerization is lower that it is expected based on results on ethylene copolymerization with other α-olefins, ii) presence of higher α-olefins increases the rate of ethylene polymerization,[49,50] while presence of H_2 causes decay in polymerization rate,[51] and iii) the reaction order in ethylene polymerization is significantly higher than 1 (reported values vary between 1.7 and 2), while in the case of other α-olefins is close to 1.[48,51] To meet this eccentricity of ethylene polymerization several mechanisms have been proposed,[44–47,52] but despite all the efforts and due to vast number of different ZN catalysts some questions are still open.

1.5 Spectroscopic methods as powerful tools for characterizing ZN catalysts

Being powerful tools for material characterization,[53] spectroscopic techniques were also employed to shed light on ZN catalysts.[22,23,25,29,54–62] So far, mainly ZN precatalysts and aged catalysts have been investigated with the accent on $MgCl_2$ and donor properties, from whom that of Ti sites were hypothesized. However, some recent studies successfully disclosed the properties of Ti sites in activated catalysts as well.[54,62,63] These results will be briefly summarized in this section, since they will be useful for interpreting the data collected during this thesis work. The following sections should not be intended as a summary of all the works present in the literature where spectroscopic methods are applied to ZN catalysts, they simply report a very short overview of the most significant and recent results relevant to this thesis work.

1.5.1 Electronic properties of ZN catalysts studied by DR UV-Vis, XAS and NEXAFS spectroscopies

Understanding of electronic properties of ZN catalysts is of big importance since it is well known that they influence monomer insertion into the Ti-R bond. To this aim, DR UV-Vis, Ti K-edge XAS and Ti $L_{2,3}$-edge NEXAFS spectroscopies are among the most useful techniques. Generally speaking, these three techniques are based on electronic excitations: the type of excited electrons is different, while the arrival state is the same.[64] In the case of Ti K-edge X-ray absorption (XAS) spectroscopy hard X-rays excite the Ti(*1s*) electrons, which are further promoted either to localized states (Ti(*3d*) levels or Cl(π) levels, X-ray adsorption near edge structure (XANES) region) or to the continuum (Extended X-ray adsorption fine structure (EXAFS) region).[24,63,65] Ti $L_{2,3}$-edge NEXAFS spectroscopy is based on excitation of Ti(*2p*) electrons to Ti(*3d*) levels by soft X-rays.[62,66] Finally, in DR UV-Vis spectroscopy two types of electron excitations can occur: i) LMCT from HOMO mainly centered on the ligand and LUMO mainly centered on Ti (UV region), and ii) d-d transitions between filled and empty orbitals of Ti, thus possible just for reduced Ti species (Vis region).[22,25,62,67] The results obtained by these three spectroscopic techniques are complementary to each other which helps in puzzling of the electronic properties of ZN (pre)catalyts.

Though the literature on ZN precatalysts and catalyst are very rich, just recently a comprehensive study dealing with electronic properties of both ZN precatalysts and catalysts have been published.[62] In the following, we will shortly present a few recent results, which might be useful for interpreting the data collected during this thesis work. Figure 4. 4 shows the DR UV-Vis spectra of three ZN precatalysts synthetized following different routes. Based on theory, it is expected that in all the precatalysts the oxidation state of Ti is 4+ and that Ti sites are 6-coordinated, mainly by Cl ligands.[62] Because d orbitals of Ti(IV) are empty, only LMCT from chlorine to Ti are observable in DR UV-Vis spectra. But, due to crystal field splitting of Ti d orbitals in dt_{2g} and de_g (separated by $\Delta_{CF}=10\Delta q$) the LMCT bands are split in two bands. Bands labeled with A are assigned to LMCT from Cl(π) to Ti(dt_{2g}), while those labeled with B are assigned to LMCT from Cl(π) to Ti(de_g). Without entering into the details, it was demonstrated that bands of type A are very sensitive to the local structure of Ti sites, while that is not the case for bands of type B.[62]

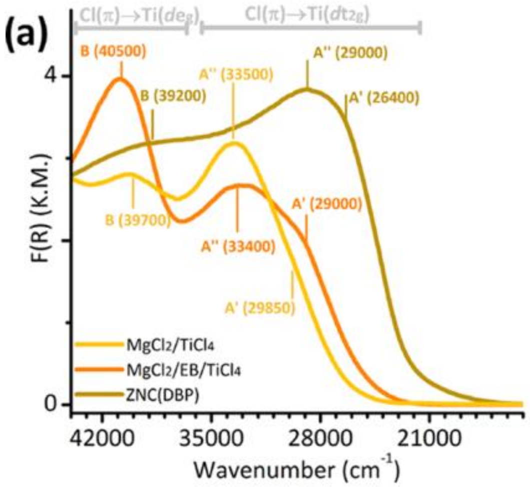

Figure 4. 4 DR UV-Vis spectra of three ZN precatalysts.[62] $MgCl_2/TiCl_4$ and $MgCl_2/EB/TiCl_4$ catalysts were prepared by titanation of high-surface ball-milled $MgCl_2$ with difference that in $MgCl_2/EB/TiCl_4$ catalyst ethylbenzoate was used as electron donor. In the case of chemically activated ZNC(DBP) precatalyst n-dibutyl phthalate was used as electron donor.

Figure 4. 5 reports the Ti $L_{2,3}$-edge NEXAFS spectra of the same ZN precatalysts, with assignment of the main bands. A complete analysis of the data is reported in the original paper. For the purpose of this thesis, it is sufficient to say that these data demonstrate that in all the three samples at least two different families of Ti sites are co-existing, which is concluded based on de_g peak splitting in two components.[62]

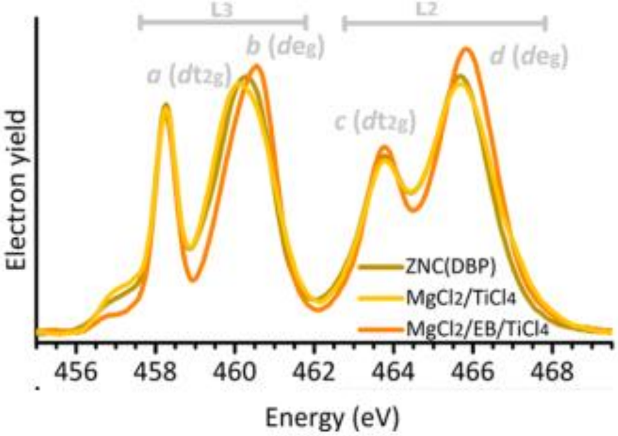

Figure 4. 5. Ti $L_{2,3}$-exge NEXAFS spectra of three ZN precatalysts already discussed in Figure 4. 4.[62]

Electronic properties of the ZN catalysts formed after activation of above discussed three ZN precatalysts with TEA (Al:Ti=2) were also assessed and significant changes in DR UV-Vis spectra relative to corresponding precatalysts were observed, as reported in Figure 4. 6. Namely, almost in all cases, absorption bands due to Cl(π) to Ti(dt_{2g}) shifted to higher energies by around 7000 cm^{-1}. This indicates that a fraction of Ti(IV) sites is reduced to Ti(III).[68] Also in the lower energy range (10000-20000 cm^{-1}) new bands relative to d-d transition appeared suggesting the presence Ti(III) sites. The position and intensity of these bands are indicative of the aggregation state of the Ti(III) sites (isolated sites or $TiCl_3$ clusters).[62]

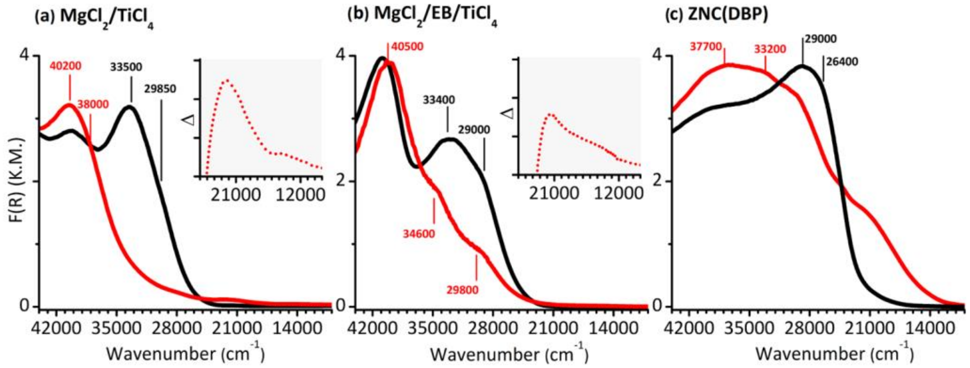

Figure 4. 6 DR UV-Vis spectra of a) $MgCl_2/TiCl_4$, b) $MgCl_2/EB/TiCl_4$ and c) ZNC (DBP) catalysts before (black spectra) and after (red spectra) activation with TEA (Al:Ti=2).[62]

The Ti $L_{2,3}$-edge NEXAFS spectra of the same catalysts are shown in Figure 4. 7. In both cases *a* and *b* bands decrease in the intensity and at the same time new bands, *a'* and *b'*, appear. Also this behavior is ascribed to reduction of a fraction of

Ti(IV) sites to Ti(III). The changes are less pronounced in the case of ZNC(DBP), which is due to formation of $TiCl_3$ clusters.[62]

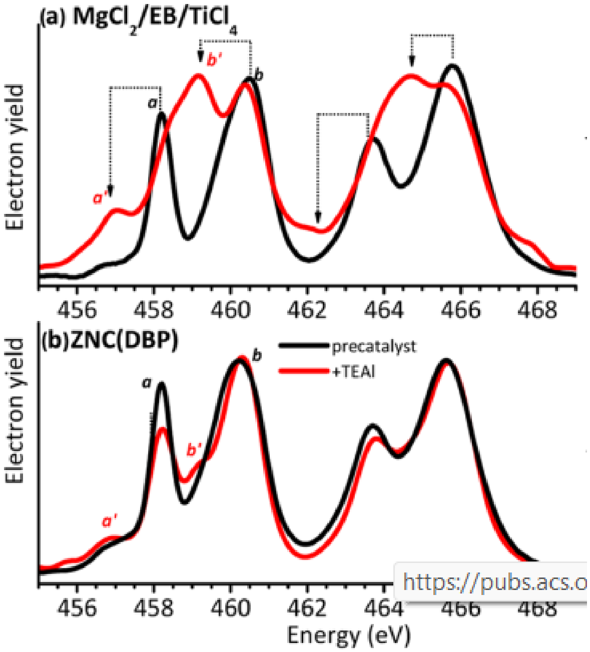

Figure 4. 7 Ti $L_{2,3}$-egde NEXAFS spectra of $MgCl_2$/EB/$TiCl_4$ (Part a) and ZNC (DBP) (Part b) precatalysts (black) after corresponding catalysts after activation with TEA in Al:Ti ratio 2 (red).[62]

Finally, XANES spectroscopy was also employed in the past to investigate heterogeneous ZN precatalysts and corresponding catalysts obtained after activation with TEA or trioctylaluminum (TOAl).[63] The spectroscopic fingerprints of the precatalysts drastically change upon activation with alkyl aluminums. Namely, the edge shifts to lower energy which corresponds to reduction of the Ti species. Changes were also observed in the pre-edge peak, which decreases in intensity and becomes more structured. Pre-edge features of activated ZN catalyst were observed to be overlapped with those of $TiCl_3$ clusters. However, it must be noted that in the XANES spectrum of $TiCl_3$ a sharp band at 4980 eV (with a shoulder at 4977 eV) is present, which is enhanced by multiple scattering contributions that are typical for crystalline materials.[63]

1.5.2 Local structure of ZN catalysts as revealed by EXAFS spectroscopy

Complementary data on the local structure of Ti sites can be obtained by using extended X-ray fine structure absorption spectroscopy (EXAFS), which is an element selective spectroscopic technique, whose potentials were shown for different transition metals grafted on silica surface.[22,69–72] It was reported that after activation of $MgCl_2$/ZN precatalyst with alkyl aluminum (TEA and TOAl) EXAFS spectra completely change, which indicate that activator has significant role in definition of local structure of both Ti sites and $MgCl_2$ phase, later also confirmed by X-ray powder diffraction (XRD).[25,63] By fitting the EXAFS results it was demonstrated that Cl ligands at two different lengths are present, at shorter ($Ti\text{-}Cl_{short}$) and longer ($Ti\text{-}Cl_{long}$) distances while coordination number were reported to be 5.1 and 5.3 for $MgCl_2$/ZN catalyst activated with TEA and TOAl, respectively (coordination number of $\beta\text{-}TiCl_3$ is 6).[63] Smaller coordination numbers relative to that of $\beta\text{-}TiCl_3$ indicate that there is at least one coordination vacancy in activated catalysts.[63]

1.5.3 Accessibility of surface sites in ZN catalysts as revealed by IR spectroscopy with CO as probe molecule

The accessibility of surface sites in ZN catalysts can be investigated by means of IR spectroscopy with probe molecules.[53] CO is often used as a probe molecule for ZN catalytic systems since it can distinguish between sites of different strength due to its very soft basic character.[53,73]

On the surface of bare $MgCl_2$ support and of ZN precatalyst, two types of Mg surface sites accessible to CO at 100 K were reported. The first ones are weakly acidic 5-coordinated Mg^{2+} sites (contributing at about 2160 cm^{-1}), while the second ones are strongly acidic 4-coordinated Mg^{2+} sites (contributing around 2180 cm^{-1}).[74] The Ti(IV) sites are not accessible by CO. In activated catalysts, Ti(III) sites become accessible to CO and this is manifested in IR spectra by the appearance of weak bands at about 2100 cm^{-1}.[29,54,58,75]

Beside coordinating to Ti(III) sites, CO can further insert into Ti-R bond with formation of Ti-acyl species.[76] Interestingly, CO is used in polyolefin industry to evaluate the number of active sites in ZN catalysts.[77–79] These is done by determining the amount of CO, that must be added to the gas-phase reactor to completely stop the polymerization reaction, from which amount of Ti sites is calculated. Ability of CO to insert into Ti-R bond was demonstrated by means of measurements with ^{13}CO[80] and by IR spectroscopy of CO adsorption over both model [54,61,74,81] and industrial[58] $MgCl_2$/ZN catalysts.

2. Silica-supported Ziegler-Natta precatalyst

2.1. Motivation

The object of this work is a silica-magnesium-titanium precatalyst provided by SABIC and synthetized according to patent US 4374753.[19] The synthesis procedure has been described in Chapter 2, Section 1.1, and consists in reacting dehydroxylated silica with a solution of a dibutyl magnesium, which later is reacted with $TiCl_4$. The aim of the work was to unveil the structure of the precatalyst at a molecular level, focusing the attention on both the $MgCl_2$ phase and the Ti sites, as a preliminary step to understand the properties of the catalyst after activation with aluminum alkyl.

Before starting the experimental investigation, we collected the few information present in the literature on similar precatalysts. Already in 1973, it was reported that addition of Grignard reagents in combination with an ether can reduce $TiCl_4$, to give soluble $TiCl_3 \cdot MgCl_2 \cdot$ether complexes.[82] Addition of alcohols can also modify the chemical structure of the obtained compound, and leads to a precatalyst that, once activated, produces polymers with low molecular weight.[19,83–85] Alcohol is often added when dibutyl magnesium is used as organometallic precursor; its primary role is to scavenge the alkyl aluminum compounds which are unavoidably present in dibutyl magnesium solutions, to increase their solubility in hydrocarbons. Indeed, alcohols react with alkyl aluminums to yield alkoxides.[27]

A comparison between alcohol-modified and alcohol-free silica-magnesium-titanium catalysts is reported in an early work of Hoff and co-workers, [83] who investigated the effect of increasing amount of 1-butanol on both reactivity and polyethylene properties, as well as on the catalyst composition. A summary of the results is reported in Table 4.1. Butanol-modified catalysts give lower molecular weight PE and have reactivities slightly greater than the alcohol-free catalysts.[83] Ti(III) and Ti(IV) amounts were measured by titration and it was demonstrated that the amount of Ti(III) in precatalyst decreases with increase of 1-butanol amount. However, neither amount of Ti(III) not that of Ti(IV) can be correlated with polymer melt index and reactivity. Within the same study 1-butanol effect on polymerization of ethylene was disclosed and best performing catalyst in ethylene polymerization was obtained for catalyst activated with TiBA (Al:Ti=5) and with BuOH/Mg ratio of 1, where 43% of Ti is trivalent while the rest it tetravalent. Although already in the precatalyst Ti(III) sites are present they are not active in ethylene polymerization, and activation with alkyl aluminum must be done before polymerization, which indicate that those Ti(III) are not alkylated and/or accessible to monomer.

Table 4.1. Ethylene polymerization with 1-butanol modified silica-magnesium-titanium catalysts.

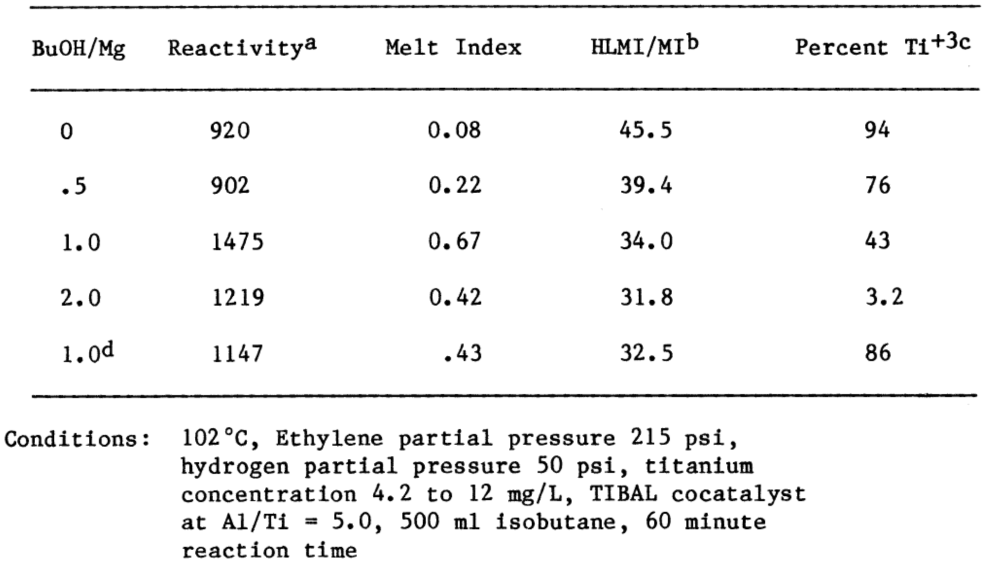

BuOH/Mg	Reactivity^{a}	Melt Index	HLMI/MI^{b}	Percent Ti^{+3c}
0	920	0.08	45.5	94
.5	902	0.22	39.4	76
1.0	1475	0.67	34.0	43
2.0	1219	0.42	31.8	3.2
1.0^{d}	1147	.43	32.5	86

Conditions: 102 °C, Ethylene partial pressure 215 psi, hydrogen partial pressure 50 psi, titanium concentration 4.2 to 12 mg/L, TIBAL cocatalyst at Al/Ti = 5.0, 500 ml isobutane, 60 minute reaction time

In this work we systematically investigated the properties of the best performing silica-magnesium-titanium precatalyst reported by Pullukat and Hoff, by means of a multi-technique approach comprising structural, electronic, and vibrational methods. Electronic properties were investigated by means of Ti K-edge XANES, Ti $L_{2,3}$-edge NEXAFS and DR UV-Vis spectroscopies, while local structure of Ti sites were disclosed by IR (both Mid- and Far-IR) and EXAFS spectroscopies. Two reference samples have been measured along with the precatalyst: a β-$TiCl_3$ polymorph kindly donated by Prof. V. Busico (University of Naples); a $MgCl_2$-supported ZN precatalyst synthetized at JAIST, which was object of an extensive characterization in our previous work.[86] The two reference samples will be referred to as β-$TiCl_3$ and ZNC(DBP), respectively.

2.2. Electronic properties: co-presence of Ti(IV) and Ti(III) sites

The Ti K-edge XANES, Ti $L_{2,3}$-edge NEXAFS and the DR UV-Vis-NIR spectra of the SiO_2/ZN precatalyst, compared to those of two reference compounds, are shown in Figure 4. 8. The discussion will start from the highest energy excitations, i.e., from Ti K-edge XANES spectra (Figure 4. 8A).

In the Ti K-edge XANES spectrum of the SiO_2/ZN precatalyst a weak pre-edge peak at 4968.8 eV is present (inset in Figure 4. 8A). This pre-edge peak is also present in the spectrum of ZNC(DBP), thus slightly shifted to higher energies. On the contrary, the same pre-edge peak cannot be found in the spectrum of β-$TiCl_3$. This peak is assigned to the Ti(*1s*)→Ti(*3pd*) localized transition and is allowed only for titanium sites with low symmetry and/or highly symmetric titanium sites but lacking the inversion centre (for example perfectly tetrahedral), while it is forbidden for titanium sites in an almost perfect octahedral symmetry (as in the case of β-$TiCl_3$). Presence of this pre-edge peak in the spectrum of the precatalyst suggests that most of the titanium sites do not have a perfect octahedral symmetry, while its low intensity (about 0.2 in normalized absorption) points toward high coordination numbers, more precisely to distorted 6-fold or 5-fold coordination.

"Double" absorption edge at 4974.7 and 4977.0 eV (evaluated as the maxima of the first derivative) can be observed in the edge region of the XANES spectrum of the SiO_2/ZN precatalyst. This is attributed to Ti(*1s*)→Cl(*4p*) dipole-allowed transitions.[22,63,65] XANES spectrum of β-$TiCl_3$ shows similar but more intense features at exactly the same position. The reason why these features are more intense for β-$TiCl_3$ is because they are enhanced by the multiple scattering contributions coming from collinear Cl-Ti-Cl scattering paths typical for Ti(III) sites in an almost perfect octahedral coordination. The position of these features confirms the presence of Ti(III) phase in the SiO_2/ZN precatalyst. The XANES spectra of two precatalysts are very similar to each other, but the edge peak is shifted for roughly 1.4 eV in the case of ZNC(DBP) precatalyst, which is expected when just Ti(IV) species are present. The significantly lower intensity of the Ti(*1s*)→Cl(*4p*) features in the XANES spectrum of the SiO_2/ZN precatalyst indicates that the multiple scattering contributions are limited.

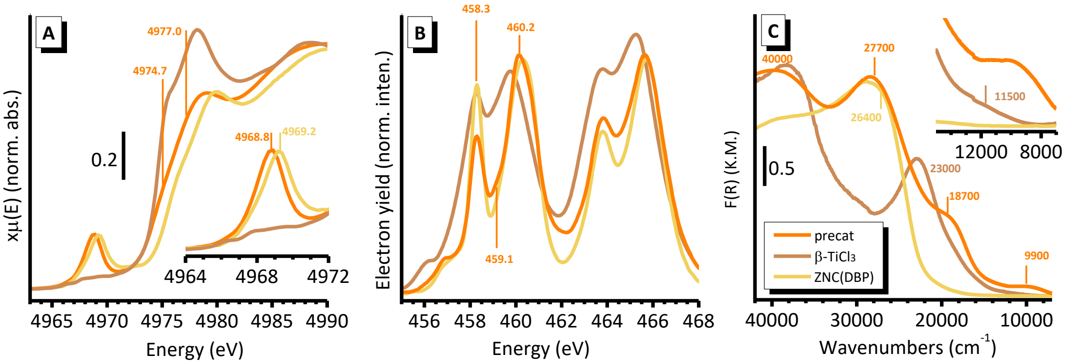

Figure 4. 8 . Normalized Ti K-edge XANES spectra (part A), normalized Ti $L_{2,3}$-edge NEXAFS spectra (part b) and DR UV-Vis-NIR spectra (part C) of the SiO_2/ZN precatalyst (orange), compared to those of β-$TiCl_3$ (brown) and ZNC(DBP) (yellow) reference samples. The inset in part A shows a magnification of the pre-edge peak, while that in part C highlights the region characteristic of d-d

transitions. The main features of each spectrum are also indicated (for the assignment refer to the main text) and the color code is the same in the three parts.

The Ti $L_{2,3}$-edge NEXAFS spectrum of SiO_2/ZN precatalyst is compared to those of reference samples in Figure 4. 8B. Hereby, it is important to note that the spectra were acquired in total electron yield (TEY) mode, which is highly surface sensitive (probing depth of few nm). In general, a Ti 2*p* NEXAFS spectrum originates from the $2p^63d^n \rightarrow 2p^53d^{n+1}$ electronic transition. The L_3-edge is due to the $2p_{3/2}$ excitations, and is better defined than the L_2-edge, which originates from the $2p_{1/2}$ excitations. The spectrum of the SiO_2/ZN precatalyst is very similar to that of ZNC(DBP), with two main differences. First one is that the peak associated to the d_{t2g} orbitals (at 458.3 eV) is less intense, as expected when a fraction of Ti(III) sites is present in the sample. In fact, for Ti(III) sites the low-lying d_{t2g} orbitals are already occupied by one electron, hence the probability for this electronic transition is lower than for a Ti(IV) site, where the d_{t2g} orbitals are totally empty. The second difference is an additional and weak peak observed in the spectrum of SiO_2/ZN precatalyst and centered between the two main ones, at about 459.1 eV, again indicating the presence of a fraction of Ti(III) species.[62]

Finally, the DR UV-Vis spectrum of the SiO_2/ZN precatalyst (Figure 4. 8C) features four main absorption bands, centred at about 10000, 19000, 27700 and 40000 cm^{-1}, which are responsible for the brownish colour of the sample.

- The intensity and position of the lowest energy absorption band, at 10000 cm^{-1}, indicate that it is due to a localized, Laporte forbidden, but spin allowed $t_{2g} \rightarrow e_g$ *d-d* transition for Ti(III) sites in a distorted octahedral symmetry.[68] A band as such low energies was never reported for isolated Ti(III) sites, but a very weak band at about 11500 cm^{-1} is observed in the spectrum of β-$TiCl_3$ (inset in Figure 4. 8C).
- The absorption band at slightly higher wavenumbers, 12000 cm^{-1}, was reported for hexahalotitanates, where the $TiCl_6^-$ anion is surrounded by different cations, while the band at around 19000 cm^{-1} was observed in the spectra of different O-bonded Ti(III) complexes.[87]
- The band centred at around 19000 cm^{-1} is also distinctive for a *d-d* transitions. However, in SiO_2/ZN precatalyst its intensity is extremely high since it approaches that of charge-transfer transitions. Similarly intense absorption bands occurring after the first spin-allowed transition and overlapping with other ligand-field bands up to the charge-transfer edge, have been reported for the α- and β-$TiCl_3$.[22,25,62,87] Just for the sake of

comparison, a band at comparable position, at 23000 cm^{-1}, was observed in the spectrum of β-$TiCl_3$. The most probable assignment of these band, taking into account both intensity and position, is that of inter-site hopping transitions of the type $2(3d^1)\rightarrow 3d^0+3d^2$, involving two Ti(III) sites bridged by a common chloride ligand.

- The last two bands appearing at highest energies and centred at 27700 and 40000 cm^{-1} are very similar to those observed in ZNC(DBP) and are assigned to ligand-to-metal Cl(π)→Ti($3dt_{2g}$) charge-transfer, suggesting the presence of monomeric Ti(IV) sites but in distorted octahedral geometry.[24,64,88]

To summarize, *the three electronic spectroscopies confirm the co-existence of two Ti phases in the SiO_2/ZN precatalyst*. *A fraction of the Ti sites are in the form of small Ti(III) clusters similar to β-$TiCl_3$.* These Ti(III) sites are bridged by common chloride ligands, thus are able to communicate each other by exchanging a *d* electron. It is worth mentioning that, according to the pioneering works of Natta and co-workers,[89] the chemical composition of the $TiCl_3$ phase obtained upon reaction of $TiCl_4$ with alkyl aluminum compounds strongly depends on the molar ratio: low Al:Ti mole ratio, as in the present case, should favour amorphous $TiCl_3$ products containing appreciable amounts of aluminium. *A remaining part of Ti sites is not reduced and accounts for Ti(IV) sites in a distorted octahedral geometry*.

2.3. Local structure

The local structure of Ti sites in SiO_2/ZN precatalyst was investigated by IR (both in Mid- and Far-IR regions) and EXAFS spectroscopies. IR spectra of SiO_2/ZN precatalyst and reference samples are shown in Figure 4. 9. Mid-IR spectrum of the SiO_2/ZN precatalyst is dominated by vibrational features of silica (Figure 4. 9A). However, absorption bands assigned to the vibrational modes of alkyl chains, both in the stretching region (2000-2800 cm^{-1}) and in the bending region (1500 – 1350 cm^{-1}) can be observed. More in detail, the band at about 2970 cm^{-1} is due to the presence of -O-R species, likely -OBu species. Broad bands at 3660, 3500 and 3250 cm^{-1} indicate the presence of a few H-bonded -OH groups,[90] that remained on silica surface despite it was chemically dehydroxylated. Both -OBu and -OH surface species are clearly a consequence of the synthesis procedure, during which 1-butanol was added.[19]

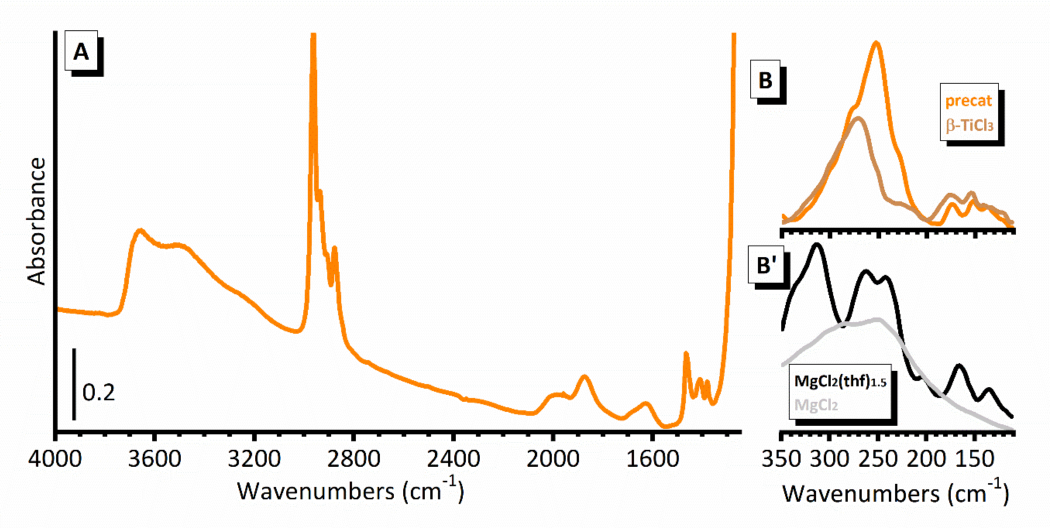

Figure 4. 9 Mid-IR (part A) and Far-IR (parts B and B') spectra of the SiO_2/ZN precatalyst (orange), compared to those of β-$TiCl_3$ (dark yellow), $MgCl_2(thf)_{1.5}$ (black) [25] and ball-milled $MgCl_2$ (gray)[17] reference samples.

In the Far-IR region (Figure 4. 9B and B'), the only region of transparency is below 350 cm^{-1}, because at higher wavenumbers vibration of silica framework are so intense to saturate the spectrum. The spectrum of the SiO_2/ZN precatalyst is characterized by a very narrow band centred at 252 cm^{-1}, with a tail at 277 cm^{-1} and three weak bands in the 210 - 120 cm^{-1} region. The latter features are very similar to those observed in the spectrum of β-$TiCl_3$ (brown spectrum in Figure 4. 9B), which is very well in agreement with DR UV-Vis results. The rather narrow band positioned at 252 cm^{-1} falls in a region typical for v(Mg-Cl_{bridge}) vibrations that involve bridging chlorine species. For better understanding, in Figure 4. 9B' are represented the Far-IR spectra of two reference compounds, $MgCl_2(thf)_{1.5}$ molecular complex (black spectrum)[25] and a ball-milled $MgCl_2$ sample characterized by crystals of nanometric dimension (grey spectrum).[17] As it can be appreciated from the Figure 4. 9B', the full-width-at-half-maximum of the v(Mg-Cl_{bridge}) band is very narrow for the molecular complex, while the same vibration for bulk $MgCl_2$ gives rise to a very broad band which stretches in the whole 350 – 140 cm^{-1} region. In the spectrum of $MgCl_2(thf)_{1.5}$ a narrow band centred at 312 cm^{-1} can be observed, and it is assigned to the v(Mg-$Cl_{terminal}$) vibration of terminal chlorine species.

Thus, Far-IR spectroscopy indicates that t*he $MgCl_2$ phase in the precatalyst has a molecular character*, pretty similar to that of $MgCl_2(thf)_{1.5}$ complex, where bridged Mg-Cl-Mg chlorine species dominate over the terminal Mg-Cl ones. Most probably, these molecularly dispersed $MgCl_2$ species are *stabilized by both* *adsorbed $TiCl_x$ and surface butoxide groups that are behaving as capping functional groups (that binds $MgCl_2$ and $TiCl_x$ phases).*

Ti K-edge EXAFS spectroscopy, which is element selective, allows us to clarify which is, in average, the local structure of the titanium sites. Figure 4. 10A shows the modulus of the Fourier-Transformed k^2-weighted EXAFS function of the SiO_2/ZN precatalyst, compared to those of β-$TiCl_3$ (divided by a factor of 3) and ZNC(DBP) references, while Figure 4. 10B shows the corresponding imaginary parts. It can be observed that the spectra of the two precatalysts are much weaker than that of crystalline β-$TiCl_3$, for roughly 1/3. This cannot be explained just considering smaller coordination numbers in the titanium coordination sphere (which would mean less than 3 ligands per each titanium sites) and/or a reduced dimensionality of the titanium phase. A similar behaviour was previously reported for both unsupported and silica-supported ZN precatalysts synthetized from tetrahydrofuranate precursors,[22,24,25,63,65] and explained in terms of the presence in the titanium coordination sphere of several ligands at similar coordination distances, whose contributions are at least partially out-of-phase.

Another relevant observation is that in the spectrum of the SiO_2/ZN precatalyst two peaks at 1.35 and 2.07 Å (phase-uncorrected) separated by a dip can be observed. This is oppositely to what was observed in the spectrum of β-$TiCl_3$, where a single intense peak at 1.93 Å is present. Intermediate behaviour of the spectrum of ZNC(DBP) was observed, since it shows a dominant peak at 1.74 Å, with a shoulder at 1.19 Å, latter better visible in the imaginary part. These differences clearly indicate that the local structure around the titanium sites is not the same in the three samples.

A rigorous fit of the EXAFS signal for the SiO_2/ZN and ZNC(DBP) precatalysts is complicated due to combination of several factors: i) the relatively short k-range that can be safely used in the analysis, ii) the co-presence of several ligands in Ti coordination sphere, that, however, contribute at similar distance but are partially out-of-phase, and, iii) the co-presence of at least two structurally different titanium phases which apply just for SiO_2/ZN precatalyst and was previously demonstrated. Details on the EXAFS data analysis are reported in Ref.[91]. Here we will just summarize the main results.

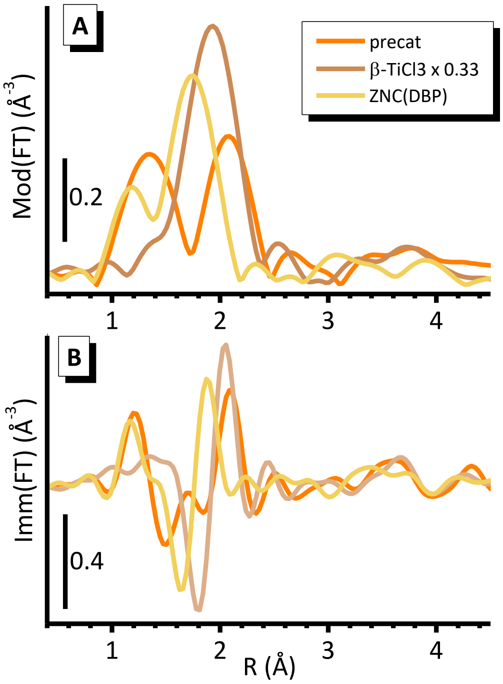

Figure 4. 10 k_2-weighted |FT| (part A) and Imm(FT) (part B) of the EXAFS function for the SiO_2/ZN precatalyst, compared to those of β-$TiCl_3$ and ZNC(DBP) as references. It is worth noticing that the spectrum of β-$TiCl_3$ has been divided by three for a better comparison.

In Figure 4. 11 the two best fits and the most relevant scattering paths contributing to the fit of EXAFS spectra of SiO_2/ZN precatalyst are represented. The fraction of Ti(III) sites that is present in the form of $TiCl_3$ clusters was determined by fitting the 2.2 – 5.0 Å region. This region is dominated by the multiple scattering (MS) contributions of collinear Cl-Ti-Cl scattering paths. It accounts for 41% of the total Ti sites and it is in good agreement with earlier report,[83] where the percentage of Ti(III) in a precatalyst with similar composition was estimated to be 43%. The first shell average Ti-Cl distance for this Ti(III) phase is that typical of $TiCl_3$ polymorphs (2.48 ± 0.02 Å). Debye-Waller factor (0.010 ± 0.008 Å^2) is slightly larges which is probably induced by the small size and heterogeneity of the clusters.

Subsequently, the structural parameters related to the $TiCl_3$ phase were fixed, and a first shell fit of the remaining 59% of titanium was attempted. Good fits were obtained only upon including three different Ti-Cl contributions at short, medium, and long distances (Cl_s, Cl_m and Cl_l, respectively). A similar structure was calculated for Ti(IV) sites in models of $TiCl_4$-capped $MgCl_2$ nanoplates. For those systems six chlorine ligands around Ti(IV) sites can be classified in three couples with different Ti-Cl distances, being the terminal chlorine species at shorter distance than the bridged ones.[92] An equally good fit was obtained by considering 5 chlorine ligands and 1 oxygen. These results are compatible with what discussed so far and suggest that, *beside the highly dispersed $TiCl_3$ phase, the remaining of the titanium (60%) is present in the form of monomeric Ti(IV), with a distorted octahedral symmetry determined mainly by chlorine ligands, but possibly also by one butoxide ligand.*

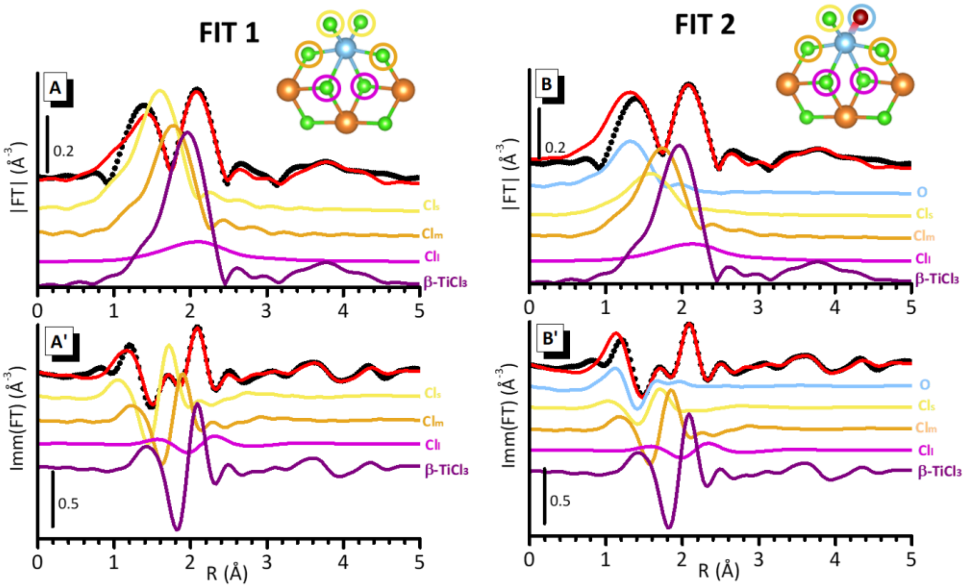

Figure 4. 11 Analysis of the EXAFS spectrum for the SiO_2/ZN precatalyst. Parts A and A': FIT1, which includes the contribution of only chlorine ligands. The experimental phase-uncorrected FT of the $k^2\chi(k)$ EXAFS function is shown in modulus and imaginary parts (dotted curves in parts A and B respectively), overlapped to the result of the fit (red lines). The relevant scattering paths are also shown, vertically translated for clarity. Parts B and B': same as parts A and A', for FIT2, which includes the contributions of one oxygen ligand instead of a chlorine at short distance. The inset in part A shows the model used in FIT1, as reported in Ref. [92], while that in part B has been obtained from the previous one upon substituting a Cl_s ligand with an oxygen (of a butoxide moiety).

2.4. Accessibility of the Ti sites

The accessibility of Ti sites in the SiO_2/ZN precatalyst was accessed by means of probe molecule IR spectroscopy. CO was chosen as a probe molecule due to its soft basic character and ability to discriminate between surface sites of different acidity.[53,73] Moreover, CO is widely used for characterization of high-surface area materials,[53,93,94] and it's potential as a probe molecule was demonstrated also in the field of olefin polymerization catalysis.[17,54,55,58,74,75,95]

Figure 4. 12 shows IR spectra of CO adsorbed on SiO_2/ZN precatalyst at 100 K. Spectra are shown after subtraction of the spectrum collected prior CO was dosed and as function of CO coverage (θ). The spectrum at maximum CO coverage ($θ_{max}$) is characterized by three main features that behave differently upon lowering CO pressure.

- Band at 2136 cm^{-1} is the most intense one and at the same time the first one to disappear upon lowering CO pressure, indicating weak interactions. Hence, this band is assigned to physisorbed CO.[93]
- Next band, at 2155 cm^{-1} also goes down rapidly with decrease of CO pressure, and it is attributed to CO in interaction with very weak Lewis acid sites (LAS).[96] A band at comparable position was observed when CO was adsorbed on model $MgCl_2$ and was assigned to 5-fold coordinated Mg^{2+} sites.[56,74]
- Finally, the band centred at 2181 cm^{-1} is the most resistant to lowering CO coverage, which indicates strong interaction of CO. This band can be assigned to CO in interaction with stronger LAS, more specifically, 4-fold coordinated Mg^{2+} sites.[56,74]

Importantly, no band was observed around 2100 cm^{-1} where band ascribable to CO in interaction with Ti(III) sites should fall. This suggests that Ti(III) sites present in the precatalyst are not alkylated and/or not accessible to CO.

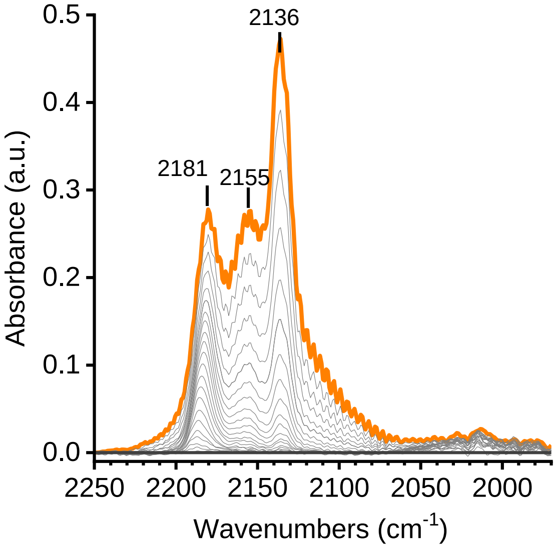

Figure 4. 12 IR spectra of CO adsorbed at 100 K on the SiO_2/ZN precatalyst as a function of CO coverage ϴ (from $ϴ_{max}$ in orange colour to zero in dark grey). The spectra are shown after subtraction of the spectrum prior the dosage of CO in ν(C≡O) region.

3. Silica-supported Ziegler-Natta catalyst

3.1. Motivation

In this last part of the work, we deepen the investigation of our silica-magnesium-titanium system, by studying the effect of the aluminium-alkyl activator on the molecular structure of the catalyst. In particular, we focused our attention on the structural and electronic properties of the Ti sites in the activated catalyst as a function of both the concentration and the type of the activator. Moreover, we studied the accessibility of the activated Ti sites to carbon monoxide, which was selected as insertion probe to mimic the interaction of the catalyst with the monomer. Finally, we investigated the behaviour of the catalyst in action by studying the kinetics of gas phase ethylene polymerization in very mild conditions (comparable to those used for the spectroscopic measurements). The whole set of data offer an unprecedent view on the spatial distribution of the different Ti phases in the catalyst particles.

3.2 Electronic properties

The electronic properties of the Ti sites in the SiO_2/ZN catalyst activated with different amounts of TEA were investigated by means of different spectroscopic techniques. Figure 4. 13 shows the Ti K-edge XANES, the Ti $L_{2,3}$-edge NEXAFS and the DR UV-Vis spectra of the SiO_2/ZN precatalyst and of activated catalysts with different amounts of TEA.

The most relevant changes observed upon addition of TEA to the SiO_2/ZN precatalyst Ti K-edge XANES spectra (Figure 4. 13A), are the following:

- a gradual shift of the edge to lower energy, of about 0.7 eV for Al:Ti=1.0, of 1.0 eV for Al:Ti=3.25, up to about 2.0 eV for Al:Ti=10.0;
- an attenuation in the intensity and a shift in energy of the pre-edge peak (inset in Figure 4. 13A).

Up to 3.25 eq. of TEA, the changes observed in the XANES spectra indicate that a fraction of the Ti(IV) in the SiO_2/ZN precatalyst are reduced to Ti(III) species. At the highest Al:Ti ratio over-reduction of a fraction of the Ti sites to Ti(II) takes place. This process most probably involves the $TiCl_3$ clusters that are already present in the SiO_2/ZN precatalyst.

The $L_{2,3}$-edge NEXAFS spectrum of the SiO_2/ZN catalyst activated with 3.25 eq. of TEA is very similar to that of the SiO_2/ZN precatalyst (Figure 4. 13B). The only relevant difference is that the peak at 458.3 eV, attributed to the electronic transition from the Ti $2p_{3/2}$ orbitals to the Ti d_{t2g} orbitals, slightly decreases in intensity. This suggests that a fraction of Ti(IV) is reduced to Ti(III) sites. However, the observed changes are fewer than it was expected for the reduction of a substantial fraction of Ti(IV) to Ti(III), as indicated by XANES. We anticipate that this is probably due to the surface-sensitivity of NEXAFS spectroscopy when acquired in TEY mode, which implies that only the surface of the catalyst particles is probed, and not the interior.

Further, the electronic properties of SiO_2/ZN catalyst activated with different amounts of TEA, starting from very low (Al:Ti=0.65) to moderate (Al:Ti=3.25), were assessed by means of DR UV-Vis spectroscopy (Figure 4. 13C). Based on the spectral behavior, activation can be divided in two steps depending on TEA amount:

- At lower TEA amount (up to 1 eq.) reduction of a fraction of monomeric Ti(IV) takes place. This is manifested by a decrease in intensity of the band at 27700 cm^{-1} which was assigned to LMCT from Cl(π) to Ti(d_{t2g}) involving Ti(IV) sites in a distorted octahedral geometry. Concomitantly, the band at around 40000 cm^{-1} increases in intensity, suggesting that part of Ti(IV) is reduced to Ti(III). These two observations are very well in agreement with electronegativity rules of Jorgensen[68] saying that upon reduction of Ti(IV) to Ti(III) LMCT bands shifts upward for about 7000 cm^{-1}.
- With increasing TEA amounts new bands can be observed at around 22000 and 15500 cm^{-1}, the second band with pronounced tail at lower energies. These two band are very similar to what was observed for α-$TiCl_3$, and thus are assigned to inter-site hopping transitions of the type $2(3d^1) \rightarrow 3d^0 + 3d^2$ involving two Ti(III) sites bridged by a common chlorine ligand.[62,97]

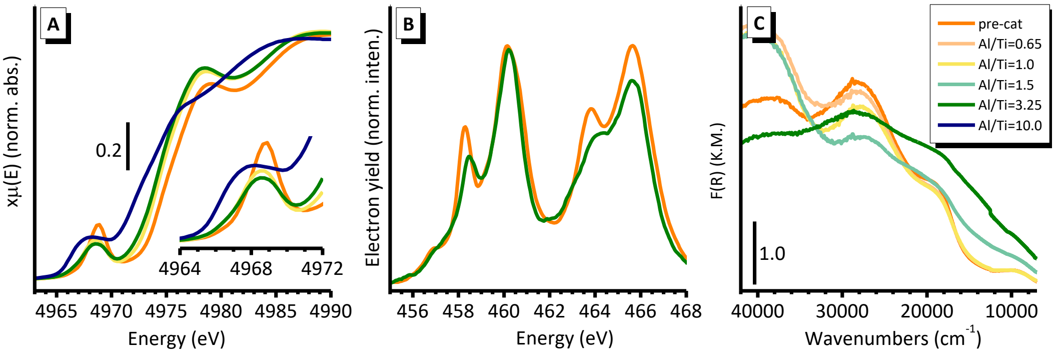

Figure 4. 13 Part A) Normalized Ti K-edge XANES spectra, Part B) normalized Ti $L_{2,3}$-edge NEXAFS spectra, and Part C) DR UV-Vis-NIR of the SiO_2/ZN precatalyst (orange), and of the corresponding catalysts after activation with TEA in different amounts (expressed in terms of Al:Ti ratio). The inset in part A shows a magnification of the pre-edge peak.

Above discussed results demonstrate that *addition of small amounts of TEA (below 1.0 eq.) to the SiO_2/ZN precatalyst leads to the reduction of a fraction of the Ti(IV) sites to isolated Ti(III) species. At higher TEA amounts (above 1.0 eq.) the reduction of the Ti(IV) sites is completed, but also the aggregation of Ti(III) species to clusters having electronic properties similar to those of the α-$TiCl_3$ polymorph occurs. Moreover, eventually over-reducing a fraction of the Ti species to Ti(II) cannot be excluded.*

As far as the location of these different Ti(III) species on the catalyst particles is concerned, it is important to notice that the invariance of the Ti $L_{2,3}$-edge NEXAFS spectrum to TEA addition suggests that *the $TiCl_3$ clusters (both those originally present in the precatalyst and those induced by activation with TEA) are mainly formed at the exterior of the catalyst particles*. In fact, as demonstrated in our previous work,[62] the experimental Ti $L_{2,3}$-edge NEXAFS spectra of $TiCl_3$ polymorphs are very similar to the spectrum of highly dispersed Ti(IV) chloride species. Hence, in the presence of $TiCl_3$ clusters at the exterior of the catalyst particles, the Ti $L_{2,3}$-edge NEXAFS spectrum collected in TEY mode will be invariably dominated by their signals, making virtually impossible to reveal the reduction of isolated Ti(IV) sites.

3.3 Local structure of the Ti sites

Figure 4. 14 shows the Fourier-Transformed k^2-weighted EXAFS function of the SiO_2/ZN catalyst activated with increasing amounts of TEA, in both Modulus (part A) and Imaginary (part B) parts. When compared with the spectrum of the SiO_2/ZN precatalyst, addition of 1.0 and 3.25 eq. of TEA causes the decrease in intensity of the first peak (centred at ca. 1.35 Å, phase-uncorrected) and the increase of the second one (centred at ca. 2.07 Å, phase-uncorrected). As discussed in the previous section, these two peaks are the result of the overlap of three types of chlorine ligands and/or 1 oxygen ligand, characterized by different bond distances. The observed changes indicate that after activation of TEA the local structure around the Ti sites is significantly modified. However, the data analysis is very complex due co-existence of more than two Ti phases, which makes the extraction of meaningful quantitative results from the EXAFS data analysis. These phases are: 1) $TiCl_3$ clusters similar to β-$TiCl_3$ polymorph (the same are already present in the precatalyst); 2) residual monomeric Ti(IV) sites with a very heterogeneous local structure (already present in the precatalyst); 3) isolated Ti(III) sites deriving from the reduction of the monomeric Ti(IV) sites; 4) $TiCl_3$ clusters similar to the α-$TiCl_3$ polymorph, whose formation is promoted by amounts of TEA larger than 1.0 eq.

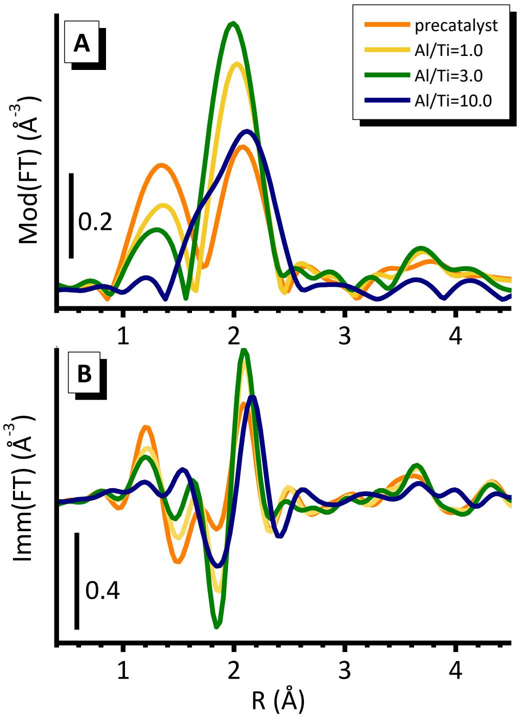

Figure 4. 14 k^2-weighted |FT| (part A) and Imm(FT) (part B) of the EXAFS function for the SiO_2/ZN catalyst, and of the corresponding catalyst after activation with TEA in different amount (expressed in terms of Al:Ti ratio).

Addition of 10 eq. of TEA, which corresponds to over-reduction of the Ti sites as determined by the XANES region, causes a complete change in the EXAFS spectrum, not only in the first shell region, but also at longer distances, where the signal due to the multiple scattering contributions of collinear Cl-Ti-Cl paths is totally disrupted. This spectrum confirms that over-reduction deeply involves the $TiCl_3$ clusters already present in the SiO_2/ZN precatalyst.

3.4 Accessibility of surface sites: IR spectroscopy of CO adsorbed at 100 K

Figure 4. 15 shows the FT-IR spectra (in the ν(C≡O) region) of CO adsorbed at 100 K on the SiO_2/ZN precatalyst (a), and on SiO_2/ZN catalyst activated with 1.5 eq. of TEA (b), 2.5 eq. of TEA (c) and 3.25 eq. of TEA (d). All the spectra are shown after subtraction of the spectrum collected before CO dosage, and as a function of the CO coverage (θ). Since the results obtained for the SiO_2/ZN precatalyst were discussed in previous section, and here are shown just for the sake of comparison, discussion will start from the catalyst activated with 1.5 eq. TEA.

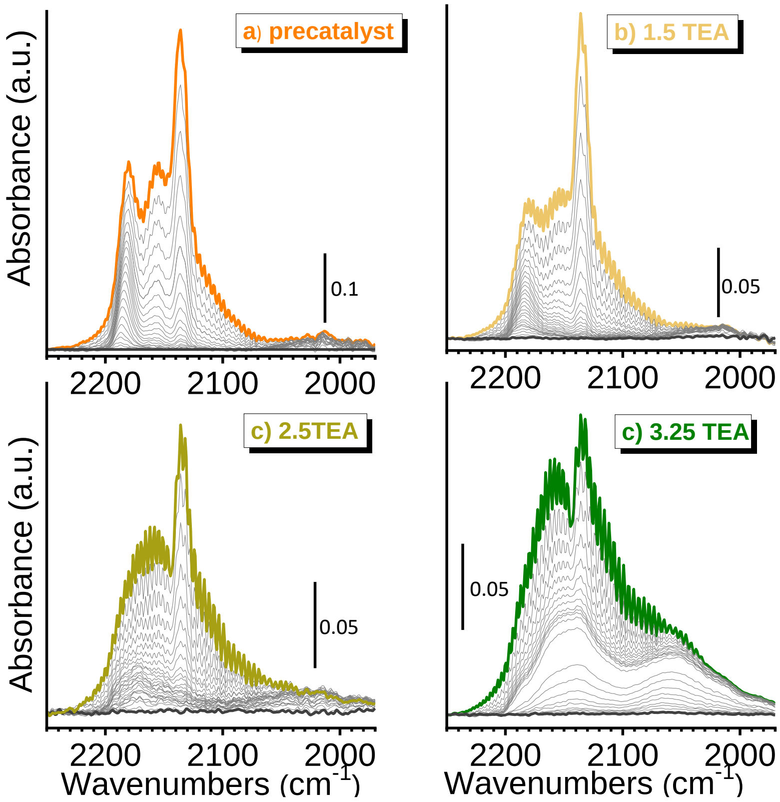

Figure 4. 15 IR spectra (in the ν(C≡O) region) of CO adsorbed at 100 K on the SiO_2/ZN precatalyst (a) and on SiO_2/ZN catalysts activated with 1.5 eq. TEA (b), 2.5 eq. TEA (c) and 3.25 eq. TEA (d) as the function of CO coverage. The spectra are shown after subtraction of the spectrum prior the dosage of CO.

The spectrum of SiO_2/ZN catalyst activated with 1.5 eq TEA at maximum CO coverage is very similar to that of the precatalyst, with three main bands at 2136, 2155, and 2181 cm^{-1}, which have been already ascribed to physisorbed CO,[93]and to CO in interaction with 5-fold and 4-fold coordinated Mg^{2+} sites, respectively.[56,74] These latter two bands are relatively less intense than in the precatalyst.

In the spectra of the SiO_2/ZN catalysts activated with 2.5 and 3.25 eq. of TEA, only the band at 2136 cm^{-1} remains well distinguished, while at higher wavenumbers a very broad band takes the place of the two narrow bands discussed above, detailed with two components at around 2166 and 2146 cm^{-1} in the spectra of the SiO_2/ZN catalyst activated with 3.25 eq. of TEA. The assignment of this broad envelope of bands is not straightforward, even though the most probable explanation is to associate them to CO adsorbed at residual under-coordinated Mg^{2+} cations. In addition, a broad band is also observed at 2065 cm^{-1}, very well evident for the catalyst activated with 3.25 eq of TEA. This band is assigned to CO adsorbed on Ti^{3+} species.[54,58,75] A band at similar position, 2076 cm^{-1}, was reported for CO adsorbed on a model $MgCl_2$-supported ZN catalyst,[54] and at a slightly higher wavenumbers (2091 cm^{-1}) for CO adsorbed on an industrial $MgCl_2$-supported ZN catalyst.[58]

3.5 Insertion of CO into the Ti-R bonds

Since it is known that CO can insert into the Ti-R bond,[54,76,98,99] at the same way as the monomer does, the experiments of CO adsorption on ZN catalysts activated with different amounts of TEA were also performed at 300 K. Figure 4. 16 shows the IR spectra of CO adsorption on SiO_2/ZN catalyst activated with 3.25 eq. TEA in the ν(C≡O) (Figure 4. 16A) and ν(C=O) (Figure 4. 16B) regions, respectively. Spectra are shown after subtraction of the spectrum collected before CO was dosed and as function of time, starting from black spectrum (1 min) to olive spectrum (30 min).

Starting the discussion from the ν(C≡O) region (Figure 4. 16A), the spectra are characterized by three bands centered at 2137, 2065 and 2022 cm^{-1}. The first two bands are present since the beginning and well-reproduce the experiment done at 100 K and consequently have the same assignment. The last band centered at 2022 cm^{-1} grows in intensity over time, and it is assigned to CO in interaction with Ti(III) sites, that are evidently less accessible than those characterized by the band at 2065 cm^{-1}.

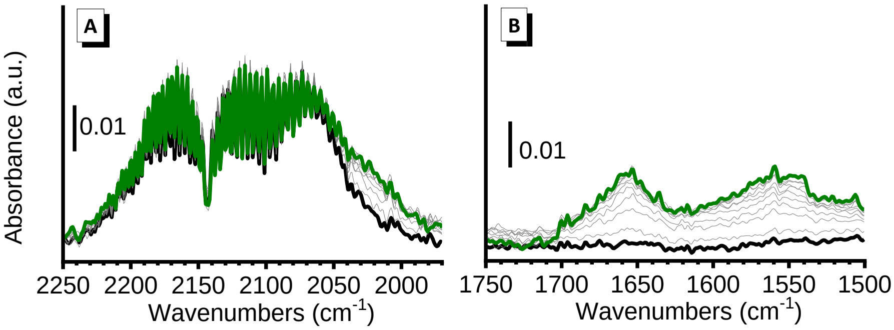

Figure 4. 16 IR spectra of CO adsorption on SiO_2/ZN catalyst activated with 3.25 eq. TEA in ν(C≡O) region (left) and ν(C=O) region (right). The spectra are shown after subtraction of spectrum collected before CO addition and as function of time.

In the ν(C=O) region (Figure 4. 16B) two bands centered at 1658 and 1548 cm^{-1} grow in intensity over time. Both bands are assigned to Ti-acyl species that are formed upon CO insertion into the Ti-R bond. This agrees with the literature where it is reported that Ti-acyl derivatives absorb between 1620 and 1470 cm^{-1}, depending on the type of X or R groups, and on the η^2-coordination to the Ti sites: the larger the η^2-coordination, the lower ν(C=O).[98,99]

The same experiment was systematically performed on SiO_2/ZN catalysts activated with increasing amounts of TEA, starting from 1.5 eq. TEA to 4.0 eq. TEA. Figure 4. 17 shows the IR spectra of CO adsorbed at 300 K on SiO_2/ZN catalysts activated with different amounts of TEA as a function of time (from black spectrum (1 min) to spectrum in corresponding color (60 min)). For the sake of clarity, the spectra are shown after subtraction of the CO roto-vibrational profile, in ν(C≡O) (top) and ν(C=O) (bottom) regions and for easier comparison spectra are normalized to the optical thickness of the pellet. Irrespective of the amount of TEA:

1) *CO detects two different types of Ti(III) sites, the former coordinates CO immediately (band at 2065 cm^{-1}), while the other needs more time to coordinate CO (band at 2022 cm^{-1}).*
2) *Two types of Ti-acyl species are formed upon CO insertion into Ti-R bond, differing in the extent of η^2-coordination to Ti*. However, at this point it is very difficult to state if these two types of acyl species are formed after CO coordination to two types of Ti(III) sites or just one of them.

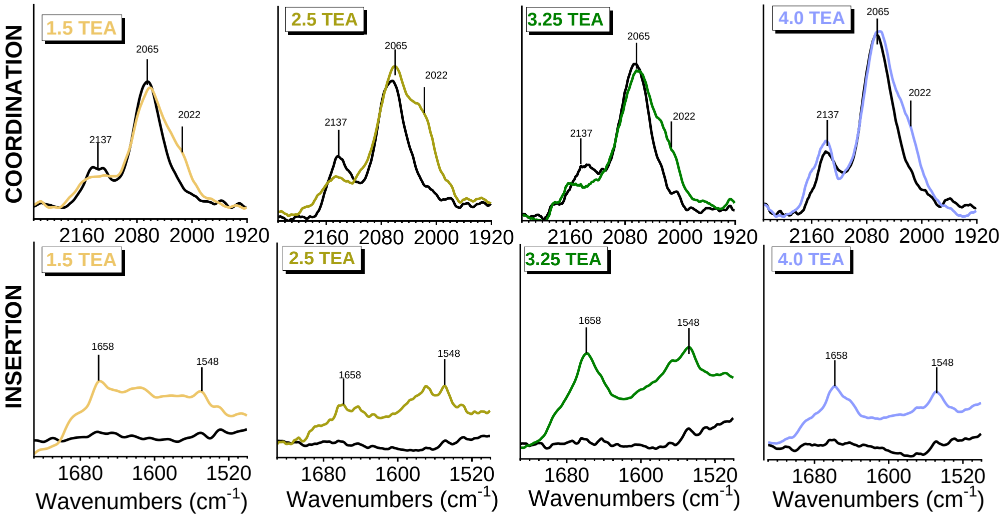

Figure 4. 17 IR spectra of CO adsorbed at SiO_2/ZN catalysts activated with increasing amounts of TEA in ν(C≡O) (top) and ν(C=O) (bottom) regions. Spectra are shown after normalization to the optical thickness of the pellet and as function of time starting from black spectra (1 min) to spectra in corresponding color (60 mins). The spectrum of gaseous CO was subtracted in all the spectra for clarity.

It is important to note that a clear correlation between TEA amount and amount of CO coordinated to Ti(III) sites and/or inserted into the Ti-R bond was not found.

To understand whether the Ti(III) sites detected by CO are active in ethylene polymerization or not, CO adsorption at 300 K was done before and after ethylene polymerization on the SiO_2/ZN catalyst activated with 3.25 eq. TEA and results are shown in Figure 4. 18. After contact with ethylenefor a short time, the Ti(III) sites are no longer accessible to CO, and as consequence very few acyl species are observable. It is hard to say if this is due to real employment of Ti(III) sites in ethylene polymerization or due to formation of thick layer of PE that restricts the access of CO to Ti(III) sites.

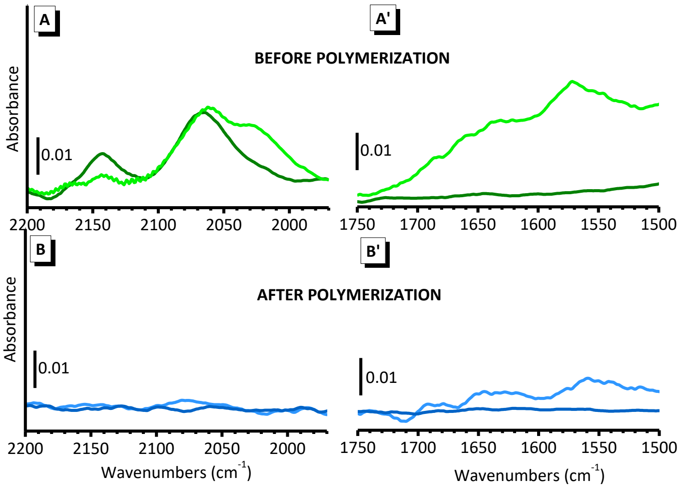

Figure 4. 18 IR spectra of CO adsorbed before (top) and after (bottom) ethylene polymerization over SiO_2/ZN catalyst activated with 3.25 eq. TEA. Spectra are shown in ν(C≡O) region (parts A and B) and ν(C=O) (parts A' and B') and as function of time (from dark green and dark blue (1min) to light green and light blue (60 min)). The spectrum of gaseous CO was subtracted in all the spectra for clarity.

3.6 Adsorption of d-acetonitrile at 300 K and insertion into the Ti-R bond

Since d-acetonitrile demonstrated its potential as a probe molecule for SiO_2/MAO/metallocene-based catalytic systems, the same approach was used to investigate SiO_2/ZN catalysts. Figure 4. 19 shows the time resolved IR spectra of d-acetonitrile adsorbed at 300 K on the SiO_2/ZN catalyst activated with 3.25 eq. TEA. It must be noted that spectra for all activated catalysts look very similar and that is the reason why just one of them is shown. Additional experiments were performed on SiO_2/TEA and SiO_2/ZN precatalyst to confirm that no d-acetonitrile insertion occurs. As can be seen from the Figure 4. 19, new bands in the 2480-1450 cm^{-1} region appear immediately after d-acetonitrile dosage. Since all bands were discussed in detail in previous chapter, herein the discussion will be shortened.

- The band at 2108 cm^{-1} is not analytically relevant, and has been taken as an indication of the total amount of d-acetonitrile present on the sample;[100,101]
- The most intense band around 2310 cm^{-1} is ascribed to v(C≡N) of d-acetonitrile coordinated to Lewis acid sites, both Al(III) sites in TEA[57] and coordinatively unsaturated Ti sites. This band will be not used in further analysis since the amount of TEA vary for each experiment, so it is hard to distinguish between contributions coming from TEA and coordinatively unsaturated Ti site.
- The band at 1628 cm^{-1} is assigned to the v(C=N) vibration of aza-alkenylidene derivatives of Ti formed upon d-acetonitrile insertion into Ti-R bond.[102–104] It is interesting to observe that this band is much broader than that observed upon insertion of d-acetonitrile into the M-CH_3 bond in metallocene-based catalysts, which is a direct consequence of the much higher heterogeneity of sites.

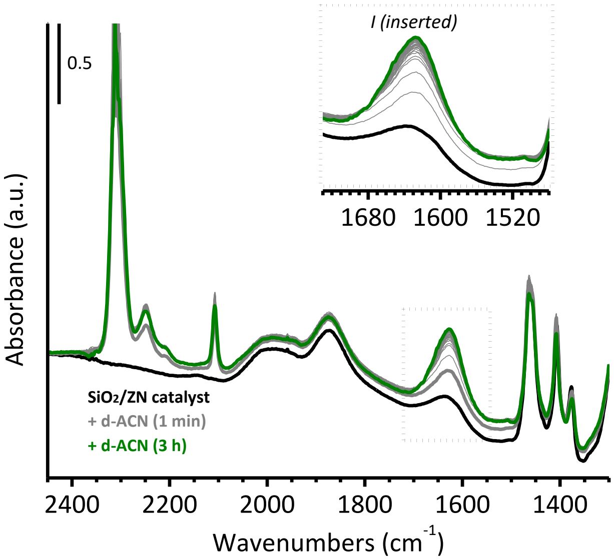

Figure 4. 19 Time resolved IR spectra of d-acetonitrile adsorbed on SiO_2/ZN catalyst (activated with 3.25 eq. TEA). The spectra are shown in 2450-1300 cm^{-1} region starting from black spectra (spectra of bare catalyst) to green spectrum that is collected in the presence of acetonitrile after 3h. Inset shows 1730-1480 cm^{-1} region in order to emphasize the band related to d-acetonitrile inserted into Ti-R bond

A series of systematic IR experiments with d-acetonitrile adsorbed at 300 K were performed on SiO_2/ZN catalysts activated with different amounts of TEA. Figure 4. 20 shows the IR spectra in ν(C=N) region of the Ti- aza-alkenylidene species after 3 hours of interaction with d-acetonitrile. The spectra have been normalized to the optical thickness of the pellet for enabling comparison. The following observation can be done:

- irrespective of the amount of TEA, the ν(C=N) band associated to d-acetonitrile inserted into the Ti-R bond is always at the same position and is characterized by the same band. This suggests that *the distribution of active sites is does not change drastically upon changing theamount of TEA.*
- There is no linear correlation between intensity of the ν(C=N) band and amount of TEA, which means that *the amount of active sites able to insert d-acetonitrile does not scale linearly with the amount of the activator*.

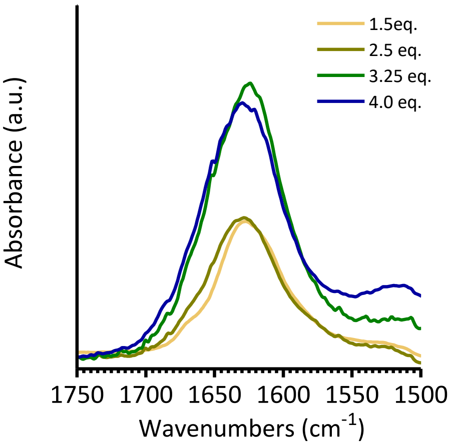

Figure 4. 20 IR spectroscopy of d-acetonitrile adsorbed on SiO_2/ZN catalysts activated with different amount of TEA in 1730-1480 cm^{-1}. Spectra are shown after normalization to the optical thickness of the pellet after 3 hours of interaction with d-acetonitrile.

3.7 Kinetics of ethylene polymerization

We evaluated the kinetics of ethylene polymerization under very mild conditions (similar to those adopted during the spectroscopic measurements) as a function of the Al:Ti ratio. Figure 4. 21 shows the reciprocal of ethylene pressure as a function of time. It was observed that the activity increases upon increasing the Al:Ti ratio. Moreover, *the best fit of experimental data was obtained for second reaction order, no matter how much TEA was used for activation*, which agrees with literature on ethylene polymerization on supported Ti-based Ziegler-Natta catalysts, where reaction orders 1.7-2.0 were reported.[105]

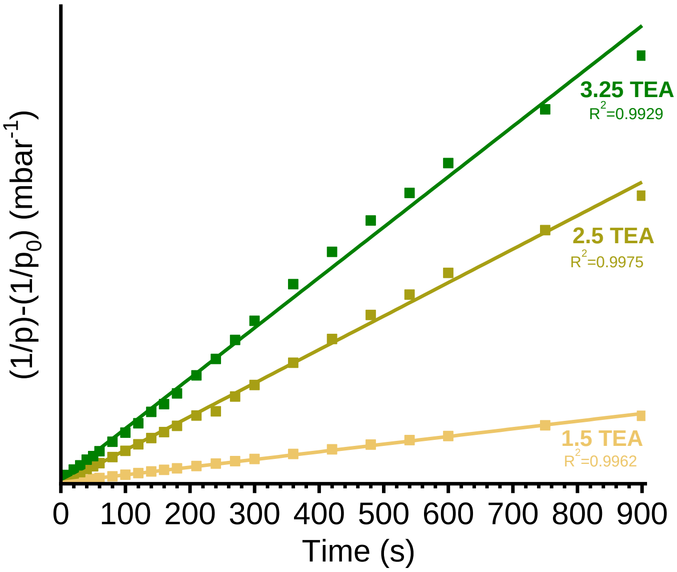

Figure 4. 21 Kinetics of ethylene polymerization for SiO_2/ZN catalysts activated with different amounts of TEA. The experimental data are reported as squares, while the lines are the best linear fits (with indicated R^2 values).

The problem regarding the dependence of ethylene polymerization rate on monomer concentration is still controversial,[106] and several explanations have been proposed to account for this unusual behaviour. Most of them brings up a dynamic equilibrium between active Ti-alkyl species with (at least) one open coordination vacancy available for ethylene insertion, and inactive (or dormant) species with the Ti coordination sphere saturated, hence not available for ethylene coordination. For example, according to the “trigger” mechanism proposed by Ystenes,[48] an ethylene molecule coordinated to an active site can be incorporated into the propagating chain only when a second ethylene molecule is coordinated, hence if the Ti-alkyl species has at least two open coordination vacancies. For Matsko et al.[106] the coordination sphere in inactive Ti-alkyl species is saturated by excess of Al-alkyl but may become active via interaction with ethylene. According to Kissin et al.[45–47] an inactive Ti-CH_2CH_3 species is rapidly formed from the active one in defect of ethylene via a strong β-agostic interaction with the hydrogen atom of the methyl group.

At present we have no elements for describing the structure of the active and dormant Ti sites. However, our observation by IR spectroscopy of two types of Ti-acyl species in the presence of CO, among which one is characterized by a strong

η^2-coordination with Ti, suggests that also C-H agostic interactions might play a role in the equilibrium between active and dormant sites. We speculate that the Ti-alkyl sites forming η^2-coordinated acyl species in the presence of CO are also those prone to become inactive during ethylene polymerization through C-H agostic interactions.

3.8 Fragmentation of the catalyst particles facilitates the detection of the active sites by Ti $L_{2,3}$-edge NEXAFS spectroscopy

As the last point catalyst behaviour during ethylene polymerization was investigated by Ti $L_{2,3}$-edge NEXAFS spectroscopy in total electron yield mode (TEY). Figure 4. 22 represents the spectrum of the SiO_2/ZN catalyst activated with 3.25 eq. of TEA (already discussed in Figure 4. 13) and a sequence of spectra collected after small pulses of ethylene were sent to the cell with catalyst. After first pulse of ethylene spectra changed dramatically, and these changes are even more pronounced when more pulses of ethylene were sent. This results in completely different shape of last spectra relative to the initial one. Specifically, the last spectrum is half less intense then the first one, and in L_3 region new peaks at 456.5, 458.2 and 459.5 eV can be seen. These peaks are very similar to those observed in the Ti L_3-edge NEXAFS of a model $MgCl_2$-supported ZN catalyst after activation by TEA, and assigned to monomeric and alkylated Ti(III) species.[62]

The decrease in intensity of the spectra can be explained by the formation of an insulating PE layer, which lowers the probability to collect the electrons escaping from the sample. On the other hand, the change in the spectral shape was completely unexpected because polymeric chain is not dissimilar from an alkyl group, thus electronic features of the active sites upon ethylene insertion into Ti(III)-R bond should be the same.[62] However, spectra reported in Figure 4. 22 suggests that *during ethylene polymerization, new Ti(III) sites, previously not detected, gradually emerge at the surface, so can be detected by TEY-NEXAFS. Indeed, this is what is expected to occur during catalyst particle fragmentation.* It can be also concluded that the experimental procedure adopted for this experiment (i.e., small ethylene pulses under inert flow), which was necessary for performing the measurements in total electron yield, also allowed to reduce the polymerization rate in the early reaction stages, thus avoiding the formation of a PE layer at the exterior of the catalyst particles. This allowed the entrance of ethylene and the growth of PE inside the particles, with a consequent stress build-up ultimately favouring the fragmentation of the catalyst.

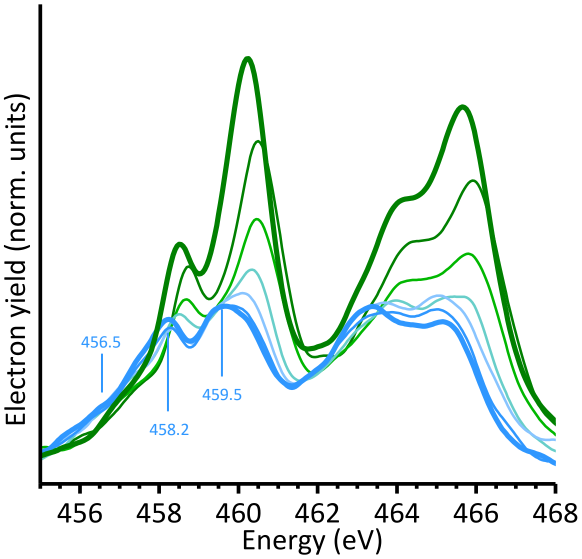

Figure 4. 22 Ti $L_{2,3}$-edge NEXAFS spectrum of the SiO_2/ZN catalyst activated with 3.25 eq. of TEA (green) and evolution of the spectra in the presence of small ethylene pulses (from green to blue). The whole sequence of spectra was collected in a few minutes.

4. Conclusions

Industrially relevant SiO_2/ZN precatalyst and corresponding catalysts were investigated by a whole set of complementary spectroscopic techniques. It is worth noting that, even though this type of catalyst is widely used in the fluidized-bed reactor for ethylene polymerization since 1980s, there was not a clear hypothesis on its structure at molecular level.

By synergetic use of different spectroscopic techniques, it was possible to disclose the structural, electronic, and vibrational properties of the SiO_2/ZN precatalyst at a molecular level. The co-presence of Ti(III) and Ti(IV) species is confirmed and it is in good agreement with previous reports on similar catalytic systems.[83] The Ti(III) sites belong to small clusters having electronic similar to β-$TiCl_3$ polymorph, but they are highly dispersed. The Ti(IV) sites are found to be monomeric and mainly surrounded by chlorine ligands present at three different distances (short, medium and long) and with distorted octahedral symmetry. Nevertheless, the presence of one oxo-butyl ligand around Ti(IV) cannot be excluded. Both Ti(III) and Ti(IV) species are inter-connected with nanometric $MgCl_2$ "quantum dots" having a molecular character and which are at least partially stabilized also by butoxide moieties. The only sites of these $MgCl_2$ molecular clusters that are accessible to CO as molecular probe are uncoordinated Mg^{2+}

cations. Since, it is expected that chemically dehydroxylated silica contains very few silanol groups, that are known to be reactive towards different catalyst components (alkyl aluminums, $MgCl_2$ and $TiCl_4$), it is expected that this $MgCl_2$ nanoparticles are just dispersed on silica surface.

By combining several highly sensitive spectroscopic methods we proved the co-existence of numerous Ti phases in the activated SiO_2/ZN catalyst, differing both in terms of oxidation (Ti(IV), Ti(III) and even Ti(II)) and aggregation (isolated or clusters) state, whose relative amount is a function of the Al:Ti molar ratio. The accessible Ti(III) sites in the activated catalyst were probed by CO, which is a molecule able not only to coordinate to the Ti sites but also to insert into the Ti-alkyl bond, mimicking the behaviour of the olefin monomer. Two types of Ti(III) sites were distinguished: the former, with a higher effective charge, is immediately accessible, while the latter has a lower effective charge and coordination of CO is kinetically slower. Also, two type of Ti-acyl species were formed upon insertion of CO into the Ti-alkyl bond, differing in the extent of the η^2-coordination to Ti.

It was also possible to develop a hypothesis about spatial distribution of Ti sites present in the SiO_2/ZN catalyst(s). $TiCl_3$ clusters are formed both during the catalyst synthesis and during the catalyst activation by trialkyl aluminium. The formation of this clusters is favoured at the exterior of the catalyst particles. When $TiCl_3$ clusters are present, their electronic features invariably dominate both the Ti $L_{2,3}$-edge NEXAFS and DR UV-Vis spectra, disabling the detection of isolated Ti(III) species. The presence of isolated Ti(III) species also at the exterior of the activated catalyst particle is demonstrated by IR spectroscopy, which detects a family of Ti(III) sites able to coordinate CO immediately. Instead, exclusively monomeric Ti species are formed inside the catalyst particles, both during the precatalyst synthesis (in the form of Ti(IV)) and during catalyst activation (in the form of alkylated Ti(III)). These species coordinate CO at longer times due to diffusion limitations, and become visible by Ti $L_{2,3}$-edge NEXAFS only after pronounced catalyst particle fragmentation, which is achieved by working under very mild pre-polymerization conditions.

References

1. Ziegler, K., Holzkamp, E., Breil, H. & Martin, H. Das Mulheimer Normaldruck-Polyiithylen-Verfahren. *Angewandte Chemie* **67**, 541–548 (1955).

2. Natta, G. Kinetic Studies of a-Olefin Polymerization. *JOURNAL OF POLYMER SCIENCE* **24**, 21–48 (1959).

3. Chadwick, J. C., Garoff, T. & Severn, J. R. Ziegler – Natta Catalysts in Polyolefin Synthesis. in *Tailor-made Polymers Via Immobilization of Alpha-Olefin Polymerization Catalysts* (eds. Severn, J. R. & Chadwick, J. C.) 43–60 (Wiley-VCH, 2007).

4. Grau, E. *et al.* Tetrahydrofuran in TiCl4/THF/MgCl2: A non-innocent ligand for supported Ziegler-Natta polymerization catalysts. *ACS Catal* **3**, 52–56 (2013).

5. Galli, P. & Vecellio, G. Technology: driving force behind innovation and growth of polyolefins. *Prog Polym Sci* **26**, 1287–1336 (2001).

6. Busico, V. Metal-catalysed olefin polymerisation into the new millennium:a perspective outlook. *Dalton Transactions* 8794–8802 (2009) doi:10.1039/b910542p.

7. Liu, B., Nitta, T., Nakatani, H. & Terano, M. Stereospecific Nature of Active Sites on TiCl 4 /MgCl 2 Ziegler-Natta Catalyst in the Presence of an Internal Electron Donor. *Macromolecular Chemical Physics* **204**, 395–402 (2003).

8. Kissin, Y. v. Multicenter Nature of Titanium-Based Ziegler-Natta Catalysts: Comparison of Ethylene and Propylene Polymerization Reactions. *J Polym Sci A Polym Chem* **41**, 1745–1758 (2003).

9. Soares, J. B. P. & McKenna, T. F. L. *Polyolefin Reaction Engineering*. (WILEY-VCH Verlag GmbH & CO, 2012).

10. Gupta, V., Patil, H. & Naik, D. Propylene polymerization catalyst system. (2011).

11. Gupta, V. *et al.* Spheroidal particles for olefin polymerization catalyst. (2014).

12. Kashiwa, N. The Discovery and Progress of MgCl 2-Supported TiCl4 Catalysts. *J Polym Sci A Polym Chem* **42**, 1–8 (2003).

13. Galli, P., Luciani, L., Cecchin, G. & Gab, P. Advances in the Polymerization of Polyolefins with Coordination Catalysts. *Die Angewandte Makromolekulare Chemie* **94**, 63–89 (1981).

14. Leinonen, T. & Denfil, P. Preparation of olefin polymerisation catalyst component. (2003).

15. Correa, A., Piemontesi, F., Morini, G. & Cavallo, L. Key elements in the structure and function relationship of the MgCl 2/TiCl4/Lewis base Ziegler-Natta catalytic system. *Macromolecules* **40**, 9181–9189 (2007).

16. Wu, L., Lynch, D. T. & Wanke, S. E. Kinetics of gas-phase ethylene polymerization with morphology-controlled MgCl2-supported TiCl4 catalyst. *Macromolecules* **32**, 7990–7998 (1999).

17. Piovano, A. *et al.* Revisiting the identity of δ-MgCl2: Part II. Morphology and exposed surfaces studied by vibrational spectroscopies and DFT calculation. *J Catal* **387**, 1–11 (2020).

18. Pullukat, T. J. & Hoff, R. E. Silica-based Ziegler-Natta catalysts: A patent review. *Catal Rev Sci Eng* **41**, 389–428 (1999).

19. Pullukat, T. J. & Hoff, R. E. Polymerization Catalyst and Method. (1983).

20. Shida, M., Pullukat, T. J. & Hoff, R. E. Polymerization catalysts. (1981).

21. Nowlin, T. E. & Wagner, K. P. Highly active catalyst composition for polymerizing alfa-olefins. (1984).

22. Groppo, E., Seenivasan, K. & Barzan, C. The potential of spectroscopic methods applied to heterogeneous catalysts for olefin polymerization. *Catal Sci Technol* **3**, 858–878 (2013).

23. Groppo, E., Lamberti, C., Bordiga, S., Spoto, G. & Zecchina, A. The structure of active centers and the Ethylene Polymerization mechanism on the Cr/SiO2 catalyst: A frontier for the characterization methods. *Chem Rev* **105**, 115–183 (2005).

24. Groppo, E. *et al.* Activation and In Situ Ethylene Polymerization on Silica-Supported Ziegler-Natta Catalysts. *ACS Catal* **5**, 5586–5595 (2015).

25. Seenivasan, K., Sommazzi, A., Bonino, F., Bordiga, S. & Groppo, E. Spectroscopic investigation of heterogeneous Ziegler-Natta catalysts: Ti and Mg chloride tetrahydrofuranates, their interaction compound, and the role of the activator. *Chemistry - A European Journal* **17**, 8648–8656 (2011).

26. Werny, M. J. *et al.* X-ray nanotomography uncovers morphological heterogeneity in a polymerization catalyst at multiple reaction stages. *Chem Catalysis* **1**, 14131426 (2021).

27. Garoff, T. *et al.*
Procatalyst for ethylene polymer production, method for its preparation and use. (1995).

28. Kelly, M. *et al.* ENHANCED POLYOLEFIN CATALYST. (2007).

29. Milanesi, M. *et al.* Influence of the synthetic procedure on the properties of three Ziegler-Natta catalysts with the same 1,3-diether internal donor . *Catal Today* (2023).

30. Blitz, J. P. Model Silica Supported Olefn Polymerization Catalysts. in *New Advances in Polyolefins* (ed. Chung, T. C.) 1–14 (Springer Science+Business Media, 1993).

31. Blitz, J. P., Meverden, C. C. & Diebel, R. E. Reactions of Dibutylmagnesium with Modified Silica Gel Surfaces. *Lengmuir* **14**, 1122–1129 (1998).

32. Hagerty, R. O., Petsche, I. B. & Schurzky, K. G. Alpha-Olefins Polymerization Catalysts of High Productivity. (1985).

33. Hsieh, H. L., McDaniel, M. P., Martin, J. L., Smith, P. D. & Fahey, D. R. Polyolefin Catalysts Based on Titanium and Vanadium Chlorides. in *Advances in Polyolefins: The World's Most Widely Used Polymers* (eds. Seymour, R. B. & Cheng, T.) 153–170 (SPRINGER SCIENCE+BUSINESS MEDIA, 1987).

34. Busico, V., Cipullo, R., Mingione, A. & Rongo, L. Accelerating the Research Approach to Ziegler-Natta Catalysts. *Ind Eng Chem Res* **55**, 2686–2695 (2016).

35. Koshevoy, E. I., Mikenas, T. B., Zakharov, V. A., Shubin, A. A. & Barabanov, A. A. Electron Paramagnetic Resonance Study of the Interaction of Surface Titanium Species with AlR3 Cocatalyst in Supported Ziegler-Natta Catalysts with a Low Titanium Content. *Journal of Physical Chemistry C* **120**, 1121–1129 (2016).

36. Koshevoy, E. I., Mikenas, T. B., Zakharov, V. A., Volodin, A. M. & Kenzhin, R. M. Formation of isolated titanium(III) ions in superactive titanium-magnesium catalysts with a low titanium content as active sites in ethylene polymerization. *Catal Commun* **48**, 38–40 (2014).

37. Humbert, M., Norsic, S., Raynaud, J. & Monteil, V. Activity Enhancement of MgCl2-supported Ziegler-Natta Catalysts by Lewis-acid Pre-treatment for Ethylene Polymerization. *Chinese Journal of Polymer Science (English Edition)* **37**, 1031–1038 (2019).

38. Cossee, P. *Ziegler-Natta Catalysis I. Mechanism of Polymerization of a-Olefins with Ziegler-Natta Catalysts*. JOURNAL OF CATALYSIS* vol. 3 (1964).

39. Ashuiev, A. *et al.* Molecular and supported Ti(iii)-alkyls: efficient ethylene polymerization driven by the π-character of metal-carbon bonds and back donation from a singly occupied molecular orbital. *Chem Sci* **12**, 780–792 (2021).

40. Allouche, F. *et al.* Low-Coordinated Titanium(III) Alkyl—Molecular and Surface—Complexes: Detailed Structure from Advanced EPR Spectroscopy. *Angewandte Chemie - International Edition* **57**, 14533–14537 (2018).

41. Ashuiev, A. *et al. Spectroscopic Signature and Structure of Active Centers in Ziegler-Natta Polymerization Catalysts revealed by Electron Paramagnetic Resonance*.

42. Zakharov, V. A. & Yermakov, Y. I. Supported Organometallic Catalysts for Olefin Polymerization. *Catalysis Reviews* **19**, 67–103 (1979).

43. Kissin, Y. v. Active centers in Ziegler-Natta catalysts: Formation kinetics and structure. *J Catal* **292**, 188–200 (2012).

44. Kissin, Y. v. & Mink, R. I. Ethylene polymerization reactions with multicenter Ziegler-Natta catalysts-manipulation of active center distribution. *J Polym Sci A Polym Chem* **48**, 4219–4229 (2010).

45. Kissin, Y. v. Peculiarities of Ethylene Polymerization Reactions with Heterogeneous Ziegler-Natta Catalysts: Kinetic Analysis. *Macromolecular Theory and Simulation* **11**, 67–76 (2002).

46. Kissin, Y. v, Mink, R. I. & Nowlin, T. E. Ethylene Polymerization Reactions with Ziegler-Natta Catalysts. I. Ethylene Polymerization Kinetics and Kinetic Mechanism. *J Polym Sci A: Polym Chem* **37**, 4255–4272 (1999).

47. Kissin, Y. v, Mink, R. I., Nowlin, T. E. & Brandolini, A. J. Kinetics and mechanism of ethylene homopolymerization and copolymerization reactions with heterogeneous Ti-based Ziegler-Natta catalysts. *Top Catal* **7**, 69–88 (1999).

48. Ystenes, M. The Trigger Mechanism for Polymerization of e-Olefins with Ziegler-Natta Catalysts: A New Model Based on Interaction of Two Monomers at the Transition State and Monomer Activation of the Catalytic Centers. *J Catal* **129**, 383–401 (1991).

49. Muroz-Escalona, A., Hernandez, J. G. & Gallardo, J. A. Catalytic Activity and Control of the Nascent Morphology of Polyethylenes Obtained with First and Second Generation of Ziegler-Natta Catalysts. *J Appl Polym Sci* **29**, 1187–1202 (1984).

50. Kim, J. H., Tae Jeong, Y. & Ihl Woo, S. Copolymerization of Ethylene and 1-Butene with Highly active TiCl4/THF/MgCl2, TiCl4/THF/MgCl2/SiO2 and TiCl3*1/3AlCl3 Catalysts. *J Polym Sci A Polym Chem* **32**, 2979–2987 (1994).

51. Kissin, Y. v. 'HOMOGENEOUS'INTERPRETATIONOFETHYLENE POLYMERIZATION KINETICS WITH SUPPORTED ZIEGLER-NATTACATALYSTS. *Journal of Molecular Catalysis* **56**, 220–236 (1989).

52. Resconi, L., Cavallo, L., Fait, A. & Piemontesi, F. Selectivity in propene polymerization with metallocene catalysts. *Chem Rev* **100**, 1253–1345 (2000).

53. Lamberti, C., Zecchina, A., Groppo, E. & Bordiga, S. Probing the surfaces of heterogeneous catalysts by in situ IR spectroscopy. *Chem Soc Rev* **39**, 4951–5001 (2010).

54. Piovano, A., Zarupski, J. & Groppo, E. Disclosing the Interaction between Carbon Monoxide and Alkylated Ti3+Species: A Direct Insight into Ziegler-Natta Catalysis. *Journal of Physical Chemistry Letters* **11**, 5632–5637 (2020).

55. Groppo, E., Martino, G. A., Piovano, A. & Barzan, C. The Active Sites in the Phillips Catalysts: Origins of a Lively Debate and a Vision for the Future. *ACS Catal* **8**, 10846–10863 (2018).

56. Piovano, A., D'Amore, M., Thushara, K. S. & Groppo, E. Spectroscopic Evidences for TiCl4/Donor Complexes on the Surface of MgCl2-Supported Ziegler-Natta Catalysts. *Journal of Physical Chemistry C* **122**, 5615–5626 (2018).

57. Martino, G. A. *et al.* Rationalizing the Effect of Triethylaluminum on the Cr/SiO2 Phillips Catalysts. *ACS Catal* **10**, 2694–2706 (2020).

58. Pletcher, P., Welle, A., Vantomme, A. & Weckhuysen, B. M. Quality control for Ziegler-Natta catalysis via spectroscopic fingerprinting. *J Catal* **363**, 128–135 (2018).

59. Stukalov, D. v., Zakharov, V. A., Potapov, A. G. & Bukatov, G. D. Supported Ziegler-Natta catalysts for propylene polymerization. Study of surface species formed at interaction of electron donors and TiCl4 with activated MgCl2. *J Catal* **266**, 39–49 (2009).

60. Panchenko, V. N., Goryachev, A. N., Vorontsova, L. v., Paukshtis, E. A. & Zakharov, V. A. Basicity of stereoregulating electron-donor compounds in ziegler-natta catalysts: A study by infrared spectroscopy and chemical exchange reactions. *Journal of Physical Chemistry C* **118**, 28572–28579 (2014).

61. Zakharov, V. A. *et al.* SURFACE ACIDIC SITES OF HIGHLY DISPERSE MAGNESIUM CHLORIDE IR AND ESR SPECTROSCOPY STUDIES. *Macromol. Symp* **89**, 55–61 (1995).

62. Piovano, A. *et al.* Electronic Properties of Ti Sites in Ziegler-Natta Catalysts. *ACS Catal* **11**, 9949–9961 (2021).

63. Groppo, E. *et al.* XAS and XES techniques shed light on the dark side of Ziegler-Natta catalysts: Active-site generation. *ChemCatChem* **7**, 1432–1437 (2015).

64. Borfecchia, E. *et al.* Spectroscopic Methods in Catalysis and Their Application in Well-Defined Nanocatalysts. in *Studies in Surface Science and Catalysis* vol. 177 221–284 (Elsevier Inc., 2017).

65. Seenivasan, K. *et al.* Silica-supported Ti chloride tetrahydrofuranates, precursors of Ziegler-Natta catalysts. *Dalton Transactions* **42**, 12706–12713 (2013).

66. Signorile, M. *et al.* Titanium Defective Sites in TS-1: Structural Insights by Combining Spectroscopy and Simulation. *Angewandte Chemie - International Edition* **59**, 18145–18150 (2020).

67. Piovano, A., Morra, E., Chiesa, M. & Groppo, E. Tuning the Ti3+ and Al3+ Synergy in an Al2O3/TiClx Catalyst to Modulate the Grade of the Produced Polyethylene. *ACS Catal* **7**, 4915–4921 (2017).

68. Jorgensen, C. K. *Absorption Spectra and Chemical Bonding in Complexes*. (Pergamon Press, 1962).

69. Gianolio, D. *et al.* Direct evidence of adsorption induced CrII mobility on the SiO2 surface upon complexation by CO. *Chemical Communications* **46**, 976–978 (2010).

70. Groppo, E. *et al.* In situ, Cr K-edge XAS study on the Phillips catalyst: Activation and ethylene polymerization. *J Catal* **230**, 98–108 (2005).

71. Copéret, C., Chabanas, M., Petroff Saint-Arroman, R. & Basset, J. M. Surface organometallic chemistry: Homogeneous and heterogeneous catalysis: Bridging the gap through surface organometallic chemistry. *Angewandte Chemie - International Edition* **42**, 156–181 (2003).

72. Bordiga, S., Groppo, E., Agostini, G., van Bokhoven, J. A. & Lamberti, C. Reactivity of surface species in heterogeneous catalysts probed by in situ x-ray absorption techniques. *Chem Rev* **113**, 1736–1850 (2013).

73. Knozinger, H. INFRARED SPECTROSCOPY AS A PROBE OF SURFACE ACIDITY. in *Elementary Reaction Steps in Heterogeneous Catalysis* (eds. Joyner, R. W. & van Santen, R. A.) 267–285 (1993).

74. D’Amore, M. *et al.* Surface Investigation and Morphological Analysis of Structurally Disordered MgCl2 and MgCl2/TiCl4 Ziegler-Natta Catalysts. *ACS Catal* **6**, 5786–5796 (2016).

75. Piovano, A., Martino, G. A. & Barzan, C. A spectroscopic investigation of silica-supported TiClx species: a case study towards Ziegler–Natta catalysis. *Rend Lincei Sci Fis Nat* **28**, 43–49 (2017).

76. Calderazzo, F. Synthetic and Mechanistic Aspects of Inorganic Insertion Reactions. Insertion of Carbon Monoxide. *Angewandte Chemie International Edition English* **16**, 299–311 (1977).

77. Doi, Y., Murata, M., Yano, K. & Keii, T. Gas-Phase Polymerization of Propene with the Supported Ziegler Catalyst: TiCl4/MgCl2/C6H5COOC2H5/Al(C2H5)3. *Ind. Eng. Chem. Prod. Res. Dev.* **21**, 580–585 (1982).

78. Taniike, T., Sano, S., Ikeya, M., Thang, V. Q. & Terano, M. Development of a Large-Scale Stopped-Flow System for Heterogeneous Olefin Polymerization Kinetics. *Macromol React Eng* **6**, 275–279 (2012).

79. Thakur, A., Wada, T., Chammingkwan, P., Terano, M. & Taniike, T. Development of large-scale stopped-flow technique and its application in elucidation of initial Ziegler-Natta olefin polymerization kinetics. *Polymers* vol. 11 Preprint at https://doi.org/10.3390/polym11061012 (2019).

80. Bukatov, G. D., Goncharov, V. S. & Zakharov, V. A. Interaction of 14CO with Ziegler-type heterogeneous catalysts and effect of interaction products on the determination of the amount of active centers. *Makromolecular Chemistry* **187**, 1041–051 (1986).

81. Thushara, K. S., D'Amore, M., Piovano, A., Bordiga, S. & Groppo, E. The Influence of Alcohols in Driving the Morphology of Magnesium Chloride Nanocrystals. *ChemCatChem* **9**, 1782–1787 (2017).

82. Haward, R. N., Roper, A. N. & Fletcher, K. L. Highly active catalysts for ethylene polymerization by the reduction of TiCl4 with organomagnesium compounds. *Polymer (Guildf)* **14**, 365–372 (1973).

83. Hoff, R. E., Pullukat, T. J. & Dombro, R. A. Alcohol-modified Magnesium Titanium Catalysts. in *Advances in Polyolefis: The Worlds's most widely used polymers* (eds. Seymuor, R. B. & Cheng, T.) 241 (1987).

84. Hoff, R. E. Polymerization Catalyst and Method. (1983).

85. Dombro, R. A. Polymerization Method. (1984).

86. Piovano, A. *et al.* Formation of Highly Active Ziegler-Natta Catalysts Clarified by a Multifaceted Characterization Approach. *ACS Catal* **11**, 13782–13796 (2021).

87. Brisdon, B. J., Lester, T. E. & Walton, R. A. Complex halides of transition metals-III* Electronic absorption spectra of hexahalotitanates(IV), vanadates (IV), and zirconates(IV). *Spectrochimica Acta* **23**, 1969–1976 (1967).

88. Simonne, D. H. *et al.* THORONDOR: A software for fast treatment and analysis of low-energy XAS data. *J Synchrotron Radiat* **27**, 1741–1752 (2020).

89. Natta, G., Corradini, P. & Allegra, G. Struttura cristallina della forma y del tricloruro do titanio. *Rendiconti dell'Academia Nazionale dei Lincei. Classe di Scienze Fisiche, matematiche e naturali* **26**, (1959).

90. Gallas, J. P., Lavalley, J. C., Burneau, A. & Barres, O. Comparative Study of the Surface Hydroxyl Groups of Fumed and Precipitated Silicas. 4. Infrared Study of Dehydroxylation by Thermal Treatments. *Langmuir* **7**, 1235–1240 (1991).

91. Zarupski, J. *et al.* Silica-magnesium-titanium Ziegler-Natta catalysts. Part 1: structure of the pre-catalyst at a molecular level. *Journal of catalysts* (2023).

92. Takasao, G. *et al.* Machine Learning-Aided Structure Determination for TiCl 4 -Capped MgCl 2 Nanoplate of Heterogeneous Ziegler-Natta Catalyst. *ACS Catal* **9**, 2599–2609 (2019).

93. Zecchina, A. & Otero Arean, C. Diatomic Molecular Probes for Mid-IR Studies of Zeolites. *Chem Soc Rev* **25**, 187–197 (1996).

94. Zecchina, A., Scarano, D., Bordiga, S., Spoto, G. & Lamberti, C. Surface Structures of Oxides and Halides and Their Relationships to Catalytic Properties. *Advances in Catalysis* **46**, (2001).

95. Velthoen, M. E. Z. *et al.* The Multifaceted Role of Methylaluminoxane in Metallocene-Based Olefin Polymerization Catalysis. *Macromolecules* **51**, 343–355 (2018).

96. Ghiotto, F. *et al.* Probing the structure of methylalumoxane (MAO) by a combined chemical, spectroscopic, neutron scattering, and computational approach. *Organometallics* **32**, 3354–3362 (2013).

97. Clark, R. J. H. Diffuse-reflectance Spectra of Some Anhydrous Transition-Metal Halides. *Journal of American Chemical Society* **253**, 417–426 (1964).

98. Fachinetti, G., Fochi, G. & Floriani, C. Carbon Monoxide Insertion into Zirconium- and Hafnium-Carbon σ Bonds: Synthesis, and Structural and Thermodynamic Data for Alkyl- and Aryl-η-acylbis(η-cyclopentadienyl)derivatives of Zirconium (IV) and Hafnium(IV). *Journal of Chemical Society, Dalton* 1946–1951 (1977).

99. Teuben, J. H., de Boer, E. J. M., Klazinga, A. H. & Klei, E. CO activation by dicyclopentadienyl Derivatives of Titanium, Niobium and Tantalum. *Journal of Molecular Catalysis* **13**, 107–114 (1981).

100. Morterra, C., Peñarroya Mentruit, M. & Cerrato, G. Acetonitrile adsorption as an IR spectroscopic probe for surface acidity/basicity of pure and modified zirconias. *Physical Chemistry Chemical Physics* **4**, 676–687 (2002).

101. Werny, M. J. *et al.* Correlating the Morphological Evolution of Individual Catalyst Particles to the Kinetic Behavior of Metallocene-Based Ethylene Polymerization Catalysts. *JACS Au* **1**, 1996–2008 (2021).

102. Michelin, R. A., Mozzon, M. & Bertani, R. *Reactions of transition metal-coordinated nitriles*. *Coordination Chemistry Reviews* vol. 147 (1996).

103. Bochmann, M., Wilson, L. M., Hursthouse, M. B. & Motevalll, M. Insertion Reactions of Nitriles in Cationic Alkylbls(cyclopentfrdlenyl)tltanlum Complexes:The Facile Synthesis of Azaalkenylidene Titanium Complexes and the Crystal and Molecular Structure of [(Indenyl)2Ti(NCMePh)(NCPh)]BPh4. *Organometallics* **7**, 1148–1154 (1988).

104. Montanari, T., Bevilacqua, M. & Busca, G. Use of nitriles as probe molecules for the accessibility of the active sites and the detection of complex interactions in zeolites through IR spectroscopy. *Appl Catal A Gen* **307**, 21–29 (2006).

105. *Transition Metal Polymerization Catalysts*. (2010).

106. Matsko, M. A., Zakharov, V. A., Nikolaeva, M. I. & Mikenas, T. B. Kinetics of ethylene polymerization over titanium-magnesium catalysts: The reasons for the observed second order of polymerization rate with respect to ethylene. *Polyolefins Journal* **2**, 27–38 (2015).

CHAPTER 5

Conclusions and perspectives

1. Olefin polymerization catalysis & spectroscopic methods

1.1 Challenges in polyolefin catalysis

Polyolefins (POs) are indispensable materials in our everyday life, since the range of their application goes from water bottles and medical devices to earthquake resistant pipes for water and gas transport. POs also meet the high standards required nowadays, such are cost- and resource-efficiency, recyclability, low greenhouse gas emission and possibility to be produced from renewable resources.[1] The unsurpassed properties of PO resins are a direct consequence of the progresses in polymerization sciences, particularly reaction engineering and olefin polymerization catalysis. Indeed, it was the discovery of polymerization catalysts that enabled the industrial scale production of POs. Further development of polyolefin polymerization catalysts lead to their big versatility, activity and selectivity, opening the door to tailor resin properties just by slightly modifying the catalyst structure.[2]

However, despite their long-term use and many efforts to disclose their properties, the olefin polymerization catalysts are still black boxes concerning the understanding of their molecular level properties and structure-activity relationship. Molecular-scale properties are of particular importance since they influence the catalyst activity, productivity, selectivity and, thus, the properties of the final product. This lack of knowledge lead to mainly empirical development of these catalysts, although nowadays modern techniques such as (DFT-driven) high-throughput screening are used to design polymerization catalysts. Although it cannot be said that trial-and-error approach was not successful in designing olefin polymerization catalysts, the rational design is necessary in order to meet all standards required regarding polymerization process, product properties but also social, economic and ecologic ones and the only way to do so is the understanding of molecular properties of these catalysts.

1.2 Spectroscopic methods may help

The difficulties in understanding PO catalysts at molecular level arise from their complexity, the small number of metal sites and even smaller number of active sites, as well as from their enormous air and moisture sensitivity. To overcome these difficulties, it is necessary to work in inert atmosphere and to use very sensitive techniques. This is where spectroscopies can contribute, due to their high sensitivity and robustness.

Even though magnetic spectroscopies have been not discussed in this thesis, it is important to recall that they are among the characterization techniques able to selectively detect the fingerprints of active sites thanks to their extreme sensitivity to precise isotopes and/or oxidation states and to their high tunability through the modulation of the magnetic field and the application of specific pulse sequences. As far as heterogeneous ZN catalysts is concerned, ^{13}C NMR spectroscopy has been extensively used to investigate the influence of electron donors in ZN pre-catalysts.[3–5] Very recently, the resolution has been enhanced by transferring the larger polarization of free radicals in the solvent to targeted NMR active nuclei via classical cross-polarization approach (the so called dynamic nuclear polarization surface-enhanced NMR spectroscopy, DNP-SENS).[6,7] Upon activation of ZN catalysts, the reduction of the Ti centers to the paramagnetic +3 oxidation state makes NMR measures terribly difficult, but it opens the possibility to probe the interactions of the Ti sites with the surroundings by use of advanced EPR spectroscopy: 2-D HYSCORE experiments have been performed to directly measure the hyperfine interaction of Ti^{3+} with ^{27}Al nuclei from the activator.[8–11] In the field of homogeneous olefin polymerization catalysts,[12–16] advanced NMR techniques have been pivotal to disclose the structure and self aggregation tendency of ion pairs (IPs) between the cationic active species and the anion, derived from the activation of a neutral precursor with a suitable cocatalyst. The structure and reactivity of IPs have been elucidated for many systems, taking also advantage of NOE and diffusion NMR experiments, which might provide information on the relative position of the ions, the self-aggregation tendency of the entire IPs, and the location of the counterion in the coordination sphere of the metal cation. However, similar works on heterogenized catalysts are much rare.

Similarly, optical spectroscopies (in particular UV-Vis and IR) have the potential to provide plenty of information on the active sites. The potential of these techniques is well demonstrated in the field of heterogeneous catalysis,[17] while they are still underdeveloped for the characterization of heterogeneous olefin polymerization catalysts.[18–20] This is an apparent contradiction, since both UV-Vis and IR spectrophotometers are widely available in most of the modern research laboratories, making them accessible to any researcher eager to work in the field. Nevertheless, the research groups with expertise in spectroscopic techniques have usually a scarce knowledge of polymerization catalysis, undermining all the efforts for the characterization of the active sites. Also the opposite is true, researchers expert in polymerization catalysis, as well as industrial researchers, have usually a scarce familiarity with spectroscopic methods, which creates difficulties in establishing a synergic and constructive dialog.

UV-Vis and IR spectroscopies can be applied to investigate the precatalysts, as well as the catalysts in the presence of the Al-alkyl activator, in the absence and in the presence of probes, including the monomer itself, which means under *operando* conditions. The possibility to couple them with the use of probe molecules gives to these techniques a ‘superpower’, since the right choice of the probe allows to extract indirect information on the active sites with unprecedent details. In the Physical Chemistry group at the Department of Chemistry of the University of Torino, I found a fertile background in the field of optical spectroscopy applied to heterogeneous catalysts. Within this thesis work, I tried to push further the experimental set-ups to their limits.

2. Main achievement of this PhD thesis

This PhD project dealt with a molecular level investigation of industrially relevant silica-supported catalysts for ethylene polymerization. The project was sponsored by the Dutch Polymer Institute (Project #813, MULTIPOL), and the catalysts were provided by an industrial DPI partner (SABIC). Two types of catalysts for polyethylene production have been objects of research, both of them supported on a polymer-grade silica: a ZN catalyst and three metallocene-based catalysts. The final goal was the same in both cases, that is, understanding as much as possible about the structure of the active sites at a molecular level.

2.1 Specific achievements

For the ZN catalyst, the composition itself was extremely complex, with a multitude of ingredients reacting together during the synthesis to give a completely undefined precatalyst. This is actually quite common in the field of ZN catalysts, which are by definition hierarchical multi-component materials. The precatalyst and the Al-alkyl activated catalysts have been systematically investigated by using IR and UV-Vis spectroscopies, in the presence of different probe molecules, in different experimental conditions. Additionally, Ti K-edge and Ti $L_{2,3}$-edge XAS spectroscopy was also applied. The experimental data have been patiently and carefully analyzed and compared, up to reach a final picture. We demonstrated the co-existence of multiple phases in the precatalyst, which undergo structural changes in the presence of the activator, resulting in even more phases in the final catalyst, whose relative amount is a function of the activation conditions (Al/Ti ratio). We were able to quantify the relative amount of these phases, and we also made hypothesis on their spatial distribution within the catalyst particle, which is a topic of great relevance when dealing with the problem of catalyst fragmentation.

For the metallocene-based catalysts, the initial composition was much more defined. In fact, the synthesis procedure involved the reaction of the metallocene precursor with MAO activator in solution, and the deposition of the active phase on a chemically dehydroxylated silica. Hence, the active phase should be the same as that formed in solution, but heterogenized. Nevertheless, the molecular level structure and reactivity of the active sites was not clear, if not because the structure of the activator is anything than understood. UV-Vis and IR spectroscopies were useful to clarify the nature of the ion-pairs, which in turn influences the accessibility of the cation, as well as the inherent insertion ability of the M-Me bond, which is the elementary step driving the polymerization rate.

2.2 More general achievements

In more general terms, during this PhD project we developed an experimental methodology based on time-resolved IR spectroscopy with insertion probes, which allows to obtain simultaneously information on the catalyst properties at a molecular level and on their polymerization ability. This was achieved by the synergetic use of insertion probe molecules (d-acetonitrile, carbon monoxide) and monomers (1-hexene and ethylene). In particular, by performing systematic experiments on different catalysts in the same experimental conditions, this approach allows to determine the relative fraction of accessible sites, as well as their inherent ability to insert the probe into the M-C bond.

There are several advantages in using insertion probe molecules instead of monomers. First, only one insertion event can happen vs. the thousands of insertion events occurring during the polymerization, which means that there is no formation of a polymer layer at the catalyst surface. This greatly simplifies the application of optical spectroscopies (and other spectroscopic methods), which are inherently sensible to the presence of large amount of polymers. For example, formation of a polymer layer rapidly leads to the saturation of transmission IR spectra, and completely changes the light scattering properties of the catalyst powder, with important consequences on diffuse reflectance measurements. Also, the presence of a polymer layer around the catalyst particles masks the active sites, which escape detection by means of surface-sensitive spectroscopic methods.

Second, insertion of CO and acetonitrile into the M-C bond follows much slower kinetics (from minutes to hours) than insertion of the monomer (milliseconds). This allows to collect spectra at a standard time resolution, without resorting to ultra-fast acquisition modes, which are not always accessible and are usually accompanied by a worst signal/noise ratio.

The occurrence of a single insertion event and the much slower kinetics contribute to avoid the problem of the exothermicity of the reaction. In fact, olefin polymerization is a highly exothermic process, which leads to a relevant increase of temperature at the microscopic level. At an industrial scale, if not controlled, the generated heat can increase the reaction rate, generating additional heat and thus leading to polymer melting and ultimately to process problems. On a laboratory scale, within a spectroscopic reactor cell, temperature control is not straightforward, hence the experiments performed in the presence of the monomers are intrinsically affected by an increase of temperature, which might be more or less relevant depending on the activity of the catalyst and on the experimental set-up. For this reason, kinetic data collected within spectroscopic cells during olefin polymerization should be analyzed with caution. On the contrary, insertion kinetics of probes such as CO and acetonitrile are not affected by this problem, and hence should give a more realistic evaluation of the intrinsic ability of each catalyst to competently act during the first step of the reaction.

3. Final remarks

All in all, within this work the enormous potential of optical spectroscopies in investigating industrial silica-supported (but also homogeneous) olefin polymerization catalysts was demonstrated. Although this field of research is often defined as mature, the need for advanced PO materials is higher than ever, and it can be enabled only by understanding the polymerization process from the bottom, which means understanding the catalyst which produces the polymer.

In very general terms, it is almost impossible to do “advanced” without knowing the “fundamentals”, and PO catalysts do not refute this statement. On the other hand, it is also true that very often the most basic things are the hardest to be understood.

References

1. Stürzel, M., Mihan, S. & Mülhaupt, R. From Multisite Polymerization Catalysis to Sustainable Materials and All-Polyolefin Composites. *Chem Rev* **116**, 1398–1433 (2016).

2. Gagleitner, M. & Severn, J. R. Designing Polymer Properties. in *Tailor-made Polymers Via Immobilization of Alpha-Olefin Polymerization Catalysts* (eds. Severn, J. R. & Chadwick, J. C.) 1–39 (Wiley-VCH, 2007).

3. Tijssen, K. C. H., Merijn Blaakmeer, E. S. & Kentgens, A. P. M. Solid-state NMR studies of Ziegler-Natta and metallocene catalysts. *Solid State Nucl Magn Reson* **68**, 37–56 (2015).

4. Blaakmeer, E. S. M., Antinucci, G., van Eck, E. R. H. & Kentgens, A. P. M. Probing Interactions between Electron Donors and the Support in MgCl2-Supported Ziegler-Natta Catalysts. *Journal of Physical Chemistry C* **122**, 17865–17881 (2018).

5. Blaakmeer, E. S. M. *et al.* Structural Characterization of Electron Donors in Ziegler-Natta Catalysts. *Journal of Physical Chemistry C* **122**, 5525–5536 (2018).

6. Yakimov, A. v., Mance, D., Searles, K. & Copéret, C. A Formulation Protocol with Pyridine to Enable Dynamic Nuclear Polarization Surface-Enhanced NMR Spectroscopy on Reactive Surface Sites: Case Study with Olefin Polymerization and Metathesis Catalysts. *Journal of Physical Chemistry Letters* **11**, 3401–3407 (2020).

7. Yakimov, A. *et al.* DNP-SENS Formulation Protocols to Study Surface Sites in Ziegler-Natta Catalyst MgCl2Supports Modified with Internal Donors. *Journal of Physical Chemistry C* **125**, 15994–16003 (2021).

8. Piovano, A., Thushara, K. S., Morra, E., Chiesa, M. & Groppo, E. Unraveling the Catalytic Synergy between Ti3+and Al3+Sites on a Chlorinated Al2O3: A Tandem Approach to Branched Polyethylene. *Angewandte Chemie - International Edition* **55**, 11203–11206 (2016).

9. Morra, E. *et al.* Probing the Coordinative Unsaturation and Local Environment of Ti 3+ Sites in an Activated High-Yield Ziegler-Natta Catalyst . *Angewandte Chemie* **127**, 4939–4942 (2015).

10. Podvorica, L. *et al.* Isolated Ti(III) Species on the Surface of a Pre-active Ziegler Natta Catalyst. *Appl Magn Reson* **51**, 1515–1528 (2020).

11. Ashuiev, A. *et al.* Spectroscopic Signature and Structure of Active Centers in Ziegler-Natta Polymerization Catalysts revealed by Electron Paramagnetic Resonance.

12. Tensi, L., Froese, R. D. J., Kuhlman, R. L., Macchioni, A. & Zuccaccia, C. Interception of Elusive Cationic Hf–Al and Hf–Zn Heterobimetallic Adducts with Mixed Alkyl Bridges Featuring Multiple Agostic Interactions. *Chemistry - A European Journal* **26**, 3758–3766 (2020).

13. Sian, L., Macchioni, A. & Zuccaccia, C. Understanding the Role of Metallocenium Ion-Pair Aggregates on the Rate of Olefin Insertion into the Metal-Carbon Bond. *ACS Catal* **10**, 1591–1606 (2020).

14. Rocchigiani, L. *et al.* Synthesis, characterization, interionic structure, and self-aggregation tendency of zirconaaziridinium salts bearing long alkyl chains. *Organometallics* **30**, 100–114 (2011).

15. Rocchigiani, L., MacChioni, A. & Zuccaccia, C. NMR studies on the dynamic behavior of zirconaaziridinium ion pairs in solution. *Organometallics* **31**, 4076–4079 (2012).

16. Ciancaleoni, G. *et al.* Discriminating halogen-bonding from other noncovalent interactions by a combined NOE NMR/DFT approach. *Chemistry - A European Journal* **21**, 440–447 (2015).

17. Lamberti, C., Zecchina, A., Groppo, E. & Bordiga, S. Probing the surfaces of heterogeneous catalysts by in situ IR spectroscopy. *Chem Soc Rev* **39**, 4951–5001 (2010).

18. Piovano, A. & Groppo, E. Flexible ligands in heterogeneous catalysts for olefin polymerization: Insights from spectroscopy. *Coordination Chemistry Reviews* vol. 451 Preprint at https://doi.org/10.1016/j.ccr.2021.214258 (2022).

19. Groppo, E., Seenivasan, K. & Barzan, C. The potential of spectroscopic methods applied to heterogeneous catalysts for olefin polymerization. *Catal Sci Technol* **3**, 858–878 (2013).

20. Groppo, E., Martino, G. A., Piovano, A. & Barzan, C. The Active Sites in the Phillips Catalysts: Origins of a Lively Debate and a Vision for the Future. *ACS Catal* **8**, 10846–10863 (2018).

CHAPTER 6

Scientific publications

1. Articles published on International Journals (ISI)

(* corresponding author)

I. Alessandro Piovano*, Jelena Zarupski, Elena Groppo, Disclosing the Interaction between Carbon Monoxide and Alkylated Ti^{3+} Species: Direct Insight into Ziegler-Natta Catalysis, The Journal of Physical Chemistry Letters, **2020**, 11 (14), 5632–5637

II. Maximilian J. Werny#, Jelena Zarupski#, Iris C. ten Have, Alessandro Piovano, Coen Hendriksen, Nicolaas H. Friederichs, Florian Meirer*, Elena C. Groppo*, Bert M. Weckhuysen*, Correlating the Morphological Evolution of Individual Catalysts Particles to the Kinetic Behavior of Metallocene-Based Ethylene Polymerization Catalysts, JACS Au, **2021**, 1 (11), 1996–2008
Authors marked with # contributed equally.

THE JOURNAL OF
PHYSICAL CHEMISTRY
Letters

pubs.acs.org/JPCL

Letter

Disclosing the Interaction between Carbon Monoxide and Alkylated Ti^{3+} Species: a Direct Insight into Ziegler–Natta Catalysis

Alessandro Piovano,* Jelena Zarupski, and Elena Groppo

Cite This: *J. Phys. Chem. Lett.* 2020, 11, 5632–5637

Read Online

ACCESS | Metrics & More | Article Recommendations | Supporting Information

ABSTRACT: In the field of Ziegler–Natta catalysis for olefin polymerization, carbon monoxide (CO) is used in the industrial practice to quench the reaction when it proceeds too fast, approaching critical levels for the plant safety. The quenching effect is explained as due to the reversible coordination of CO to the titanium active sites, but no direct evidence has been ever reported. In this work, we designed a series of experiments to monitor CO adsorption at variable temperatures on a model Ziegler–Natta catalyst by means of FT-IR spectroscopy. For the first time, we have been able to spectroscopically detect CO coordinated to alkylated Ti^{3+} sites and the Ti–acyl species formed upon the subsequent insertion of CO into the Ti^{3+}–alkyl bond, both in the absence and in the presence of the olefin monomer. In perspective, this has important implications for the characterization of the active sites in industrial Ziegler–Natta catalysts, even under working conditions.

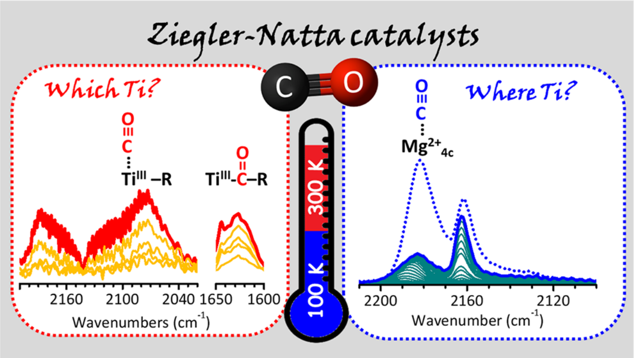

Synthetic polymers are nowadays one of the main features of anthropogenic activities, emblematic of the continuously evolving society and of the growing human impact on the planet. More than 60% of these materials is constituted by polyolefins, whose widespread development has been drastically increasing since 1950s, i.e., since the almost simultaneous inventions of Ziegler–Natta and Phillips catalysts, which are still the most used in the field.[1,2] Ziegler–Natta catalysts are heterogeneous multicomponent and hierarchical systems, whose composition has been optimized over the years mainly through a trial-and-error approach, passing across many different generations.[3,4] Nowadays, they are constituted by four main components interconnected with each other.[5] The precursors of the catalytic sites are $TiCl_x$ species chemisorbed on a nanostructured high-surface-area $MgCl_2$, which contributes to the stereoselectivity of the catalyst.[6−10] Organic electron-rich compounds (called electron donors) are usually added to the catalyst to improve the productivity and stereospecificity.[4,10,11] The $TiCl_x$ precursors need to be activated by an Al–alkyl cocatalyst before being effective in olefin polymerization. According to the well-established Cossee–Arlman mechanism, the cocatalyst has the double role of reducing and alkylating the titanium centers, replacing a chlorine ligand with an alkyl group and creating a coordinative vacancy, which is essential for the subsequent insertion of the monomer.[12]

Some fundamental questions about the structure and working of Ziegler–Natta catalysts are still open, setting the bar for the rational design of new and more efficient processes. Spectroscopic techniques have the potential to make up for this lack, unveiling the different species on the catalyst and monitoring their evolution during the catalyst synthesis and under reaction conditions. This is valid in general for heterogeneous catalysts,[13] and it has been recently demonstrated to be a valuable approach also for characterizing Ziegler–Natta catalysts through a step-by-step approach, so as to isolate the contribution of each component, thus overcoming the intrinsic complexity of the catalyst.[14] In this respect, FT-IR spectroscopy of adsorbed CO has been proved to be a powerful technique to probe the $MgCl_2$ surface as well as the distribution of the titanium species in Ziegler–Natta precatalysts,[15−17] and more recently it has been used to assess the overall condition of some industrial Ziegler–Natta catalysts and predict their effectiveness in catalyzing olefin polymerization.[18]

Potentially, the use of a CO probe might be further exploited to get direct information on the titanium active sites and their structure and reactivity, as widely done for many other heterogeneous catalysts,[19,20] including Cr-based catalysts for olefin polymerization.[21,22] As a matter of fact, CO is used in

Received: May 29, 2020
Accepted: June 25, 2020
Published: June 25, 2020

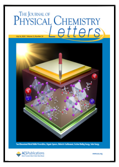

https://dx.doi.org/10.1021/acs.jpclett.0c01665
J. Phys. Chem. Lett. 2020, 11, 5632–5637

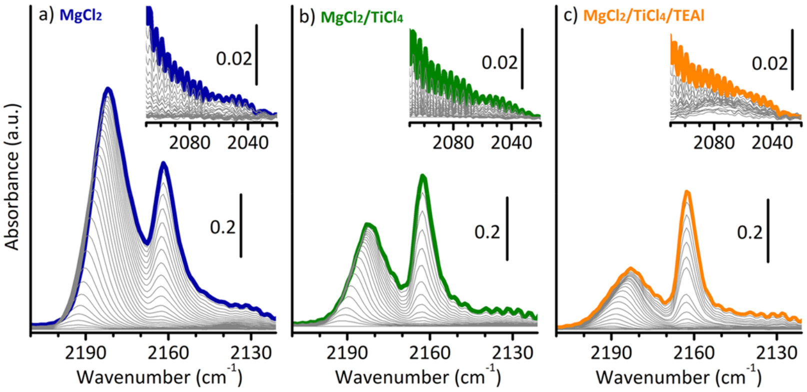

Figure 1. FT-IR spectra in the $\nu(C{\equiv}O)$ region of CO adsorbed at 100 K on $MgCl_2$ (a), $MgCl_2/TiCl_4$ (b), and $MgCl_2/TiCl_4$/TEAl (c), as a function of CO coverage (θ_{max} in bold colors). The insets show a magnification of the 2110−2020 cm^{-1} region. The spectra are shown after subtraction of spectrum of the catalyst prior CO dosage.

the polyolefin industry to temporarily quench the polymerization reaction when it is running too fast to reach critical conditions for the plant.[23,24] The ability of CO to poison Ti-based catalysts in a reversible way was used since the beginning as one of the principal evidence of coordinative unsaturation of the active titanium centers.[25] The CO interaction interrupts the polymerization reaction until CO is slowly removed by the cocatalyst or the monomer itself, so that the initial catalytic activity is restored.[26] Following this principle, the CO inhibition effect was used traditionally as one of the methods to determine the amount of active sites in Ziegler−Natta catalysts, by evaluating the CO/Ti ratio that must be injected into the reactor to completely stop the gas-phase polymerization reaction.[27−30] Moreover, the use of CO labeled with ^{14}C and ^{13}C demonstrated that the coordinated CO molecules further react with the active centers, inserting into the Ti−alkyl bonds and generating carbonyl groups, detected into the CO-quenched polymer chains.[31,32] Tritto et al. investigated this reaction, contacting a Ziegler−Natta catalyst with CO in the absence of any monomer and hydrolyzing the catalyst with HCl: in the extracted organic compounds they revealed the presence of carbonyls and their derivatives, thus confirming the rearrangement of CO with the alkyl groups of the activated titanium centers even in the absence of the monomer.[33]

However, no information has ever been achieved about the direct bond between Ti and CO, because of a combination of experimental difficulties, as the low amount of active sites, their strong sensitivity to poisons, and, quite important, their weak interaction with CO. Only recently Pletcher and co-workers have exploited CO as a direct characterization tool for an industrial Ziegler−Natta catalyst, monitoring CO adsorption at 100 K with FT-IR spectroscopy to assess the catalyst deterioration under different environmental conditions.[18] From the deconvolution of the complex $\nu(C{\equiv}O)$ signal they tentatively assigned a band at 2091 cm^{-1} to CO in interaction with Ti^{3+} sites,[18] but a deeper investigation of that interaction was out of topic for that study, and a more accurate description is still missing. Herein, we address this point by designing and performing a series of FT-IR experiments aimed at pursuing the few titanium sites active in ethylene polymerization in a model Ziegler−Natta catalyst.

The catalyst was synthesized as discussed in ref 14, where each step of the synthesis was characterized by multiple spectroscopic techniques. Briefly, a $MgCl_2$−6MeOH precursor was prepared by azeotropic distillation[34] and successively dealcoholated under a dynamic vacuum at 200 °C to get a high-surface-area $MgCl_2$ (100 m^2/g).[17] Afterward, $TiCl_4$ was dosed from the vapor phase and heated at 90 °C for 1 h to promote its chemisorption on $MgCl_2$ surface. The excess of $TiCl_4$ was outgassed at the same temperature under dynamic vacuum. The so formed $MgCl_2/TICl_4$ Ziegler−Natta precatalyst contains ca. 1 wt % of Ti.[17] Finally, the $MgCl_2/TiCl_4$ precatalyst was activated by triethylaluminum (TEAl) at room temperature from the vapor phase, at an Al:Ti ratio of 1:1. The final Ziegler−Natta catalyst will be hereafter referred to as $MgCl_2/TiCl_4$/TEAl. Although this synthesis procedure differs from the standard industrial routes, it has the advantage to be performed altogether inside the same measurement cell, allowing us to monitor the changes occurring in the sample by FT-IR spectroscopy of adsorbed CO at each step of the synthesis.

In a first series of experiments, the surface changes were probed by CO adsorption at 100 K. Figure 1 shows three sequences of spectra, in the $\nu(C{\equiv}O)$ region, collected at 100 K as a function of the CO coverage (θ), for CO adsorbed on $MgCl_2$ (part a), $MgCl_2/TiCl_4$ (part b), and $MgCl_2/TiCl_4$/TEAl (part c). Although spectra analogous to those shown in Figure 1a,b were already discussed in our previous work,[17] they are here reported for the sake of comparison and briefly discussed in the following. When CO is dosed at 100 K on $MgCl_2$ (Figure 1a), two bands are observed at 2182 and 2163 cm^{-1} (at the maximum coverage, θ_{max}), the former more intense and more resistant to degassing than the latter. They have been assigned to CO adsorbed on strongly acidic and weakly acidic Mg^{2+} sites, respectively, which are specific of the different exposed surfaces.[17] For $MgCl_2$ obtained from the conversion of an alcoholate precursor, the relative extent of the exposed surfaces depends on the alcohol.[16,35,36] When the alcohol is methanol, the surfaces exposing strongly acidic Mg^{2+} sites (i.e., (110), (015), and (012)), are the most favored. In the spectrum of CO adsorbed on the $MgCl_2/TiCl_4$ precatalyst (Figure 1b) the band at 2182 cm^{-1} is drastically less intense than before, while the band at 2163 cm^{-1} is almost unchanged. This was taken as an indication that the strongly acidic Mg^{2+} sites are no more available for CO adsorption because they are selectively occupied by chemisorbed $TiCl_x$ species,[17] in agreement with recent theoretical calculations.[37−41]

After activation of $MgCl_2/TiCl_4$ precatalyst by TEAl (Figure 1c), the FT-IR spectrum of CO adsorbed at 100 K does not show significant changes in the distribution of the accessible surface sites. The band at 2163 cm^{-1} is almost unaffected, while that at 2182 cm^{-1} slightly decreases in intensity with respect to the precedent step. As a matter of fact, although TEAl does not selectively occupy any specific site at $MgCl_2$ surface, after reaction with the chemisorbed $TiCl_x$ species the so formed diethylaluminum chloride (DEAC) byproduct likely adsorbs on $MgCl_2$ surface in close proximity of the Ti center.[42] No additional bands due to the interaction of CO with aluminum cations are detected, which would have been expected over 2200 cm^{-1}.[43] However, by carefully looking at the sequence of the spectra as a function of CO coverage, a very weak band can be noticed at around 2076 cm^{-1}, not present in the previous spectra and very resistant to the lowering of CO pressure (inset in Figure 1c). A band at a similar position was attributed by Pletcher et al. to CO interacting with Ti^{3+} sites,[18] although the same authors warned about the possible misunderstanding with the signal of CO in interaction with the Mg^{2+} sites through the O atom.[44]

In order to better clarify the situation, CO adsorption on the $MgCl_2/TiCl_4$/TEAl catalyst was repeated at room temperature. Indeed, at room temperature the interaction of CO with the bare $MgCl_2$ surface is almost negligible, while the CO inhibiting effect on the titanium centers is effective even at 60−100 °C, which is the typical temperature of industrial olefin polymerization. Because of the very low intensity of the band under scrutiny, an instrumental setup with a very short optical path was adopted, to minimize the roto-vibrational contribution of CO in the gas phase.

Figure 2a reports the spectrum of CO adsorbed at room temperature on the $MgCl_2/TiCl_4$/TEAl catalyst and its evolution upon lowering θ. At θ_{max}, the spectrum (spectrum 1) is characterized by two absorption bands at 2185 and 2076 cm^{-1}, springing out from the roto-vibrational profile of CO gas. The former corresponds to a small fraction of CO molecules adsorbed on the strongly acidic Mg^{2+} even at room temperature.[17] The latter recalls what is already reported in the inset of Figure 1c, but much more resolved. The observation of this band even when CO is adsorbed at room temperature on $MgCl_2/TiCl_4$/TEAl allows discarding the hypothesis of CO O-bonded to Mg^{2+} cations, which can be observed only when CO is adsorbed at 100 K. Hence, we definitely ascribe it to CO in interaction with Ti^{3+} sites. It is worth noticing that the position of the band is the result of a balance between the polarizing effect of Ti^{3+} ions, which have a Lewis acid nature, and the π-back-donation due to the unpaired electron in the external d orbital of the reduced titanium cation. This band decreases rapidly upon decreasing the CO pressure, indicating that the interaction of CO with the Ti^{3+} sites is quite weak at room temperature and fully reversible.

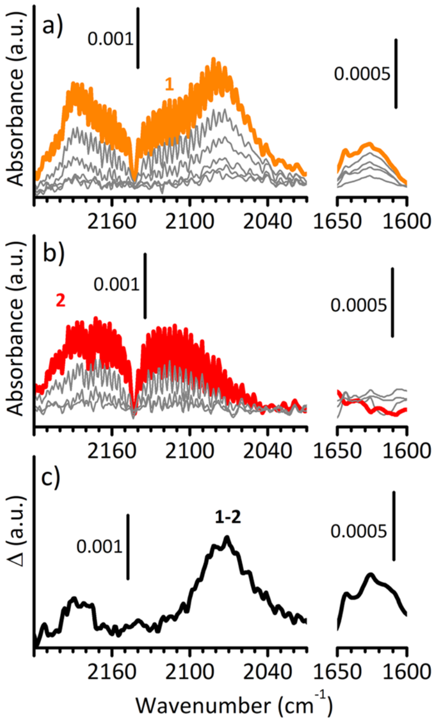

Figure 2. (a) FT-IR spectra of CO adsorbed at room temperature on $MgCl_2/TiCl_4$/TEAl as a function of CO coverage (θ_{max} in orange, spectrum 1). The spectra are shown after subtraction of that of the catalyst prior CO dosage. (b) Same as in part a, but after exposing $MgCl_2/TiCl_4$/TEAl to O_2 (θ_{max} in red, spectrum 2). (c) Difference spectrum obtained by subtracting spectrum 2 to spectrum 1.

Finally, a very weak feature is also detected at ca. 1625 cm^{-1}. This band is assigned to ν(C═O) of a Ti—acyl species formed upon insertion of CO into the Ti—alkyl bond, similarly to what happens in carbonylation reactions.[45] This observation is in agreement with the previously cited literature reporting the presence of carbonyl groups in the CO-quenched polymer chains.[31,32] As a matter of fact, CO insertion into a metal−carbon σ bond is well documented for most of 3d, 4d, and 5d elements, and it has been demonstrated to proceed by alkyl migration,[46] in the same way as olefin insertion in Cossee−Arlman mechanism.[12] Also this band is reversible upon decreasing the CO pressure, although at a slower rate with respect to CO coordinated to Ti^{3+} sites. This behavior indicates that the removal of CO from the Ti—C bond requires the restoration of the coordination vacancy at the Ti site and is a direct evidence that the reverse reaction, i.e., CO insertion into the Ti—C bond, proceeds through a coordination stage.

In order to further verify the nature of the bands at 2076 and 1625 cm^{-1}, CO adsorption on the $MgCl_2/TiCl_4$/TEAl catalyst was repeated after exposing the sample to oxygen, with the intention to oxidize the accessible Ti^{3+} sites making them no more visible by CO. As a matter of fact, it has been reported that the accessible Ti^{3+} in Ziegler−Natta catalysts reacts with O_2 via an electron-transfer mechanism to give an O_2^- superoxo radical in interaction with Ti^{4+}.[47] The spectra are reported in Figure 2b as a function of θ, while Figure 2c shows the difference spectrum obtained by subtracting spectrum 2 to spectrum 1, emphasizing the effect of O_2. As expected, at θ_{max} (spectrum 2) the absorption bands at 2076 and 1625 cm^{-1} are not present anymore. Interestingly, also the band at 2185 cm^{-1} is no more visible. This suggests that the few strongly acidic Mg^{2+} cations previously probed by CO are no more accessible after exposure of the catalyst to O_2, likely because O_2^- superoxo species or their derivatives are adsorbed also on Mg^{2+} sites, as demonstrated to occur on defective MgO.[48−50] Evidence for the formation of O_2^- superoxo species on the $MgCl_2/TiCl_4$/TEAl catalyst are present in the (not shown) FT-IR spectrum of the oxidized catalyst, displaying a broad absorption in the 1150−1000 cm^{-1} region, which is the spectral region characteristic for the ν(O−O) vibration of adsorbed superoxo species,[51] but not well-defined because of both the heterogeneity of the reactive sites and the possible evolution paths for the newly formed adsorbates.

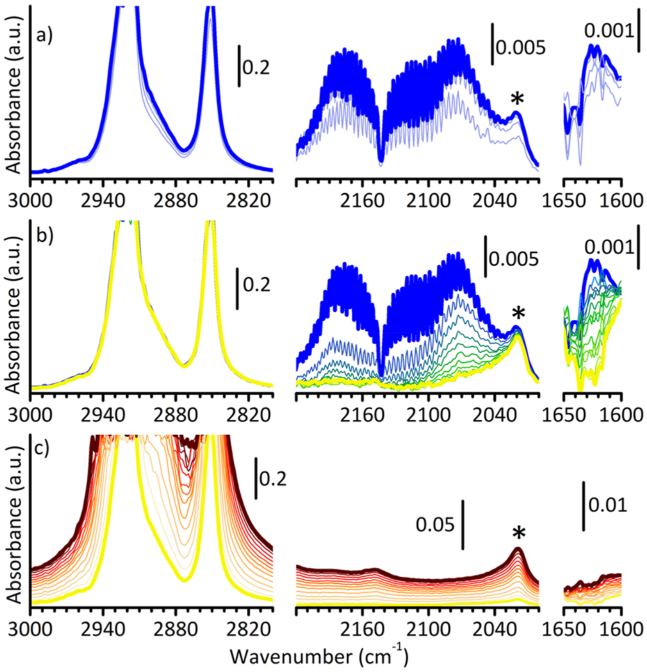

Figure 3. (a) FT-IR spectra collected as a function of time (up to bold spectrum in blue) during exposure of $MgCl_2/TiCl_4$/TEAl to a 1:1 mixture of C_2H_4/CO (equilibrium pressure = 100 mbar) at room temperature. The last spectrum is collected after 40 s. (b) FT-IR spectra collected during the subsequent controlled degassing of the reaction cell at room temperature (from θ_{max} in blue to θ_{min} in yellow). (c) FT-IR spectra collected as a function of time during exposure of $MgCl_2/TiCl_4$/TEAl to pure ethylene (equilibrium pressure = 50 mbar), from yellow to brown. The last spectrum is collected after 5 min. All the spectra are shown after subtraction of the spectrum of $MgCl_2/TiCl_4$/TEAl catalyst, in three different spectral regions: the $\nu(CH_2)$ in the left (for PE), the $\nu(C\equiv O)$ in the middle (for adsorbed CO), and the $\nu(C{=}O)$ in the right (for Ti—acyl). The band indicated with an asterisk is due to PE (combination of wagging modes).[52]

A final experiment was performed to probe with CO the Ti^{3+} species during ethylene polymerization. To this aim, a mixture of CO and ethylene (equilibrium pressure = 100 mbar, 1:1 molar ratio) was dosed on $MgCl_2/TiCl_4$/TEAl, mimicking the condition experienced by the catalyst in the industrial plant when CO is used to avoid the reactor fouling.[23,24] The results are shown in Figure 3, which reports the FT-IR spectra collected when the catalyst is exposed to the C_2H_4/CO mixture (part a), during the subsequent degassing (part b), and finally after exposing it back to pure ethylene (part c). The spectra are reported in three spectral regions, corresponding to $\nu(CH_2)$, $\nu(C\equiv O)$, and $\nu(C{=}O)$. As soon as the C_2H_4/CO mixture is introduced into the reaction cell (Figure 3a) ethylene polymerization immediately starts, as demonstrated by the fast appearance of two bands at 2920 and 2852 cm^{-1}, assigned to the asymmetric and symmetric $\nu(CH_2)$ modes of PE.[52] However, the reaction rapidly stops after 40 s, along with the coordination of CO to the Ti sites (band at 2072 cm^{-1}) and the insertion into the Ti—alkyl bond (band at 1620 cm^{-1}). Interestingly, both the $\nu(C{=}O)$ of Ti—acyl and the $\nu(C\equiv O)$ of CO adsorbed on Ti^{3+} sites are slightly downward shifted with respect to what is observed upon adsorption of CO on $MgCl_2/TiCl_4$/TEAl in the absence of ethylene (Figure 2a). The shift of the former band may be caused by different spatial dispositions of the Ti—acyl species as hypothesized for the carbonylation of organotitanium complexes,[45] while the shift of the latter band witnesses a larger contribution of the π-back-donation from the Ti d orbitals to the π^* orbital of CO, meaning that the polymer chains have a higher electron-releasing effect than the initial ethyl group. Moreover, both bands at 2072 and 1620 cm^{-1} are more intense in the present experiment, at equal optical thickness of the samples. This observation suggests that during ethylene polymerization more Ti^{3+} sites become accessible to incoming molecules, in good agreement with the results of kinetic experiments.[53]

Figure 3b shows the evolution of the main spectral features during the subsequent degassing in a controlled way. Both the bands at 2072 and 1620 cm^{-1} gradually decrease in intensity up to disappearance, while the spectroscopic manifestations of PE remain unaltered. Upon dosing back pure ethylene ($P_{C_2H_4}$ = 50 mbar), the polymerization reaction starts again and proceeds at constant speed for the successive 5 min, until the experiment was interrupted (Figure 3c). The experiment demonstrates that the poisoning effect of CO is reversible, in agreement with the industrial finding,[26] thus confirming that the results obtained in this work at lab-scale and on a model Ziegler−Natta catalyst are actually representative for the real catalytic process.

All in all, the whole set of spectroscopic data discussed in this work finally fulfills the lack of direct experimental evidence for the interaction between CO and the Ti active sites in Ziegler−Natta catalysts, that was so far just hypothesized on the basis of indirect proofs coming from kinetic experiments and from the analysis of the CO-quenched polymers. Indeed, we have been able to detect the CO coordinated to alkylated Ti^{3+} sites and the Ti—acyl species formed upon subsequent insertion of CO into the Ti^{3+}—alkyl bond. In more detail, we have found that both species are sensible to the intrinsic properties of the catalytic site and to the reaction environment and that both species are reversible upon decreasing the CO pressure, the former faster than the latter. Therefore, our study, carried out on a model Ziegler−Natta catalyst, demonstrates that FT-IR spectroscopy of CO adsorption is a powerful characterization technique for both monitoring the distribution of the active sites and inspecting their intrinsic properties, thus disclosing an effective and easily affordable way to investigate the more complex industrial Ziegler−Natta catalysts, under different working conditions.

■ ASSOCIATED CONTENT

Supporting Information

The Supporting Information is available free of charge at https://pubs.acs.org/doi/10.1021/acs.jpclett.0c01665.

Experimental details about the characterization technique and the working procedures (PDF)

■ AUTHOR INFORMATION

Corresponding Author

Alessandro Piovano − *Department of Chemistry, INSTM and NIS Centre, University of Torino, 10125 Torino, Italy; DPI, 5600 AX Eindhoven, The Netherlands;* orcid.org/0000-0002-5784-6897; Email: alessandro.piovano@unito.it

Authors

Jelena Zarupski – *Department of Chemistry, INSTM and NIS Centre, University of Torino, 10125 Torino, Italy; DPI, 5600 AX Eindhoven, The Netherlands*

Elena Groppo – *Department of Chemistry, INSTM and NIS Centre, University of Torino, 10125 Torino, Italy; DPI, 5600 AX Eindhoven, The Netherlands;* orcid.org/0000-0003-4153-5709

Complete contact information is available at: https://pubs.acs.org/10.1021/acs.jpclett.0c01665

Author Contributions

The manuscript was written through contributions of all authors.

Notes

The authors declare no competing financial interest.

■ ACKNOWLEDGMENTS

The work forms part of the research programme of DPI, project #802.

■ REFERENCES

(1) *Market Report: Global Catalyst Market*, 3rd ed.; Acmite Market Intelligence: Ratingen, Germany, 2015.

(2) Hutley, T. J.; Ouederni, M. Polyolefins - The History and Economic Impact. In *Polyolefin Compounds and materials*; AlMa'adeed, M. A.-A., Krupa, I., Eds.; Springer: Switzerland, 2016; pp 13–50.

(3) Galli, P.; Vecellio, G. Technology: driving force behind innovation and growth of polyolefins. *Prog. Polym. Sci.* **2001**, *26* (8), 1287–1336.

(4) Vittoria, A.; Meppelder, A.; Friederichs, N.; Busico, V.; Cipullo, R. Demystifying Ziegler-Natta Catalysts: The Origin of Stereoselectivity. *ACS Catal.* **2017**, *7* (7), 4509–4518.

(5) Albizzati, E.; Giannini, U.; Collina, G.; Noristi, L.; Resconi, L. Catalysts and polymerizations. In *Polypropylene Handbook*; Moore, E. P. J., Ed.; Hanser-Gardner Publications: Cincinnati, OH, 1996.

(6) Kakugo, M.; Miyatake, T.; Naito, Y.; Mizunuma, K. Microtacticity distribution of polypropylenes prepared with heterogeneous Ziegler-Natta catalysts. *Macromolecules* **1988**, *21* (2), 314–319.

(7) Kioka, M.; Makio, H.; Mizuno, A.; Kashiwa, N. Tacticity distribution of polypropylene prepared by MgCl2-supported titanium catalyst. *Polymer* **1994**, *35* (3), 580–583.

(8) Noristi, L.; Marchetti, E.; Baruzzi, G.; Sgarzi, P. Investigation on the particle growth mechanism in propylene polymerization with MgCl2-supported ziegler-natta catalysts. *J. Polym. Sci., Part A: Polym. Chem.* **1994**, *32* (16), 3047–3059.

(9) Chadwick, J. C.; van der Burgt, F.; Rastogi, S.; Busico, V.; Cipullo, R.; Talarico, G.; Heere, J. J. R. Influence of Ziegler-Natta catalyst regioselectivity on polypropylene molecular weight distribution and rheological and crystallization behavior. *Macromolecules* **2004**, *37* (26), 9722–9727.

(10) Busico, V. Giulio Natta and the Development of Stereoselective Propene Polymerization. In *Polyolefins: 50 years after Ziegler and Natta I*; Kaminsky, W., Ed.; Springer: Berlin, 2013; Vol. *257*, pp 37–57.

(11) Ratanasak, M.; Rungrotmongkol, T.; Saengsawang, O.; Hannongbua, S.; Parasuk, V. Towards the design of new electron donors for Ziegler-Natta catalyzed propylene polymerization using QSPR modeling. *Polymer* **2015**, *56*, 340–345.

(12) Cossee, P. Ziegler-Natta catalysis I. Mechanism of polymerization of α-olefins with Ziegler-Natta catalysts. *J. Catal.* **1964**, *3* (1), 80–88.

(13) Bañares, M. A. Operando Spectroscopy: the Knowledge Bridge to Assessing Structure–Performance Relationships in Catalyst Nanoparticles. *Adv. Mater.* **2011**, *23* (44), 5293–5301.

(14) Piovano, A.; Pletcher, P.; Velthoen, M. E. Z.; Zanoni, S.; Chung, S.-H.; Bossers, K.; Jongkind, M. K.; Fiore, G.; Groppo, E.; Weckhuysen, B. M. Genesis of MgCl2-based Ziegler-Natta Catalysts as Probed with Operando Spectroscopy. *ChemPhysChem* **2018**, *19* (20), 2662–2671.

(15) Zakharov, V. A.; Paukshtis, E. A.; Mikenas, T. B.; Volodin, A. M.; Vitus, E. N.; Potapov, A. G. Surface acidic sites of highly disperse magnesium chloride: IR and ESR spectroscopy studies. *Macromol. Symp.* **1995**, *89*, 55.

(16) Thushara, K. S.; D'Amore, M.; Piovano, A.; Bordiga, S.; Groppo, E. The Influence of Alcohols in Driving the Morphology of Magnesium Chloride Nanocrystals. *ChemCatChem* **2017**, *9* (10), 1782–1787.

(17) D'Amore, M.; Thushara, K. S.; Piovano, A.; Causà, M.; Bordiga, S.; Groppo, E. Surface Investigation and Morphological Analysis of Structurally Disordered MgCl2 and MgCl2/TiCl4 Ziegler–Natta Catalysts. *ACS Catal.* **2016**, *6* (9), 5786–5796.

(18) Pletcher, P.; Welle, A.; Vantomme, A.; Weckhuysen, B. M. Quality control for Ziegler-Natta catalysis via spectroscopic fingerprinting. *J. Catal.* **2018**, *363*, 128–135.

(19) Zecchina, A.; Otero Areán, C. Diatomic molecular probes for mid-IR studies of zeolites. *Chem. Soc. Rev.* **1996**, *25*, 187–197.

(20) Lamberti, C.; Zecchina, A.; Groppo, E.; Bordiga, S. Probing the surfaces of heterogeneous catalysts by in situ IR spectroscopy. *Chem. Soc. Rev.* **2010**, *39*, 4951–5001.

(21) Groppo, E.; Lamberti, C.; Bordiga, S.; Spoto, G.; Zecchina, A. The structure of active centers and the ethylene polymerization mechanism on the Cr/SiO$_2$ catalyst: a frontier for the characterization methods. *Chem. Rev.* **2005**, *105* (1), 115–184.

(22) Groppo, E.; Martino, G. A.; Piovano, A.; Barzan, C. The active sites in the Phillips catalysts: origins of a lively debate and a vision for the future. *ACS Catal.* **2018**, *8*, 10846–10863.

(23) Cook, J. E.; Hagerty, R. O.; Jacob, F. W. Reactor system for rapid kill gas injection to gas phase polymerization reactors. US4834947, 1989.

(24) Craddock, R. E., III; Jenkins, J. M., III; Tighe, M. T. Method and apparatus for stopping reaction in a gas phase polymerization reactor system. US5399320, 1995.

(25) Desert, X.; Carpentier, J.-F.; Kirillov, E. Quantification of active sites in single-site group 4 metal olefin polymerization catalysis. *Coord. Chem. Rev.* **2019**, *386*, 50–68.

(26) Caut, A. D. The determination of active centres in olefin polymerisation. *Br. Polym. J.* **1981**, *13* (1), 22–26.

(27) Doi, Y.; Murata, M.; Yano, K.; Keii, T. Gas-phase polymerization of propene with the supported Ziegler catalyst: TiCl4/MgCl2/C6H5COOC2H5/Al (C2H5) 3. *Ind. Eng. Chem. Prod. Res. Dev.* **1982**, *21* (4), 580–585.

(28) Mejzlík, J.; Lesná, M.; Kratochvíla, J. Determination of the number of active centers in Ziegler-Natta polymerizations of olefins. In *Catalytical and Radical Polymerization*; Springer: Berlin, Heidelberg, 1986; pp 83–120.

(29) Taniike, T.; Sano, S.; Ikeya, M.; Thang, V. Q.; Terano, M. Development of a Large-Scale Stopped-Flow System for Heterogeneous Olefin Polymerization Kinetics. *Macromol. React. Eng.* **2012**, *6* (6–7), 275–279.

(30) Thakur, A.; Wada, T.; Chammingkwan, P.; Terano, M.; Taniike, T. Development of Large-Scale Stopped-Flow Technique and its Application in Elucidation of Initial Ziegler–Natta Olefin Polymerization Kinetics. *Polymers* **2019**, *11* (6), 1012.

(31) Bukatov, G. D.; Goncharov, V. S.; Zakharov, V. A. Interaction of 14CO with Ziegler-type heterogeneous catalysts and effect of interaction products on the determination of the amount of active centers. *Makromol. Chem.* **1986**, *187* (5), 1041–1051.

(32) Shiono, T.; Ohgizawa, M.; Soga, K. Reaction between carbon monoxide and a Ti-polyethylene bond with a MgCl2-supported TiCl4 catalyst system. *Makromol. Chem.* **1993**, *194* (7), 2075–2085.

(33) Tritto, I.; Sacchi, M. C.; Locatelli, P. On the insertion reaction of carbon oxides into metal-carbon bonds of Ziegler-Natta catalysts. *Makromol. Chem., Rapid Commun.* **1983**, *4* (9), 623–627.

(34) Gnanakumar, E. S.; Gowda, R. R.; Kunjir, S.; Ajithkumar, T. G.; Rajamohanan, P. R.; Chakraborty, D.; Gopinath, C. S. MgCl2−6CH3OH: a simple molecular adduct and its influence as a porous support for olefin polymerization. *ACS Catal.* **2013**, *3* (3), 303−311.

(35) Andoni, A.; Chadwick, J. C.; Niemantsverdriet, H. J. W.; Thune, P. C. The Role of Electron Donors on Lateral Surfaces of MgCl2-Supported Ziegler-Natta Catalysts: Observation by AFM and SEM. *J. Catal.* **2008**, *257* (1), 81−86.

(36) Andoni, A.; Chadwick, J. C.; Niemantsverdriet, H. J. W.; Thune, P. C. A preparation method for well-defined crystallites of Mgcl(2)-supported Ziegler-Natta catalysts and their observation by AFM and SEM. *Macromol. Rapid Commun.* **2007**, *28* (14), 1466−1471.

(37) Puhakka, E.; Pakkanen, T. T.; Pakkanen, T. A. Theoretical investigations on Ziegler-Natta catalysis: models for the interactions of the TiCl4 catalyst and the MgCl2 support. *Surf. Sci.* **1995**, *334* (1), 289−294.

(38) D'Amore, M.; Credendino, R.; Budzelaar, P. H. M.; Causá, M.; Busico, V. A periodic hybrid DFT approach (including dispersion) to MgCl2-supported Ziegler−Natta catalysts − 1: TiCl4 adsorption on MgCl2 crystal surfaces. *J. Catal.* **2012**, *286*, 103−110.

(39) Cheng, R. H.; Luo, J.; Liu, Z.; Sun, J. W.; Huang, W. H.; Zhang, M. G.; Yi, J. J.; Liu, B. P. Adsorption of TiCl4 and electron donor on defective MgCl2 surfaces and propylene polymerization over Ziegler-Natta catalyst: A DFT study. *Chin. J. Polym. Sci.* **2013**, *31* (4), 591−600.

(40) Credendino, R.; Liguori, D.; Fan, Z.; Morini, G.; Cavallo, L. Toward a Unified Model Explaining Heterogeneous Ziegler-Natta Catalysis. *ACS Catal.* **2015**, *5* (9), 5431−5435.

(41) Breuza, E.; Antinucci, G.; Budzelaar, P. H. M.; Busico, V.; Correa, A.; Ehm, C. MgCl2-supported Ziegler-Natta catalysts: A DFT-D "flexible-cluster" approach. TiCl4 and probe donor adducts. *Int. J. Quantum Chem.* **2018**, *118* (21), No. e25721.

(42) Hu, J.; Han, B.; Shen, X.; Fu, Z.; Fan, Z. Probing the roles of diethylaluminum chloride in propylene polymerization with MgCl2-supported ziegler-natta catalysts. *Chin. J. Polym. Sci.* **2013**, *31* (4), 583−590.

(43) Muddada, N. B.; Olsbye, U.; Fuglerud, T.; Vidotto, S.; Marsella, A.; Bordiga, S.; Gianolio, D.; Leofanti, G.; Lamberti, C. The role of chlorine and additives on the density and strength of Lewis and Bronsted acidic sites of gamma-Al2O3 support used in oxy-chlorination catalysis: A FTIR study. *J. Catal.* **2011**, *284* (2), 236−246.

(44) Piovano, A.; D'Amore, M.; Wada, T.; Bruzzese, P. C.; Takasao, G.; Thakur, A.; Chammingkwan, P.; Terano, M.; Civalleri, B.; Bordiga, S.; Taniike, T.; Groppo, E. Revisiting the identity of δ-MgCl2: Part II. Morphology and exposed surfaces studied by vibrational spectroscopies and DFT calculation. *J. Catal.* **2020**, *387*, 1−11.

(45) Fachinetti, G.; Floriani, C. Insertion of carbon monoxide into titanium—carbon bonds. *J. Organomet. Chem.* **1974**, *71* (1), C5−C7.

(46) Calderazzo, F. Synthetic and Mechanistic Aspects of Inorganic Insertion Reactions. Insertion of Carbon Monoxide. *Angew. Chem., Int. Ed. Engl.* **1977**, *16* (5), 299−311.

(47) Morra, E.; Giamello, E.; Van Doorslaer, S.; Antinucci, G.; D'Amore, M.; Busico, V.; Chiesa, M. Probing the coordinative unsaturation and local environment of Ti3+ sites in an activated high-yield Ziegler-Natta catalyst. *Angew. Chem., Int. Ed.* **2015**, *54* (16), 4857−4860.

(48) Lunsford, J. H.; Jayne, J. P. Electron Paramagnetic Resonance of Oxygen on ZnO and Ultraviolet-Irradiated MgO. *J. Chem. Phys.* **1966**, *44* (4), 1487−1492.

(49) Tench, A. J.; Holroyd, P. The identification of O2− adsorbed on magnesium oxide. *Chem. Commun. (London)* **1968**, No. 8, 471−473.

(50) Giamello, E.; Murphy, D.; Garrone, E.; Zecchina, A. Formation of superoxide ions upon oxygen adsorption on magnesium-doped magnesium oxide: An EPR investigation. *Spectrochim. Acta, Part A* **1993**, *49* (9), 1323−1330.

(51) Hayyan, M.; Hashim, M. A.; AlNashef, I. M. Superoxide Ion: Generation and Chemical Implications. *Chem. Rev.* **2016**, *116* (5), 3029−3085.

(52) Krimm, S.; Liang, C. Y.; Sutherland, G. B. B. M. Infrared Spectra of High Polymers. II. Polyethylene. *J. Chem. Phys.* **1956**, *25* (3), 549−562.

(53) Kissin, Y. V. Active centers in Ziegler-Natta catalysts: Formation kinetics and structure. *J. Catal.* **2012**, *292*, 188−200.

JACS Au
AN OPEN ACCESS JOURNAL OF THE AMERICAN CHEMICAL SOCIETY

Correlating the Morphological Evolution of Individual Catalyst Particles to the Kinetic Behavior of Metallocene-Based Ethylene Polymerization Catalysts

Maximilian J. Werny,[∇] Jelena Zarupski,[∇] Iris C. ten Have, Alessandro Piovano, Coen Hendriksen, Nicolaas H. Friederichs, Florian Meirer,[*] Elena Groppo,[*] and Bert M. Weckhuysen[*]

Cite This: *JACS Au* 2021, 1, 1996−2008

Read Online

ACCESS | Metrics & More | Article Recommendations | Supporting Information

ABSTRACT: Kinetics-based differences in the early stage fragmentation of two structurally analogous silica-supported hafnocene- and zirconocene-based catalysts were observed during gas-phase ethylene polymerization at low pressures. A combination of focused ion beam-scanning electron microscopy (FIB-SEM) and nanoscale infrared photoinduced force microscopy (IR PiFM) revealed notable differences in the distribution of the support, polymer, and composite phases between the two catalyst materials. By means of time-resolved probe molecule infrared spectroscopy, correlations between this divergence in morphology and the kinetic behavior of the catalysts' active sites were established. The rate of polymer formation, a property that is inherently related to a catalyst's kinetics and the applied reaction conditions, ultimately governs mass transfer and thus the degree of homogeneity achieved during support fragmentation. In the absence of strong mass transfer limitations, a layer-by-layer mechanism dominates at the level of the individual catalyst support domains under the given experimental conditions.

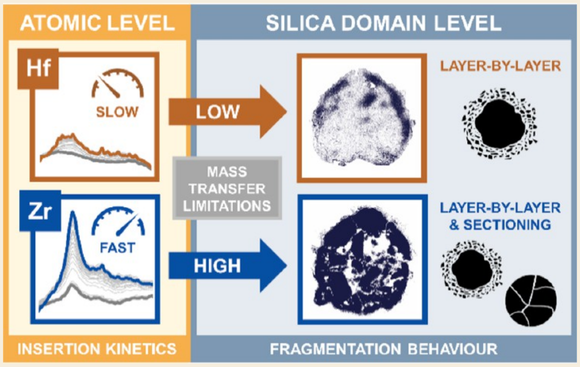

KEYWORDS: *FIB-SEM, fragmentation, kinetics, mass transfer limitations, metallocenes, PiFM, polymerization, probe molecules*

INTRODUCTION

In supported olefin polymerization catalysts, the process of support fragmentation is essential for maintaining a high catalyst activity, controlling the morphology of the polymer particles, and achieving a homogeneous distribution of catalyst residues throughout the polymer matrix.[1,2] During catalyst particle fragmentation, mechanical forces, which arise from the formation of solid polymer at the active sites of the catalyst, cause the support to disintegrate into smaller fragments. As both polymerization and fragmentation proceed, new active sites are continuously exposed to the reaction environment. Ultimately, mass transfer limitations, due to the buildup of polymer and pore blocking, can be partially overcome and the catalyst activity can be sustained or even increased. Since the early reaction stages are critical in defining the morphology of the final polymer particles, several studies have been dedicated toward understanding the process mechanistically. Two simplified models, namely, the layer-by-layer and sectioning models, are often used to describe experimentally observed fragmentation pathways during early reaction stages.[3−9] While the layer-by-layer model involves the progressive fragmentation of the support from its external surface to the interior, the sectioning model is described by a more pronounced and coarser crack formation through the entire catalyst particle, thereby cleaving it into multiple larger fragments. Generally speaking, the morphology, porosity, and mechanical rigidity of the catalyst support all critically affect fragmentation and hence the final polymer morphology and properties.[1,3,10−12] The process also strongly depends on the inherent properties of the catalyst's active sites, the applied reaction conditions, and heat and mass transfer limitations.[6,8,9,11,13,14] Thus, with the aim of obtaining a more comprehensive understanding of fragmentation and the key factors behind it, characterization approaches covering both the scale of the single polymerizing particle and the atomic scale of the active sites must be adopted.

In this work, we introduce a multiscale approach that links the morphological evolution of individual catalyst particles to the kinetic behavior of their active sites. Two structurally analogous silica-supported bridged bis-indenyl metallocene

Received: July 22, 2021
Published: October 8, 2021

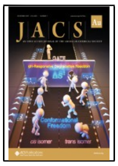

catalysts, which were preactivated with methylaluminoxane (MAO) as a cocatalyst (SiO_2/MAO/M, M = Hf/Zr) during the catalyst synthesis, were examined. Despite the structural similarity of the hafnocene and zirconocene precursors, the two catalysts yielded substantially different productivities when tested in gas-phase ethylene polymerization, with SiO_2/MAO/Zr displaying a more than 40× higher productivity than SiO_2/MAO/Hf. The lower activity of hafnocene complexes compared to zirconocene complexes has long been attributed to an inherently lower chain propagation rate, which results from a stronger metal−carbon bond.[15−18] More recently, a correlation with the predominantly ionic character of the Hf−C bond was established.[19] MAO is also known to be a poor activator for hafnocene complexes as it forms rather stable heterodinuclear compounds with "free" trimethylaluminum (TMA) in equilibrium with its oligomeric part.[20,21] The structurally analogous SiO_2/MAO/Hf and SiO_2/MAO/Zr catalysts, representing two extremes in terms of activity, are thus expected to behave differently during the early stages of the reaction and are therefore ideal candidates for testing our multiscale approach.

The conceptual approach of our work is illustrated in Figure 1. A combination of focused ion beam-scanning electron microscopy (FIB-SEM) and infrared photoinduced force microscopy (IR PiFM) was employed to assess the morphology of individual catalyst particle cross-sections (i.e., the spatial distribution of the support and polymer phases as well as macropores) during the early stages of gas-phase ethylene polymerization (Figure 1A). At the same time, IR spectroscopy in the presence of *d*-acetonitrile as a probe molecule was used to evaluate the fraction of accessible metal sites and their ability to insert electron-rich molecules into the $M{-}CH_3$ bond. The latter represents an elementary step in olefin polymerization catalysis (Figure 1B). Finally, by comparing the morphological data obtained at the single-particle level to the compositional and kinetic data collected at the atomic scale, correlations between the catalyst performance and the properties of the active sites were established.

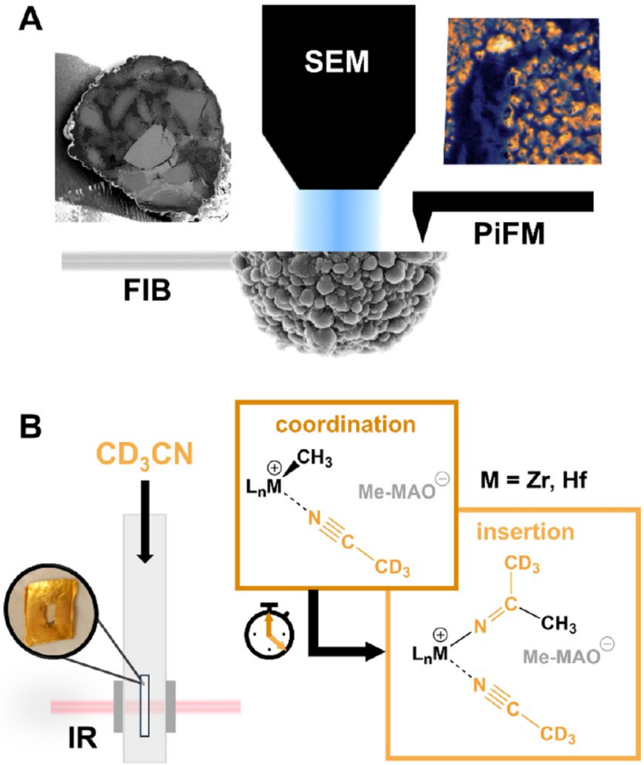

Figure 1. Schematic overview of the multiscale characterization approach applied to the SiO_2/MAO/M (M = Hf, Zr) ethylene polymerization catalysts and the information provided by each technique. (A) Correlated focused ion beam-scanning electron microscopy (FIB-SEM) and infrared photoinduced force microscopy (IR PiFM). (B) Time-resolved IR spectroscopy in the presence of *d*-acetonitrile (d-ACN) as a probe molecule.

RESULTS AND DISCUSSION

Assessment of the Catalyst Performance

The SiO_2/MAO/Hf and SiO_2/MAO/Zr catalysts were prepared following a two-step procedure. First, the 2,2′-biphenylene-bis-2-indenyl MCl_2 complexes were suspended in dried toluene and contacted with MAO at an Al:M ratio of 150. Then, polymer-grade SiO_2 (D_{50} = 25.0 μm, precalcined at 600 °C) was added to the solution to form a slurry, followed by solvent removal at room temperature to produce a free-flowing yellow powder. More experimental details are provided in Section S1 of the Supporting Information. It must be noted that the active species (ion-pairs or heterodinuclear complexes with free TMA) were already formed in solution and then impregnated onto the silica support. The final catalysts do not require any additional activation.

The two catalysts were then tested in the gas-phase polymerization of ethylene using pressurized reactors. Under the adopted experimental conditions (T = 87 °C, P_{C2H4} = 15 bar, and triisobutylaluminum (TiBA) as scavenger; Section S2 and Table S1), SiO_2/MAO/Zr displayed a productivity of about 6300 $g_{PE}/(g_{cat}{\cdot}h)$, while the SiO_2/MAO/Hf system displayed a productivity of 150 $g_{PE}/(g_{cat}{\cdot}h)$ (Table S1). The high temperatures and pressures that were employed during these initial catalytic tests resulted in fast reaction kinetics and high polymer yields (Table S1, see ethylene uptake profiles in Figure S1), thereby impeding any studies on the early stage fragmentation of the two catalyst systems under industrial conditions.

Internal Morphology of the Catalyst Particles

To obtain low polymer yield samples that are representative of the initial stages of ethylene polymerization (i.e., the prepolymerization regime), the two catalysts were prepolymerized in gas phase under mild conditions (i.e., 1.6 bar C_2H_4 and room temperature; Section S3, Table S2, and Figure S2). Remarkably, the two catalysts displayed very similar productivities under the given prepolymerization conditions after 60 min of ethylene polymerization, contrary to the previously mentioned gas-phase polymerization experiments (SiO_2/MAO/Hf, 6.7 g of polyethylene (PE) per gram of catalyst; SiO_2/MAO/Zr, 5.8 g of PE per gram of catalyst; Table S2). By means of FIB cutting according to a procedure from the literature,[22] the cross-sections of randomly selected catalyst particles were accessed and consequently imaged at a nanometer-scale resolution using SEM and PiFM. The SEM images were segmented for the improved visualization of the fragmentation process (Figures 2, 3, S2, and S3; see the Supporting Information for further details).

Figures 2 and 3 show representative cross-sectional SEM images of the SiO_2/MAO/Hf and SiO_2/MAO/Zr catalyst materials, respectively, at multiple reaction stages (i.e., pristine and after 10, 30, and 60 min of ethylene polymerization). As

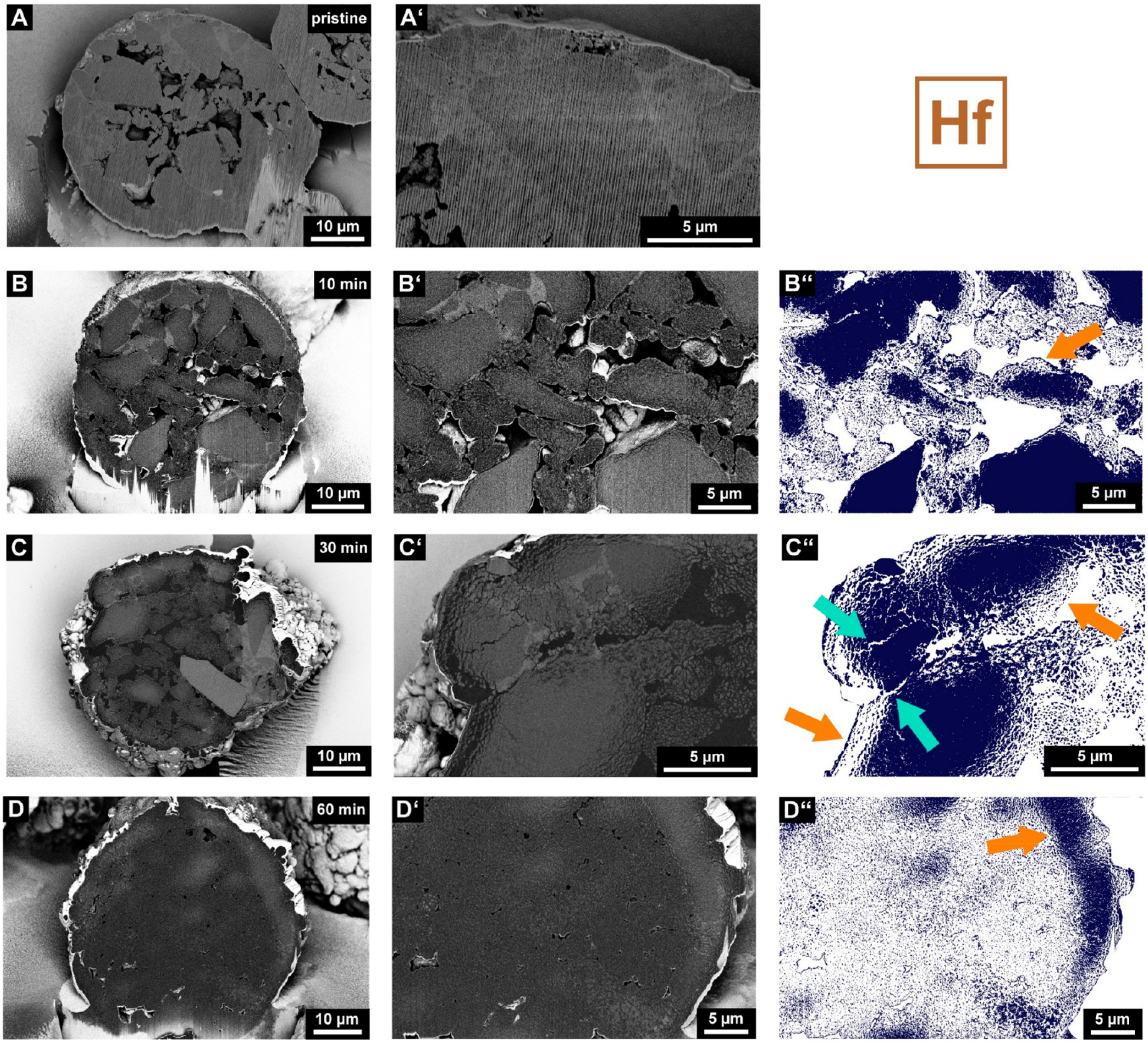

Figure 2. Scanning electron microscopy (SEM) images displaying the cross-sections of a pristine (A and A′), 10 (B and B′) min, 30 (C and C′) min, and 60 min (D and D′) prepolymerized particle of the SiO_2/MAO/Hf catalyst material. Images were acquired in backscattered electron mode (BSE; silica support, light gray; polyethylene, dark gray; pores, predominantly black). The close-up images (B′, C′, and D′) were segmented (B″, C″, and D″) to clearly illustrate fragmentation events and the morphology of the particles (the silica support is represented in dark blue, and layer-by-layer and sectioning pathways are indicated by orange and turquoise arrows, respectively). Vertical lines, which originate from the focused ion beam (FIB) cutting procedure, are visible in certain SEM images.

can be seen in the SEM images of the pristine catalyst particles (Figures 2A and A′ and 3A and A′), the spherical support of the particles is constituted by several larger domains of silica that are bound to each other by a phase with a different density, presumably alkali silicate.[3] Furthermore, the catalyst particles feature numerous macropores that are postulated to be partially connected (Figures S3 and S4). This interconnected pore network is highly beneficial for ethylene diffusion into the particle interior, especially in the initial reaction stages.

The segmented SEM images of the 10 min prepolymerized SiO_2/MAO/Hf and SiO_2/MAO/Zr particle cross-sections (Figures 2B−B″ and 3B−B″) do indeed indicate polymerization activity in the particle interior. In the case of the SiO_2/MAO/Hf system, most of the larger constituent silica domains (light gray in the backscattered electron mode, BSE) display mild fragmentation in their outer sphere after 10 min of polymerization (Figures 2B−B″). The smaller silica domains, on the other hand, feature a more advanced degree of fragmentation that penetrates the entire silica domain. Up to this reaction stage, we assume that gas-phase ethylene can freely diffuse into the internal pore space of the particle and polymerize on all exposed external and internal surface areas of the catalyst particle. In general, only a limited amount of PE (dark gray in BSE mode) was formed, and large macropores were still clearly visible in the particle. Under the given reaction conditions, the individual silica domains seem to fragment according to a layer-by-layer mechanism (indicated

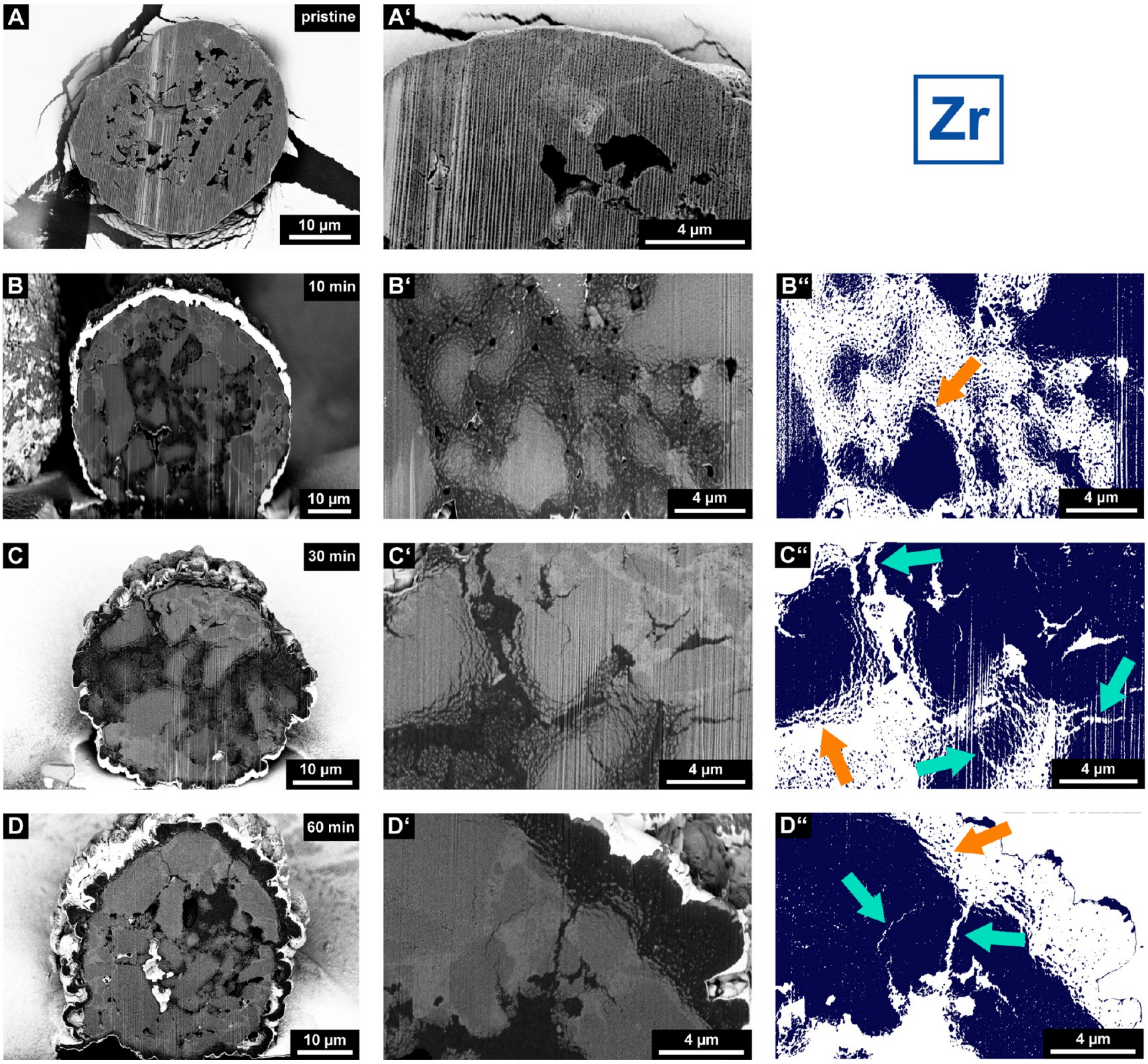

Figure 3. Scanning electron microscopy (SEM) images displaying the cross-sections of a pristine (A and A′), 10 (B and B′) min, 30 (C and C′) min, and 60 min (D, D′) prepolymerized particle of the SiO_2/MAO/Zr catalyst material. Images were acquired in backscattered electron mode (BSE; silica support, light gray; polyethylene, dark gray; pores, predominantly black). The close-up images (B′, C′, and D′) were segmented (B″, C″, and D″) to clearly illustrate fragmentation events and the morphology of the particles (the silica support is represented in dark blue, and layer-by-layer and sectioning pathways are indicated by orange and turquoise arrows, respectively). Vertical lines, which originate from the focused ion beam (FIB) cutting procedure, are visible in certain SEM images.

by an orange arrow in Figure 2B″), provided that ethylene gas can access the inner volume of the particle.

Further polymerization evidently leads to a significant decrease in the macropore volume and more pronounced fragmentation (Figure S3). While the 30 min polymerized catalyst particle (Figures 2C–C″) still features larger isolated fragments of the support in the size range of micrometers, the 60 min polymerized particle (Figures 2D–D″) is characterized by a high degree of homogeneous support fragmentation. In fact, the cross-section shows nanometer-sized fragments that are finely dispersed in the PE matrix (Figure 2D″). Remnants of the support in the outer sphere of the catalyst point to the active involvement of the particle interior in the polymerization process, presumably due to the absence of strong mass transfer limitations (Figure 2D″). While the catalyst predominantly fragmented according to a layer-by-layer mechanism (Figures 2B″, C″, and D″; indicated by orange arrows), local diffusion limitations and stress build-up may, to a limited extent, induce the formation of larger cracks in the support matrix at higher PE yields (i.e., sectioning at the support granulate level, indicated by turquoise arrows in Figure 2C″; also refer to Figure S5).

When comparing the SiO_2/MAO/Zr catalyst system to the SiO_2/MAO/Hf system, no pronounced differences in catalyst support fragmentation are apparent after 10 min of ethylene polymerization (Figures 3B–B″). Similar to the SiO_2/MAO/Hf catalyst material, accessible silica domains begin to fragment according to a layer-by-layer mechanism upon

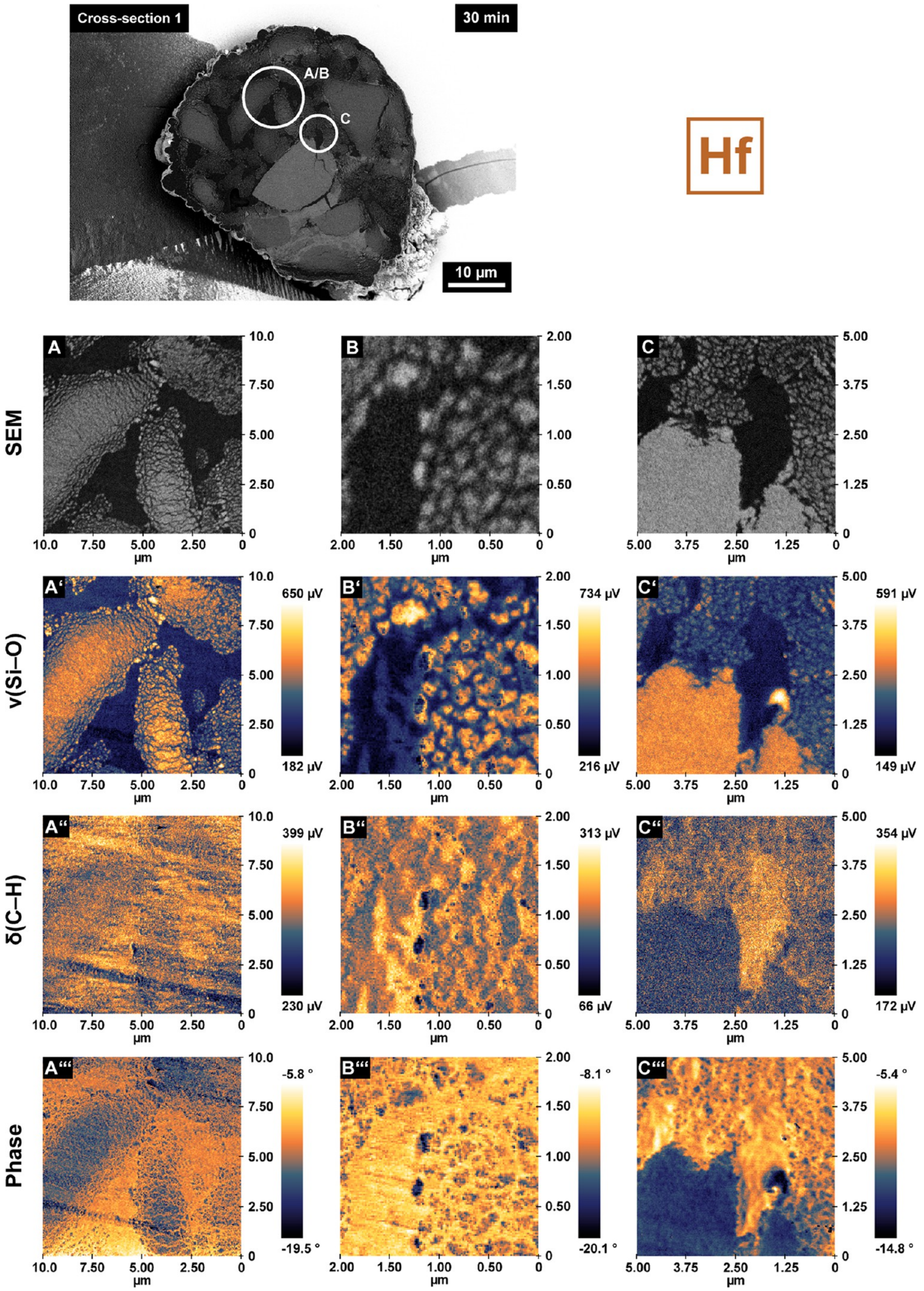

Figure 4. Local catalyst morphology as recorded by scanning electron microscopy (SEM; A, B, C), chemical composition as imaged by infrared photoinduced force microscopy (IR PiFM) (ν(Si–O), 1050–1030 cm^{-1}, A′–C′ and δ(C–H), 1472–1460 cm^{-1}, A″–C″), and relative mechanical properties as determined by phase shift imaging (A‴–C‴). All data were collected on the cross-sections of a single 30 min prepolymerized SiO$_2$/MAO/Hf particle (same particle as in Figure 2C, characterized at a different depth; measurement areas are indicated by circles in the SEM images). Images in panels B–B‴ were recorded in the same area as those in panels A–A‴ but at a higher magnification.

exposure to ethylene (Figure 3B″, indicated by an orange arrow). Indications of a more heterogeneous fragmentation pathway are, however, visible in the later reaction stages (Figure 3C−C″ and D−D″). In contrast to the SiO_2/MAO/Hf system, large unfragmented support domains are still visible after 30 min for the SiO_2/MAO/Zr system (Figures 3C−C″). Interestingly, the cross-section of the 60 min prepolymerized particle also features sizable pristine support domains along with a thick polymer layer that covers the outer surface of the catalyst particles (Figures 3D−D″ and Figure S4). While the layer-by-layer mechanism dominates the fragmentation in the early reaction stages at both the silica domain and the particle level (indicated by orange arrows in Figure 3), the sectioning mechanism contributes more strongly under the imposed mass transfer limitations at later reaction stages (indicated by turquoise arrows in Figure 3). With the particle practically enveloped in a growing layer of PE yet still active in certain domains, the significant accumulation of stress in the particle becomes inevitable. This pressure buildup induces ruptures and more pronounced crack formation,[23] resulting in the cleavage of larger support fragments (indicated by turquoise arrows in Figures 3C″ and D″). It must be noted that the outer layers of the catalyst particles in both catalyst systems seem to fragment gradually according to a layer-by-layer mechanism (as indicated by an orange arrow for SiO_2/MAO/Zr in Figure 3D″).

To verify our observations, additional particles of the two 60 min prepolymerized catalysts were investigated (Figure S5). While most of the particles within a particular batch demonstrated the expected fragmentation behavior, a certain degree of interparticle heterogeneity was nevertheless apparent. A strong correlation between the catalyst particle fragmentation and the particle size[24−26] as well as that between the dimensions, accessibility, and connectivity of the macropore network is expected. This can account for differences in the fragmentation degree and, possibly, the involvement of a particular fragmentation mechanism.

Chemical Composition at a Sub-20 nm Resolution

In principle, the analysis of the SEM images of both catalysts (Figures 2 and 3) via segmentation into their constituent phases (i.e., PE, silica, and pore space; Figures S3 and S4), should yield the relative composition of each cross-section. However, the analysis is hampered by (i) the limited number of particles that are assessed per reaction stage; (ii) the 2D nature of the data; (iii) the degree of polymerization, which varies between particles (Figure S5); and (iv) the detection limit (resolution) of the applied SEM technique. Indeed, at high degrees of polymerization and fragmentation, such as those in the 30 and 60 min prepolymerized SiO_2/MAO/Hf cross-sections, a substantial amount of silica fragments remains undetected due to their high dispersion and limited size (nanometer regime).

A nanoscale imaging technique that is arguably better suited to uncovering structural and compositional heterogeneities in our challenging composite materials is PiFM. In the field of polymer science and related disciplines, PiFM[27,28] has been extensively used together with AFM-IR[29−33] to characterize multicomponent polymer materials at high spatial resolutions. Inspired by this, we used PiFM to characterize the cross-sections of a single 30 min prepolymerized SiO_2/MAO/Hf particle at multiple locations and depths (Figures 4, S6, S7, S8, all cross-section 2; and S9, cross-section 1). Nanoscale infrared and topographic imaging[27,28,34−40] yielded information on both the chemical composition and morphology of the sample at a sub-20 nm resolution.

Figure 4 shows correlated SEM images, IR PiFM, and phase shift maps collected at different locations on the above-mentioned particle cross-section (the image in panel B was recorded in the same area as panel A but at higher magnification). The IR PiFM maps were recorded in noncontact mode[36] (amplitude ratio set point of 80%, attractive van der Waals force regime; see Table S3 and the Supporting Information for more details) at characteristic wavelengths for the Si−O stretching vibration[41,42] (1050−1030 cm^{-1}, ν, Figure 4A′−C′) and the symmetric C−H bending vibration of the methylene group[30−32] (1472−1460 cm^{-1}, δ, Figure 4A″−C″). The IR PiFM data stand in excellent agreement with the corresponding SEM images and yield a remarkably clear differentiation between the silica and PE phases. Multiple larger domains of the silica support have partially fragmented following the layer-by-layer mechanism. Silica fragments smaller than 50 nm, infused with polymer that was presumably formed upon exposure of new active sites to ethylene gas, can be observed in the periphery of these domains (Figures 4A′ and B′). Figure 4C−C″ shows a polymer-rich domain in close proximity to a larger network of cracks in the support (Figure S7, cross-section 1). It is conceivable that the emergence of larger amounts of polymer in this particular area resulted in the accumulation of stress in the support, ultimately inducing the formation of cracks. Alternatively, the buildup of stress over the entire particle may have also contributed. Irrespective of the exact formation pathway, the emergence of large and partially unfilled cracks in the pristine support (Figure S7, cross-section 1) will expose new active sites that will consequently contribute to the polymerization and fragmentation of the particle. A similar showcase for PE-induced crack formation is provided in the Supporting Information (Figure S8, cross-section 2).

Interestingly, the phase shift maps in Figure 4 (Figure 4A‴−C‴) display a striking amount of detail, revealing a complex network of overlapping thread-like PE domains in close vicinity to the formed fragments. In general, the phase channel represents a promising complementary imaging tool[43,44] due to its correlation with mechanical material properties. It corresponds to the absolute difference in phase between the external excitation (driver) and the tip response and is governed by the dissipation of energy from the tip to the sample.[39] This energy dissipation is strongly affected by mechanical material properties such as stiffness, adhesion, and viscoelasticity.[45−47] In general, the set point and drive amplitude of the cantilever must be optimized to obtain qualitative insights into the mechanical properties of a given material.[48,49] In our case, phase maps were recorded at a 60% set point and 3 nm drive amplitude to enhance the tip−sample contact[36] (hard tapping regime, repulsive interactions dominant; Table S3 and Figure S9).

As is evident from Figures 4A‴−C‴, higher phase shift values were obtained for PE, therefore indicating a lower repulsion of the tip from the polymer-rich domains relative to the silica fragments. This is assumed to be a result of the lower mechanical stiffness and higher viscoelasticity of the PE phase. The overall negative phase shift values result from the net repulsive and dissipative force experienced during heavy tapping (Table S3 and Figure S9).

Point spectra recorded of the silica domains, PE/silica composites (Figure 5), and reference materials (Figures S10 and S11) further helped to unambiguously assign the imaged phases. Due to the high degree of intermixing of the silica and PE, it was not possible to acquire point spectra of pure PE on the prepolymerized catalyst cross-section. Furthermore, the PE phase displayed a high sensitivity toward the incident IR laser beam (Figure S12, see Supporting Information for further details). Despite this, PiFM proved to be suitable for the detection and differentiation of the pristine and fragmented support domains, the bulk polymer phase, and the related composite phases at an unparalleled spatial resolution (<20 nm) and also yielded insights into fragmentation events and the associated release of buried active sites.

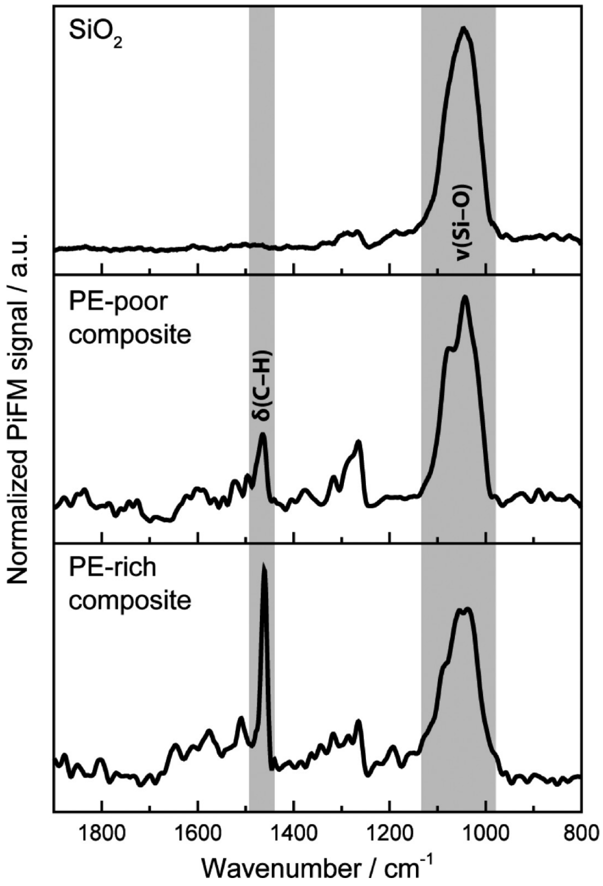

Figure 5. Normalized PiFM spectra of the silica support and of PE/silica composites with different amounts of PE.

Probing the Kinetics of Insertion into the M−CH_3 Bond

To elucidate the reasons for the different fragmentation behaviors of the two catalysts and their similar productivities under prepolymerization conditions, we designed a series of FT-IR spectroscopy experiments in the presence of acetonitrile as a probe molecule. FT-IR spectroscopy of adsorbed probes is one of the most sensitive methods to retrieve information on the properties of surface sites and has been largely used to characterize heterogeneous catalysts at a molecular level.[50,51] This also applies to heterogeneous olefin polymerization catalysts such as the Phillips[52,53] and Ziegler-Natta[54−57] catalysts. Owing to its mildly basic character, CO is often used as a molecular probe to differentiate between sites based on their acidity. Previous works demonstrate that CO at 100 K is indeed able to probe Lewis acid sites (LAS) belonging to MAO/TMA in SiO_2/MAO/metallocene catalyst materials, while it has more difficulty reaching the metallocene cations.[58−60] By being inserted into metal−alkyl bonds, CO can also form acyl species.[61] Furthermore, CO has traditionally been used to quantify the number of active sites in polymerization catalysts.[62−68]

In this work, acetonitrile was chosen as a probe molecule over CO due to its comparatively higher basicity.[69−74] Hence, it is better suited to probing metal cations. More importantly, acetonitrile can also be inserted into transition metal alkyl bonds to form aza-alkenylidenes, as demonstrated for different cationic titanium and zirconium complexes.[75−78] By using acetonitrile as a probe molecule, the acidity and number of the active sites and their ability to insert electron-rich molecules can be assessed simultaneously. All are critical factors in the context of olefin polymerization. It is important to note that the insertion of acetonitrile into the metal−alkyl bond is not affected by diffusion limitations (related to the buildup of polymer at the particle surface). Therefore, the insertion rates evaluated by this method provide direct insights into the inherent insertion ability of the active sites. To the best of our knowledge, there are no similar reports in literature on the use of acetonitrile as a probe or insertion molecule for silica-supported metallocene-based catalyst materials.

The insertion rate of acetonitrile and thus the reactivity of the SiO_2/MAO/Hf and SiO_2/MAO/Zr catalyst materials was determined by means of time-resolved FT-IR spectroscopy. A blank experiment was also conducted on a SiO_2/MAO material for comparison. Deuterated acetonitrile (d-ACN) was used to overcome band doubling due to Fermi resonance effects.[70] As a consequence of its interaction with the LAS sites, the $\nu(C{\equiv}N)$ vibrational mode is expected to increase in energy with respect to the vibrational mode of the free molecule (2265 cm^{-1}). This shift is proportional to the strength of the Lewis acid−base couple. Moreover, the $\nu(C{=}N)$ vibration of the aza-alkenylidene species is expected to decrease in another well-defined spectral region (1720−1600 cm^{-1}) without overlapping with the bands of chemisorbed d-ACN. Figure 6 shows the sequence of FT-IR spectra for SiO_2/MAO, SiO_2/MAO/Hf, and SiO_2/MAO/Zr upon exposure to d-ACN over a period of 3 h in the spectral region of 2400−1300 cm^{-1}. The insets show a magnification of the same spectra in the 1720−1600 cm^{-1} range to highlight the bands assigned to the Zr- and Hf aza-alkenylidene species (spectra are reported after the subtraction of the spectrum collected before the introduction of d-ACN).

The initial spectra of the SiO_2/MAO, SiO_2/MAO/Zr, and SiO_2/MAO/Hf catalyst materials (black in Figure 6) are very similar to each other and are dominated by the vibrational features of silica. In addition to these, a limited number of low-intensity bands can be observed. The bands at 1500−1350 cm^{-1} are assigned to the bending vibrational modes of CH_3 groups belonging to MAO (i.e., Al−CH_3 species), Si−CH_3, or Si−O−Al$(CH_3)_2$ species, which might originate from the reaction of MAO/TMA with siloxane bridges at the silica surface. According to Ystenes et al.,[79] the $\delta_{asym}(CH_3)$ vibrations of terminal Al−CH_3 in MAO are expected to appear at approximately 1435 cm^{-1}, while the corresponding $\delta_{sym}(CH_3)$ vibrational mode is expected to appear around 1300 cm^{-1} and is hence not detectable due to the broad and intense modes of SiO_2, which dominate the spectral region below 1350 cm^{-1}. The $\delta_{asym}(CH_3)$ mode of the −OCH_3 species is expected

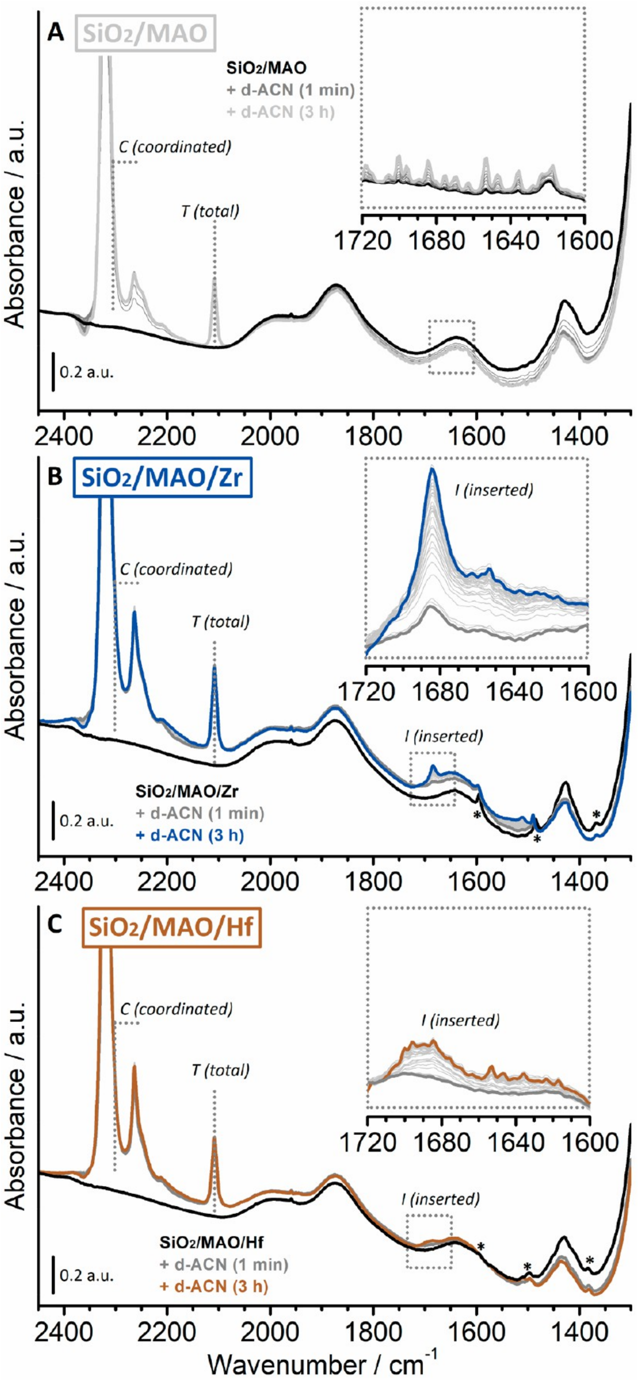

Figure 6. FT-IR spectra recorded of the SiO_2/MAO reference material before (black) and after (gray) the interaction with d-ACN at room temperature over a time period of 3 h (light gray) (A). The inset shows the 1720−1600 cm^{-1} region for the same sequence of FT-IR spectra after the subtraction of the spectrum collected prior to the introduction of d-ACN. Comparable FT-IR spectra for the SiO_2/MAO/Zr (B) and SiO_2/MAO/Hf (C) catalyst materials. The bands labeled with asterisks (*) are attributed to vibrations of the indenyl ligands in SiO_2/MAO/Zr and SiO_2/MAO/Hf, respectively.

to contribute at around 1470 cm^{-1} [79] but is barely identifiable in our spectra (low intensity and broad band). Finally, the very weak and narrow bands labeled with asterisks are attributed to the vibrations of the indenyl ligands in the activated zirconocene and hafnocene complexes.

In all cases, several intense absorption bands immediately appeared in the 2400−2000 cm^{-1} region upon introduction of d-ACN, which are discussed as follows:

1) The absorption band at 2108 cm^{-1} (indicated as *T*, total in Figure 6) is due to $\nu(CD_3)$. This band is insensitive to the absorption sites[71] and thus not analytically relevant. It will therefore be used as an internal standard to quantify the total amount of d-ACN on the sample, comprising d-ACN coordinated to the LAS sites (belonging to both MAO/TMA and the methylated metallocenes) and physisorbed d-ACN. The concentration of d-ACN in the sample depends on both the equilibrium pressure and the sample mass, the latter being difficult to evaluate due to the complexity of the experimental procedure.
2) In the $\nu(C{\equiv}N)$ region (2400−2200 cm^{-1}), all spectra are dominated by an intense and symmetric absorption band centered at 2320 cm^{-1} (i.e., an upward shifted by 55 cm^{-1} with respect to that of free d-ACN at 2265 cm^{-1}), which is due to the interaction of d-ACN with LAS sites. The band accounts for both the LAS sites of the MAO/TMA species and the Zr or Hf cations (for comparison, d-ACN adsorbed on coordinatively unsaturated Al(III) sites on a triethylaluminum (TEAl)-pretreated SiO_2 features a band at 2317 cm^{-1}).[80] We expect that the MAO/TMA species are predominantly probed by d-ACN because of their much higher relative content in the two samples (Al/M = 150). Since the associated band rapidly goes out of scale, the total amount of accessible LAS sites was derived from the spectral intensity at 2300 cm^{-1} for each experiment (indicated as *C*, coordinated in Figure 6).
3) A second absorption band was observed in the same spectral region at 2265 cm^{-1} with a shoulder at around 2250 cm^{-1}. The former is ascribed to liquid-like d-ACN and is the only absorption band that decreases in intensity upon degassing (not shown).[81] The assignment of the shoulder is more challenging. The low frequency of the $\nu(C{\equiv}N)$ band suggests a bridging coordination mode, as was observed for other ligands and as suggested for nitriles interacting with two cations in zeolites.[82] The appearance of this absorption band indicates the presence of LAS sites that are close enough to each other to be simultaneously complexed by both the nitrogen lone pair and the π-type bonding electrons of the same acetonitrile molecule. A similar absorption band was also observed for d-ACN adsorbed on a Cr(II)/SiO_2 Phillips catalyst material activated with TEAl and attributed to a Cr(II)···Al(III) bimetallic species.[80]
4) In the presence of d-ACN, the SiO_2/MAO/Zr (Figure 6B) and SiO_2/MAO/Hf (Figure 6C) catalyst materials feature additional weak absorption bands that appear in the 1700−1300 cm^{-1} spectral region, which slowly grow in intensity over time. In particular, two well-defined absorption bands appear at 1684 and 1690 cm^{-1} for the SiO_2/MAO/Zr and SiO_2/MAO/Hf catalyst materials, respectively (labeled as band *I*, inserted in Figure 6B and C). These absorption bands are attributed to the $\nu(C{=}N)$ of an aza-alkenylidene species that is formed due to the insertion of d-ACN into the Zr−CH_3 and Hf−CH_3 bonds (Figure 1B). At the same time, all the

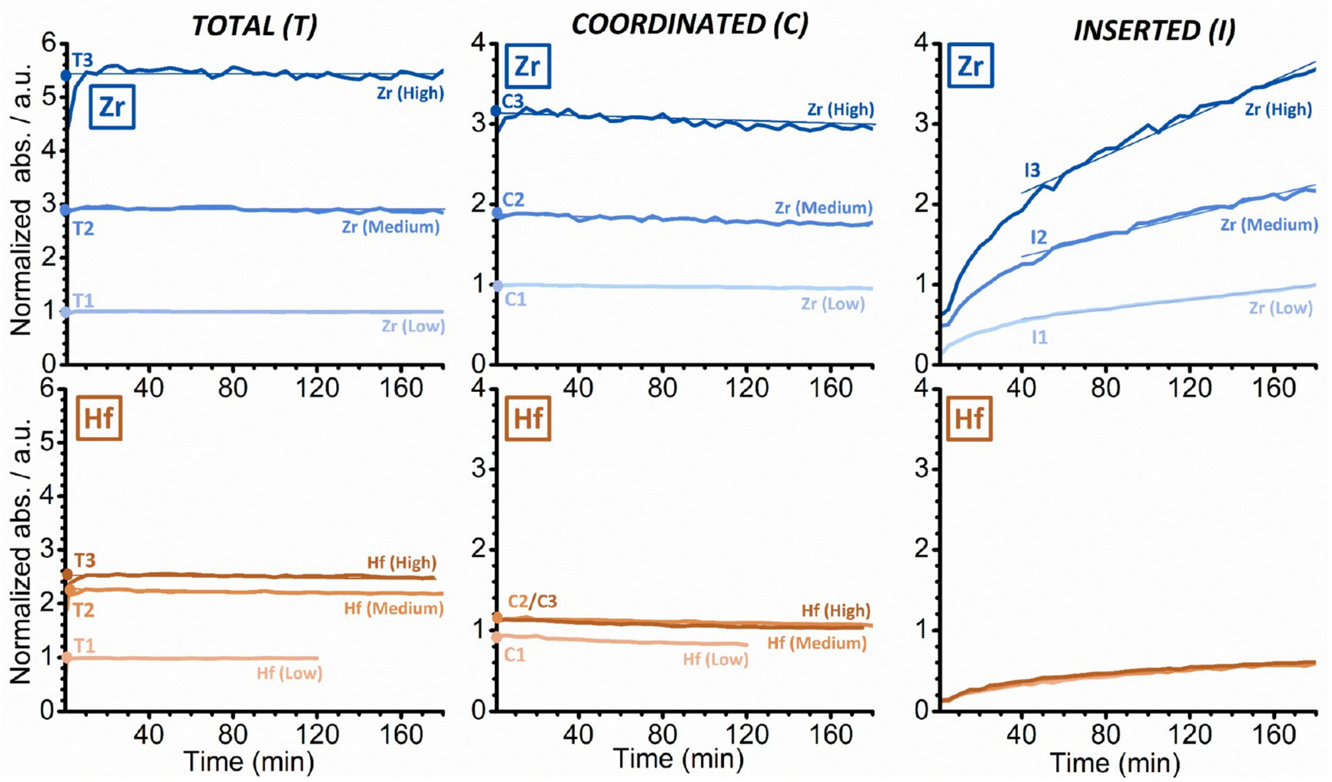

Figure 7. Evolution of the intensities of the FT-IR absorption bands *T* (total amount of d-ACN), *C* (coordinated d-ACN), and *I* (inserted d-ACN) as a function of time, which were derived from a series of experiments in which SiO_2/MAO/Zr (top) and SiO_2/MAO/Hf (bottom) were treated with d-ACN at three different concentrations (high, medium, and low). The data were normalized to the optical thickness of the pellets and rescaled with respect to the Zr (Low) experiment for comparison.

absorption bands ascribed to the activated metallocene complexes (asterisks) were perturbed. For example, the absorption bands of SiO_2/MAO/Zr at 1593 and 1485 cm^{-1} are upward shifted by a few inverse centimeters, while the absorption band at 1370 cm^{-1} is lower in intensity. Altogether, this suggests that the coordination modes of the indenyl ligand are changing concomitantly to the coordination of d-ACN to the Zr or Hf cation and its subsequent insertion into the metal−alkyl bond.

In fact, the two absorption bands at 1684 and 1690 cm^{-1}, which are ascribed to the Zr and Hf aza-alkenylidene species respectively, grow at different rates. A significantly faster increase was observed for the SiO_2/MAO/Zr system in comparison to that for the SiO_2/MAO/Hf system. Interestingly, the rate of insertion of d-ACN in the M−CH_3 bond correlates well with the catalyst productivity in ethylene polymerization, as determined by the previously mentioned gas-phase experiments (15 bar ethylene, 87 °C), and not with those determined from the relatively mild prepolymerization experiments. Based on the literature,[19−21] our experimental observations may be explained by both: (1) a lower number of active species in the SiO_2/MAO/Hf catalyst material due to the formation of stable heterodinuclear compounds with TMA and (2) a different inherent insertion ability of the electron-rich d-ACN in the M−CH_3 bonds in the two catalysts.

To clarify the reasons behind the different behaviors of the two structurally analogous catalysts, a series of FT-IR spectroscopy experiments with different d-ACN concentrations, similar to those discussed in Figure 6, were conducted. In total, three experiments were performed for each catalyst (high, medium and low d-ACN concentration). Some of the experiments were repeated to verify the reproducibility of the results. In all experiments, the intensities of the bands *T* (total amount of d-ACN), *C* (coordinated d-ACN), and *I* (inserted d-ACN) were monitored as a function of time (Figure 7, after normalization to the optical pellet thickness and rescaling to the Zr (low) experiment for comparison).

For both the SiO_2/MAO/Zr system and the SiO_2/MAO/Hf system, the *T* and *C* bands almost immediately reach their maximum intensity (left and middle in Figure 7, respectively), irrespective of the d-ACN concentration. Based on this, we conclude that there are no intrinsic diffusion limitations. The *C* bands, on the other hand, slightly decrease in intensity over time due to the gradual insertion of coordinated d-ACN into the M−CH_3 bond. The maximum intensities of the *T* and *C* bands were determined by extrapolating the linear part at time zero ($t = 0$) and are reported in Figure S13. In contrast to these, band *I* (right in Figure 7) grew at an almost constant rate after the first 30 min and did not saturate even after 3 h of reaction. This observation is in agreement with the very slow insertion kinetics of d-ACN in other zirconocene and hafnocene complexes, as reported in the literature.[75−78] The insertion rate was derived from the slope of a linear fit that was applied to the curves and can also be found in Figure S13.

For the SiO_2/MAO/Zr system, the amount of coordinated d-ACN was found to depend on the total d-ACN concentration (Figures 7 and S12): The higher the concentration or pressure of the electron-rich probe, the higher the fraction of the sites able to coordinate it (comprising both the LAS sites of MAO/TMA and the zirconocene cations). This correlation, however, was not linear.

A threefold increase in the total concentration (from T1 to T2) led to twice the amount of coordinated d-ACN (from C1 to C2), while a further twofold increase (from T2 to T3) only resulted in 1.6× the number of coordinated species (from C2 to C3). Interestingly, the d-ACN insertion rates scale perfectly with the fraction of sites able to coordinate d-ACN, i.e., *I* increases by a factor of 2 from I1 to I2 and by a factor of 1.7 from I2 to I3.

Contrary to the SiO_2/MAO/Zr system, the intensities of the three bands *T*, *C*, and *I* in the SiO_2/MAO/Hf system rapidly reached a saturation level. Moreover, for comparable d-ACN total concentrations (*T*), the amount of coordinated d-ACN (*C*) was lower for SiO_2/MAO/Hf than for SiO_2/MAO/Zr. This difference became more pronounced at higher d-ACN concentrations. The data stand in agreement with the reported detrimental effect of MAO/TMA on hafnocene complexes relative to comparable zirconocene complexes.[20,21] However, this only partly explains the lower insertion rate for the SiO_2/MAO/Hf system. A comparison of the experiments performed on the two catalysts at low d-ACN concentrations (T1) revealed that the number of sites coordinating d-ACN (C1) in the SiO_2/MAO/Hf system corresponds to 90% of those found in the SiO_2/MAO/Zr system, while the insertion rate (I1) is only 75% of that observed for the SiO_2/MAO/Zr system. These findings indicate that the insertion kinetics of d-ACN in the SiO_2/MAO/Hf system are inherently slower than in the SiO_2/MAO/Zr system. As recently suggested,[19] this is explained by the more pronounced ionic character of the Hf−C bond compared to the Zr−C bond and, consequently, the larger enthalpic contribution to the activation barrier for Hf−C bond cleavage.

As a final comment, the limited amount of d-ACN that can adsorb on SiO_2/MAO/Hf (i.e., *T* and *C* signals do not increase significantly when moving to a high d-ACN concentration) might be also explained by a filling of the pore channels that facilitate the diffusion of d-ACN. This hypothesis is compatible with the above-discussed theory on stable heterodinuclear compounds that are formed with TMA.

Correlating Data from Different Length Scales

Based on the time-resolved FT-IR data, which were collected in the presence of d-acetonitrile, we conclude that the insertion kinetics of the SiO_2/MAO/Zr catalyst material are notably faster that those of the SiO_2/MAO/Hf catalyst material. This is mainly due to the following two reasons: (i) the active sites are more accessible (i.e., less stable heterodinuclear compounds with TMA) in SiO_2/MAO/Zr and (ii) the active sites are intrinsically faster. According to the FIB-SEM and IR PiFM data, the faster kinetics of the SiO_2/MAO/Zr catalyst material result in the buildup of large amounts of PE at the particle surface as well as in any accessible pores. The imposed diffusion limitations restrict the access of ethylene molecules to the particle interior, thereby limiting both polymerization and concurrent fragmentation under the given experimental conditions. In contrast to this, the kinetically slower SiO_2/MAO/Hf catalyst system seems to be less affected by diffusion limitations, which manifests in a more homogeneous fragmentation of the catalyst support. This hypothesis is also reflected by the unexpectedly low PE yield of the kinetically superior SiO_2/MAO/Zr catalyst in comparison that of the SiO_2/MAO/Hf catalyst under prepolymerization conditions, i.e., 5.8 g of PE per gram of the SiO_2/MAO/Zr catalyst vs 6.7 g of PE per gram of the SiO_2/MAO/Hf catalyst (Table S2). In fact, low PE yields, which are linked with the buildup of the polymer at the particle surface and thus mass transfer limitations, have also recently been reported by Zanoni et al.[9] for a comparable silica-supported zirconocene during gas-phase ethylene polymerization at both 9 and 15 bar.

CONCLUSIONS

Our multiscale combined microscopy and spectroscopy approach, which is based on focused ion beam−scanning electron microscopy (FIB-SEM), infrared photoinduced force microscopy (IR PiFM), and time-resolved IR spectroscopy of adsorbed d-acetonitrile (d-ACN), delivered new mechanistic insights into the early stage fragmentation of two structurally analogous metallocene-based catalyst materials with different kinetic profiles during the gas-phase polymerization of ethylene. As summarized in Figure 8, insertion kinetics and associated mass transfer limitations were identified as being critical for the homogeneity of catalyst support fragmentation during the early reaction stages of ethylene polymerization. In the absence of strong mass transfer limitations that are imposed by both the surface buildup of polyethylene and pore filling, the individual support domains disintegrate more uniformly according to a layer-by-layer mechanism, as was observed for the kinetically slower SiO_2/MAO/Hf catalyst material. Stronger mass transfer limitations, as evident for the faster SiO_2/MAO/Zr catalyst material, significantly inhibit or delay fragmentation during the initial reaction stages of ethylene polymerization under given experimental conditions. This is postulated to induce higher stress accumulation and thus a larger contribution from the sectioning mechanism at the level of the individual silica domains and, possibly, the particle level.

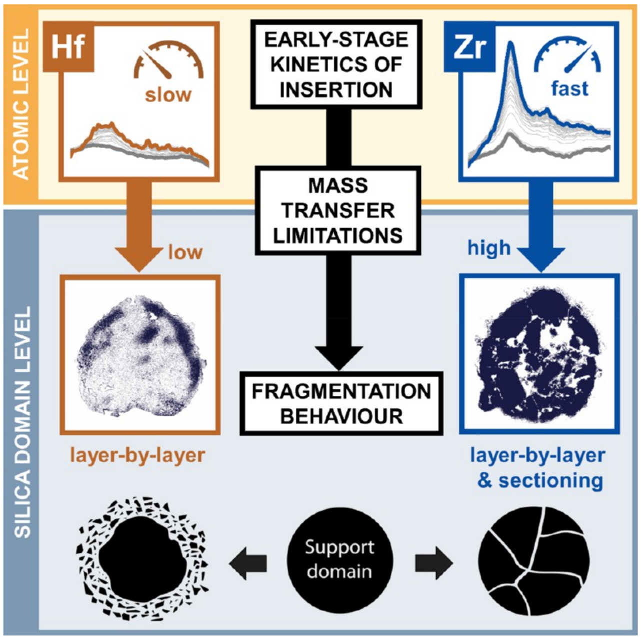

Figure 8. Schematic illustration of the main insights gained from our multiscale microscopy−spectroscopy approach. Insertion kinetics and associated mass transfer limitations are critical for the homogeneity of catalyst support fragmentation during the early stages of ethylene polymerization.

Time-resolved IR spectroscopy in the presence of d-ACN provided an explanation for the different experimentally observed insertion kinetics. Not only are the active sites of SiO_2/MAO/Hf less accessible (due to more stable heterodinuclear adducts with TMA), they are also intrinsically slower than the active sites of SiO_2/MAO/Zr. It is worth noticing that these conclusions are in agreement with theoretical and experimental data reported in literature. This unprecedented spectroscopic approach can also be applied to similar catalysts to evaluate their accessibility and insertion behavior.

The correlated FIB-SEM-IR PiFM approach, on the other hand, delivered highly resolved morphological information and facilitated the spectroscopic identification of the support, polymer, and composite phases. It represents a novel analytical approach that can also be extended to other industrial-grade catalysts for obtaining information on structure, chemical composition, and mechanical parameters at unparalleled spatial resolutions and, in the case of full catalyst particles, at variable probing depths via FIB cutting.

■ ASSOCIATED CONTENT

Supporting Information

The Supporting Information is available free of charge at https://pubs.acs.org/doi/10.1021/jacsau.1c00324.

Information on catalyst preparation, testing, prepolymerization, and characterization (PDF)

■ AUTHOR INFORMATION

Corresponding Authors

Bert M. Weckhuysen − *Inorganic Chemistry and Catalysis group, Debye Institute for Nanomaterials Science, Utrecht University, 3584 CG Utrecht, The Netherlands; Dutch Polymer Institute (DPI), 5600 AX Eindhoven, The Netherlands;* orcid.org/0000-0001-5245-1426; Email: b.m.weckhuysen@uu.nl

Elena Groppo − *Department of Chemistry, INSTM and NIS Centre, University of Torino, 10135 Torino, Italy; Dutch Polymer Institute (DPI), 5600 AX Eindhoven, The Netherlands;* orcid.org/0000-0003-4153-5709; Email: elena.groppo@unito.it

Florian Meirer − *Inorganic Chemistry and Catalysis group, Debye Institute for Nanomaterials Science, Utrecht University, 3584 CG Utrecht, The Netherlands; Dutch Polymer Institute (DPI), 5600 AX Eindhoven, The Netherlands;* orcid.org/0000-0001-5581-5790; Email: f.meirer@uu.nl

Authors

Maximilian J. Werny − *Inorganic Chemistry and Catalysis group, Debye Institute for Nanomaterials Science, Utrecht University, 3584 CG Utrecht, The Netherlands; Dutch Polymer Institute (DPI), 5600 AX Eindhoven, The Netherlands;* orcid.org/0000-0002-5714-3446

Jelena Zarupski − *Department of Chemistry, INSTM and NIS Centre, University of Torino, 10135 Torino, Italy; Dutch Polymer Institute (DPI), 5600 AX Eindhoven, The Netherlands*

Iris C. ten Have − *Inorganic Chemistry and Catalysis group, Debye Institute for Nanomaterials Science, Utrecht University, 3584 CG Utrecht, The Netherlands*

Alessandro Piovano − *Department of Chemistry, INSTM and NIS Centre, University of Torino, 10135 Torino, Italy; Dutch Polymer Institute (DPI), 5600 AX Eindhoven, The Netherlands;* orcid.org/0000-0002-5784-6897

Coen Hendriksen − *SABIC Technology Center, 6167 RD Geleen, The Netherlands*

Nicolaas H. Friederichs − *SABIC Technology Center, 6167 RD Geleen, The Netherlands*

Complete contact information is available at: https://pubs.acs.org/10.1021/jacsau.1c00324

Author Contributions

$^{\nabla}$These authors contributed equally. M.J.W. performed the FIB-SEM experiments, I.C.t.H. and M.J.W. carried out the PiFM experiments, and J.Z. and A.P. conducted the probe molecule FT-IR experiments. C.H. and N.H.F. provided the metallocene-based catalyst samples. The manuscript was written through contributions of all authors. All authors have given approval to the final version of the manuscript.

Funding

The research was funded by a grant from the Dutch Polymer Institute (DPI, P.O. Box 902, 5600 AX Eindhoven, The Netherlands) and represents a part of the Research Program of DPI project no. 813. Additional funding comes from The Netherlands Center for Multiscale Catalytic Energy Conversion (MCEC), a Dutch Research Council (NWO) Gravitation program funded by the Ministry of Education, Culture and Science of the government of The Netherlands.

Notes

The authors declare no competing financial interest.

■ ACKNOWLEDGMENTS

Our appreciation goes to Derek Nowak (Molecular Vista Inc.) for his advice on PiFM.

■ REFERENCES

(1) Severn, J. R.; Chadwick, J. C.; Duchateau, R.; Friederichs, N. Bound but Not Gagged" - Immobilizing Single-Site α-Olefin Polymerization Catalysts. *Chem. Rev.* **2005**, *105* (11), 4073−4147.

(2) Soares, J. B. P.; McKenna, T. F. L. *Polyolefin Reaction Engineering*, 1st ed.; Wiley-VCH: Weinheim, Germany, 2012.

(3) Fink, G.; Steinmetz, B.; Zechlin, J.; Przybyla, C.; Tesche, B. Propene Polymerization with Silica-Supported Metallocene/MAO Catalysts. *Chem. Rev.* **2000**, *100* (4), 1377−1390.

(4) Fink, G.; Tesche, B.; Korber, F.; Knoke, S. The Particle-Forming Process of SiO_2-Supported Metallocene Catalysts. *Macromol. Symp.* **2001**, *173* (1), 77−87.

(5) Horáčková, B.; Grof, Z.; Kosek, J. Dynamics of Fragmentation of Catalyst Carriers in Catalytic Polymerization of Olefins. *Chem. Eng. Sci.* **2007**, *62* (18−20), 5264−5270.

(6) Machado, F.; Lima, E. L.; Pinto, J. C.; McKenna, T. F. An Experimental Study on the Early Stages of Gas-Phase Olefin Polymerizations Using Supported Ziegler−Natta and Metallocene Catalysts. *Polym. Eng. Sci.* **2011**, *51* (2), 302−310.

(7) Bossers, K. W.; Valadian, R.; Zanoni, S.; Smeets, R.; Friederichs, N.; Garrevoet, J.; Meirer, F.; Weckhuysen, B. M. Correlated X-Ray Ptychography and Fluorescence Nano-Tomography on the Fragmentation Behavior of an Individual Catalyst Particle during the Early Stages of Olefin Polymerization. *J. Am. Chem. Soc.* **2020**, *142* (8), 3691−3695.

(8) Bossers, K. W.; Valadian, R.; Garrevoet, J.; van Malderen, S.; Chan, R.; Friederichs, N.; Severn, J.; Wilbers, A.; Zanoni, S.; Jongkind, M. K.; et al. Heterogeneity in the Fragmentation of Ziegler Catalyst Particles during Ethylene Polymerization Quantified by X-Ray Nanotomography. *JACS Au* **2021**, *1* (6), 852−864.

(9) Zanoni, S.; Nikolopoulos, N.; Welle, A.; Vantomme, A.; Weckhuysen, B. Early-Stage Particle Fragmentation Behavior of a

Commercial Silica-Supported Metallocene Catalyst. *Catal. Sci. Technol.* **2021**, *11* (15), 5335−5348.

(10) Weickert, G.; Meier, G. B.; Pater, J. T. M.; Westerterp, K. R. The Particle as Microreactor: Catalytic Propylene Polymerizations with Supported Metallocenes and Ziegler-Natta Catalysts. *Chem. Eng. Sci.* **1999**, *54* (15−16), 3291−3296.

(11) McKenna, T. F.; Soares, J. B. P. Single Particle Modelling for Olefin Polymerization on Supported Catalysts: A Review and Proposals for Future Developments. *Chem. Eng. Sci.* **2001**, *56* (13), 3931−3949.

(12) Böhm, L. L. The Ethylene Polymerization with Ziegler Catalysts: Fifty Years after the Discovery. *Angew. Chem., Int. Ed.* **2003**, *42* (41), 5010−5030.

(13) McKenna, T.; Mattioli, V. Progress in Describing Particle Growth for Polyolefins: A Look at Particle Morphology. *Macromol. Symp.* **2001**, *173*, 149−162.

(14) McKenna, T. F. L.; Di Martino, A.; Weickert, G.; Soares, J. B. P. Particle Growth during the Polymerisation of Olefins on Supported Catalysts, 1 - Nascent Polymer Structures. *Macromol. React. Eng.* **2010**, *4* (1), 40−64.

(15) Resconi, L.; Cavallo, L.; Fait, A.; Piemontesi, F. Selectivity in Propene Polymerization with Metallocene Catalysts. *Chem. Rev.* **2000**, *100* (4), 1253−1345.

(16) Ewen, J. A.; Haspeslach, L.; Atwood, J. L.; Zhang, H. Crystal Structures and Stereospecific Propylene Polymerizations with Chiral Hafnium Metallocene Catalysts. *J. Am. Chem. Soc.* **1987**, *109* (21), 6544−6545.

(17) Rieger, B.; Troll, C.; Preuschen, J. Ultrahigh Molecular Weight Polypropene Elastomers by High Activity "Dual-Side" Hafnocene Catalysts. *Macromolecules* **2002**, *35* (15), 5742−5743.

(18) Laine, A.; Linnolahti, M.; Pakkanen, T. A.; Severn, J. R.; Kokko, E.; Pakkanen, A. Comparative Theoretical Study on Homopolymerization of α-Olefins by Bis(Cyclopentadienyl) Zirconocene and Hafnocene: Elemental Propagation and Termination Reactions between Monomers and Metals. *Organometallics* **2010**, *29* (7), 1541−1550.

(19) Machat, M. R.; Fischer, A.; Schmitz, D.; Vöst, M.; Drees, M.; Jandl, C.; Pöthig, A.; Casati, N. P. M.; Scherer, W.; Rieger, B. Behind the Scenes of Group 4 Metallocene Catalysis: Examination of the Metal-Carbon Bond. *Organometallics* **2018**, *37* (16), 2690−2705.

(20) Busico, V.; Cipullo, R.; Pellecchia, R.; Talarico, G.; Razavi, A. Hafnocenes and MAO: Beware of Trimethylaluminum! *Macromolecules* **2009**, *42* (6), 1789−1791.

(21) Ehm, C.; Cipullo, R.; Budzelaar, P. H. M.; Busico, V. Role(s) of TMA in Polymerization. *Dalt. Trans.* **2016**, *45* (16), 6847−6855.

(22) De Winter, D. A. M.; Meirer, F.; Weckhuysen, B. M. FIB-SEM Tomography Probes the Mesoscale Pore Space of an Individual Catalytic Cracking Particle. *ACS Catal.* **2016**, *6* (5), 3158−3167.

(23) Grof, Z.; Kosek, J.; Marek, M. Modeling of Morphogenesis of Growing Polyolefin Particles. *AIChE J.* **2005**, *51* (7), 2048−2067.

(24) Tisse, V. F.; Prades, F.; Briquel, R.; Boisson, C.; McKenna, T. F. L. Role of Silica Properties in the Polymerisation of Ethylene Using Supported Metallocene Catalysts. *Macromol. Chem. Phys.* **2010**, *211* (1), 91−102.

(25) Taniike, T.; Funako, T.; Terano, M. Multilateral Characterization for Industrial Ziegler − Natta Catalysts toward Elucidation of Structure − Performance Relationship. *J. Catal.* **2014**, *311*, 33−40.

(26) Bashir, M. A.; Monteil, V.; Boisson, C.; McKenna, T. F. L. Experimental Proof of the Existence of Mass-Transfer Resistance During Early Stages of Ethylene Polymerization with Silica Supported Metallocene/MAO Catalysts. *AIChE J.* **2017**, *63* (10), 4476−4490.

(27) Gu, K. L.; Zhou, Y.; Morrison, W. A.; Park, K.; Park, S.; Bao, Z. Nanoscale Domain Imaging of All-Polymer Organic Solar Cells by Photo-Induced Force Microscopy. *ACS Nano* **2018**, *12* (2), 1473−1481.

(28) Sun, C.; Pan, F.; Bin, H.; Zhang, J.; Xue, L.; Qiu, B.; Wei, Z.; Zhang, Z. G.; Li, Y. A Low Cost and High Performance Polymer Donor Material for Polymer Solar Cells. *Nat. Commun.* **2018**, *9* (1), 1−10.

(29) Dazzi, A.; Prater, C. B.; Hu, Q.; Chase, D. B.; Rabolt, J. F.; Marcott, C. AFM − IR : Combining Atomic Force Microscopy and Infrared Spectroscopy for Nanoscale Chemical Characterization. *Appl. Spectrosc.* **2012**, *66* (12), 1365−1384.

(30) Eby, T.; Gundusharma, U.; Lo, M.; Sahagian, K.; Marcott, C.; Kjoller, K. Reverse Engineering of Polymeric Multilayers Using AFM-Based Nanoscale IR Spectroscopy and Thermal Analysis. *Spectrosc. Eur.* **2012**, *24* (3), 18−21.

(31) Tang, F.; Bao, P.; Su, Z. Analysis of Nanodomain Composition in High-Impact Polypropylene by Atomic Force Microscopy-Infrared. *Anal. Chem.* **2016**, *88*, 4926−4930.

(32) Kelchtermans, M.; Lo, M.; Dillon, E.; Kjoller, K.; Marcott, C. Characterization of a Polyethylene-Polyamide Multilayer Film Using Nanoscale Infrared Spectroscopy and Imaging. *Vib. Spectrosc.* **2016**, *82*, 10−15.

(33) Nguyen-Tri, P.; Ghassemi, P.; Carriere, P.; Nanda, S.; Assadi, A. A.; Nguyen, D. D. Recent Applications of Advanced Atomic Force Microscopy in Polymer Science: A Review. *Polymers* **2020**, *12* (5), 1142.

(34) Nowak, D.; Morrison, W.; Wickramasinghe, H. K.; Jahng, J.; Potma, E.; Wan, L.; Ruiz, R.; Albrecht, T. R.; Schmidt, K.; Frommer, J.; et al. Nanoscale Chemical Imaging by Photoinduced Force Microscopy. *Sci. Adv.* **2016**, *2* (3), No. e1501571.

(35) Fu, D.; Park, K.; Delen, G.; Attila, Ö.; Meirer, F.; Nowak, D.; Park, S.; Schmidt, J. E.; Weckhuysen, B. M. Nanoscale Infrared Imaging of Zeolites Using Photoinduced Force Microscopy. *Chem. Commun.* **2017**, *53* (97), 13012−13014.

(36) Murdick, R. A.; Morrison, W.; Nowak, D.; Albrecht, T. R.; Jahng, J.; Park, S. Photoinduced Force Microscopy: A Technique for Hyperspectral Nanochemical Mapping. *Jpn. J. Appl. Phys.* **2017**, *56* (8S1), No. 08LA04.

(37) Delen, G.; Monai, M.; Meirer, F.; Weckhuysen, B. M. In Situ Nanoscale Infrared Spectroscopy of Water Adsorption on Nanoislands of Surface-Anchored Metal-Organic Frameworks. *Angew. Chem.* **2021**, *133* (3), 1644−1648.

(38) Li, J.; Jahng, J.; Pang, J.; Morrison, W.; Li, J.; Lee, E. S.; Xu, J. J.; Chen, H. Y.; Xia, X. H. Tip-Enhanced Infrared Imaging with Sub-10 nm Resolution and Hypersensitivity. *J. Phys. Chem. Lett.* **2020**, *11* (5), 1697−1701.

(39) Almajhadi, M. A.; Uddin, S. M. A.; Wickramasinghe, H. K. Observation of Nanoscale Opto-Mechanical Molecular Damping as the Origin of Spectroscopic Contrast in Photo Induced Force Microscopy. *Nat. Commun.* **2020**, *11* (1), 1−9.

(40) ten Have, I. C.; Duijndam, A. J. A.; Oord, R.; Berlo-van den Broek, H. J. M.; Vollmer, I.; Weckhuysen, B. M.; Meirer, F. Photoinduced Force Microscopy as an Efficient Method Towards the Detection of Nanoplastics. *Chem. Methods* **2021**, *1* (5), 205−209.

(41) Ocaña, M.; Fornés, V.; Serna, C. J. The Variability of the Infrared Powder Spectrum of Amorphous SiO_2. *J. Non-Cryst. Solids* **1989**, *107*, 187−192.

(42) Almeida, R. M. Comment on "Infrared-Reflectance Spectra of Heat-Treated, Sol-Gel-Derived Silica. *Phys. Rev. B: Condens. Matter Mater. Phys.* **1996**, *53* (21), 14656−14658.

(43) Ruddick, V. J.; Badyal, J. P. S. AFM Study of the Breakup of Catalyst Particles during Ethylene Polymerization. *J. Phys. Chem. B* **1997**, *101* (10), 1791−1793.

(44) Pang, G. K. H.; Baba-Kishi, K. Z.; Patel, A. Topographic and Phase-Contrast Imaging in Atomic Force Microscopy. *Ultramicroscopy* **2000**, *81* (2), 35−40.

(45) Schmitz, I.; Schreiner, M.; Friedbacher, G.; Grasserbauer, M. Phase Imaging as an Extension to Tapping Mode AFM for the Identification of Material Properties on Humidity-Sensitive Surfaces. *Appl. Surf. Sci.* **1997**, *115* (2), 190−198.

(46) Magonov, S. N.; Elings, V.; Whangbo, M. H. Phase Imaging and Stiffness in Tapping-Mode Atomic Force Microscopy. *Surf. Sci.* **1997**, *375* (2−3), L385−L391.

(47) Scott, W. W.; Bhushan, B. Use of Phase Imaging in Atomic Force Microscopy for Measurement of Viscoelastic Contrast in

Polymer Nanocomposites and Molecularly Thick Lubricant Films. *Ultramicroscopy* **2003**, *97* (1−4), 151−169.

(48) Bar, G.; Thomann, Y.; Brandsch, R.; Cantow, H. J.; Whangbo, M. H. Factors Affecting the Height and Phase Images in Tapping Mode Atomic Force Microscopy. Study of Phase-Separated Polymer Blends of Poly(Ethene-Co-Styrene) and Poly(2,6-Dimethyl-1,4-Phenylene Oxide). *Langmuir* **1997**, *13* (14), 3807−3812.

(49) Wang, L. Role of Damping in Phase Imaging in Tapping Mode Atomic Force Microscopy. *Surf. Sci.* **1999**, *429* (1), 178−185.

(50) Zecchina, A.; Areán, C. O. Diatomic Molecular Probes for Mid-IR Studies of Zeolites. *Chem. Soc. Rev.* **1996**, *25* (3), 187−197.

(51) Lamberti, C.; Zecchina, A.; Groppo, E.; Bordiga, S. Probing the Surfaces of Heterogeneous Catalysts by in Situ IR Spectroscopy. *Chem. Soc. Rev.* **2010**, *39* (12), 4951−5001.

(52) Groppo, E.; Lamberti, C.; Bordiga, S.; Spoto, G.; Zecchina, A. The Structure of Active Centers and the Ethylene Polymerization Mechanism on the Cr/SiO_2 Catalyst: A Frontier for the Characterization Methods. *Chem. Rev.* **2005**, *105* (1), 115−183.

(53) Groppo, E.; Martino, G. A.; Piovano, A.; Barzan, C. The Active Sites in the Phillips Catalysts: Origins of a Lively Debate and a Vision for the Future. *ACS Catal.* **2018**, *8* (11), 10846−10863.

(54) Zakharov, V. A.; Paukshtis, E. A.; Mikenas, T. B.; Volodin, A. M.; Vitus, E. N.; Potapov, A. G. Surface Acidic Sites of Highly Disperse Magnesium Chloride: IR and ESR Spectroscopy Studies. *Macromol. Symp.* **1995**, *89* (1), 55−61.

(55) Thushara, K. S.; D'Amore, M.; Piovano, A.; Bordiga, S.; Groppo, E. The Influence of Alcohols in Driving the Morphology of Magnesium Chloride Nanocrystals. *ChemCatChem* **2017**, *9* (10), 1782−1787.

(56) D'Amore, M.; Thushara, K. S.; Piovano, A.; Causà, M.; Bordiga, S.; Groppo, E. Surface Investigation and Morphological Analysis of Structurally Disordered $MgCl_2$ and $MgCl_2/TiCl_4$ Ziegler−Natta Catalysts. *ACS Catal.* **2016**, *6* (9), 5786−5796.

(57) Pletcher, P.; Welle, A.; Vantomme, A.; Weckhuysen, B. M. Quality Control for Ziegler-Natta Catalysis via Spectroscopic Fingerprinting. *J. Catal.* **2018**, *363*, 128−135.

(58) Velthoen, M. E. Z.; Muñoz-Murillo, A.; Bouhmadi, A.; Cecius, M.; Diefenbach, S.; Weckhuysen, B. M. The Multifaceted Role of Methylaluminoxane in Metallocene-Based Olefin Polymerization Catalysis. *Macromolecules* **2018**, *51* (2), 343−355.

(59) Panchenko, V. N.; Danilova, I. G.; Zakharov, V. A.; Paukshtis, E. A. An IR-Spectroscopic Study of the State of Zirconium in Supported Zirconocene Catalysts. *Kinet. Catal.* **2004**, *45* (4), 547−553.

(60) Marsella, J. A.; Curtis, C. J.; Bercaw, J. E.; Caulton, K. G. Low-Temperature Infrared Study of d° Carbonyl Complexes. *J. Am. Chem. Soc.* **1980**, *102* (24), 7244−7246.

(61) Piovano, A.; Zarupski, J.; Groppo, E. Disclosing the Interaction between Carbon Monoxide and Alkylated Ti^{3+} Species: A Direct Insight into Ziegler-Natta Catalysis. *J. Phys. Chem. Lett.* **2020**, *11* (14), 5632−5637.

(62) Desert, X.; Carpentier, J. F.; Kirillov, E. Quantification of Active Sites in Single-Site Group 4 Metal Olefin Polymerization Catalysis. *Coord. Chem. Rev.* **2019**, *386*, 50−68.

(63) Doi, Y.; Murata, M.; Yano, K.; Keii, T. Gas-Phase Polymerization of Propene with the Supported Ziegler Catalyst: $TiCl_4/MgCl_2/C_6H_5COOC_2H_5/Al(C_2H_5)_3$. *Ind. Eng. Chem. Prod. Res. Dev.* **1982**, *21* (4), 580−585.

(64) Taniike, T.; Sano, S.; Ikeya, M.; Thang, V. Q.; Terano, M. Development of a Large-Scale Stopped-Flow System for Heterogeneous Olefin Polymerization Kinetics. *Macromol. React. Eng.* **2012**, *6* (6−7), 275−279.

(65) Thakur, A.; Wada, T.; Chammingkwan, P.; Terano, M.; Taniike, T. Development of Large-Scale Stopped-Flow Technique and Its Application in Elucidation of Initial Ziegler-Natta Olefin Polymerization Kinetics. *Polymers* **2019**, *11* (6), 1012.

(66) Bukatov, G.; Goncharov, V.; Zakharov, V. Interaction of ^{14}CO with Ziegler-type Heterogeneous Catalysts and Effect of Interaction Products on the Determination of the Amount of Active Centers. *Makromol. Chem.* **1986**, *187* (5), 1041−1051.

(67) Shiono, T.; Ohgizawa, M.; Soga, K. Reaction between Carbon Monoxide and a Ti-polyethylene Bond with a $MgCl_2$-supported $TiCl_4$ Catalyst System. *Makromol. Chem.* **1993**, *194* (7), 2075−2085.

(68) Tritto, I.; Sacchi, M. C.; Locatelli, P. On the Insertion Reaction of Carbon Oxides into Metal-carbon Bonds of Ziegler-Natta Catalysts. *Makromol. Chem., Rapid Commun.* **1983**, *4* (9), 623−627.

(69) Knözinger, H. Infrared Spectroscopy as a Probe of Surface Acidity. *Elem. React. Steps Heterog. Catal.* **1993**, 267−285.

(70) Knoezinger, H.; Krietenbrink, H. Infrared Spectroscopic Study of the Adsorption of Nitriles on Aluminium Oxide. Fermi Resonance in Coordinated Acetonitrile. *J. Chem. Soc., Faraday Trans. 1* **1975**, *71*, 2421−2430.

(71) Morterra, C.; Peñarroya Mentruit, M.; Cerrato, G. Acetonitrile Adsorption as an IR Spectroscopic Probe for Surface Acidity/Basicity of Pure and Modified Zirconias. *Phys. Chem. Chem. Phys.* **2002**, *4* (4), 676−687.

(72) Morterra, C.; Cerrato, G.; Novarino, E.; Peñarroya Mentruit, M. On the Adsorption of Acetonitrile on Pure and Sulfated Tetragonal Zirconia (t-ZrO_2). *Langmuir* **2003**, *19* (14), 5708−5721.

(73) Escalona Platero, E.; Peñarroya Mentruit, M.; Morterra, C. Fourier Transform Infrared Spectroscopy Study of CD_3CN Adsorbed on Pure and Doped γ-Alumina. *Langmuir* **1999**, *15* (15), 5079−5087.

(74) Cerruti, M.; Bolis, V.; Magnacca, G.; Morterra, C. Surface Chemical Functionalities in Bioactive Glasses. The Gas/Solid Adsorption of Acetonitrile. *Phys. Chem. Chem. Phys.* **2004**, *6* (9), 2468−2479.

(75) Bochmann, M.; Wilson, L. M. Synthesis and Insertion Reactions of Cationic Alkylbis(Cyclopentadienyl) Titanium Complexes. *J. Chem. Soc., Chem. Commun.* **1986**, *0* (21), 1610−1611.

(76) Jordan, R. F.; Bajgur, C. S.; Dasher, W. E.; Rheingold, A. L. Hydrogenation of Cationic Dicyclopentadienyl Zirconium(IV) Alkyl Complexes. Characterization of Cationic Zirconium(IV) Hydrides. *Organometallics* **1987**, *6* (5), 1041−1051.

(77) Bochmann, M.; Wilson, L. M.; Hursthouse, M. B.; Motevalli, M. Insertion Reactions of Nitriles in Cationic Alkylbis-(Cyclopentadienyl)Titanium Complexes: The Facile Synthesis of Azaalkenylidene Titanium Complexes and the Crystal and Molecular Structure of $[(Indenyl)_2Ti(NCMePh)(NCPh)]BPh_4$. *Organometallics* **1988**, *7* (5), 1148−1154.

(78) Alelyunas, Y. W.; Jordan, R. F.; Echols, S. F.; Borkowsky, S. L.; Bradley, P. K. *Organometallics* **1991**, *10* (5), 1406−1416.

(79) Ystenes, M.; Eilertsen, J. L.; Liu, J.; Ott, M.; Rytter, E.; Støvneng, J. A. Experimental and Theoretical Investigations of the Structure of Methylaluminoxane (MAO) Cocatalysts for Olefin Polymerization. *J. Polym. Sci., Part A: Polym. Chem.* **2000**, *38* (17), 3106−3127.

(80) Martino, G. A.; Piovano, A.; Barzan, C.; Rabeah, J.; Agostini, G.; Bruekner, A.; Leone, G.; Zanchin, G.; Monoi, T.; Groppo, E. Rationalizing the Effect of Triethylaluminum on the Cr/SiO_2 Phillips Catalysts. *ACS Catal.* **2020**, *10* (4), 2694−2706.

(81) Zecchina, A.; Guglielminotti, E.; Coluccia, S.; Borello, E. Infrared Spectra of Nitriles of Chromia-Silica Catalyst. *J. Chem. Soc. A* **1969**, 2196−2199.

(82) Montanari, T.; Bevilacqua, M.; Busca, G. Use of Nitriles as Probe Molecules for the Accessibility of the Active Sites and the Detection of Complex Interactions in Zeolites through IR Spectroscopy. *Appl. Catal., A* **2006**, *307* (1), 21−29.

ACKNOWLEDGEMENTS

‘What we call the beginning is often the end. And to make an end is to make a beginning. The end is where we start from.’

T.S. Eliot

The end of very challenging and intense, but at same time the most beautiful period of my life arrived, and it is time to thank to all the people who was here.

The first one is my supervisor Prof. Elena Groppo who always believed in me and supported me. Her science enthusiasm and curiosity were very virulent and inspirational pushing me advance in my research. I was positively surprised many times by her patience and understanding of different situations and problems, never judging but trying to help. To illustrate her influence on my professional life, is just enough to say that when I started PhD my knowledge about topic was quite modest, and without her I will hardly be where I’m today. Elena was not just my supervisor but also a person to ask for advice and opinion, always available and sincere. Thank you for giving me this opportunity and for all the lessons I have learnt from you!

Dr. Alessandro Piovano, my lab tutor and BF who show me how to perform the experiments, supporting me during first months in the lab. He was always kind and available, making my beginning much easier. He also shared his knowledge and experience selflessly, inspiring me to learn more and more.

All Via Quarello lab members. It was a great pleasure to work in such friendly and positive environment.

The Utrech Univeristy team. Dr. Max Werny, Dr. Florian Meirer and Prof. Bert Weckhuysen for knowledge and data exchange, suggestions, and ideas. I’m very proud on the work our two teams did within the MULTIPOL project.

Nicolaas Friederichs and Dr. Coen Hendriksen from SABIC for sample procurement, and for stimulating and inspiring our research. Dr. Edrisse Chermak, always from SABIC, for his efforts to perform DFT calculations on our metallocene catalysts.

Dutch Polymer Institute, not just for founding this project but also for giving me the possibility to meet the best experts in the field coming from both academia and industry, to learn from them and to work with some of them.

My family members. Uncles Igor and Radovan, Aunt Sandra, brothers Viktor and Vladan (trough they are my cousins, I consider them as brothers since we grow

up together, loving and fighting as siblings). Thank you for always being here, especially during hard times.
My grannies Milica and Mirjana, and my mother Ljudmila. The line is underlined, and I hope you are proud on me, as I’m proud to be your granddaughter and daughter.

My most significant ones, Ferenc and Lazar for their boundless love, understanding and support.